Coherent Multiple-Quantum Multidimensional Fluorescence Spectroscopy

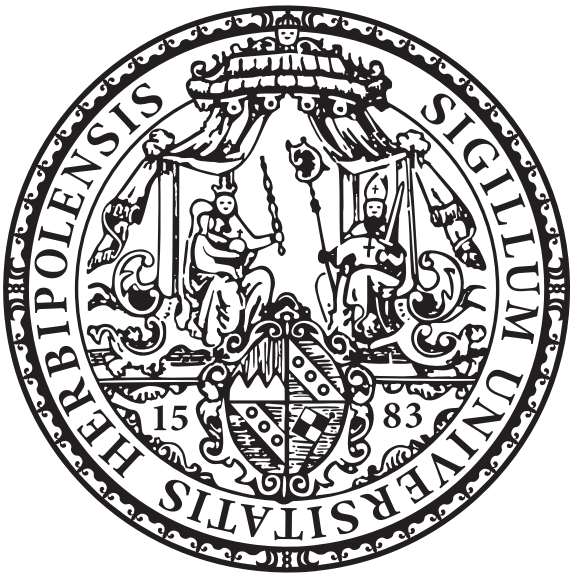

Dissertation zur Erlangung
des naturwissenschaftlichen Doktorgrades (Dr. rer. nat.)
an der Fakultät für Chemie und Pharmazie
der Julius-Maximilians-Universität Würzburg

vorgelegt von

Stefan Müller

aus Fulda

Würzburg, 2021

Eingereicht bei der Fakultät für Chemie und Pharmazie am

25. Mai 2021

Gutachter der schriftlichen Arbeit

1. Gutachter: Prof. Dr. Tobias Brixner

2. Gutachter: Prof. Dr. Roland Mitrić

Prüfer des öffentlichen Promotionskolloquiums

1. Prüfer: Prof. Dr. Tobias Brixner

2. Prüfer: Prof. Dr. Roland Mitrić

3. Prüfer: Prof. Dr. Dr. h.c. Todd B. Marder

4. Prüfer: Prof. Dr. Ann-Christin Pöppler

5. Prüfer: Prof. Dr. Ingo Fischer

Datum des öffentlichen Promotionskolloquiums

22. Juli 2021

Doktorurkunde ausgehändigt am

_____

List of Publications

This thesis is based on the following references:

[1] S. Mueller, J. Lüttig, L. Brenneis, D. Oron, and T. Brixner.
Observing multiexciton correlations in colloidal semiconductor quantum dots via multiple-quantum two-dimensional fluorescence spectroscopy.
ACS Nano **15**, 4647–4657 (2021).

[2] P. Malý, S. Mueller, J. Lüttig, C. Lambert, and T. Brixner.
Signatures of exciton dynamics and interaction in coherently and fluorescence-detected four- and six-wave-mixing two-dimensional electronic spectroscopy.
The Journal of Chemical Physics **153**, 144204 (2020).

[3] S. Mueller and T. Brixner.
Molecular coherent three-quantum two-dimensional fluorescence spectroscopy.
The Journal of Physical Chemistry Letters **11**, 5139–5147 (2020).

[4] S. Mueller, J. Lüttig, P. Malý, L. Ji, J. Han, M. Moos, T. B. Marder, U. H. F. Bunz, A. Dreuw, C. Lambert, and T. Brixner.
Rapid multiple-quantum three-dimensional fluorescence spectroscopy disentangles quantum pathways.
Nature Communications **10**, 4735 (2019).

[5] T. Kennweg, S. Mueller, T. Brixner, and W. Pfeiffer.
QDT — a Matlab toolbox for the simulation of coupled quantum systems and multidimensional spectroscopy.
in preparation (2021).

[6] P. Malý, S. Müller, J. Lüttig, M. Schreck, C. Lambert, and T. Brixner.
Coherently and fluorescence-detected four- and six-wave-mixing two-dimensional electronic spectroscopy: Measuring multi-exciton dynamics and delocalization.
The 22nd International Conference on Ultrafast Phenomena 2020, F. Kärtner, M. Khalil, R. Li, F. Légaré, and T. Tahara, eds., OSA Technical Digest (Optical Society of America, 2020), paper Tu4A.4.

[7] P. Malý, J. Lüttig, S. Mueller, M. Schreck, C. Lambert, and T. Brixner.
Coherently and fluorescence-detected two-dimensional electronic spectroscopy: Direct comparison on squaraine dimers.
Physical Chemistry Chemical Physics **22**, 21222–21237 (2020).

[8] S. Müller, S. Draeger, N. Klosterhalfen, and T. Brixner.
Fluorescence-detected two-quantum and one-quantum–two-quantum 2D electronic spectroscopy of Rhodamine 700.
EPJ Web of Conferences **205**, 03012 (2019).

[9] S. Mueller, S. Draeger, X. Ma, M. Hensen, T. Kenneweg, W. Pfeiffer, and T. Brixner.
Fluorescence-detected two-quantum and one-quantum–two-quantum 2D electronic spectroscopy.
The Journal of Physical Chemistry Letters **9**, 1964–1969 (2018).

Additional publications:

[10] R. König, S. Müller, R. E. Dinnebier, B. Hinrichsen, P. Müller, A. Ribbens, J. Hwang, R. Liebscher, M. Etter, and C. Pistidda.
The crystal structures of carbonyl iron powder — revised using in situ synchrotron XRPD.
Zeitschrift für Kristallographie – Crystalline Materials **232**, 835–842 (2017).

The peer-reviewed journal articles [1–4] have been used in this dissertation. The table below summarizes to which extent material from these publications has been reused in text passages of this dissertation. Permissions to reproduce copyrighted material were obtained from the corresponding journals, as stated below. In case figures were reproduced completely or in part, an appropriate additional statement at the end of the corresponding figure caption is given.

Publication		**Use**	**Dissertation**
Ref. [1]		text and figures reproduced	pp. 55–83
Ref. [2]	pp. 4–5	figure adapted in part and modified, new text	pp. 130–132
	pp. 11–13	text modified and extended	pp. 132–140
	pp. S1–S6	text modified and extended, figures adapted in part and modified	pp. 132–140
	pp. 5–6	text modified and extended	pp. 140–142
	p. 5	text modified and extended, figure reproduced in part	pp. 143–144
	p. 8, pp. 10–13	text modified and extended, figures adapted and modified	pp. 144–149
	p. 6, pp. S8–S9	text modified, figure adapted and modified, table reproduced	pp. 172–174
Ref. [3]		text and figures reproduced	pp. 29–53
Ref. [4]		text and figures reproduced	pp. 85–124

Permissions to reproduce copyrighted work in this thesis

Remarks:

All footnotes in Chapters 2–4 were not part of the respective research publications and are therefore additional annotations by the author.

The operator notation by a "hat" is omitted throughout this work, i.e.,"$\hat{H}$" is expressed by "H" etc.

Table of Contents

Chapter 1

General Introduction

1.1 Preface

Everything that we can perceive around us through our eyes is matter interacting with light. Visible light can be absorbed, causing the formation of electronically excited states, the properties of which ultimately determine important properties of matter. In fact, our world would be quite a lifeless place if there were no excited states.

Spectroscopy is our tool that sheds light on the properties of excited states by measuring the matter response to light. A variety of spectroscopic methods have been developed to consolidate our understanding of matter, using probes ranging from long radio-frequency to short x-ray waves. Although visible light seems almost trivial to us due to its omnipresence, its interaction with the electronic structure of quantum systems is a central component of a research field at the interface between chemistry and physics.

Why do we need to develop new spectroscopic methods? We are still in the process of deciphering the essential mechanisms that could one day give us the key to cover our growing energy demands. With regard to the current climate debate, new concepts for energy generation are in greater demand than ever. The field of light–matter interaction is in this respect of particular importance for the development of photovoltaics. Building artificial devices that efficiently produce electric energy benefits from precise knowledge of the underlying physics. Sophisticated spectroscopic approaches help to identify and scrutinize the crucial processes which are responsible for efficient energy conversion, such that chemistry and material science can be inspired to design the appropriate target systems.

Erwin Hahn's demonstration of a spin echo in 1950 laid the foundation to develop sequences of pulsed electromagnetic radiation, which manipulate a system in such a sophisticated way, so that one could unveil detailed information about its intricate ge-

ometrical properties [11, 12]. 14 years after Hahn's experiment, the optical analogue to the spin echo – a photon echo – was demonstrated [13]. Since then, coherent optical spectroscopies have continuously been further developed as a means to study the static and dynamical properties of the electronic structure of quantum systems. Finally, the advent of the femtosecond laser provided the time resolution required to measure the ultrafast processes associated with electronically excited states. Very recently, the development of a method to generate the ultrashort high-intensity laser pulses needed for such experiments, has been awarded with the Nobel Prize in Physics [14]. These high-intensity laser pulses set the stage to develop nonlinear spectroscopic methods that interrogate excitation dynamics with unprecedented detail. As such, coherent multidimensional spectroscopy emerged as a method that disentangles intricate details about ultrafast coherent dynamics, energy transport, and couplings.

The purpose of the following introduction is to give the reader an overview of the most essential concepts needed to theoretically describe fluorescence-detected multidimensional spectroscopy. In particular, we will focus on the density matrix as a basis for a sample system description. Then, we will learn how we can reveal the system properties by utilizing phase-coherent pulse sequences, and in turn construct two-dimensional (2D) and three-dimensional (3D) spectra. To this end, we will introduce response function theory, which is employed as a tool to interpret the experimental spectra presented in this work. The last section deals with phase cycling, an experimental procedure that allows us to simultaneously acquire a multitude of nonlinear signals, and which is exploited in this work to measure novel types of nonlinear signals.

1.2 Concepts of Coherent Multidimensional Fluorescence Spectroscopy

1.2.1 Density Matrix Formalism and Quantum Coherences

The quantum-mechanical state of an isolated microscopic system is described by the wave function $|\psi\rangle$ in Hilbert space. The wave function is a rather abstract entity that ultimately carries all information about the system – it can be interpreted as the amplitude of a "matter wave" [15, 16]. The temporal evolution of the system is described by the time-dependent formulation of the famous Schrödinger equation,

$$\frac{\partial}{\partial t}|\psi(t)\rangle = -\frac{i}{\hbar}H(t)|\psi(t)\rangle\,, \tag{1.1}$$

where $H(t)$ denotes the Hamiltonian that governs the system dynamics.[1] The connection of $|\psi(t)\rangle$ to the molecular electronic or excitonic states, as investigated in this work, can be found by expanding the wave function as a linear combination of stationary system eigenstates $|n\rangle$ with frequencies ω_n and expansion coefficients c_n by

$$|\psi(t)\rangle = \sum_n c_n \mathrm{e}^{-\mathrm{i}\omega_n t}|n\rangle\,, \tag{1.2}$$

which is a solution for Eq. (1.1) in absence of an external field [17]. The state energies E_n are then given by $H_0|n\rangle = E_n|n\rangle$, where H_0 is the stationary Hamiltonian.

While Eq. (1.1) describes dynamics of a system represented by a single wave function, that is, a "pure" state [18], the wave function formulation lacks to describe phenomena which a spectroscopist frequently observes in "real samples," that is, a statistical mixture of quantum systems. Every investigated sample system in this work is composed of molecules or nanocrystals in a solvent. Since every component may experience a different environment, we can not deal with an ensemble of identical components. Thus, we need to use a system description that considers mixed states and further allows us to introduce a suitable treatment for the system-bath interaction later on. This requirement is met by using a statistical system formulation in terms of a density matrix $\rho(t)$,[2]

$$\rho(t) \equiv |\psi(t)\rangle\langle\psi(t)| = \sum_m \sum_n c_m^* \mathrm{e}^{\mathrm{i}\omega_m t} c_n \mathrm{e}^{-\mathrm{i}\omega_n t}|n\rangle\langle m|\,, \tag{1.3}$$

[1] $\hbar = 1.055 \times 10^{-34}$Js [17].

[2] The density matrix is formally an operator. As this density operator commutes with H, both ρ and H have the same set of eigenfunctions. This means that $|\psi\rangle$ is an eigenfunction to ρ as it fulfills the eigenvalue problem $\rho|\psi\rangle = |\psi\rangle\langle\psi|\psi\rangle = \mathbb{1}|\psi\rangle$, where $\mathbb{1}$ results from the normalization of $|\psi\rangle$ [18].

where we made use of Eq. (1.2) [17, 19]. The temporal evolution of the density matrix can be expressed as

$$\begin{aligned}\frac{\partial}{\partial t}\rho(t) = \frac{\partial}{\partial t}\big(|\psi(t)\rangle\langle\psi(t)|\big) &= \left(\frac{\partial}{\partial t}|\psi(t)\rangle\right)\langle\psi(t)| + |\psi(t)\rangle\left(\frac{\partial}{\partial t}\langle\psi(t)|\right) \\ &= -\frac{i}{\hbar}H(t)\,|\psi(t)\rangle\langle\psi(t)| + \frac{i}{\hbar}\,|\psi(t)\rangle\langle\psi(t)|\,H(t), \end{aligned} \tag{1.4}$$

where we used Eq. (1.1) and its complex-conjugated form to finally yield the Liouville–von Neumann equation [17],

$$\frac{\partial}{\partial t}\rho(t) = -\frac{i}{\hbar}\left[H(t), \rho(t)\right], \tag{1.5}$$

where the commutator $[H(t), \rho(t)]$ is defined by $H(t)\rho(t) - \rho(t)H(t)$. For purposes of spectroscopy, we can invoke the time-dependent Hamiltonian

$$H(t) = H_0 + H_{\text{ext}}(t) = H_0 - \mu E(t), \tag{1.6}$$

where $H_{\text{ext}}(t)$ is described by the transition dipole moment operator μ and the external electric field $E(t)$.

An important distinction is made between diagonal and off-diagonal density matrix elements. For the diagonal elements ($n = m$), we obtain [19]

$$\rho_{nn}(t) = \langle n|\,\rho(t)\,|n\rangle = |c_n(t)|^2 \tag{1.7}$$

with the probability density $|c_n(t)|^2$, which is equivalent to the probability of finding the system in state $|n\rangle$. In that sense, all diagonal elements of the density matrix describe populations of the system. Note that c_n is now time-dependent due to the coupling to an external field [17]. Off-diagonal density matrix elements ($n \neq m$) are given by

$$\rho_{nm}(t) = \langle n|\,\rho(t)\,|m\rangle = c_m^*(t)c_n(t)\mathrm{e}^{\mathrm{i}(\omega_m - \omega_n)t}, \tag{1.8}$$

which represent "coherences," that is, coherent superpositions of the system eigenstates $|m\rangle$ and $|n\rangle$, oscillating with the difference of their frequencies ω_m and ω_n, respectively.

It is worth noting that the density matrix is an alternative system description that operates in the "more directly interpretable" basis of probabilities. Hence, in contrast to the wave function, the density matrix conveniently allows us to associate its matrix elements with specific observables [18] using the relation

$$\langle\mathcal{A}\rangle = \mathrm{Tr}\left\{\mathcal{A}\rho\right\}, \tag{1.9}$$

where $\langle\mathcal{A}\rangle$ is the expectation value of an operator $\mathcal{A}$ and "Tr" is the trace. Importantly, the density matrix contains, like the wave function, all information about the system.

The Liouville–von Neumann equation [Eq. (1.5)] allows us to determine the dynamical evolution of the system under the effect of the Hamiltonian $H(t)$. However, as seen from Eqs. (1.7) and (1.8), populations behave as constant and coherences oscillate "forever." Thus, two important aspects are still missing – pure dephasing, which is phase loss of the coherences caused by environmental fluctuations, and population decay. To include these, Eq. (1.5) can be extended to

$$\frac{\partial}{\partial t}\rho(t) = -\frac{\mathrm{i}}{\hbar}\left[H(t), \rho(t)\right] + \mathcal{D}\rho(t), \tag{1.10}$$

where the superoperator $\mathcal{D}$ accounts for relaxation and dephasing processes [20]. In particular, $\mathcal{D}$ can be constructed in a sophisticated manner accounting for the system-bath interaction, resulting, for example, in the so-called Lindblad master equation [21, 22], which is further discussed in Sec. 2.5.3. For now, we shall use a phenomenological relaxation description that utilizes exponential pure dephasing associated with a time T_2^* and population decay by T_1 [17]. Throughout this introduction, we will exemplarily consider a system which is described by a ground state $|g\rangle$, a first excited state $|e\rangle$ and a doubly excited state $|f\rangle$ in Hilbert space (Fig. 1.1a). This three-level system provides the basis to discuss the essential features of a nonlinear spectrum as it will be shown later. Let us excite our sample system with a single optical pulse with center frequency ω_0 at $t = 0$ (Fig. 1.1b) using a field strength that induces a *nonlinear response*. For the sake of simplicity, this pulse shall be infinitesimally short. Using Eq. (1.10), we can calculate the resulting density matrix dynamics, as schematically illustrated in Fig. 1.1c.

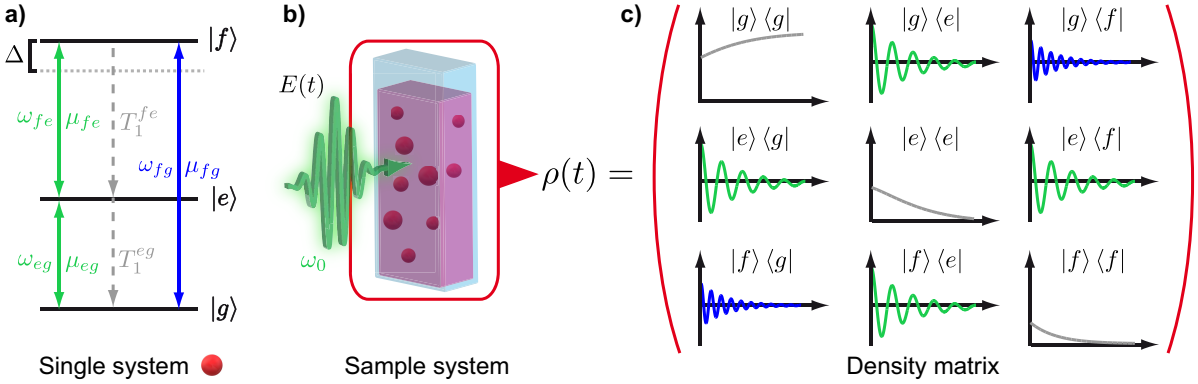

Figure 1.1. Propagation of the density matrix induced by a single short pulse. (a) Level scheme of a single system with eigenstates $|g\rangle$, $|e\rangle$, and $|f\rangle$ with associated transition frequencies ω_{nm}, transition dipole moments μ_{nm}, population relaxation times T_1^{nm}, and "anharmonicity" $\Delta = \omega_{fe} - \omega_{eg}$. (b) Sample system, consisting of an ensemble of quantum systems embedded in a solvent bath and interacting with an electric field $E(t)$, yielding (c) the dynamics of the density matrix elements. One- and two-quantum coherences are drawn in green and blue, respectively, while populations are drawn in gray.

The excitation by a single pulse initiates dynamics in all density matrix elements. One can show that this is a consequence of the perturbative expansion of the density matrix, which is discussed in the next section. For now, we shall just consider the result in terms of the individual density matrix elements. Considering the coherences, the $|e\rangle\langle g|$ matrix element is induced by a single light-field interaction and hence oscillates with a frequency that is close to the center frequency of the light pulse. Such a coherence represents a so-called single-quantum (1Q) coherence (green in Fig. 1.1). Similarly, the $|f\rangle\langle e|$ matrix element oscillates with a frequency close to $|e\rangle\langle g|$, thus it also represents a 1Q coherence. As the $|f\rangle\langle g|$ matrix element oscillates at nearly twice the frequency of ω_0, we speak of a two-quantum (2Q) coherence, often also called double-quantum coherence (blue in Fig. 1.1). The 2Q coherence belongs to the family of so-called "multiple-quantum coherences," referred to in the title of this thesis. Generally, multiple-quantum coherence refers to coherent superpositions of excited electronic states with another electronic state, which energetically differ in more than one excitation quantum of visible light.[3]

From the dynamical evolution of the density matrix (Fig. 1.1c), we can infer a wealth of information about the system. In particular, population decay rates can be characterized by the decay of the diagonal elements whereas the off-diagonal elements are damped by the homogeneous dephasing time T_2 which is given by [17]

$$\frac{1}{T_2} = \frac{1}{2T_1} + \frac{1}{T_2^*}. \tag{1.11}$$

In addition, the oscillation frequencies of the coherences give us access to the state energies, whereas the transition dipole moments are proportional to the initial amplitude of each matrix element. Evidently, the system Hamiltonian imprints its information on the density matrix elements. Hence, if we were able to *completely measure* the density matrix, we could ultimately reconstruct the full system Hamiltonian. How can we accomplish this goal experimentally? Employing a single optical pulse and detecting the system response would not be sufficient, as we can not interrogate any dynamics. By using two time-delayed pulses, we could interrogate some dynamics, but since many dynamical processes take place simultaneously (Fig. 1.1c), the obtained signal would be somewhat ambiguous. Thus, let us go one step further and consider that we could prepare correlations between density matrix elements. This is where 2D spectroscopy sets in. By using multipulse experiments, one constructs and probes *excitation pathways*, that is, sequences of concatenated density matrix elements. As we will see in the

[3]The term "multiple-quantum coherence" was originally used in NMR spectroscopy to describe superpositions between nuclear spin states that differ by more than one unit in the magnetic quantum number, requiring multiple quanta of the excitation radio-frequency fields [23, 24].

next sections, a particular task of 2D spectroscopy is to separate off groups of certain excitation pathways from the nonlinear response of the system, facilitating us to study intricate system details resulting from (dynamical) interactions between states such as energy transfer processes and electron correlations.

1.2.2 Response Functions and Double-Sided Feynman Diagrams

In the previous section, we have seen that the density matrix provides a practical basis for the system description, holding a wealth of information. The key to a complete characterization of the nonlinear response of a system lies in the construction of excitation pathways, the entirety of which constitute the nonlinear system response. Let us now design an experiment that traces pathways through the system density matrix. The basic principle is to utilize multiple consecutive interactions with a laser field to manipulate the density matrix [17]. To accomplish this, one could plug in time-delayed multipulse fields into $H_{\text{ext}}(t)$ of the Hamiltonian in Eq. (1.6) and solve the differential equation (1.10) numerically (see Secs. 2.5.3 and 4.5.6). However, this approach demands a relatively high computational cost, which makes approximate treatments attractive. In order to adequately approximate the nonlinear response of open quantum systems, perturbation theory has proven to be particularly valuable [19, 25]. As we will see in the following, a beneficial consequence of a perturbative treatment is the ability to dissect the nonlinear response function into intuitively understandable diagrams which represent the individual excitation pathways.

At the beginning of each perturbative approach, one formulates a series expansion, in this case of the system's density matrix at a time t' in powers n of the external field,

$$\rho_I(t') = \sum_{n=0} \rho_I^{(n)}(t'), \tag{1.12}$$

where we introduced the interaction picture by the subscript I. In the interaction picture, every operator $\mathcal{O}(t')$ is formulated by means of the evolution operator $U(t', t_0)$ as [26]

$$\mathcal{O}_I(t') = U^\dagger(t', t_0)\mathcal{O}(t')U(t', t_0) = \mathrm{e}^{\frac{\mathrm{i}}{\hbar}H_0(t'-t_0)}\mathcal{O}(t')\mathrm{e}^{-\frac{\mathrm{i}}{\hbar}H_0(t'-t_0)}. \tag{1.13}$$

Inserting Eq. (1.12) into the Liouville–von Neumann equation [Eq. (1.5)] using nth-order perturbation theory [18, 27] yields a general expression for the nth-order density matrix:

$$\begin{aligned}\rho_I^{(n)}(t') = (-1)^n \left(\frac{\mathrm{i}}{\hbar}\right)^n \int_{t_0}^{t'} \mathrm{d}\tau_n \int_{t_0}^{\tau_n} \mathrm{d}\tau_{n-1} \int_{t_0}^{\tau_{n-1}} \mathrm{d}\tau_{n-2}, \cdots \int_{t_0}^{\tau_2} \mathrm{d}\tau_1 \\ \times \Big[H_{I,\text{ext}}(\tau_n), \Big[H_{I,\text{ext}}(\tau_{n-1}), \Big[H_{I,\text{ext}}(\tau_{n-2}), \Big[\cdots, \Big[H_{I,\text{ext}}(\tau_1), \rho_I^{(0)}(t_0)\Big] \cdots \Big]\Big]\Big]\Big],\end{aligned} \tag{1.14}$$

where τ_n is the explicit time at which the nth interaction with the external field takes place [26]. The zeroth-order density matrix $\rho_I^{(0)}(t_0)$ represents the unperturbed system [17], which we define to be in the ground-state population. Now, we shall associate $\rho_I^{(n)}(t')$ with an experimentally accessible observable by using Eq. (1.9). In this respect, employing the projector $\mathcal{A} = \mu$ on an odd density matrix order refers to detecting a coherently emitted signal. In particular, the third-order density matrix is the one that provides the basis to describe coherently detected 2D and transient absorption spectroscopy [19]. In this work, however, we will focus on fourth- and sixth-order nonlinear signals probed via fluorescence emission. The generation of fluorescence, which is proportional to an excited-state population, is associated with a density matrix of an even order. We can access our observable by invoking a projection operator $\mathcal{A}$ defined as

$$\mathcal{A} = \sum_{m \neq g} \Phi_m \left| m \right\rangle \left\langle m \right|, \tag{1.15}$$

which projects onto the excited states of the system, weighted by their fluorescence quantum yields Φ_m, and then use $\mathcal{A}_I$ on $\rho_I^{(n)}(t')$ via Eq. (1.9) to obtain the nth-order population $p^{(n)}$ with $n = 2, 4, 6, \cdots$,

$$\begin{aligned} p^{(n)}(t') \equiv \langle \rho_I^{(n)}(t') \rangle = \int_0^\infty \mathrm{d}t_n \int_0^\infty \mathrm{d}t_{n-1} \cdots \int_0^\infty \mathrm{d}t_1 Q^{(n)}\left(t_n, t_{n-1}, \cdots, t_1\right) \\ \times E(t' - t_n) E(t' - t_n - t_{n-1}) \cdots E(t' - t_n - t_{n-1} \cdots - t_1), \end{aligned} \tag{1.16}$$

where $Q^{(n)}$ is the nth-order nonlinear response function [2, 19]

$$\begin{aligned} Q^{(n)}(t_n, \cdots, t_1) = \left(\frac{i}{\hbar}\right)^n \Theta(t_n)\Theta(t_{n-1}) \cdots \Theta(t_1) \\ \times \mathrm{Tr}\Big\{ \mathcal{A} U(t_n) \left[\mu, U(t_{n-1}) \left[\mu, U(t_{n-2}) \cdots \left[\mu, U(t_1) \left[\mu, \rho^{(0)}(t_0)\right]\right] \cdots \right]\right] \Big\}. \end{aligned} \tag{1.17}$$

In Eqs. (1.16) and (1.17), we switched to the time differences t_n between successive field interactions as defined by the relations $t_n = t' - \tau_n$, $t_{n-1} = \tau_n - \tau_{n-1}, \cdots, t_1 = \tau_2 - \tau_1$ (Fig. 1.2a) [2, 18, 27–29]. The Heaviside functions Θ in Eq. (1.17) account for the causality of the response, that is, they constrain the integration in Eq. (1.16) to positive times [2, 18]. The function $Q^{(n)}$ contains information about all excitation pathways that characterize the system properties. By explicitly calculating the trace over the n-fold commutator in Eq. (1.17), one generally obtains the sum over 2^n different terms, from which each one describes a group of excitation pathways [30]. This is a consequence of μ acting on both sides of the density matrix $\rho(t_0)$ (i.e., either on the "ket" or on the

"bra" side), resulting in different groups of interaction patterns [27]. One can employ an external field with K collinear pulses with phases φ_k according to

$$E(t') = \sum_{k=1}^{K} \left[E_k(t' - \tau_k) \mathrm{e}^{\mathrm{i}\omega_0(t'-\tau_k)-\mathrm{i}\varphi_k} + E_k(t' - \tau_k) \mathrm{e}^{-\mathrm{i}\omega_0(t'-\tau_k)+\mathrm{i}\varphi_k} \right], \tag{1.18}$$

where E_k is the pulse envelope. By inserting this field into Eq. (1.16), one would finally obtain $2^n \times (2K)^K$ terms. The number of all possible pathway terms, however, can be greatly reduced by considering strict time ordering of the individual interactions, that is, $\tau_1 < \tau_2 < \cdots < \tau_n$, and by employing the rotating-wave approximation [17, 19]. The remaining terms can then be distinguished by their total phases $\pm\varphi_1 \pm \varphi_2 \pm \cdots \pm \varphi_K$, where the sign permutations are a result of the definition of $E(t')$ [Eq. (1.18)] [30]. Exactly these individual terms can diagrammatically be represented as so-called double-sided Feynman diagrams. A general example for such a diagram is shown in Fig. 1.2b.

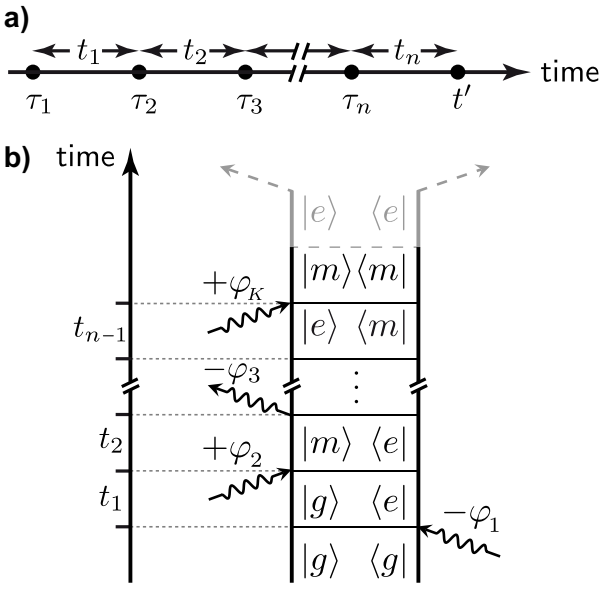

Figure 1.2. Displaying the perturbation of the density matrix by double-sided Feynman diagrams. (a) Definition of time variables. Points represent absolute times, whereas the arrows refer to time intervals. Interaction times of the dipole operator with the density matrix are denoted by τ. (b) Anatomy of a double-sided Feynman diagram. Such diagrams display the perturbation of the density matrix by the phases φ of the interacting light fields (wavy arrows). After perturbation, the final population state $|m\rangle \langle m|$ relaxes nonradiatively (denoted by a horizontal gray dashed line) to the population of the first excited state $|e\rangle \langle e|$, which is proportional to the fluorescence emission (dashed gray arrows). As Kasha's rule holds, the part of the diagram depicted in gray is usually omitted.

Based on Ref. [19], the essential rules for these diagrams are the following:

- Time proceeds from the botton to the top.

- An interaction with a light field is represented by an arrow (drawn as wavy arrows in Fig. 1.2). The arrow direction denotes the sign of the phase that the system acquires. An arrow pointing to the right denotes an interaction with $\exp(-\mathrm{i}\omega_0 t' + \varphi)$, whereas an arrow pointing to the left stands for $\exp(+\mathrm{i}\omega_0 t' - \varphi)$.
- An arrow pointing towards a "ket" or "bra" represents excitation, whereas an arrow pointing away represents de-excitation.
- Each diagram ends in an excited state population (e.g., $|m\rangle\langle m|$ in Fig. 1.2b).
- The sign of each diagram is determined by $(-1)^j$, where j is the number of light-field interactions from the right side.

The part depicted in gray in Fig. 1.2b can usually be omitted since every system investigated in this work emits fluorescence from its first-excited electronic state (Kasha's rule [31]) and thus, every higher excited state is expected to yield fluorescence "indirectly" via nonradiative relaxation into the emitting state, which is represented by $|e\rangle\langle e|$ in Fig. 1.2b. In such a case, $\Phi_m = \Phi_e$ holds in in Eq. (1.15).

1.2.3 Multipulse Experiments

How can we now extract the excitation pathways from the nonlinear response? With Eq. (1.16), we have an expression which connects our observable with the convolution of the external electric field (i.e., our "experiment") with an entity that contains the response of the system, that is, the entirety of all pathways, which is represented by $Q^{(n)}$. In other words, the fluorescence emission of the system is now a function of the excitation fields. However, there is still some ambiguity in this relationship, as we can not yet distinguish between different excitation pathways. We therefore make use of the fact that coherences evolve with specific phases. In this respect, we tailor our pulse sequence so that the individual pulse phases precisely match to those of the individual coherences. Moreover, we exploit the circumstance that the imprinted phase information is preserved from excitation step to excitation step, as the excitation sequence itself is fully coherent. Thus, a pulse train with a specific phase pattern acts as a selective probe for a certain class of excitation pathways. In other words, we *encode* certain classes of excitation pathways into the fluorescence emission by judicious choice of the excitation pulse phases. Of course, we want to receive *all* possible pathway classes, but this will be the task of "phase cycling," which we discuss at the end of this chapter [29].

For now, let us focus on the extraction of different classes of excitation pathways mentioned above. We shall consider the fourth-order population to introduce the concept. The sixth-order response will be the subject of the subsequent chapters. The simplest fluorescence-detected 2D experiment consists of a sequence of three fully collinear phase-

coherent pulses [12, 29],[4]

$$\begin{aligned} E(t') = {} & E_1\,(t'-t-\tau)\,\mathrm{e}^{-\mathrm{i}\omega_0(t'-t-\tau)+\mathrm{i}\alpha\varphi_1} \\ & + E_2\,(t'-t)\,\mathrm{e}^{-\mathrm{i}\omega_0(t'-t)+\mathrm{i}\beta\varphi_2} \\ & + E_3\,(t')\,\mathrm{e}^{-\mathrm{i}\omega_0 t'+\mathrm{i}\gamma\varphi_3} + \text{c.c.}, \end{aligned} \tag{1.19}$$

where we relabeled the interpulse delays with the so-called coherence times τ and t (Fig. 1.3). In addition, we introduced the coefficients α, β, and γ ($\alpha, \beta, \gamma \in \mathbb{Z}$) in order to uniquely describe the interaction pattern of the phases φ_i ($i = 1, 2, 3$) acquired from the first, the second, and the third pulse, respectively [29]. Note that, in fourth order, the four interactions are spread over three pulses. This gives rise to three different possibilities, in which one of the pulses interacts *twice* (Fig. 1.3).

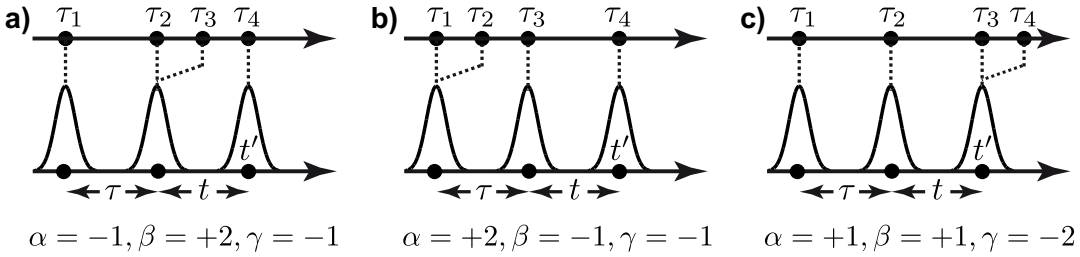

Figure 1.3. Interaction possibilities of a three-pulse sequence inducing a fourth-order response. The four interactions are distributed over three pulses, whereby either (a) the middle, (b) the first, or (c) the last pulse interacts twice. The interpulse delays τ and t correspond to the delay labeling convention used in this thesis. Each interaction possibility can be described by a phase-specific interaction pattern, which is represented by the phase coefficients α, β, and γ (bottom).

The absolute values of α, β and γ in Fig. 1.3 can thereby be viewed as a generalization of the number of excitation quanta involved in a transition between electronic states [33]. We can define three different electric fields by inserting the various combinations of α, β, and γ of Fig. 1.3 into Eq. (1.19). For simplicity, let us assume for the following that the field envelopes are delta functions, justifying the strict time-ordering mentioned above [18]. Then, by inserting each corresponding electric field separately into Eq. (1.16), we obtain three different *nonlinear signal contributions*. Since these signals nicely illustrate some elementary features of fluorescence-based 2D spectroscopy, we discuss them on the example of our three-level system (Fig. 1.1a) in the following.

[4] Conceptually, such a sequence is analogous to the so-called COSY (correlated spectroscopy) sequence of NMR spectroscopy, both of which generally correlate coherences [12, 32].

Rephasing One-Quantum–One-Quantum Contribution

The first contribution can be characterized by the values $\alpha = -1$, $\beta = +2$, $\gamma = -1$ (Fig. 1.3a) and visualized by double-sided Feynman diagrams in Fig. 1.4. Evidently, the twice interacting middle pulse gives rise to three different pathways that all have a common motif – the phase conjugation between the coherence density matrix elements. As the conjugate of $\mathrm{e}^{\mathrm{i}\omega t}$ is $\mathrm{e}^{-\mathrm{i}\omega t}$, such phase conjugation is equivalent to a sign change of time. While our time always proceeds linearly forward, the time for the coherences that evolve over t runs formally parallel "backwards." This leads to the phenomenon of "rephasing," which can be understood as the inversion of dephasing, also known as "photon echo" [13, 34]. The practical consequence of this is that the rephasing signal allows one to separate homogeneous from inhomogeneous broadening [17]. In this thesis, we call this signal the "rephasing 1Q–1Q signal," because it correlates 1Q coherences, as evident from the double-sided Feynman diagrams of Fig. 1.4.

The response function formalism allows us to calculate each pathway via

$$Q_1(t,\tau) = -2\Phi_e\Theta(t)\Theta(\tau)\left(\frac{i}{\hbar}\right)^4 \mu_{eg}^4 \mathrm{e}^{\mathrm{i}(\omega_0-\omega_{eg})(t-\tau)} L_{\mathrm{R1Q1Q}}, \tag{1.20}$$

$$Q_2(t,\tau) = -\Phi_e\Theta(t)\Theta(\tau)\left(\frac{i}{\hbar}\right)^4 \mu_{eg}^2\mu_{fe}^2 \mathrm{e}^{-\mathrm{i}(\omega_0-\omega_{eg})\tau} \mathrm{e}^{\mathrm{i}(\omega_0-\omega_{fe})t} L_{\mathrm{R1Q1Q}}, \tag{1.21}$$

$$Q_3(t,\tau) = \Phi_f\Theta(t)\Theta(\tau)\left(\frac{i}{\hbar}\right)^4 \mu_{eg}^2\mu_{fe}^2 \mathrm{e}^{-\mathrm{i}(\omega_0-\omega_{eg})\tau} \mathrm{e}^{\mathrm{i}(\omega_0-\omega_{fe})t} L_{\mathrm{R1Q1Q}}, \tag{1.22}$$

where L_{R1Q1Q} is the rephasing line shape function,

$$L_{\mathrm{R1Q1Q}} = \exp\left(-\gamma_{1\mathrm{Q}}(\tau+t) - \frac{1}{2}\sigma^2(\tau-t)^2\right), \tag{1.23}$$

phenomenologically accounting for line broadening caused by the pure dephasing rate $\gamma_{1\mathrm{Q}}$ of 1Q coherences ($\gamma_{1\mathrm{Q}} = 1/T_2^*$), and inhomogeneous line broadening, which is quantified by σ [17]. Pathway Q_1 is weighted by a factor of two because of "time ordering." This means that there are two indistinguishable possibilities, $|g\rangle\langle e| \xrightarrow{+\varphi_2} |g\rangle\langle g| \xrightarrow{+\varphi_2} |e\rangle\langle g|$ and $|g\rangle\langle e| \xrightarrow{+\varphi_2} |e\rangle\langle e| \xrightarrow{+\varphi_2} |e\rangle\langle g|$, which is a result of the second pulse interacting both on "bra" and "ket" simultaneously.

It can be seen that Q_2 and Q_3 feature quite similar expressions, but they have opposite signs: these pathways interfere destructively. For the following, we assume $\mu_{eg} = \mu_{ef}$, and $\Phi_e = 1$ and $\Phi_f = 0.5$, leading to a non-complete destructive interference of Q_2 and Q_3. Using the expressions above, we can formally depict each pathway in frequency space (Fig. 1.4, bottom) by using a 2D Fourier transform with respect to τ and t. However, in a real experiment, one would always obtain a signal arising from the interference

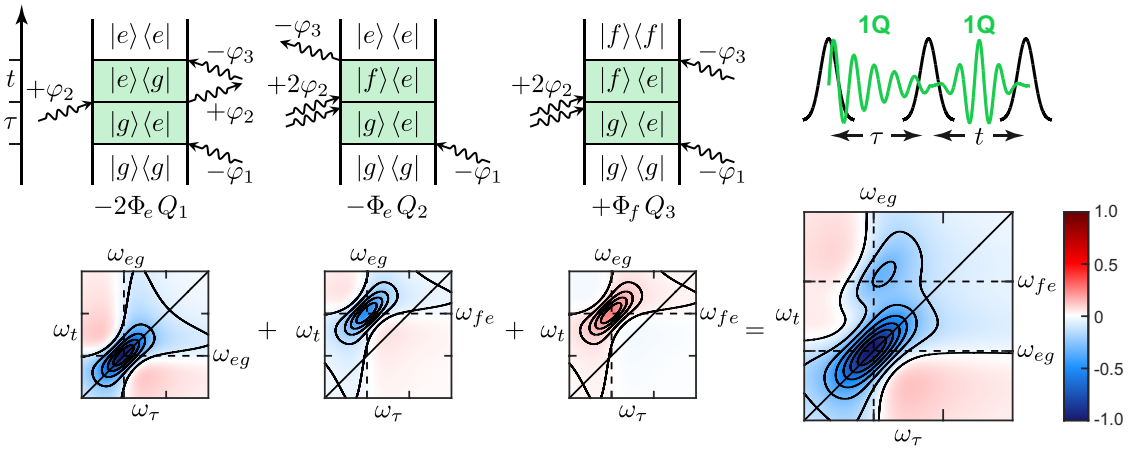

Figure 1.4. Rephasing 1Q–1Q 2D spectroscopy. The rephasing signal has the total phase $\varphi_{\mathrm{R1Q1Q}} = -\varphi_1 + 2\varphi_2 - \varphi_3$. For a three-level system (Fig. 1.1a), three pathways (top) contribute to the signal, with their weight labeled below. The representation of the real part of each pathway (normalized to Q_1) in 2D frequency space is shown at the bottom. The sum over all pathways yields the real-valued rephasing 1Q–1Q 2D spectrum (bottom right, normalized to its highest absolute value). In all frequency–frequency plots, the diagonal is drawn where $\omega_\tau = \omega_t$.

(i.e., the sum) of all pathways, which is depicted at the bottom right of Fig. 1.4. This rephasing 1Q–1Q 2D spectrum shows a diagonal peak, resulting from the correlation of the resonance ω_{eg} with itself, whereas the cross peak indicates that the resonances ω_{eg} and ω_{fe} are coupled. The linewidth along the diagonal corresponds to the inhomogeneous linewidth, whereas the antidiagonal linewidth is the homogeneous linewidth [35].

Two-Quantum–One-Quantum contribution

The second contribution corresponds to $\alpha = +2$, $\beta = -1$, $\gamma = -1$ (Fig. 1.3b), and the respective Feynman diagrams are shown in Fig. 1.5. The double interaction of the first pulse initially creates a 2Q coherence, which is then converted to a 1Q coherence by the second pulse. The individual pathways can be expressed as

$$Q_4(t,\tau) = -\Phi_e \Theta(t)\Theta(\tau) \left(\frac{i}{\hbar}\right)^4 \mu_{eg}^2 \mu_{fe}^2 \mathrm{e}^{\mathrm{i}(2\omega_0 - \omega_{fg})\tau} \mathrm{e}^{\mathrm{i}(\omega_0 - \omega_{eg})t} L_{\mathrm{2Q1Q}}, \tag{1.24}$$

$$Q_5(t,\tau) = -\Phi_e \Theta(t)\Theta(\tau) \left(\frac{i}{\hbar}\right)^4 \mu_{eg}^2 \mu_{fe}^2 \mathrm{e}^{\mathrm{i}(2\omega_0 - \omega_{fg})\tau} \mathrm{e}^{\mathrm{i}(\omega_0 - \omega_{fe})t} L_{\mathrm{2Q1Q}}, \tag{1.25}$$

$$Q_6(t,\tau) = \Phi_f \Theta(t)\Theta(\tau) \left(\frac{i}{\hbar}\right)^4 \mu_{eg}^2 \mu_{fe}^2 \mathrm{e}^{\mathrm{i}(2\omega_0 - \omega_{fg})\tau} \mathrm{e}^{\mathrm{i}(\omega_0 - \omega_{fe})t} L_{\mathrm{2Q1Q}}, \tag{1.26}$$

with the 2Q–1Q line shape function,

$$L_{\mathrm{2Q1Q}} = \exp\left(-\gamma_{\mathrm{2Q}}\tau - \gamma_{\mathrm{1Q}}t - \frac{1}{2}\sigma^2(\tau + t)^2\right). \tag{1.27}$$

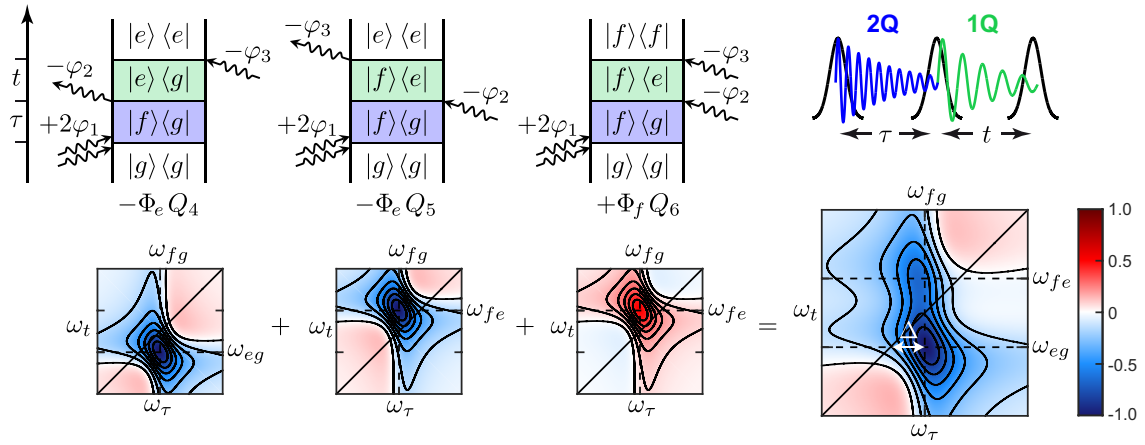

Figure 1.5. 2Q–1Q 2D spectroscopy. The 2Q–1Q signal has the phase $\varphi_{2Q1Q} = +2\varphi_1 - \varphi_2 - \varphi_3$. For a three-level system (Fig. 1.1a), three pathways (top) contribute to the signal. The representation of the real part of each pathway in 2D frequency space (normalized to Q_4) is shown in the panels below. The sum over all pathways yields the real-valued 2Q–1Q 2D spectrum (bottom right, normalized to its highest absolute value), where $\Delta = \omega_{fg} - 2\omega_{eg}$. In all 2D plots, the diagonal is drawn where $\omega_\tau = 2\omega_t$.

Again, by summing over all Fourier-transformed pathways, one obtains a 2Q–1Q 2D spectrum (Fig. 1.5, bottom right). As it correlates different coherence types, it only contains cross peaks. A special feature of 2Q–1Q 2D spectra (sometimes called double-quantum 2D spectra), is that they directly map out the frequency of state $|f\rangle$, which itself is accessed by a resonant two-photon transition. Hence, if $|f\rangle$ is a true doubly excited state (that is, it is characterized by a two-particle wave function), then the 2Q–1Q 2D spectrum is particularly suitable to determine electron correlation energies [36–38]. The correlation energy Δ is then directly quantifiable by the shift of the peak along the 2Q axis with respect to twice the energy of the first excited state (Fig. 1.1a), at least for systems with a small number of states and relatively small linewidths [39]. For more complex systems, the situation is often not as clear as presented in Fig. 1.5, so that one needs to employ theoretical modeling to extract the value of Δ (see also Chapter 3). It is worth noting that, in contrast to the 1Q–1Q contribution, there is no phase conjugation between the coherences, thus, this signal is classified as "nonrephasing." This results in resonances that are inhomogeneously broadened along both the diagonal and the antidiagonal [compare the signs in the line shape functions of Eqs. (1.23) and (1.27)].

One-Quantum–Two-Quantum Contribution

The third fourth-order signal accessible by three excitation pulses is the 1Q–2Q signal contribution with $\alpha = +1, \beta = +1, \gamma = -2$ (Fig. 1.3c). The consequence of the double

interaction of the last pulse is the emergence of a formally inverted 2Q–1Q process, leading to the correlation of 1Q coherence evolving over τ, and 2Q coherence evolving over t. The 1Q–2Q signal is composed of just two pathways (Fig. 1.6), which can be written as

$$Q_7(t,\tau) = -2\Phi_e\Theta(t)\Theta(\tau)\left(\frac{i}{\hbar}\right)^4 \mu_{eg}^2\mu_{fe}^2 \mathrm{e}^{\mathrm{i}(\omega_0-\omega_{eg})\tau}\mathrm{e}^{\mathrm{i}(2\omega_0-\omega_{fg})t}L_{1\mathrm{Q}2\mathrm{Q}}, \tag{1.28}$$

$$Q_8(t,\tau) = \Phi_f\Theta(t)\Theta(\tau)\left(\frac{i}{\hbar}\right)^4 \mu_{eg}^2\mu_{fe}^2 \mathrm{e}^{\mathrm{i}(\omega_0-\omega_{eg})\tau}\mathrm{e}^{\mathrm{i}(2\omega_0-\omega_{fg})t}L_{1\mathrm{Q}2\mathrm{Q}}, \tag{1.29}$$

where $L_{1\mathrm{Q}2\mathrm{Q}}$ is the 1Q–2Q line shape function,

$$L_{1\mathrm{Q}2\mathrm{Q}} = \exp\left(-\gamma_{1\mathrm{Q}}\tau - \gamma_{2\mathrm{Q}}t - \frac{1}{2}\sigma^2(\tau+t)^2\right). \tag{1.30}$$

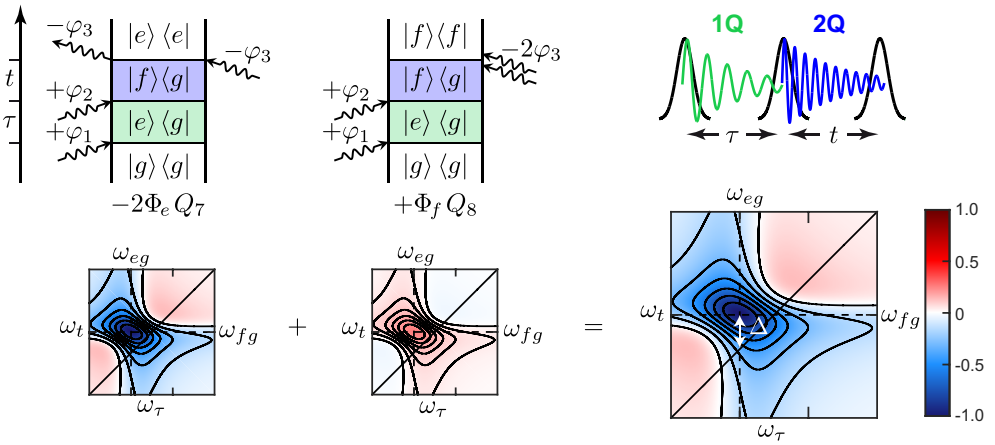

Figure 1.6. 1Q–2Q 2D spectroscopy. The 1Q–2Q signal has the total phase $\varphi_{1\mathrm{Q}2\mathrm{Q}} = +\varphi_1 + \varphi_2 - 2\varphi_3$. For a three-level system (Fig. 1.1a), only two pathways (top) contribute to the signal. The representation of the real parts of these pathways in 2D frequency space (normalized to Q_7) is shown in the panels below. The sum over all pathways yields the real-valued 1Q–2Q 2D spectrum (bottom right), where $\Delta = \omega_{fg} - 2\omega_{eg}$. In all frequency–frequency plots, the diagonal is drawn where $2\omega_\tau = \omega_t$.

The 1Q–2Q signal is exclusive to population-based 2D spectroscopy and there is no such counterpart that could be constructed using coherent signal detection. Coherent signal detection requires that a "radiative" 1Q coherence evolves over t [29], but a 2Q coherence does not directly emit a signal field [40]. However, as we will see in this work, a general consequence of probing nonlinear signals with an even order is the access to "1Q–NQ"-type contributions. Such contributions seem to be equivalent to those of "NQ–1Q" type at first sight, however, when comparing Figs. 1.5 and 1.6, it turns out that the 1Q–NQ contributions feature a higher degree of coherence selectivity. The reason behind that

is the sole contribution of ground–excited 1Q coherences to the signal, generally leading to fewer pathways. (Note that the 2Q–1Q signal can also induce the excited–doubly excited 1Q coherence $|f\rangle\langle e|$.) From a practical point of view, this property makes the 1Q–2Q signal even better suited to measure electron correlation energies, as there are generally less resonances in the 2D spectra [9, 29]. These 1Q–2Q and 1Q–3Q 2D spectra will be used to study exciton correlations in semiconductor quantum dots in Chapter 3.

1.2.4 From 2D to 3D Spectroscopy

In the preceding section, we have seen that a three-pulse sequence enables one to construct correlations of coherences that have the same or different numbers of the excitation quanta required to generate them. With that, we were able to probe coupling of a doubly excited state to a singly excited state. However, by altering the excitation sequence, one can also probe coupling *between* singly excited states [41–43].

For the following, let us consider a three-level system without a doubly excited state, but where two singly excited states $|e\rangle$ and $|e'\rangle$ are energetically close to each other (Fig. 1.7a). Since we employ broadband laser pulses, we can prepare superpositions of both excited states with the ground state, which are both 1Q coherences. Employing a rephasing 1Q–1Q sequence, that is, with three pulses, we would obtain a 1Q–1Q 2D spectrum shown in Fig. 1.7b. This time, we choose the representation in absolute signal values and we calculate the signal by numerical solution of the Lindblad master equation [21] (see also below). Cross peaks above and below the diagonal result from $|e\rangle$ and $|e'\rangle$ being coupled, which is mediated by $|g\rangle$.

Let us now go one step further and employ a four-pulse sequence with the aim of probing the same signal type (Fig. 1.7c.) Formally, we split the double interaction of the second pulse into two consecutive interactions. For that purpose, we introduce the middle delay T, and the additional coefficient δ for the phase coefficient of the last pulse [29]. Now, each pulse interacts once with the system. Note that for $T = 0$ (Fig. 1.7b), we obtain the same result as if we had employed a three-pulse sequence.

What do we gain by probing the fourth-order response by four pulses? By scanning the middle delay T, also known as "population time" or "waiting time," our experiment gains sensitivity to population dynamics and coherences between electronic states, whereas the latter can be characterized by an oscillation frequency of less than one quantum of the incident photon frequency. Such coherences are called zero-quantum (0Q) coherences. In this work, however, we will often use the term "0Q" as a general term for both nonoscillatory population dynamics and the aforementioned oscillatory dynamics. We can visualize the resulting "1Q–0Q–1Q" contribution as a series of 1Q–1Q 2D

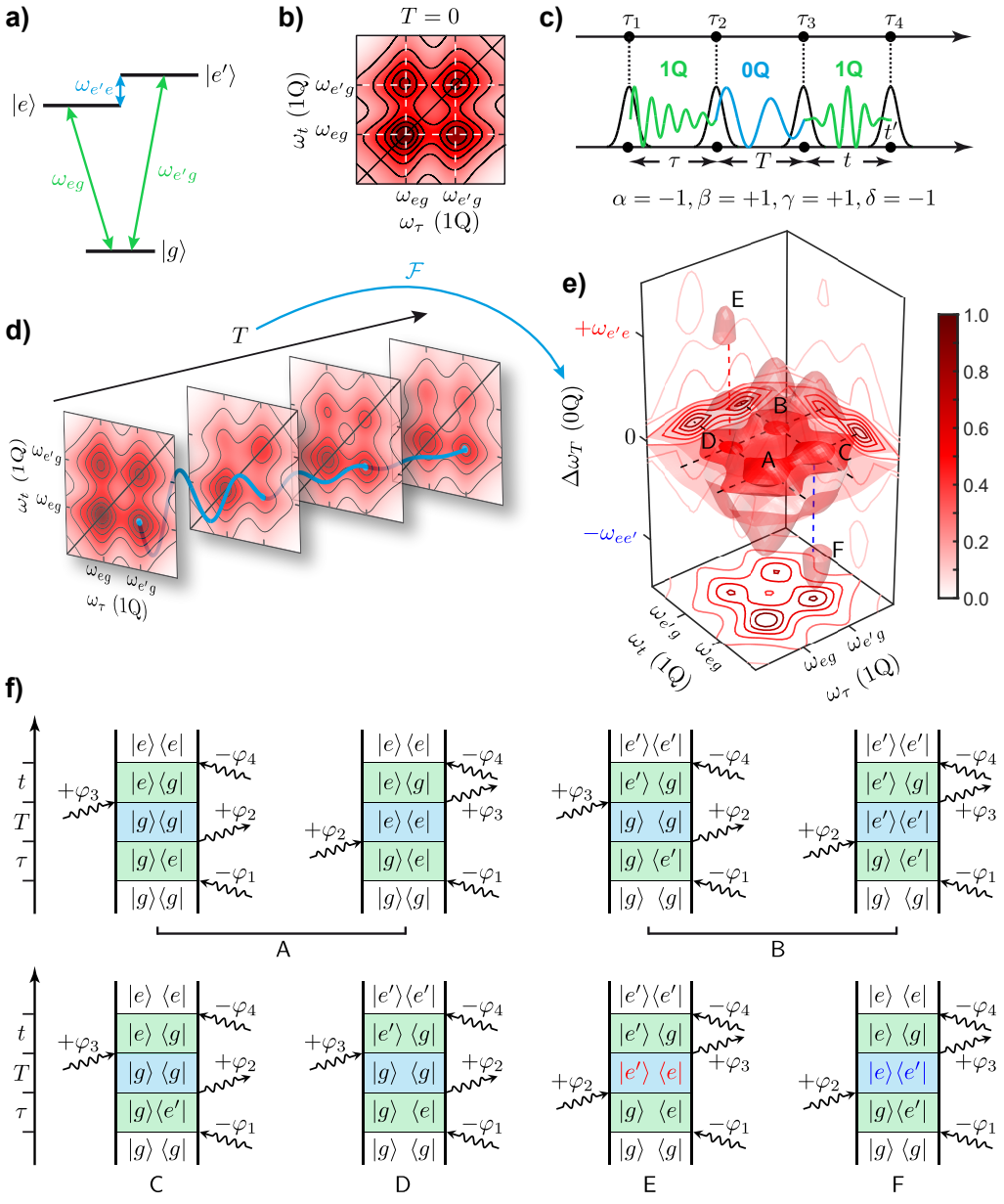

Figure 1.7. From 2D to 3D spectroscopy. (a) Level scheme of a three-level system with two singly excited states $|e\rangle$ and $|e'\rangle$ and ground state $|g\rangle$. (b) Simulated rephasing 1Q–1Q 2D spectrum, shown in absolute values (normalized to the maximum). (c) Interaction scheme of a four-pulse sequence with delays τ, T, and t inducing a fourth-order response. The interaction pattern indicated by $\alpha, \beta, \gamma, \delta$ corresponds to the rephasing 1Q–0Q–1Q signal contribution. (d) Illustration of the rephasing 1Q–0Q–1Q signal (absolute values) as 2D spectra with parametrical dependence on T, where the light blue curve indicates cross peak modulation due to 0Q coherence. The 2D spectra are normalized to the frontal one, which corresponds to $T = 0$. An additional Fourier transform ($\mathcal{F}$) generates (e) the rephasing 1Q–0Q–1Q 3D spectrum. (f) Double-sided Feynman diagrams describing the 3D peaks A–F in e.

spectra with a parametric dependence on T (Fig. 1.7d). Evidently, over the course of T, the cross peak magnitudes oscillate with a period corresponding to the frequency difference between $|e\rangle$ and $|e'\rangle$, which is schematically indicated by the light blue oscillation. In parallel to these coherent dynamics, there are also incoherent dynamics, that is, population dynamics, which can be recognized by the magnitude decrease of the upper diagonal peak and simultaneous magnitude increase of the lower cross peak over T.

Alternatively, one could perform an additional Fourier transform with respect to T to generate a three-dimensional (3D) spectrum (Fig. 1.7e). Generally, a 3D spectrum offers a maximum separation of the spectral signatures of the underlying excitation pathways and inherently includes the result of the three-pulse 2D experiment as the bottom projection of the spectral solid (compare Figs. 1.7b and e), among other projections. Importantly, while cross peaks in regular 2D spectra do not directly indicate if coupling between two excited states originates from incoherent energy transfer or coherent superposition between them, 3D cross peaks such as E and F in Fig. 1.7e are unique signatures of coherent coupling. The 3D spectrum spectrally separates contributions from population dynamics, which appear at $\Delta\omega_T = 0$, and 0Q coherences, which are shifted along the new frequency axis $\Delta\omega_T$, whereby we can also distinguish between the sign of the frequency of the 0Q coherences. In Chapter 4, we will employ 3D spectroscopy on a molecular sample system, where the sign of the 0Q coherence will help us to distinguish contributions from vibrations in the ground and the excited electronic state.

Finally, let us recall Fig. 1.1c. While the three-pulse sequences discussed in Sec. 1.2.3 can only correlate various 1Q and 2Q coherences, i.e., the off-diagonal density matrix elements, the four-pulse sequence additionally creates dynamical correlations to diagonal elements. In other words, we can unfold the full dimensionality of the fourth-order response by using four pulses. Note that, in this section, we only discussed one possible fourth-order contribution (i.e., the one that corresponds to the phase coefficients $\alpha = -1, \beta = +1, \gamma = +1, \delta = -1$). In fact, other phase sign permutations of the excitation pulses are possible, giving rise to two other signal contributions – the "non-rephasing" 1Q–0Q–1Q and 1Q–2Q–1Q contributions. Together, these three signal contributions completely characterize the fourth-order response function. This particular aspect is addressed in detail in Chapter 4.

Note that, although the 3D spectrum of Fig. 1.7e has been calculated using a non-perturbative approach (see Secs. 2.5.3 and 4.5.6), we can interpret it via double-sided Feynman diagrams (Fig. 1.7f), which result from perturbation theory. For the three-level system of Fig. 1.7a, eight different 1Q–0Q–1Q pathways can be constructed [43] which could have been calculated and summed up to yield a 3D spectrum. However, instead

of bookkeeping and summing over all pathway terms, the nonperturbative treatment inherently takes into account all contributing pathways up to an arbitrary nonlinear order. The nonperturbative approach involves less approximations compared to a perturbative calculation but requires to numerically solve a differential equation, which is computationally more expensive. In return, we can explicitly incorporate the amplitude profile of the external laser fields which in turn captures effects stemming from finite pulse durations such as pulse overlap, leading to an overall more realistic description of multidimensional spectra. In this context, it was shown that the bandwidth and the central frequency of the finite laser amplitude profile relative to the system resonances have a major influence on the observed features on the example of coherently detected 2D spectroscopy [44–47]. In virtue of these circumstances, in this work we will use a nonperturbative treatment to simulate 2D and 3D spectra close to the experiment, but at the same time we keep double-sided Feynman diagrams for interpretation purposes.

1.2.5 Designing Phase-Cycling Schemes: Isolating Coherent Signals from the Incoherent Observable

We have seen in the preceding sections that manipulating the phases of the excitation pulses is the key to select out different classes of excitation pathways, the nonlinear signal contributions. However, in a real experiment, just using a pulse sequence in which we scan the delays using a single combination of phases is insufficient to *isolate* a certain signal contribution. In Secs. 1.2.3 and 1.2.4, we disregarded the fact that, besides the desired signal contribution, the much stronger lower-order fluorescence signal is always present, preventing an unambiguous signal assignment. Thus, we need to *cycle* our pulse phases to separate the desired signals from the undesired background. This means, we repeat every 2D experiment, in which we scan the delays between the pulses, with different sets of pulse phase combinations.

Phase-cycling procedures were originally employed as integral parts of 2D NMR experiments as they efficiently suppress unwanted artifact signals [33]. In 2003, Warren and coworkers then first demonstrated the optical analogue of phase-cycled pulse sequences for fluorescence-detected 2D spectroscopy on rubidium vapor [48]. Later, Tan developed a theory for the selection of phase-cycling schemes for collinear optical 2D spectroscopy [29]. He focused on fourth-order nonlinear signals using three- and four-pulse sequences. This phase-cycling scheme selection procedure was then extended to 2D spectroscopy in the pump–probe geometry [49, 50]. During the creation of this thesis, the application of phase cycling was also demonstrated in collinear coherence-detected third- [51] and fifth-order [52] 2D electronic spectroscopy.

Here, we focus on fourth- and sixth-order nonlinear signals. Sixth-order signals are of particular interest because they access information which go beyond the three-level system of Fig. 1.1a such as triply excited states, their coupling to the manifold of other excited states, and higher-order electron correlations [53, 54]. As we will see in the following, by cycling the phases in a sophisticated way, we are able to simultaneously capture the signals from *both* nonlinear orders. In particular, we will address the question which phase-cycling schemes for three- and four-pulse sequences are sufficient and most economical to unambiguously recover the aforementioned signals.

Let us begin with three-pulse sequences. In Sec. 1.2.3, we have seen that nonlinear signal contributions can generally be distinguished by unique sets of coefficients α, β, and γ. These coefficients relate to the total phase $\varphi_{\text{tot.}} = \alpha\varphi_1 + \beta\varphi_2 + \gamma\varphi_3$ with which each contribution is oscillating [29]. For these coefficients, two rules can be formulated:

$$\alpha + \beta + \gamma = 0, \tag{1.31}$$

$$|\alpha| + |\beta| + |\gamma| \leq 6. \tag{1.32}$$

The first rule is a direct consequence of the requirement to have a final population state in every pathway in order to probe fluorescence. This is only achieved if the number of interactions with a negative phase sign is equal to the number of interactions with a positive phase sign (see also the Feynman diagrams in Figs. 1.4–1.7). The second rule in Eq. (1.32) follows from our premise to consider signals up to sixth order. Equation (1.31) also states that α, β, and γ are dependent on each other [29]. This is useful, since we can reference the phases of the second and third pulse to the phase of the first pulse by $\varphi_{21} = \varphi_2 - \varphi_1$ and $\varphi_{31} = \varphi_3 - \varphi_1$. The entirety of all signals p can then generally be formulated as a sum (i.e., a Fourier series) via

$$p\left(\tau, t, \varphi_{21}, \varphi_{31}\right) = \sum_{\beta,\gamma} \tilde{p}_{(3)}(\tau, t, \beta, \gamma) \mathrm{e}^{\mathrm{i}(\beta\varphi_{21} + \gamma\varphi_{31})}, \tag{1.33}$$

where each set of β and γ is now sufficient to relate to a three-pulse-specific nonlinear signal contribution $\tilde{p}_{(3)}$. A discrete 2D Fourier transformation of this series finally gives us access to the desired nonlinear signal contributions:

$$\tilde{p}_{(3)}(\tau, t, \beta, \gamma) = \frac{1}{LM} \sum_{m=0}^{M-1} \sum_{l=0}^{L-1} p\left(\tau, t, l\Delta\varphi_{21}, m\Delta\varphi_{31}\right) \mathrm{e}^{-\mathrm{i}l\beta\Delta\varphi_{21}} \mathrm{e}^{-\mathrm{i}m\gamma\Delta\varphi_{31}}, \tag{1.34}$$

where $\Delta\varphi_{21} = 2\pi/L$ and $\Delta\varphi_{31} = 2\pi/M$ relate to experimental phase increments. In this respect, the double sum over p can be viewed as the "raw data" of the experiment. Expression (1.34) determines whether a signal contribution of interest can be resolved

on a periodic 2D phase grid with the number of experimental sample steps L and M, which refer to a certain phase-cycling scheme, denoted as "$1\times L\times M$." Importantly, if we sample $\Delta\varphi_{21}$ and $\Delta\varphi_{31}$ in sufficient steps, then we could simply weight out a desired nonlinear signal from the raw data by inserting the signal-specific set of β and γ into Eq. (1.34) [29]. In other words, we can *decode* one contribution after another from the measured signal. But which phase-cycling scheme would be sufficient to discriminate between the fourth-order signals *and* those of sixth order?

For that purpose, let us "illustrate" various phase-cycling schemes by representing the φ_{21}-space and the φ_{31}-space in polar coordinates (Fig. 1.8). For each φ-space, we draw a separate unit circle. The number of phase-cycling steps L and M divides the respective circle into equally sized sections, with the peripheral portion of a section representing a phase increment of $\Delta\varphi_{21}$ or $\Delta\varphi_{31}$. Then, we plot the signal-specific weighting factors $\mathrm{e}^{-\mathrm{i}\beta\Delta\varphi_{21}}$ and $\mathrm{e}^{-\mathrm{i}\gamma\Delta\varphi_{31}}$ as "signal vectors" in the polar coordinate systems of φ_{21} and φ_{31}, respectively. A positive (negative) value of β or γ thereby corresponds to a clockwise (counter-clockwise) rotation in steps of $\Delta\varphi_{21}$ and $\Delta\varphi_{31}$ with respect to zero phase (black line). Up to sixth order, there are 36 different second-, fourth-, and sixth-order signals (including their conjugates), as dictated by the conditions (1.31) and (1.32) (see Table A1 in Appendix A). First, we shall only focus on the three fourth-order signals discussed in Sec. 1.2.3, to get a grasp of the concept. Note that we consider the complex conjugated 1Q–2Q contribution (denoted with an asterisk in Fig. 1.8) for the sake of clarity.

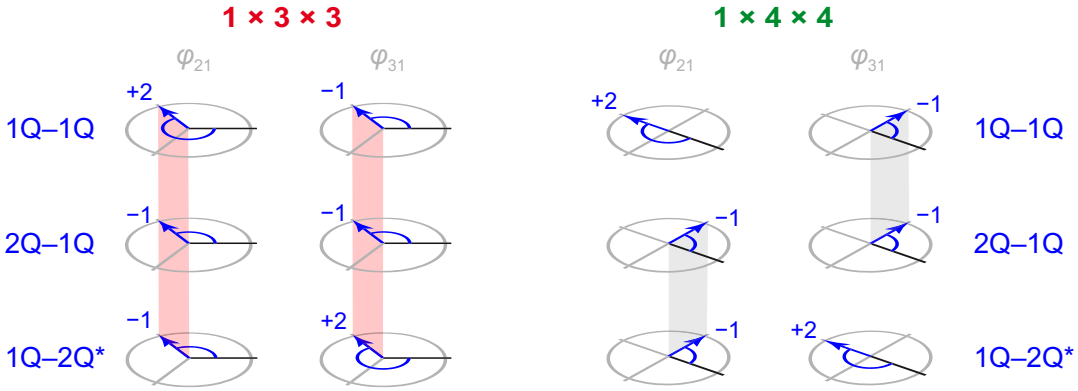

Figure 1.8. Diagrammatic representation of phase-cycling schemes by using the polar coordinate representation. Each φ-space is depicted as unit circles, which are sectioned into $\Delta\varphi$-fragments according to the number of phase steps. The black lines corresponds to 0 ($= 2\pi$). Each fourth-order signal (blue) is characterized by the two weights $\mathrm{e}^{-\mathrm{i}\beta\Delta\varphi_{21}}$ and $\mathrm{e}^{-\mathrm{i}\gamma\Delta\varphi_{31}}$ [compare Eq. (1.34)], which can be represented as vectors in the φ_{21}-space and the φ_{31}-space, respectively. In order to discriminate between all signals, at least one signal vector must not point in the same direction as that of another signal, which is not the case for the $1\times3\times3$ (indicated by red shaded planes), but for the $1\times4\times4$ phase-cycling scheme.

Let us start with a 1×3×3 phase-cycling scheme in Fig. 1.8 (left). This phase-cycling scheme is not sufficient to discriminate between the fourth-order signals. This is due to the fact that all signals share the same signal-vector directions in both φ-spaces, which is indicated by the red shaded planes in Fig. 1.8. If the signal vectors of two signals coincide in both φ_{21}-space and φ_{31}-space, we say that these signals are aliased. Evidently, aliasing is an inherent consequence of the periodicity of the phase [29]. In other words, there is an equivalence between the coefficients +2 and −1 due to insufficient phase cycling. In order to discriminate between two signals, the vectors of one signal must not point in the same direction as those of another signal – the vector directions have to differ in at least one φ-space. We can accomplish this by increasing the phase steps. If we increase the phase-cycling scheme to 1×4×4 (Fig. 1.8, right), we can distinguish between all fourth-order signals. This is because, although there are still ambiguities in one φ-space, as indicated by the gray shaded planes, each pair of signal vectors represents a unique configuration.

Now we include the sixth-order signals. Let us exemplarily consider the sixth-order 3Q–1Q and 1Q–3Q signals, which we will introduce in Chapter 2. If we used the 1×4×4 phase-cycling scheme to decode sixth-order signals from the raw data, we would struggle with aliasing, as shown in Fig. 1.9, left.

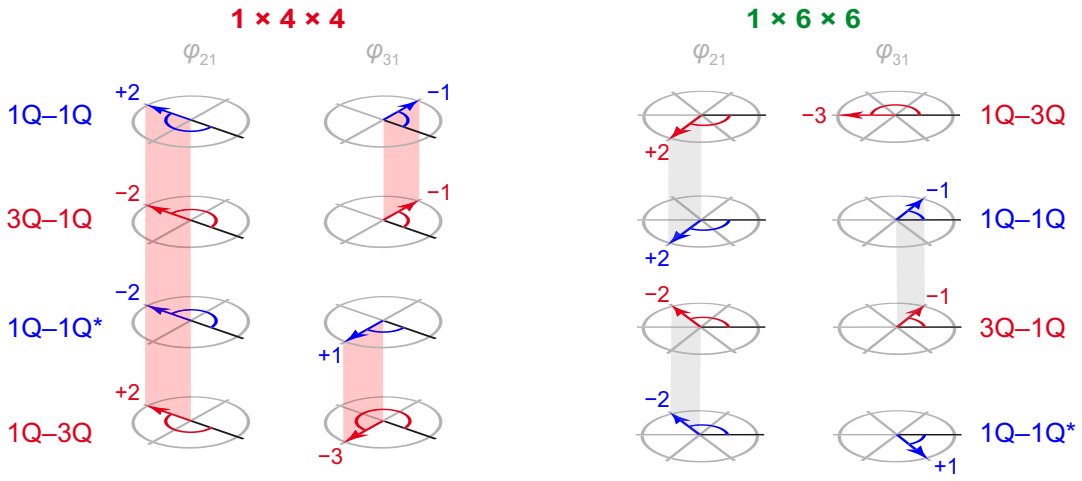

Figure 1.9. Distinguishing fourth- and sixth-order signals by phase cycling. The fourth-order 1Q–1Q signal, its complex conjugate 1Q–1Q* (blue), and the sixth-order 3Q–1Q and 1Q–3Q signals (red) are exemplarily illustrated using the diagrammatic representation of phase-cycling schemes. The 1×4×4 phase-cycling scheme (left) is insufficient to discriminate between the fourth- and sixth-order signals due to coefficient ambiguity, as indicated by the red shaded planes. The 1×6×6 scheme (right) resolves these ambiguities so that all signals can be extracted without aliasing with another.

The 3Q–1Q and 1Q–3Q signals (red) are aliased with the fourth-order 1Q–1Q signal

and the complex conjugate of the latter (blue). This time, the reason lies in the ambiguity of +2 and −2 as well as +1 and −3. Consequently, we can only use a 1×4×4 phase-cycling without aliasing if we choose our excitation power so that the sixth-order signal strength is negligible.

Only when we increase the phase cycling to 1×6×6 (Fig. 1.9, right), the signal-vector pairs correspond to unique configurations and we can discriminate between all signals. A 1×6×6-phase cycling is actually able to discriminate between all fourth-order and all sixth-order signals, as we will show in Chapter 2. This is because a six-step phase cycling resolves any ambiguity between $\pm 2, \pm 1$, and 0 in both the φ_{21}-space and in the φ_{31}-space, which ensures that the signal-specific vectors of two signals never match in both φ-spaces simultaneously.

We can perform the same analysis for a four-pulse sequence, which is shown in Appendix B. Using four pulses, one must use a 125-fold phase-cycling procedure in order to discriminate between all fourth- and sixth-order signals, which is experimentally demonstrated in Chapter 4.

1.3 Motivation, Goals and Structure of this Thesis

The traditional approach to 2D spectroscopy employs a fully noncollinear beam geometry to induce a certain nonlinear signal contribution [19, 32]. Instead of phase-cycling, one selects a specific signal by phase matching, that is, by choosing an appropriate excitation direction. Although widely established for the investigation of liquid phase systems, there are several technical difficulties [55].

Due to the coherent nature of nonresonant response of a solvent, coherent signal detection is susceptible to unwanted signals [56]. Scattering of excitation light might also pose an issue, which requires the use of specialized dual chopping or phase-cycling schemes [57] in addition to a rather complex experimental apparatus with many moving parts. Especially the latter issue is substantially crucial for the success of a coherent multidimensional experiment, since it sensitively depends on the phase stability among multiple beams. Maintaining phase stability is considerably challenging if one wants to measure phase-matched higher-order signals (i.e., signals higher than the third nonlinear order), as these signals principally require an increasing number of excitation beams [58, 59]. To retrieve the actual phase information of the acquired spectra, an additional "phasing procedure" is necessary, often carried out via a separate pump–probe measurement [55, 60–62]. This phasing procedure is not trivial for multiple-quantum [39] and higher-order signals [63, 64]. Moreover, noncollinear setups usually require a change of

the beam geometry to collect another signal contribution [32]. However, in order to completely characterize the nonlinear response, one needs access to *all* signal contributions, not just to a few. Multidimensional spectroscopy is able to unravel the comprehensive spectroscopic information to a certain nonlinear order, but only if one has the ability to collect all signal contributions up to this nonlinear order.

Especially the higher-order response contains exclusive and detailed information about the excited-state landscape of a system, such as their relaxation pathways, dynamics, interactions and correlations [52, 53, 65, 66]. In particular, the higher-order response provides direct access to multiply excited states, which remain elusive for the lower nonlinear orders. Why are these excited states so important? Knowledge about electron correlations is encrypted in such multiply excited states [36, 38, 53, 67]. In quantum chemistry, electron correlation is the central component that is crucial for an accurate system description [68]. The most accurate system description is obtained by constructing a wavefunction which includes all determinants describing excited-state configurations. In the same sense, by measuring the properties of the manifold of high-excited states through the high-order nonlinear response, we can *measure* such electron correlations and in turn construct a comprehensive picture of the system of interest.

Coherent fluorescence-detected 2D spectroscopy is a rather young addition to the family of coherent multidimensional spectroscopies. Although the first fluorescence-detected 2D experiment was carried out in 2003 [48], it has only recently become increasingly popular. This may primarily be the result of continuous further development of pulse shaping technology, which are an essential part of every fluorescence-detected 2D experiment due to the necessity to perform phase modulation [69] or phase cycling [48, 70–72]. Noteworthily, the interpretation of fluorescence-detected 2D spectra has recently been the subject of debate [73, 74], with a particular focus on 2D spectra of light-harvesting systems [75–77]. For fluorescence-detected 1D multiple-quantum signals of gas-phase systems [78], it was even claimed that these signals would be the result of collective excitations rather than microscopic multiple-quantum coherence [79]. This raises the question whether multiple-quantum signals detected by fluorescence could generally have a microscopic origin at all. Most importantly, higher-order multidimensional fluorescence spectroscopy is not yet an established technique although fluorescence-based approaches offer the best technical prerequisites like inherent phase stability, sensitive and selective signal detection, and the possibility to acquire multiple signals at once through phase cycling [9, 71, 72], which is all in contrast to the challenges of noncollinear 2D spectroscopy mentioned above.

Thus, the aim of this thesis is to establish the concept of “multiple-quantum multi-

dimensional fluorescence spectroscopy." For that purpose, phase-cycled pulse-sequences are developed, which systematically resolve and acquire *multiple* novel nonlinear signals in two and three spectroscopic dimensions in a *single* measurement. In view of the novelty of the obtained high-order nonlinear signals, i.e., signals that result from more than four interactions with the electric light field, a particular emphasis is placed on the analysis and interpretation of the obtained spectra. Hence, the use of theoretical modeling that validate and support the findings of the experiments reported in this thesis, is indispensable. The interpretation of the obtained multidimensional spectra thereby takes place in the context of the novel information content they add to the toolkit of multidimensional spectroscopy. This work shall also provide general interpretation strategies for high-order multidimensional spectra. To this end, it shall be verified that the obtained high-order fluorescence-detected multidimensional spectra contain signatures of microscopic multiple-quantum coherence.

The developed approaches in this work pursue the guiding vision of obtaining maximum amount of information about the nonlinear response up to a certain nonlinear order. This work therefore focuses especially on higher-order nonlinear signals, which are shown to be suited to analyze properties of high-excited states in molecules (Chapter 2 and 4), multiexcitonic states in semiconductor nanocrystals (Chapter 3) and ultrafast exciton–exciton annihilation in molecular heterodimers (Chapter 5). Nonetheless, the approaches in this work inherently include the previously established fourth-order nonlinear signals from the same experiments at the same time, with which couplings and dynamics of lower excited states can be investigated as well. In essence, this work addresses the question "Can we design a single, systematic approach that gives us maximum information about the nonlinear response of a system?"

A graphical outline of this thesis is given in Fig. 1.10. This thesis is organized as follows. Chapter 2 deals with the evaluation of the novel technique of multiple-quantum 2D fluorescence spectroscopy, which is based on a three-pulse sequence with 36-fold phase-cycling. This phase-cycling procedure allows one to access three fourth- and six sixth-order nonlinear signals in a single experiment (Fig. 1.10, top left). The approach is demonstrated and evaluated on a laser dye. The molecular multiple-quantum signals contain information about the properties and couplings of singly, doubly and triply excited electronic states, and are interpreted with aid of nonperturbative simulations. In addition, the potential occurrence of nonlinear wave-mixing cascades, which pose an undesired signal contamination, is also discussed and evaluated [3].

On the basis of the results of Chapter 2, Chapter 3 deals with the application of multiple-quantum 2D fluorescence spectroscopy on colloidal semiconductor quantum

dots (Fig. 1.10, top right). Here, the potential of the technique in terms of determining properties of multiexciton states is demonstrated. In that sense, multiple-quantum 2D fluorescence spectroscopy is generalized as "multiexciton 2D spectroscopy" for excitonic systems. Theoretical modelling is utilized to interpret signatures of correlations between excitons, which manifest in the observed peak patterns and line shapes [1].

In Chapter 4, the concept of multiple-quantum 2D fluorescence spectroscopy is then extended into a third spectroscopic dimension (Fig. 1.10, bottom left) by using four-pulse sequences in combination with 125-fold phase-cycling. This approach aims to obtain maximum information from a single rapid experiment by providing up to 15 different fourth- and sixth-order 3D signals. The rapid acquisition is therefore highly beneficial for the investigation of samples with limited chemical stability such as the molecular dianion of TIPS-tetraazapentacene. In particular, this four-pulse experiment unfolds the full dimensionality of the fourth-order response, enabling one to isolate spectral signatures of excited-state wave-packet dynamics, and to measure properties of two-photon excited states [4].

The approach discussed in Chapter 4 provides the technical basis for the selective study of the dynamics of interacting excitons such as in molecular aggregates, for which a sixth-order nonlinear process is required in case of fluorescence detection. Chapter 5 thus focuses on the theory and experimental demonstration of fluorescence-detected exciton–exciton interaction (FDEEI) 2D spectroscopy (Fig. 1.10, bottom right). The technique of FDEEI2D spectroscopy is applied on squaraine heterodimers, where the feasibility of tracking ultrafast exciton–exciton annihilation is demonstrated [2].

Finally, the last chapter features a general discussion of all chapters with an outlook on further advanced experiments. In particular, two new experimental techniques, multiexciton-generation 3D fluorescence spectroscopy (MEG3DFS), and five-dimensional fluorescence-detected all-resonant electronic spectroscopy (5D FLARES) are proposed and their concepts are briefly outlined.

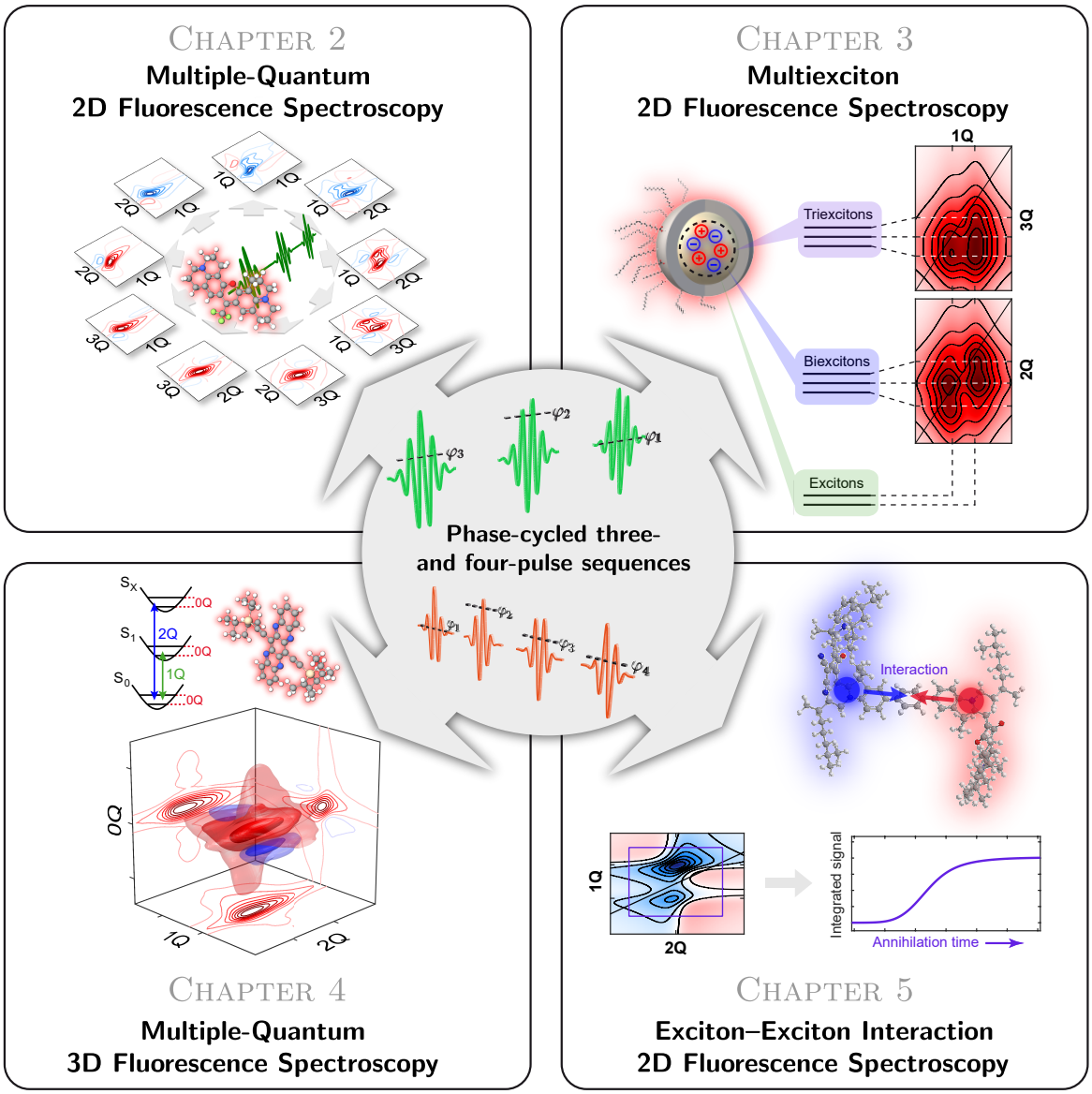

Figure 1.10. Graphical outline of this thesis. Phase-cycled three- and four-pulse sequences are developed, which systematically disentangle the electronic state landscape of molecules and nanocrystals. Chapter 2 (top left) introduces multiple-quantum 2D fluorescence spectroscopy on a molecular dye. This approach is applied to semiconductor quantum dots in Chapter 3 (top right) to systematically disentangle the manifolds of excitons, biexcitons and triexcitons. Chapter 4 (bottom left) deals with the implementation of multiple-quantum 3D fluorescence spectroscopy as a means to rapidly acquire multiple 3D spectra of molecular samples with limited chemical stability. In Chapter 5 (bottom right), a novel sixth-order nonlinear signal is developed which directly resolves ultrafast exciton–exciton annihilation in a molecular heterodimer. Reprinted in part with permission from Ref. [3]. Copyright © (2020) American Chemical Society.

Chapter 2

Molecular Coherent Three-Quantum Two-Dimensional Fluorescence Spectroscopy

We introduce molecular coherent three-quantum (3Q) two-dimensional (2D) fluorescence spectroscopy with phase cycling via shot-to-shot pulse shaping at a 1 kHz repetition rate. This allows us to acquire simultaneously, within a single scan, three fourth-order and six sixth-order signals correlating various one-quantum, two-quantum, and 3Q coherences. We demonstrate the approach on the dye molecule rhodamine 700 and reproduce all nine 2D data sets, including their absolute signal strengths, with simulations using a single, consistent set of model parameters. We observe a linear concentration dependence of all nonlinear signals, evidencing the absence of cascades and many-particle signals of non-interacting molecules. The single-beam, background-free implementation allows direct comparability between various nonlinear signal types and provides information about multiple excited states. Apart from molecules, the method is expected to be applicable to supramolecular systems, polymers, and solid-state materials with the prospect of revealing signatures of bi- and triexcitonic states.

2.1 Introduction

Coherent two-dimensional (2D) electronic spectroscopy has become a standard tool for studying ultrafast dynamics of molecular systems and is used, for example, to unveil electronic couplings, exciton dynamics, charge and energy transport, or photochemical reactions [32, 53, 80–86]. Beyond chemistry, 2D spectroscopy is applied in physics, biology, and material science, for example, to characterize dynamic processes in solar cells and organic semiconductors [87–90].

In a 2D experiment, the investigated system is irradiated by a sequence of ultrashort laser pulses triggering a multitude of excitation pathways through the excited-state manifold. These pathways carry the information about the nonlinear response of the system. Most common 2D experiments detect third-order nonlinear signals [91, 92] in a phase-matching geometry and correlate excitation and detection frequency after a certain waiting time. Because the correspondingly excited and detected coherences occur between levels that are one quantum of the incident photon energy apart, this approach delivers a time sequence of "one-quantum–one-quantum" (1Q–1Q) 2D correlation maps.

Additional information can be obtained by probing two-quantum (2Q) coherences between levels that are two quanta of the photon energy apart [36]. This can be applied for vibrational [93–96] and electronic [39, 40, 53, 67, 97–100] excitations. Employing fluorescence detection [48, 69, 71, 75] in this context is particularly helpful as it removes scattering artifacts and nonresonant solvent contributions that are problematic in the coherence-detected variants [56].

Additional information is also gained by probing higher orders in the perturbation expansion of light–matter interaction. For example, for coherence-detected spectroscopy, moving from a third-order to a fifth-order response one can unveil electronic–vibrational coupling with great detail and selectivity [59, 101], directly measure exciton–exciton annihilation dynamics [66, 102, 103], or obtain signatures of states beyond the doubly excited level such as second vibrational overtones in the infrared [104] or triexcitonic states in the visible spectral domain [53]. Moreover, the characterization of such highly excited states is relevant for tailoring many-body interactions in quantum information technology [105]. Several experiments probe highly excited states by fifth-order or even seventh-order coherent signals [53, 54, 57], and a few population-based experiments on atoms in the gas phase were reported [78, 106, 107].

Each separately obtained signal contribution, as in the examples cited above, maps the nonlinear response to a certain extent. For a comprehensive, systematic approach, it would be beneficial to collect as many signals as possible under identical excitation

conditions, preferably simultaneously, because a direct comparison of the different signals including their absolute magnitude provides additional information. Recently, three different third-order signal contributions were acquired simultaneously on the example of GaAs quantum wells [108], and we reported the simultaneous acquisition of molecular fourth-order and sixth-order three-dimensional electronic spectra using 125-fold phase cycling of four-pulse sequences and fluorescence detection [4]. In that paper, we analyzed various zero-quantum (0Q), 1Q, and 2Q correlations.[1]

In this work, we extend the concept to three-quantum (3Q) coherences by using 36-fold phase cycling of three-pulse sequences. While electronic 3Q coherences have been reported for solid-state and gas-phase systems [53, 78, 106, 107], we here introduce molecular 3Q signals. The interpretation of fluorescence-detected multidimensional spectra, especially those emerging from multiple-quantum signals, is currently under debate, which further motivates our study [74, 77–79]. We report the simultaneous isolation of three different fourth-order and six sixth-order 2D spectra and find overall excellent correspondence with simulations, including the comparison of absolute signal levels. Potential cascading contributions and many-particle signals are also investigated but found to be absent.

2.2 Results and Discussion

We analyze the various signal contributions of the experiment (Fig. 2.1a) by considering a minimal four-level energy scheme (Fig. 2.1b) with ground ($|g\rangle$), first excited ($|e\rangle$), doubly excited ($|f\rangle$), and triply excited ($|t\rangle$) electronic states. In this basis, the fluorescent electronic state of a generic molecule (S_1 in the common notation) corresponds to state $|e\rangle$. For the sake of simplicity, the scheme in Fig. 2.1b shows labels only for electronic states that represent, in fact, products of electronic-state and vibrational wave functions. All possible corresponding 1Q, 2Q, and 3Q coherences that can be constructed as superpositions among these four electronic states via one-, two-, and three-photon transitions, respectively, are displayed in Fig. 2.1b.

In the 2D experiment (Fig. 2.1c), we generate and probe correlations among the various types of coherences by phase-cycled three-pulse sequences with delays of τ (between the first and second pulses) and t (between the second and third pulses). A 36-fold (1×6×6) phase-cycling protocol allows us to simultaneously resolve and acquire nine different nonlinear signal contributions that are schematically shown in a time-domain representation in Fig. 2.1a. These contributions can be extracted according to their

[1] See Chapter 4.

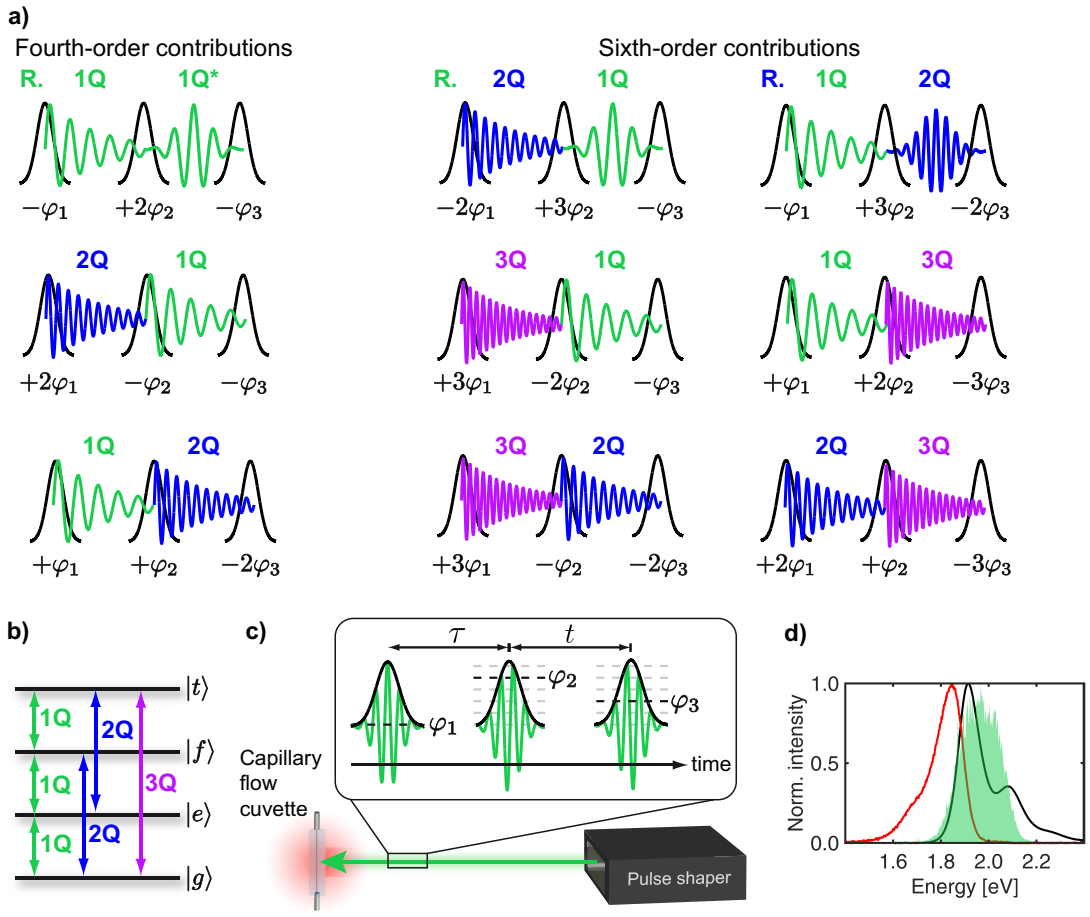

Figure 2.1. Molecular three-quantum 2D fluorescence spectroscopy. (a) Schematics of the nine multiple-quantum 2D signals that can be resolved simultaneously with 36-fold phase cycling of a three-pulse sequence, three of fourth order (left column) and six of sixth order (middle and right columns), listed along with their respective phase signatures. The prefix "R." in a corresponding color indicates rephased quantum coherences. (b) Four-electronic-level energy scheme with ground $|g\rangle$, first excited $|e\rangle$, doubly excited $|f\rangle$, and triply excited $|t\rangle$ states. Possible coherences among these states are indicated by colored double arrows, i.e., one-quantum coherences (1Q, green), two-quantum coherences (2Q, blue), and the three-quantum coherence (3Q, purple). (c) Collinear single-beam three-pulse excitation sequence (green) created by a pulse shaper and resulting fluorescence (red). Interpulse phases are sampled by scanning the absolute phases of the second and third pulses with respect to the first. (d) Linear absorption (black) of rhodamine 700 perchlorate in ethanol (0.1 mM solution), fluorescence (red), and laser spectrum (green shaded area). Reprinted with permission from Ref. [3]. Copyright © (2020) American Chemical Society.

unique phase signatures from the acquired fluorescence signal by a postprocessing routine (see Sec. 2.4) [29].

Throughout this paper, we label these signal contributions as "XQ–YQ", where X and Y represent the quanta (X, $Y = 1$, 2, or 3) of coherences (in units of photon energy) that evolve over τ and t, respectively. If the pulse-specific interaction phases generate

phase conjugation between the correlated coherences, we additionally label the signal with "R." (rephasing), whereas no additional label corresponds to a nonrephasing contribution. Rephasing techniques unveil inhomogeneous broadening [32, 109]. Note that an additional feature of population-based detection in contrast to coherent detection is the ability to detect signals in which the time ordering between coherences XQ and YQ is reversed, enabling us to further decongest overlapping quantum coherence signatures. Differences between these XQ–YQ and YQ–XQ (e.g., 2Q–1Q and 1Q–2Q) 2D spectra reveal information about relaxation pathways of higher excited states [9]. The acquisition of 1Q–2Q and 1Q–3Q 2D spectra is only possible by fourth-order and sixth-order nonlinear processes, respectively, because 2Q and 3Q coherences, which are generated in third- and fifth-order processes, cannot be detected as coherent signals as these coherences are naturally nonradiative [57]. In contrast, using fluorescence detection, the additional last pulse interaction converts the high-order quantum coherence into a population state that can fluoresce directly or indirectly via consecutive internal conversion (IC) and subsequent emission. The additional pulse interaction further enables us to exclusively acquire 3Q–2Q and 2Q–3Q signals that selectively probe couplings between doubly and triply excited states. Such signals are impossible to measure with coherent detection schemes.

For the experiment, we chose the fluorescent dye rhodamine 700 perchlorate in ethanol, which has its absorption maximum at 1.91 eV (Fig. 2.1d, black), corresponding to the S_0–S_1 electronic transition, and has a fairly high fluorescence quantum yield of 36% with a fluorescence spectrum (Fig. 2.1d, red) peaking at 1.85 eV [110]. We cover the main absorption band by sub-20 fs laser pulses with a Gaussian energy spectrum (green shaded area in Fig. 2.1d).

In Fig. 2.2, we present the real parts of all experimental 2D spectra of rhodamine 700 in ethanol that were extracted from a single scan with 36-fold phase cycling (with 150-fold averaging), shown along with simulated spectra. The arrangement of panels is the same as that of the pulse sequences in Fig. 2.1a. The real part of a 2D spectrum displays important properties because it carries the phase information about the nonlinear signal and predominantly features absorptive components. In coherently detected approaches, so-called "phasing" must be carried out to receive the correct phase of a 2D spectrum [39]. In our case, however, correct phasing is automatically and implicitly included through the phase-cycling procedure. The sign of the real part corresponds to the overall sign of the nonlinear response, which can be interpreted as the sum of all double-sided Feynman diagrams that are involved for a given phase signature within the framework of perturbation theory. We provide a Liouville pathway analysis of each signal in Fig. 2.5.

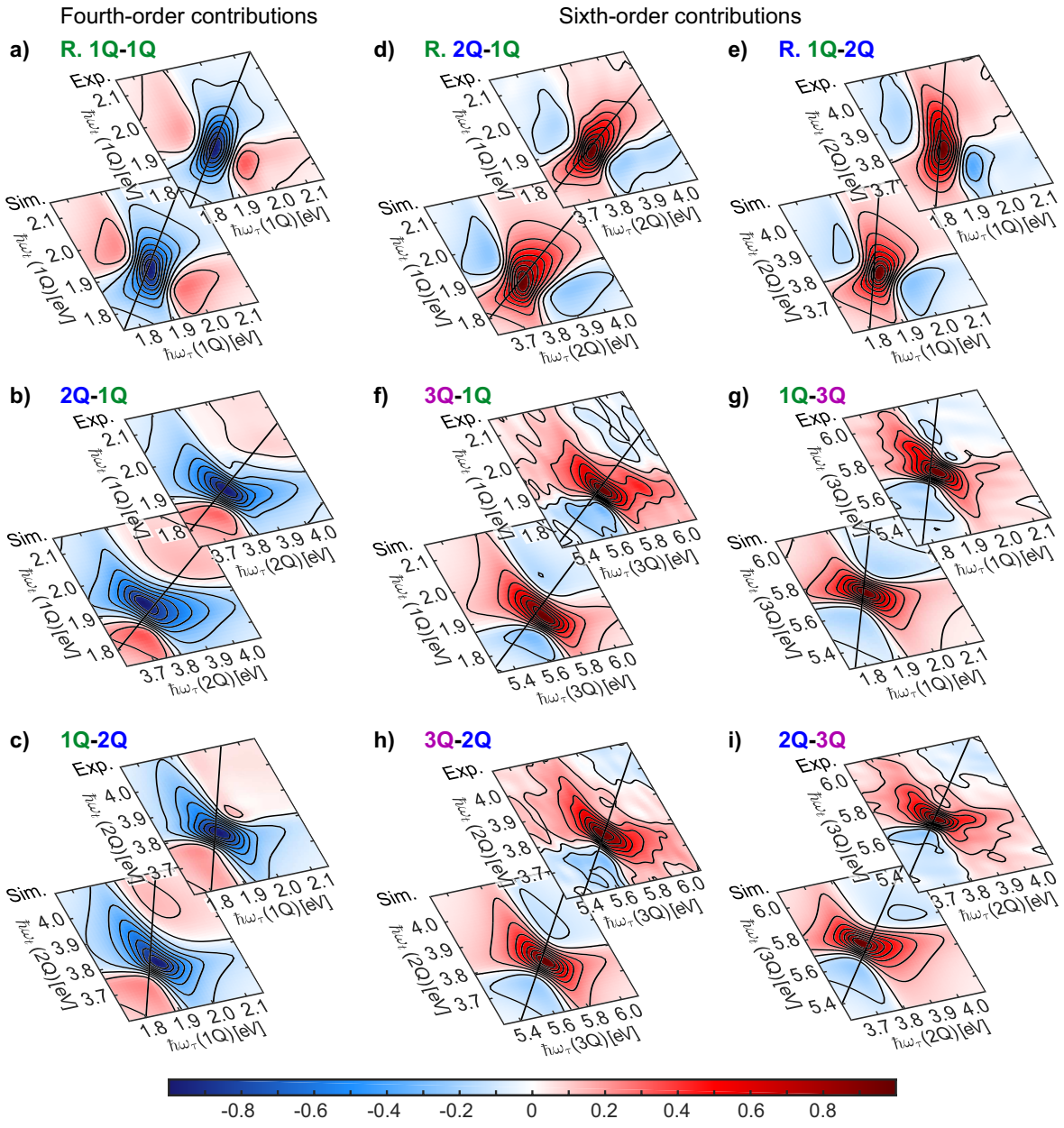

Figure 2.2. Experimental (Exp.) and simulated (Sim.) multiple-quantum 2D fluorescence spectra (real part) of rhodamine 700 in ethanol. All spectra are normalized to their respective highest absolute value. The 2D spectra are grouped into fourth-order (a-c) and sixth-order (d-i) contributions, arranged in the same order as the schematics in Fig. 2.1a, and labeled according to the type of quantum coherences that evolve during the time intervals τ (first label) and t (second label). Each spectrum is drawn with nine linearly spaced contour lines. Reprinted with permission from Ref. [3]. Copyright © (2020) American Chemical Society.

While the fourth-order spectra in Fig. 2.2a–c feature predominant negative signals (blue-colored central peak), the sign change in the sixth-order spectra (Fig. 2.2d–i, red-colored central peak) is consistent with the additional factor of i^2 in the perturbative expansion

[102]. Due to dispersive contributions to the response, all line shapes appear to be phase-twisted (that is, the main signal amplitude is flanked with opposite-signed features of a lower amplitude). All observed maximum signal amplitudes are close to the diagonal line, but small peak shifts from the diagonal on the order of a few tens of millielectronvolts to lower detection energies $\hbar\omega_t$ are visible. In addition, the R. 1Q–1Q, 2Q–1Q, 3Q–1Q, and R. 1Q–2Q 2D spectra exhibit unequal amplitudes of the flanking opposite-signed features, which further indicates the existence of resonances that are red-shifted by a magnitude that is smaller than the homogeneous line width [108]. To explain the appearances of all spectra in detail, we illustrate them in terms of the involved Liouville pathways (Fig. 2.6). As a further visualization aid, we compare the respective projections onto the 1Q mutual energy axes of the 2Q–1Q and 1Q–2Q as well as the 3Q–1Q and 1Q–3Q 2D spectra (see Sec. 2.5.2 of the Supporting Information).

For simulations, we solve the Lindblad master equation numerically [4, 21]. The optimal simulation result is approached by systematic variation of parameters, whereas we use the root-mean-square difference between experimental and simulated real-value 2D spectra as a criterion that represents the quality of the simulated line shapes and the maximal magnitudes of these spectra (normalized to the rephasing 1Q–1Q signal) as a further quantitative feedback (for details about the simulation procedure, see Sec. 2.5.3 of the Supporting Information). We vary the transition energies among level pairs, the pure dephasing times of electronic coherences that govern the lineshapes of all 2D spectra, and the transition moments between the levels that determine the relative signal magnitudes of the 2D spectra and compare the top spectra with the bottom ones. Because we compare nine different spectra in parallel and aim to derive a model that reproduces all spectra simultaneously, a high level of confidence in determining a system description is granted, further minimizing ambiguities in signal interpretation. We observe that variations in transition energy gaps influence the asymmetry of the phase-twisted line shapes and affect their tilt relative to the diagonal. As one can clearly see in Fig. 2.2, the simulation reproduces the sign of all signals and their energetic positions, line shapes, and tilt toward the diagonals very well. In addition, the relative maximal magnitudes between the various simulated contributions (Fig. 2.3a, marked by lines) correspond very well with experiment (Fig. 2.3a, marked by "x"), except for a moderate deviation of the relative magnitude of the R. 2Q–1Q signal. Note that the model was kept as simple as possible to illustrate the general behavior of the signals. Small deviations between the experiment and simulation are found, e.g., in the rephasing 1Q–1Q spectrum (Fig. 2.2a) at 1Q energies above 2.0 eV, where one diagonal and two cross peaks arise as weak features in the experimental spectrum because of coupling to a high-frequency

vibrational mode (see also the progression band in Fig. 2.1d). Such features are not visible in the simulation because we did not implement additional vibrational sublevels.

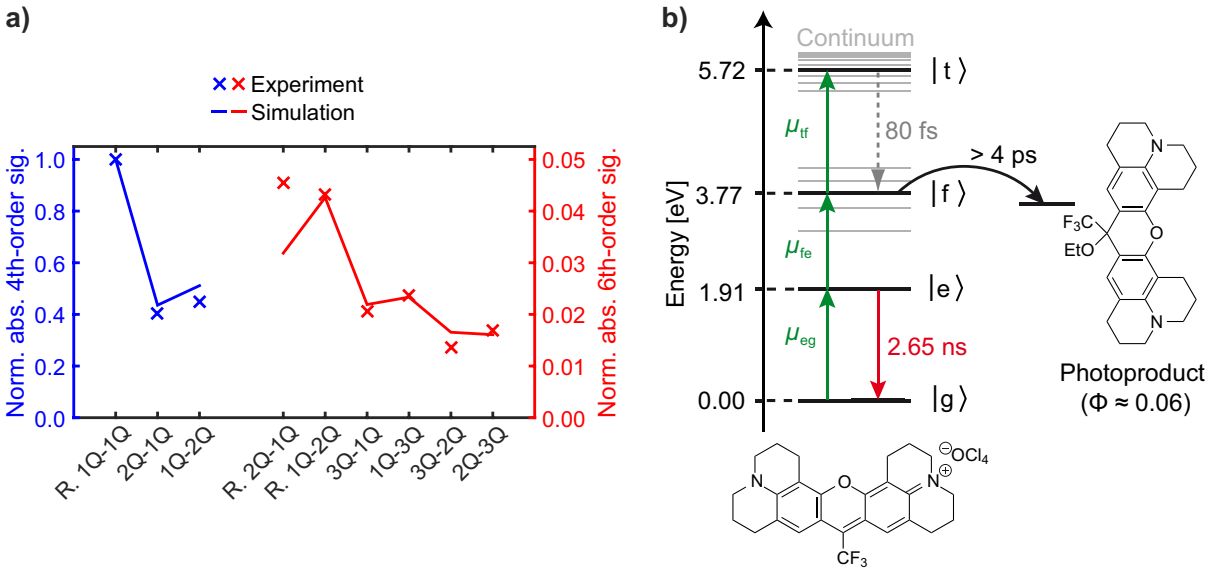

Figure 2.3. Results from theoretical modeling of the experimental data. (a) Experimental (marked by "x") and simulated (marked by lines) maximal signal magnitudes of each nonlinear signal contribution, all normalized to the magnitude of the rephasing (R.) 1Q–1Q signal. (b) Proposed model scheme for rhodamine 700 in ethanol (structural formula shown at the bottom). We assume that one particular vibrational level of each of the electronic levels (black lines) that are labeled as $|g\rangle$ (ground), $|e\rangle$ (first excited), $|f\rangle$ (doubly excited), and $|t\rangle$ (triply excited) can be predominantly accessed. Gray lines illustrate the increasing density of electronic states with an increase in energy. Vertical transitions are indicated by green arrows and corresponding transition dipole moments. Population decay between $|t\rangle$ and $|f\rangle$ is modeled via fast relaxation, whereas the population of state $|f\rangle$ is predominantly transferred to a photoproduct that itself has a low fluorescence quantum yield Φ in the ultraviolet and is not detected. The detected fluorescence signal (red arrow) is proportional to the population of state $|e\rangle$ before relaxation sets in, where the quoted number is the fluorescence lifetime. Reprinted with permission from Ref. [3]. Copyright © (2020) American Chemical Society.

From the simulation result, we derive several conclusions about the investigated system as illustrated in Fig. 2.3b. The transition energy between $|e\rangle$ and $|f\rangle$ is red-shifted by ~50 meV compared to the $|g\rangle \rightarrow |e\rangle$ transition. A somewhat larger red-shift of the $|e\rangle \rightarrow |f\rangle$ transition (62 meV) was found via coherently detected 2Q spectroscopy of the related dye rhodamine 6G [39]. To reproduce the line shapes of the 2Q-associated 2D spectra, the pure dephasing time of the 2Q coherences is set to 65 fs, which is smaller than that of the fundamental $|e\rangle\langle g|$ 1Q coherence (75 fs), thus reflecting a slightly larger energy gap fluctuation amplitude between $|g\rangle$ and $|f\rangle$ than between $|g\rangle$ and $|e\rangle$. Considering the relaxation dynamics of higher excited states in the system presented here, the comparison between 2Q–1Q and 1Q–2Q 2D spectra indicates that state $|f\rangle$

transfers almost its entire population not to $|e\rangle$ but to a different state. By inspecting the respective pathways in panels b and c of Fig. 2.5, one sees that the 2Q–1Q process captures a convolution of both $|e\rangle\langle g|$ and $|f\rangle\langle e|$ 1Q coherence dynamics, whereas the 1Q–2Q process probes only the $|e\rangle\langle g|$ coherence that oscillates at 1.91 eV. Thus, due to the $|f\rangle\langle e|$ coherence oscillating at 1.86 eV, the 2Q–1Q signal appears to be red-shifted along the 1Q axis compared to the 1Q–2Q signal (see also Fig. 2.7). However, such signatures from $|f\rangle\langle e|$ can be visible at all only if state $|f\rangle$ has a negligible quantum yield. In other words, if $|f\rangle$ had a quantum yield similar to that of $|e\rangle$, indicating $|f\rangle \rightarrow |e\rangle$ relaxation, then contributions from the $|f\rangle\langle e|$ coherence would be absent due to pathway cancellation. There can be several reasons for the negligibly small quantum yield of $|f\rangle$. We find that the most likely reason is a photoreaction of the doubly excited rhodamine 700 molecule with solvent molecules forming an adduct (Fig. 2.3b, right) because of the highly electron-withdrawing trifluoromethyl group [111]. Further possible reasons that we deem to be less likely are a high rate of intersystem crossing from $|f\rangle$ to a highly excited triplet state with subsequent relaxation to the ground state (however, potential phosphorescence cannot be captured because emission can be detected only in an interval of <1 ms in our experiment) and other fast nonradiative deactivation pathways via multiple intermediate excited singlet states, possibly via conical intersections. In the model, all three cases are simulated in an effective way by employing a fully nonradiative relaxation channel from $|f\rangle$ to $|g\rangle$, where time constants of this channel above 4 ps lead to the best results. Indeed, we find a photoreaction of the doubly excited molecule to be most likely, also because we observed a nearly complete discoloration of the originally blue rhodamine 700 solution after several 2D experiments that can be reversed by adding some drops of concentrated sulfuric acid to the colorless solution. Moreover, the energy of state $|f\rangle$ is in the vicinity of the first excited singlet state of the possible adduct that is facilitating population transfer to adduct states. We do not observe resonances of the photoproduct in the experimental 2D spectra because of its very low fluorescence quantum yield of 0.06 with a fluorescence spectrum located in the ultraviolet (around 350 nm) [111], where the employed photodetector has a low responsivity.

Focusing specifically on the novel molecular 3Q signals, we find the probed $|t\rangle$ state of rhodamine 700 manifests as a resonance at ~5.7 eV in all 3Q-associated spectra (Fig. 2.2f–i). We estimate relaxation between $|t\rangle$ and $|f\rangle$ to proceed very fast within ~80 fs, possibly via intermediate excited singlet states. From the simulation, we also find that the optical dephasing time of the 3Q coherence is only ~15 fs, leading to line broadening along the 3Q energy axes, which also can be interpreted phenomenologically as a result of the high density of states at such a high energy.

With regard to relative transition dipole moments, we observe that those between excited states are larger than the S_0–S_1 transition dipole moment μ_{eg}. Using 3Q 2D spectroscopy, we here also access such information on the $|t\rangle$ state. In particular, we find that μ_{fe} is 1.35 μ_{eg} and μ_{tf} is 1.90 μ_{eg}. These values lead to the overall smallest deviations in relative signal magnitudes (see Fig. 2.3a). It is worth noting that conventional attempts to measure such highly excited states in solution are exacerbated by the fact that multiphoton absorption of the ubiquitous solvent molecules might generate coherent signals in the same energy range as the 3Q states of the system of interest, generating strong background signals that superimpose the desired high-order quantum coherence. However, considering our experimental results, the advantage of fluorescence detection is that only the fluorescent components of the sample, i.e., the rhodamine 700 molecules, contribute to the final signal.

We now discuss the relevance of unwanted contributions such as multiparticle excitations or wave-mixing cascades that could potentially contaminate the signal and lead to erroneous conclusions. Let us first consider the case in which multiple independent 1Q coherences reside on particles of the ensemble such that the resulting undesired signal might appear in the same way as the desired multiple-quantum signal from one single particle. Such a possibility was recently discussed for phase-sensitive detection by Mukamel [79]. For nonlinear signals that contain interactions by a laser pulse with phase $\pm n\varphi$, this pulse would not act on a single molecule as discussed above, but instead the n interactions would be spread over n individual noninteracting molecules. It was concluded that the magnitudes of these many-particle signals scale nonlinearly with concentration, e.g., following a multiplicative $N(N-1)$ dependence for the case of two-quantum signals, where N is the number of molecules [79]. With regard to the second detrimental effect, cascaded signals can be an issue in high-order nonlinear spectroscopy as discovered for nonresonant fifth-order Raman experiments [58, 112]. While the potentially detrimental multiparticle signal discussed above arises from noninteracting particles, the cascading signal arises from interacting particles in the sense that they exchange photons, resulting in so-called parallel or sequential cascaded pathways that mimic a high-order signal from one molecule via two lower-order signals from distinct molecules [58, 112]. Such signals would scale quadratically with concentration for a cascade consisting of two steps. Thus, to assess the significance of both detrimental effects for the present sample, we carried out concentration-dependent measurements [58, 59, 63, 94, 113]. We show the results for three exemplary sixth-order 2Q- and 3Q-containing signals in Fig. 2.4. Results of all other nonlinear signals are shown in Fig. 2.9.

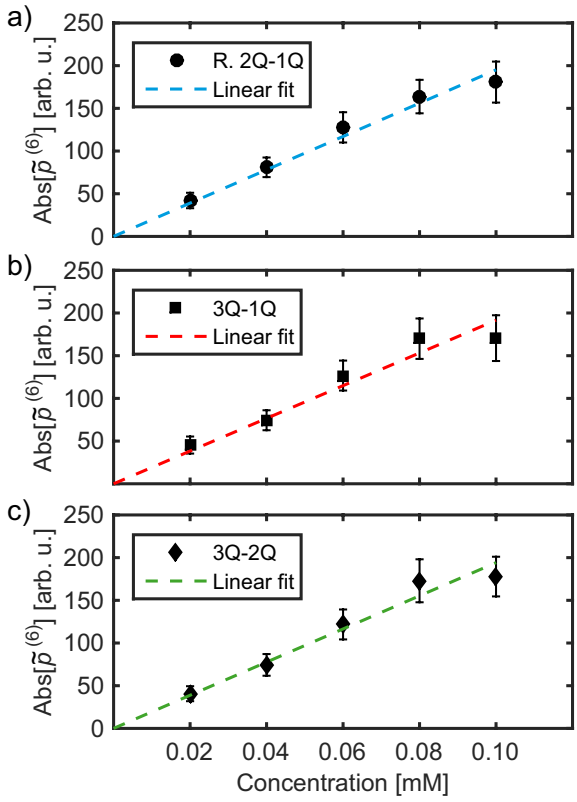

Figure 2.4. Concentration dependence of three exemplary sixth-order nonlinear signals. The data points were obtained from a single multiple-quantum 2D fluorescence measurement (with 50-fold averaging) for each concentration. The signal strength was taken as the highest absolute value in the respective time-domain data of the sixth-order (a) rephasing 2Q–1Q, (b) 3Q–1Q, and (c) 3Q–2Q signals. The error bars represent the standard deviation. Reprinted with permission from Ref. [3]. Copyright © (2020) American Chemical Society.

From Fig. 2.4, it is evident that the sixth-order signals follow a linear concentration dependence. The slight signal decrease at the highest concentration of 0.10 mM can be attributed to reabsorption [59, 63]. Consequently, possible contamination by either multiparticle signals or cascading contributions is not significant in our experiment.

2.3 Conclusion

In conclusion, we presented 3Q molecular 2D electronic spectroscopy that simultaneously acquires four different sixth-order 2D maps containing 3Q coherences, two sixth-order 2D maps containing 2Q coherences, and three fourth-order 2D maps containing 1Q and 2Q coherences. This was achieved using a single excitation beam, 36-fold (1×6×6) phase cycling using shot-to-shot pulse shaping at a repetition rate of 1 kHz, and fluorescence detection. The pulse shaper automatically leads to optimal spatiotemporal overlap of

all pulses and removes the need for geometrical beam splitting, mechanical delay stages, and elaborate measures for ascertaining phase stability between the excitation pulses. The total time window for the pulse sequence is limited to 8 ps by the current pulse shaper, but this is sufficient to record 2D maps at a spectral resolution of ≈1 meV in each dimension. We illustrated the capabilities of the method on the dye rhodamine 700 and found excellent simultaneous agreement with simulations of all nine recorded 2D maps, based on a single, consistent set of model parameters. The model also reproduced the total signal strengths of the nine 2D maps relative to each other. This enabled us to determine quantitatively the relative transition dipole moments and to estimate relaxation pathway rate constants between the excited states. We emphasize that further studies of similar or different molecular systems could provide a benchmark for semiempirical quantum-chemical methods to accurately calculate highly excited states, which is still a challenging task that is computationally costly. By studying the concentration dependence of both fourth- and sixth-order signals, we found no evidence for either cascading lower-order or multiparticle contributions, confirming our interpretation in terms of multiple-quantum signals.

Apart from applications in molecular systems, 3Q 2D fluorescence spectroscopy is suitable for studying bi- and triexcitonic states in organic and other semiconductor materials to obtain insight into many-body physics with high sensitivity and selectivity and without a spurious background.

2.4 Methods

The experimental implementation of the setup was described elsewhere [4, 9]. Briefly, a 1 kHz Ti:Sa chirped-pulse amplifier system (Spitfire Pro, Spectra-Physics, 800 nm, 35 fs) pumped a hollow-core fiber (Ultrafast Innovations GmbH) filled with 1.1 bar of Ar. The resulting white-light continuum was then guided through a dual grism compressor (Fastlite) to precompensate the chirp introduced by an acousto-optical programmable dispersive filter (Dazzler, Fastlite). The pulse shaper generated phase-cycled three-pulse trains at 1 kHz shot-to-shot modulation. The output beam was focused into a capillary flow cuvette with a square cross section of 250 µm × 250 µm (131.310-QS, Hellma), through which the sample volume (50 mL) was pumped by a microannular gear pump (mzr-2942-cy, HNP Mikrosysteme GmbH). To acquire the multiple-quantum 2D spectra of Fig. 2.2, we used a 0.1 mM solution of rhodamine 700 perchlorate (Radiant Dyes Laser Acc. GmbH) in ethanol (analytical grade, Fisher Scientific UK). Scanning of coherence times τ and t, both from 0 to 80 fs, was performed in steps of 2 fs while operating in

a fully rotating frame of the laser reference frequency of 468 THz (1.94 eV). The pulse duration at the sample position was 17 fs (determined by collinear frequency-resolved optical gating), whereas the excitation energy was 180 nJ at maximum constructive interference of all three excitation pulses. The fluorescence signal was attenuated to a linear detector response level by neutral density filters (Newport) and detected via an avalanche photodiode (APD410A2, Thorlabs). The acquisition time of a single full raw data set was approximately 1 min (without averaging). From the resulting single raw data set, we extracted each complex-valued nonlinear signal contribution $\tilde{p}^{XQ\text{–}YQ}$ that probes X-quantum coherence over τ and Y-quantum coherence over t via [29]

$$\tilde{p}^{XQ\text{–}YQ}(\tau,t,\beta,\gamma)=\frac{1}{36}\sum_{l=0}^{5}\sum_{m=0}^{5}p(\tau,t,l\Delta\varphi_{21},m\Delta\varphi_{31})\,\mathrm{e}^{-\mathrm{i}l\beta\Delta\varphi_{21}}\mathrm{e}^{-\mathrm{i}m\gamma\Delta\varphi_{31}}, \tag{2.1}$$

where we chose the following corresponding values for β and γ: rephasing 1Q–1Q, $\beta=+2$, $\gamma=-1$; 2Q–1Q, $\beta=-1$, $\gamma=-1$; 1Q–2Q, $\beta=+1$, $\gamma=-2$, rephasing 2Q–1Q, $\beta=+3$, $\gamma=-1$; rephasing 1Q–2Q, $\beta=+3$, $\gamma=-2$; 3Q–1Q, $\beta=-2$, $\gamma=-1$; 1Q–3Q, $\beta=+2$, $\gamma=-3$; 3Q–2Q, $\beta=-1$, $\gamma=-2$; and 2Q–3Q, $\beta=+1$, $\gamma=-3$. The obtained time-domain maps were apodized by a Hann window before 5-fold zero padding. To exclude artificial signals that may arise from pulse shaper nonlinearities, we conducted a full 2D measurement over 100 averages without a sample but focusing the pulse trains directly on the APD. By using neutral density filters, we ensured the same signal level on the detector as in an actual 2D experiment with fluorescence detection of the sample. The resulting 2D spectra without a sample consisted of noise only, without recognizable features above the signal-to-noise floor except for a minor signal from a pulse shaper nonlinearity in the rephasing 1Q–1Q 2D spectrum (Fig. 2.10). This verified that the nonlinear signals observed in the experiment with the sample were indeed of a molecular origin. For the investigation of the concentration dependence of the nonlinear signals, we maintained identical excitation and detection parameters over all five subsequent measurements and employed 50-fold averaging each. After isolation of each signal contribution via Eq. (2.1), no further postprocessing of the data was carried out. All experiments were conducted under ambient conditions. Simulations were carried out with MatLab R2018a using the parallel computing toolbox on a 72-core cluster. For details about the simulation procedure, see Sec. 2.5.3 of the Supporting Information.

2.5 Supporting Information

2.5.1 Pathway Analysis of the Nonlinear Signals

In this section, we provide a detailed analysis of the experimental signals from the main manuscript. We start with the complete set of double-sided Feynman diagrams of a four-level electronic system with ground state $|g\rangle$, first excited state $|e\rangle$, two- and three-quantum excited states $|f\rangle$ and $|t\rangle$, respectively, that can be accessed by 36-fold phase cycling of a three-pulse sequence with interpulse delays τ and t (Fig. 2.5).

Each pathway in Fig. 2.5 is labeled at the top with the phase signature used for its extraction via phase cycling, and at the bottom as follows: the sign of the pathway, according to the Feynman rules [19], that is positive for an even number and negative for an odd number of interactions on the right side of the diagram; a natural number denoting the weight of the pathway due to time ordering; the imaginary number i to the fourth power (i.e., +1, for fourth-order contributions) or to the sixth power (i.e., −1, for sixth-order contributions); the fluorescence quantum yield Φ_a, with $a = \{e, f, t\}$, associated with fluorescence from the final population state $|a\rangle\langle a|$ reached within each pathway; and finally a label using the letter Q according to the notation of Perdomo-Ortiz *et al.* [26] for which the subscript denotes the number of the pathway for a given signal and the superscript denotes the coherences evolving over the first and second coherence time periods as defined in Fig. 2.1a of the main paper (same color coding).

Let us discuss further some of these quantities. The factors i^4 or i^6 result from the perturbative expansion to either fourth or sixth order in the interaction with the electric light field. Multiplying the pathway sign from the Feynman diagram rules with the corresponding i^4 or i^6 explains why fourth-order signals appear with negative sign while sixth-order signals appear with positive sign in our chosen sign convention (see Fig. 2.2 in the main manuscript). The additional natural number denotes the weight of a pathway due to time ordering. Whenever a pulse interacts with phase $\pm n\varphi$, where n>1, on both bra and ket elements simultaneously, this results in n different possibilities of time ordering of individual interactions, leading to a multiplication of each pathway according to the number of n. The consideration of time ordering holds for pulses with finite duration such as those employed in our experiments. For instance, the prefactor 2 in pathway Q_1^{1Q-2Q} of Fig. 2.5c (top graph) results from two possibilities of time ordering that transfer the 2Q coherence to the final $|e\rangle\langle e|$ population at the end of the t interval: $|f\rangle\langle g| \rightarrow |f\rangle\langle e| \rightarrow |e\rangle\langle e|$ and $|f\rangle\langle g| \rightarrow |e\rangle\langle g| \rightarrow |e\rangle\langle e|$.

In addition to all these prefactors, each pathway is further weighted with the product of the involved transition dipole moments between each bra and ket element which is

not included in the labels.

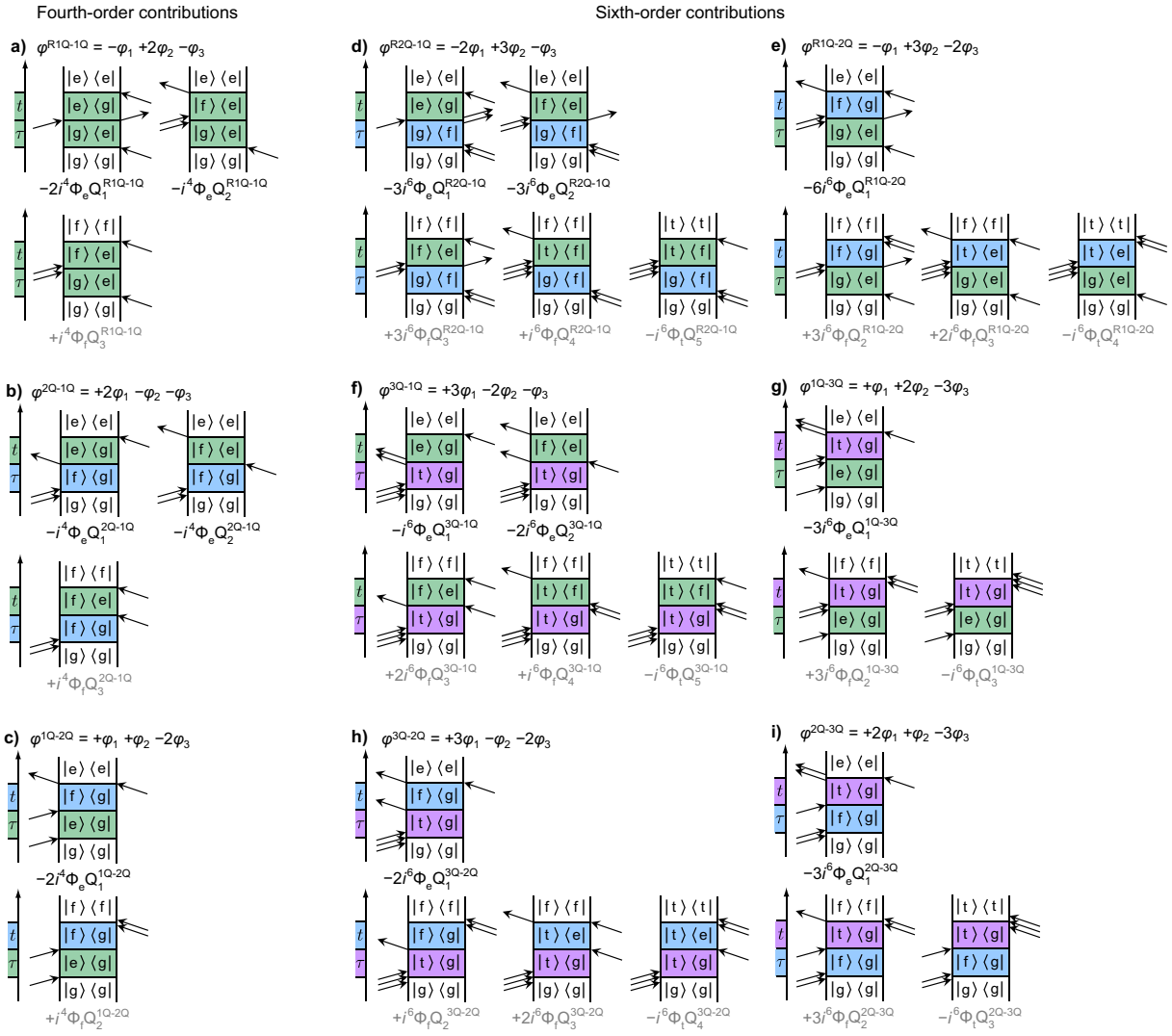

Figure 2.5. Possible multiple-quantum pathways for an electronic four-level system with ground state $|g\rangle$, first excited state $|e\rangle$, doubly excited state $|f\rangle$, and triply excited state $|t\rangle$ that can be accessed by three-pulse sequences with 36-fold phase cycling. Φ_e, Φ_f, and Φ_t denote the fluorescence quantum yields of respective pathways determined by the actual relaxation process of the final population state. The phase signature of each nonlinear signal is denoted on the top of each panel. Pathways that do not contribute to the observed experimental signals in the case of rhodamine 700 are denoted by gray bottom labels. Reprinted with permission from Ref. [3]. Copyright © (2020) American Chemical Society.

We now explain the appearance of all 2D spectra in terms of these pathways. Due to very low fluorescence quantum yield of the higher excited state $|f\rangle$, we consider many pathways to have a negligible contribution to the final signal. From assuming $\Phi_f \approx 0$

directly follows that $\Phi_t \approx 0$ because of the nonradiative relaxation channel $|t\rangle \rightarrow |f\rangle$. We denote non-contributing pathways by displaying the corresponding pathway label in gray in Fig. 2.5. Hence, only pathways with nonzero quantum yield Φ_e contribute to the observed signals. Considering the remaining pathways, we illustrate schematic 2D spectra in Fig. 2.6. Here, each contributing pathway signature in frequency space is represented as a semi-transparent colored circle, centered at its expected position in frequency space, where red denotes positive and blue denotes negative pathway sign. In this representation, dispersive components of the response, which manifest as phase twists in the experimental spectra, are neglected.

For each signal contribution, the small shifts of the maximum signal amplitude from the diagonals that we observe experimentally can either arise from a single pathway (like in the 1Q–2Q process) or the interference (or overlap in the spectral domain) of two pathway signals. For instance, in the rephasing 1Q–1Q spectrum (Fig. 2.6a), the maximum amplitude appears redshifted from the diagonal along $\hbar\omega_t$ which is due to the interference of the pathways Q_1 and Q_2 and indicated by a white cross (note that these schematics do not represent the actual line shapes observed in the experiment). Such pathway overlap signatures are also observed in the (rephasing) 2Q–1Q (Figs. 2.6b,d) and 3Q–1Q spectra (Fig. 2.6f).

A common quantity that can be accessed from multiple-quantum 2D spectra is the energy shift of a higher excited state excited by Y photons relative to Y times the energy of the first excited state. In our case, we define energy shifts of the doubly excited state, $\Delta_f = E_{fg} - 2E_{eg}$, and of the triply excited state, $\Delta_t = E_{tg} - 3E_{eg}$, where E_{ab} is the energy difference between states a and b. The quantity Δ_f was previously associated with the electron correlation energy [36]. Indeed, these energy shifts have been successfully assigned to many-body interaction energies (binding energies) in excitonic systems like quantum wells by coherently detected approaches [53, 81]. However, care must be taken if one wants to designate these energy shifts as molecular electron correlation energies in our case. The term "electron correlation" can only be used if the $|f\rangle$ and $|t\rangle$ states we observe are of true multi-electron rather than of single-electron character, which is per se unknown and difficult to ascertain experimentally. High-level quantum-chemical calculations with proper treatment of electron correlation (like multi-reference or coupled-cluster approaches) may elucidate whether multiple electrons are involved upon excitation into the $|f\rangle$ or $|t\rangle$ level. However, such a task requires enormous computational cost and is beyond the scope of our work.

We note that in contrast to coherently detected 2D spectroscopy, the 1Q–2Q, rephasing 1Q–2Q, 2Q–3Q, and 1Q–3Q contributions (Figs. 2.5c, e, g, and i, respectively) are only

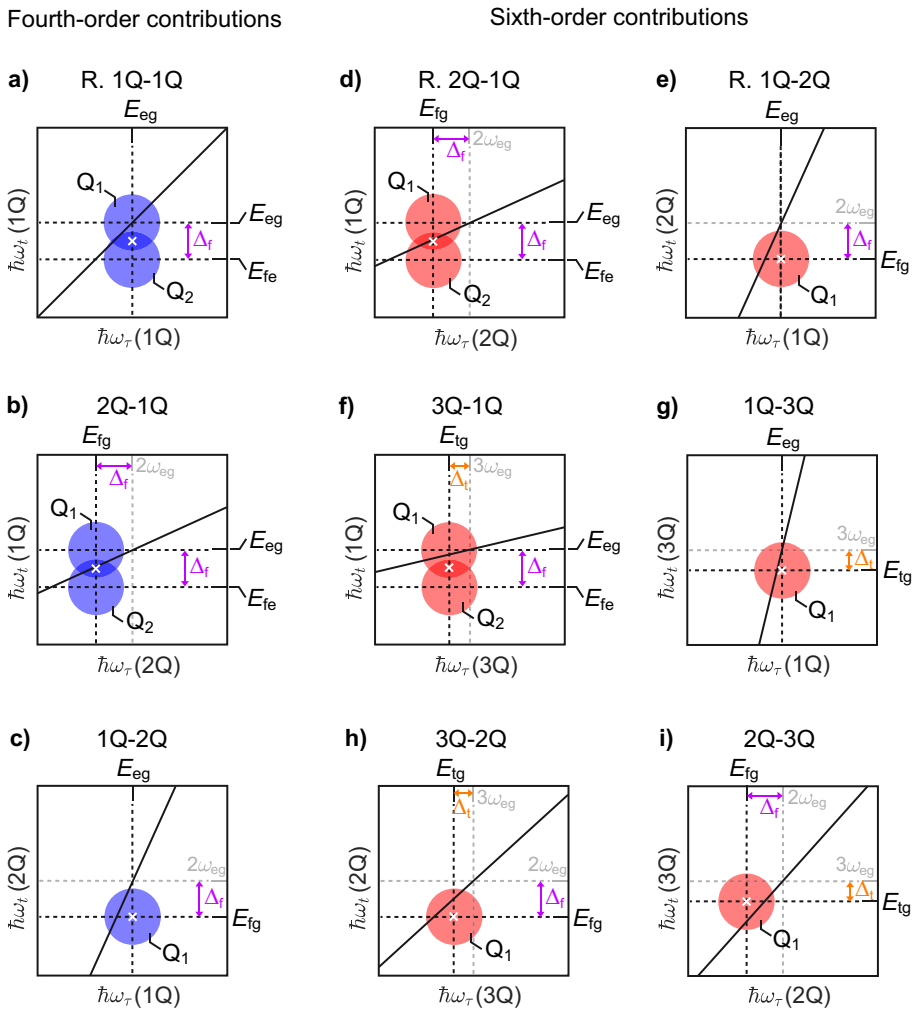

Figure 2.6. Schematic representation of the real-valued multiple-quantum 2D fluorescence spectra in terms of involved quantum pathways of Fig. 2.5. The schematics are arranged in the same order as the experimental and simulated 2D spectra in Fig. 2.2 in Sec. 2.2. In each plot, the spectral shift of the maximum amplitude from the diagonal is denoted by a white cross. Δ_f and Δ_t denote the energy shifts of the two-quantum and the three-quantum excited states, respectively, from corresponding multiples of the one-quantum excited state with energy E_{eg}. Reprinted with permission from Ref. [3]. Copyright © (2020) American Chemical Society.

accessible by population-based 2D spectroscopy because two- and three-quantum coherences are nonradiative and thus cannot be detected coherently. As it can be seen from the Feynman diagrams, the 1Q-2Q, rephasing 1Q-2Q, and 1Q-3Q processes probe fewer pathway types (which in turn means a higher quantum coherence selectivity) compared to the 2Q–1Q, rephasing 2Q–1Q, and 3Q–1Q processes, respectively. Fig. 2.6 illustrates why it is beneficial to determine the energy shifts Δ_f and Δ_t from action-based 1Q–YQ contributions, because then only one pathway contributes to the signal and the peak shifts along the 2Q (or 3Q) axis are not perturbed by other pathways such as in YQ–1Q

signals.

2.5.2 1Q Projections of 2Q and 3Q 2D Spectra

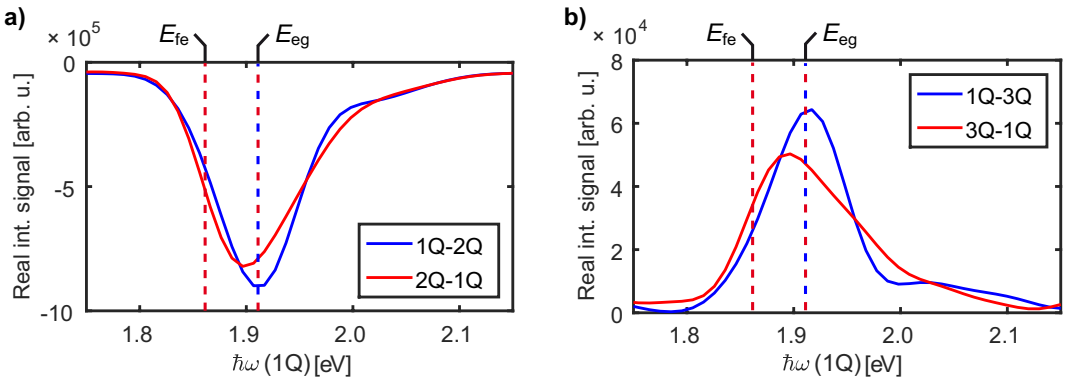

Figure 2.7. Projections of real-valued experimental nonrephasing 2D spectra of (a) the 2Q-associated fourth-order contributions (2Q–1Q and 1Q–2Q) and (b) the 3Q-associated sixth-order 2D contributions (3Q–1Q and 1Q–3Q) onto their mutual 1Q axes. The energies of the individual 1Q transitions E_{eg} and E_{fe} are indicated by dashed lines, where the color of the dashed lines matches the signal type in which these transitions can be observed. Reprinted with permission from Ref. [3]. Copyright © (2020) American Chemical Society.

In Fig. 2.7, we show the one-dimensional projections of the experimental 2Q–1Q and 1Q–2Q (Fig. 2.7a) as well as the 3Q–1Q and 1Q–3Q (Fig. 2.7b) 2D spectra onto their mutual 1Q axes, respectively. This representation illustrates that the line shapes of YQ–1Q contributions are caused by overlapping quantum pathways, while 1Q–YQ contributions do not exhibit such an effect (see also Fig. 2.6). In the fourth-order 2Q–1Q process, the second pulse is able to create either $|e\rangle\langle g|$ or $|f\rangle\langle e|$ 1Q coherences (see also Fig. 2.5b), which both contribute to the line shape of the 1Q projection, causing its overall asymmetric appearance, where the peak value of the red curve is somewhat redshifted relative to E_{eg} (Fig. 2.7a). This redshift results from the contribution of the $|f\rangle\langle e|$ coherence which oscillates at an energy of 1.86 eV, being lower in energy than the $|e\rangle\langle g|$ coherence with $E_{eg} = 1.91$ eV. The emergence of these $|f\rangle\langle e|$ coherence signatures is determined by the degree of interference between the 2Q–1Q pathways Q_2 and Q_3 (Fig. 2.5b) which in turn is dictated by the quantum yield of state $|f\rangle$. In the present case, Φ_f is negligible which leads to the observed red-shift in the 2Q–1Q 2D spectrum. In the 1Q–2Q process, however, due to a single interaction with the first pulse, the only possible 1Q coherence is the fundamental $|e\rangle\langle g|$ coherence (see also Fig. 2.5c), leading to the symmetric peak around E_{eg} which matches the linear absorption maximum energy of the molecule (Fig. 2.7a, blue).

In a similar manner, Fig. 2.7b shows that the sixth-order 3Q–1Q process (red curve) probes both $|e\rangle\langle g|$ and $|f\rangle\langle e|$ 1Q coherences (see also Fig. 2.5f), while the 1Q–3Q process (blue curve) can only generate the fundamental $|e\rangle\langle g|$ coherence, again due to the single interaction with the first pulse (Fig. 2.5g), simplifying the analysis. Note that no $|t\rangle\langle f|$ 1Q coherence signatures are observed because the $|t\rangle\langle f|$-probing pathways do not contribute due to the negligible quantum yields of states $|t\rangle$ and $|f\rangle$.

2.5.3 Simulation Details

We consider a four-level system that gives rise to a density matrix with elements $\rho(t') = \sum_m^4 \sum_n^4 P_{nm} |m\rangle\langle n|$ with $n, m \in \{g, e, f, t\}$ and treat the description of the density matrix dynamics by the Lindblad master equation [21],

$$\frac{\partial}{\partial t'}\rho(t') = -\frac{\mathrm{i}}{\hbar}[H(t'), \rho(t')] + \sum_j \frac{1}{T_j}\left(\mathcal{L}_j\rho(t')\mathcal{L}_j^\dagger - \frac{1}{2}\mathcal{L}_j^\dagger\mathcal{L}_j\rho(t') - \frac{1}{2}\rho(t')\mathcal{L}_j^\dagger\mathcal{L}_j\right), \quad (2.2)$$

where the Lindbladians $\mathcal{L}_j$ describe the relaxation processes, that is, population relaxation $\mathcal{L}_j^{\mathrm{rel}}$ and pure dephasing $\mathcal{L}_j^{\mathrm{deph}}$, which are induced by coupling to the bath. These processes are associated with respective times T_j. Population relaxation and pure dephasing can be expressed by $\mathcal{L}_j^{\mathrm{rel}} = a_n^\dagger a_m$ $(n \neq m)$ and $\mathcal{L}_j^{\mathrm{deph}} = a_n^\dagger a_n$ by using the creation and annihilation operators $a^\dagger$ and a, respectively. In Eq. (2.2), the total Hamiltonian is defined as

$$H(t') = \hbar\omega_n \sum_{n=1}^{4} |n\rangle\langle n| \; + \; \gamma_{\mathrm{ext}} E(t') \sum_{n\neq m} \mu_{nm} \left(|n\rangle\langle m| + |m\rangle\langle n|\right), \quad (2.3)$$

where the left time-independent term contains the eigenstates $|n\rangle$ with state energies $\hbar\omega_n$ and the time-dependent term on the right side describes the interaction of the system with the external electric fields $E(t')$, where μ_{nm} are the transition dipole moments. The external field strength scaling γ_{ext} is set to 0.7×10^{-3}. The electric fields are expressed as three-pulse sequences with time delay τ between the first two pulses and delay t between the second and the last pulse, where each pulse has the pulse duration τ_p and individual phase φ_i $(i = 1, 2, 3)$:

$$\begin{aligned} E(t') = &\exp\left(-\frac{4\ln 2}{\tau_p^2}(t' - t_0)^2\right)\exp\left(\mathrm{i}\omega_0(t' - \gamma_0 t_0) - \mathrm{i}\varphi_1\right) \\ &+ \exp\left(-\frac{4\ln 2}{\tau_p^2}(t' - t_0 + \tau)^2\right)\exp\left(\mathrm{i}\omega_0(t' - \gamma_0(t_0 + \tau)) - \mathrm{i}\varphi_2\right) \\ &+ \exp\left(-\frac{4\ln 2}{\tau_p^2}(t' - t_0 + \tau + t)^2\right)\exp\left(\mathrm{i}\omega_0(t' - \gamma_0(t_0 + \tau + t)) - \mathrm{i}\varphi_3\right). \end{aligned} \quad (2.4)$$

In Eq. (2.4), we choose γ_0 to be zero (fully rotating frame), whereas ω_0 is set to the laser reference frequency of the experiment. The temporal offset t_0 is set to 100 fs. The pulse duration τ_p is set to 15 fs, corresponding to the transform limit of the employed experimental Gaussian laser spectrum. In order to resolve all nine signal contributions, the phases φ_2 and φ_3 are cycled 6 times each. The time-dependent interaction of the external electric fields with the system is calculated within the rotating-wave approximation. The final simulated signal is obtained by integrating over the time-dependent population density matrix elements according to $\mathrm{Tr}\{\Pi\rho(t')\}$, where Π is a projection operator onto the excited population density matrix elements.

We now turn to describing our procedure to determine an optimal set of simulation parameters, which simultaneously fit all nine 2D spectra. Since a simultaneous optimization of all parameters is difficult to carry out in a multidimensional parameter space, our general strategy follows an optimization of one parameter at a time in sequential manner. As a starting point, we take a four-level system in an ideal "harmonic" case, i.e., with equal transition dipole moments and transition energies between each pair of states. The energy of the first excited state, E_{eg} is taken from the maximum of the linear absorption spectrum (1.91 eV). Therefore, our model neglects (dynamic) Stokes shift effects. For the starting point model, we estimate the 1Q pure dephasing time $T_{\mathrm{deph}}^{\mathrm{eg}}$ to be 75 fs which is based on prior findings on similar dyes in the literature [114]. In addition, we assume that 2Q dephasing proceeds at twice the rate of 1Q dephasing and 3Q dephasing occurs at three times the rate of 1Q dephasing. Further, we assume that the different 1Q dephasing times are equal $\left(T_{\mathrm{deph}}^{\mathrm{eg}} = T_{\mathrm{deph}}^{\mathrm{fe}} = T_{\mathrm{deph}}^{\mathrm{tf}}\right)$, and analogously for the 2Q dephasing times $\left(T_{\mathrm{deph}}^{\mathrm{fg}} = T_{\mathrm{deph}}^{\mathrm{te}}\right)$. The population relaxation time of state $|f\rangle$ is chosen to be 4 ps, where a relaxation channel $|f\rangle \rightarrow |g\rangle$ is implemented in order to reproduce the experimental finding of differing 2Q–1Q and 1Q–2Q spectra (see Sec. 2.5.2). The relaxation time between $|t\rangle$ and $|f\rangle$ is first assumed to be 100 fs.

Based on this "harmonic" electronic four-level system, we carry out successive variations of certain parameters (Fig. 2.8). Whenever an optimal parameter is found, it is incorporated into the existing model before we continue to vary the next parameter. In order to quantify the quality of the simulation, we consider two important criteria: (1) the root-mean-squared difference between experimental and simulated 2D spectra, RMSD(2D), which corresponds to the pixel-by-pixel deviation and somewhat quantifies the precision of the parameter in relation to the simulated line shape and (2) the squared difference between the relative experimental and simulated signal magnitudes (normalized to the R. 1Q–1Q contribution), SQD(Sig.). Depending on the adjusted parameter, either one or the other of the two criteria is better suited. Table 2.1 summarizes the

optimal parameters for the simulations shown in the main manuscript (Sec. 2.2) and the criteria that were employed to reach them. For example, we determine the optimal value for the transition energy E_{fe} by considering the minimal value for the sum of RMSD(2D) of the R. 1Q–1Q, 2Q–1Q and 1Q–2Q signals (Fig. 2.8a) because the resonance position of E_{fe} significantly governs the asymmetry of the line shape of these three signals.

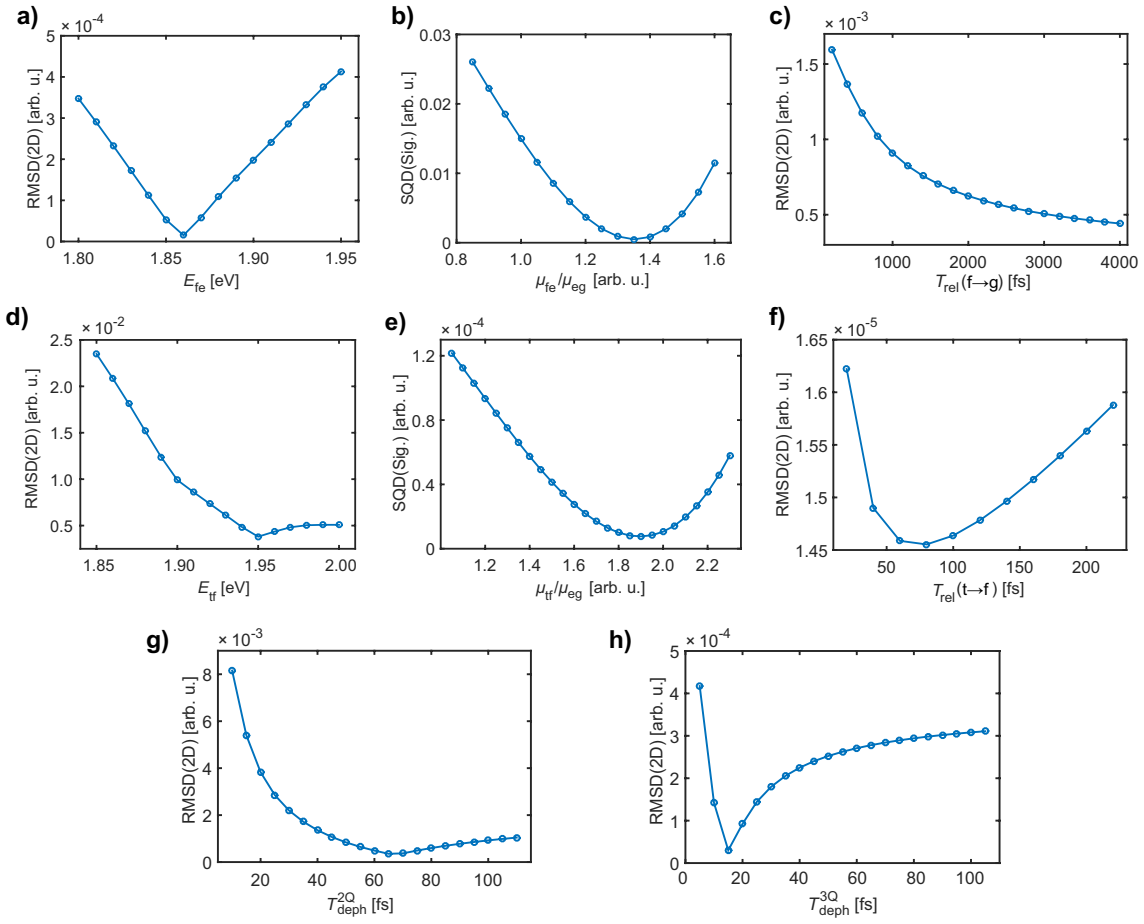

Figure 2.8. Determination of the optimal set of simulation parameters. Certain parameters were varied with regard to either the root-mean-squared difference between experimental and simulated 2D spectra [RMSD(2D)] or the squared difference between experimental and simulated relative signal magnitudes [SQD(Sig.)]. The panels show these quantities under the variation of (a) the transition energy between states $|f\rangle$ and $|e\rangle$, E_{fe}, (b) the transition dipole moment μ_{fe}, (c) the relaxation time between $|f\rangle$ and $|g\rangle$ (which models the nonradiative relaxation behavior of $|f\rangle$), (d) the transition energy between states $|t\rangle$ and $|f\rangle$, E_{tf}, (e) the transition dipole moment μ_{tf}, (f) the relaxation time between $|t\rangle$ and $|f\rangle$, (g) the pure dephasing time of 2Q coherences T^{2Q}_{deph}, and (h) the pure dephasing time of 3Q coherences T^{3Q}_{deph}. Reprinted with permission from Ref. [3]. Copyright © (2020) American Chemical Society.

Taking the optimal value for E_{fe} into account, we approach the optimal parameter for μ_{fe} by evaluating its dependence on the sum of SQD(Sig.) of the 2Q–1Q and 1Q–2Q signals (whereas μ_{eg} is fixed), due to the strong influence of the transition dipole moment

μ_{fe} on the amplitude of these signals as shown in Fig. 2.8b. Next, in order to estimate a value for the relaxation time of state $|f\rangle$, we varied $T_{\mathrm{rel}}\,(f \to g)$ between 200 fs and 4 ps, where the resulting curve in Fig. 2.8c tends to an asymptotic behavior for longer relaxation times, hence we estimate $T_{\mathrm{rel}}\,(f \to g) > 4$ ps to be a valuable result. Because $T_{\mathrm{rel}}\,(f \to g)$ strongly influences the line shapes of the 2Q–1Q and 1Q–2Q contributions, we evaluated the sum of RMSD(2D) of these two signal contributions for this purpose. In principle, the more precise value of $T_{\mathrm{rel}}\,(f \to g)$ can be found by varying it beyond 4 ps, however, this is beyond the scope of our simulations because we are mainly interested in short-time dynamics, which are the ones that have a significant effect on RMSD(2D).

Having completed the optimization of parameters that largely influence the properties of the doubly excited state, we proceed with varying parameters that are connected with the triply excited state and thus have most influence on the 3Q-associated sixth-order spectra. The evaluation criteria with respect to the parameter type are analogously chosen as stated above [considering RMSD(2D) for variation of E_{tf} and $T_{\mathrm{rel}}\,(t \to f)$, whereas considering SQD(Sig.) for varying μ_{tf}], leading to the plots of Figs. 2.8d–f. At the end, we do a refinement of the 2Q and 3Q coherence dephasing times, see Figs. 2.8g and h, respectively.

Table 2.1. Final simulation parameters, shown along with the respective method of determination. Optimal simulation parameters are found by evaluating the dependence on either the root-mean-squared difference between simulated and experimental spectra [RMSD(2D)], or on the squared deviation of experimental and simulated relative maximal signal magnitudes [SQD(Sig.)]. Confidence intervals for the parameters that were varied are visible in Fig. 2.8. Reproduced from Ref. [3].

Quantity		**Value**	**Determination method**
Transition energies	E_{eg}	1.91 eV	Maximum of linear absorption
	E_{fe}	1.86 eV	Min. [RMSD(R. 1Q–1Q) + RMSD(2Q–1Q) + RMSD(1Q–2Q)]
	E_{tf}	1.95 eV	Min. [RMSD(3Q–1Q) + RMSD(1Q–3Q) + RMSD(3Q–2Q) + RMSD(2Q–3Q)]
Transition dipole moments	μ_{eg}	0.66 a.u.	From linear absorption data according to Ref. [115]
	μ_{fe}	1.35 μ_{eg}	Min. [SQD(2Q–1Q) + SQD(1Q–2Q)]
	μ_{tf}	1.90 μ_{eg}	Min. [SQD(3Q–1Q) + SQD(1Q–3Q) + SQD(3Q–2Q) + SQD(2Q–3Q)]
Population relaxation times	$T_{\mathrm{rel}}(e \to g)$	2.65 ns	Taken from Ref. [110]
	$T_{\mathrm{rel}}(f \to g)$	4 ps	Min. [RMSD(2Q–1Q) + RMSD(1Q–2Q)]
	$T_{\mathrm{rel}}(t \to f)$	80 fs	Min. [RMSD(3Q–1Q) + RMSD(1Q–3Q) + RMSD(3Q–2Q) + RMSD(2Q–3Q)]
Pure dephasing times	$T_{\mathrm{deph}}^{\mathrm{eg}}$	75 fs	Estimated on the basis of Ref. [114]
	$T_{\mathrm{deph}}^{\mathrm{fe}}$	75 fs	Assumed $T_{\mathrm{deph}}^{\mathrm{fe}} = T_{\mathrm{deph}}^{\mathrm{eg}}$
	$T_{\mathrm{deph}}^{\mathrm{tf}}$	75 fs	Assumed $T_{\mathrm{deph}}^{\mathrm{tf}} = T_{\mathrm{deph}}^{\mathrm{eg}}$
	$T_{\mathrm{deph}}^{\mathrm{fg}}$	65 fs	Min. [RMSD(2Q–1Q) + RMSD(1Q–2Q) + RMSD(R. 2Q–1Q) + RMSD(R. 1Q–2Q) + RMSD(3Q–2Q) + RMSD(2Q–3Q)]
	$T_{\mathrm{deph}}^{\mathrm{te}}$	65 fs	Assumed $T_{\mathrm{deph}}^{\mathrm{te}} = T_{\mathrm{deph}}^{\mathrm{fg}}$
	$T_{\mathrm{deph}}^{\mathrm{tg}}$	15 fs	Min. [RMSD(3Q–1Q) + RMSD(1Q–3Q) + RMSD(3Q–2Q) + RMSD(2Q–3Q)]

2.5.4 Concentration Dependence of Sixth-Order Signals

In addition to the concentration dependence of the three exemplary sixth-order signals that are presented in Fig. 2.4 in the main manuscript, we here provide the concentration dependence of all the other nonlinear signal contributions, including those of all fourth-order signals, in Fig. 2.9.

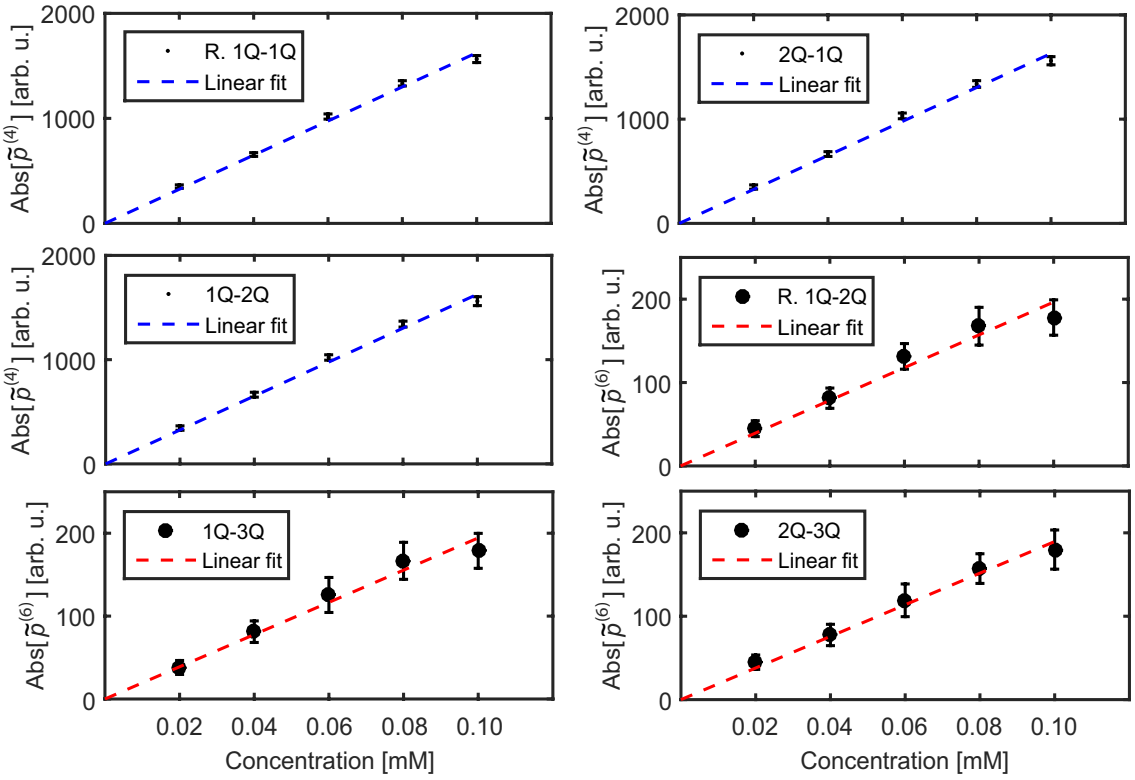

Figure 2.9. Concentration dependence of fourth-order and sixth-order nonlinear signals not shown in the main manuscript. The signal strength was taken as the highest absolute value in the respective time-domain map of each signal contribution. The data shown here originate from the same dataset from which the data of Fig. 2.4 in the main manuscript were taken. Reprinted with permission from Ref. [3]. Copyright © (2020) American Chemical Society.

2.5.5 2D Measurement Without Sample

The fourth- and sixth-order 2D spectra shown in the main manuscript are expected to arise from a convolution of the respective molecular nonlinear response function with the external electric fields. However, any other nonlinearity of the employed instrumentation, i.e., arising from the pulse shaper or the detector, could in principle be convolved with the external light fields as well and in turn produce artificial signals that would survive the phase-cycling procedure. Thus, care must be taken in order to verify the origin of the observed spectral signatures. To address this, we conducted a full 2D measurement without sample, but with direct focusing of the pulse trains on the avalanche photodiode (APD). By attenuation with neutral density filters, we ensured the same signal level on the APD as in the case of fluorescence detection of a sample. The 2D spectra of all nine signal contributions from this measurement are displayed in Fig. 2.10. It is evident that no artificial signals above the noise-floor are observed except for a diagonal "stripe" in the fourth-order rephasing 1Q–1Q 2D spectrum. This "stripe" is caused by a nonlinearity

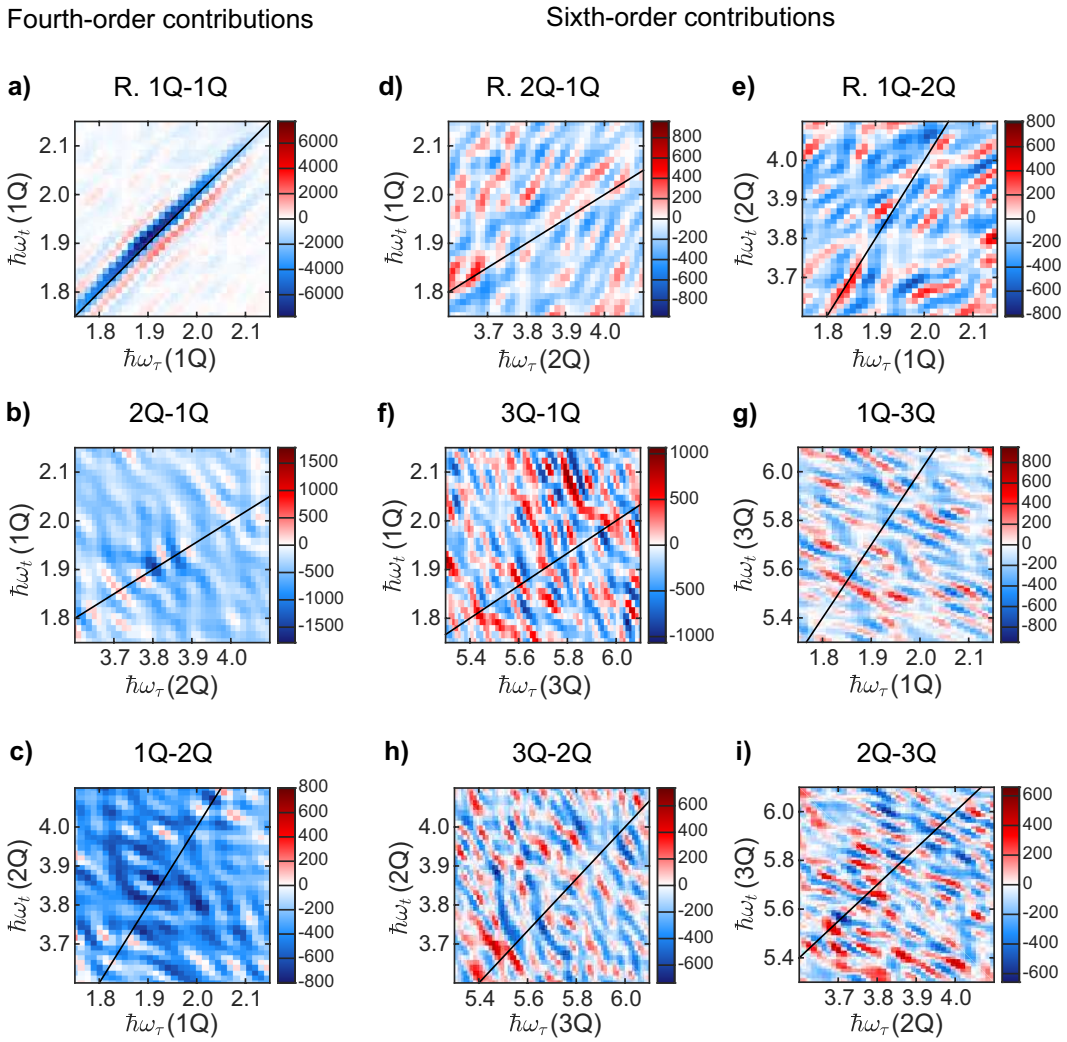

Figure 2.10. Experimental 2D spectra (real parts) which were obtained by direct focusing of the pulse sequences on the employed avalanche photodiode (APD). The same signal level on the APD as in an actual 2D experiment with fluorescence detection of the sample was maintained. Reprinted with permission from Ref. [3]. Copyright © (2020) American Chemical Society.

from the pulse shaper and is observed occasionally because it strongly depends on the exact shape of the acoustic wave within the shaper crystal in combination with the input light power. In comparison to the maximal signal level in the actual measurement of the sample (180327 arb. u.), this isolated "stripe artifact" is much smaller in magnitude (7717 arb. u.).

Summarizing, two important conclusions can be drawn: (1) Nonlinearities of the photodetector are absent and (2) except for a slight contamination of the rephasing 1Q–1Q spectrum (~4%), pulse-shaper-associated artifacts do not significantly contaminate the observed signals, especially not those of the sixth-order response.

Chapter 3

Observing Multiexciton Correlations in Colloidal Semiconductor Quantum Dots via Multiple-Quantum Two-Dimensional Fluorescence Spectroscopy

Correlations between excitons, that is, electron–hole pairs, have a great impact on the optoelectronic properties of semiconductor quantum dots and thus are relevant for applications such as lasers and photovoltaics. Upon multiphoton excitation, these correlations lead to the formation of multiexciton states. It is challenging to observe these states spectroscopically, especially higher multiexciton states, because of their short lifetimes and nonradiative decay. Moreover, solvent contributions in experiments with coherent signal detection may complicate the analysis. Here we employ multiple-quantum two-dimensional (2D) fluorescence spectroscopy on colloidal $CdSe_{1-x}S_x$/ZnS alloyed core/shell quantum dots. We selectively map the electronic structure of multiexcitons and their correlations by using two- and three-quantum 2D spectroscopy, conducted in a simultaneous measurement. Our experiments reveal the characteristics of biexcitons and triexcitons such as transition dipole moments, binding energies, and correlated transition energy fluctuations. We determine the binding energies of the first six biexciton states by simulating the two-quantum 2D spectrum. By analyzing the line shape of the three-quantum 2D spectrum, we find strong correlations between biexciton and triexciton states. Our method contributes to a more comprehensive understanding of multiexcitonic species in quantum dots and other semiconductor nanostructures.

Reprinted with permission from S. Mueller, J. Lüttig, L. Brenneis, D. Oron, and T. Brixner, *ACS Nano* **15**, 4647–4657 (2021).

3.1 Introduction

Microscopic correlations can significantly affect the optoelectronic properties of a quantum system. In a semiconductor quantum dot, optical excitation creates a confined electron–hole pair. Coulomb interactions between the charge carriers have a great impact on the resulting particle complex, the exciton, and determine its energy and lifetime. Apart from the lowest-energy exciton, commonly referred to as the band-edge exciton, quantum confinement gives rise to a spectrum of singly excited excitons that can be created under linear excitation conditions [116].

Under saturated excitation conditions, multiple excitons are generated in the same quantum dot via multiphoton processes. Because of confinement, these excitons are forced to interact strongly. Thus, higher particle complexes form, consisting of four particles (two electron–hole pairs) called biexcitons or six particles (three electron–hole pairs) called triexcitons. These multiexcitonic species form as a result of equilibrated Coulomb interactions between the electron–hole pairs of the constituent excitons. In other words, these excitons are correlated. The precise physics of such correlations facilitate quantum dot applications such as nanocrystal lasers, quantum dot solar cells exceeding the Shockley–Queisser limit, and quantum-logic gates [117–121]. The properties of multiexcitonic states in semiconductor quantum dots can vary drastically across different quantum dot classes. For example, single, epitaxially grown quantum dots can be utilized as sources for highly correlated [122] or even entangled photon pairs due to the cascaded emissive decay of biexciton states [123]. In contrast, in colloidal quantum dots like the ones investigated in this paper, multiexcitons usually relax via nonradiative Auger recombination [124]. Besides the excellent processability of colloidal quantum dots, the great tunability of their optical properties through nanocrystal size and composition makes them particularly suitable for various device applications.

Similar to the occurrence of a spectrum of single excitons, there is a spectrum of multiexcitonic states. The most prominent multiexciton is the lowest energy biexciton, also called ground-state biexciton, which can be formed upon double excitation of the lowest single-exciton transition. Higher biexciton states, which are also called the excited states of the biexciton, are discussed to be involved in the mechanism of multiexciton generation, a process by which a single photon having more than twice the band edge energy excites multiple excitons and which can enhance solar cell efficiencies [121]. However, these excited biexciton states are poorly understood, mostly due to their short-lived and nonradiative decay character, exacerbating their spectroscopic characterization. Detailed characterization of all states of the manifold of multiexci-

tons is required to gain a deeper understanding of exciton correlations and to decipher mechanisms such as carrier relaxation and multiplication, thus highlighting the need for specialized experimental probes.

Multiexcitonic states in colloidal quantum dots are usually studied by time-resolved photoluminescence and transient absorption spectroscopy [120, 125–136]. These techniques enable one to measure, for example, the energies and dynamics of biexciton states. There are also some drawbacks, however. Time-resolved photoluminescence is only sensitive to the ground-state biexciton and cannot reveal information about the higher biexcitons; transient absorption may suffer from overlapping signal contributions that lead to barely visible biexciton-associated features. This overlap is particularly strong in scenarios where the biexciton binding energies, that is, the energy shift of the biexciton state with respect to the sum of the energies of the constituent independent single-exciton transitions, are much smaller than the homogeneous line width [126].

Since multiexcitonic states strongly dictate the nonlinear optical response of quantum dots, coherent two-dimensional (2D) spectroscopy is an excellent tool to study them [137, 138]. Coherent 2D spectroscopy disentangles the nonlinear response over several frequency axes. Thus, 2D spectroscopy reveals correlation functions with high spectral and high temporal resolution, being further ideally suited to probe coherent superpositions of single excitons [138–145]. Coherent 2D spectroscopy was previously applied to colloidal quantum dot systems by detecting coherent third-order nonlinear signals, which correlate the single-exciton states of the system to each other [137–141, 144, 146–155]. This method enables one to probe multiexciton states indirectly by resolving the transitions from single-exciton states to the respective multiexciton states. Conceptually, this is similar to transient absorption spectroscopy, however with the advantage of an additional spectrally resolved pump axis [55]. In contrast to both techniques, the most direct measurement of multiexciton states can be realized by probing multiple-quantum coherences, that is, coherent superpositions of the ground state with biexciton and triexciton states [53]. These multiple-quantum 2D spectroscopies have been demonstrated on solid-state semiconductors using coherent signal detection [40, 53, 57, 99, 156, 157]. Coherently detected fifth-order two-quantum 2D spectroscopy on colloidal CdSe quantum dots was reported very recently [52]. However, the application of multiple-quantum 2D spectroscopy to colloidal quantum dots is generally challenging because of solvent artifacts. Fluorescence-based 2D spectroscopy is an alternative to coherently detected 2D spectroscopy [48, 69, 158]. We have analyzed similarities and differences and compared the advantages of the two methods [2, 7]. With fluorescence detection, solvent contributions can be minimized or even removed entirely. This approach is perfectly suited to

study colloidal semiconductor quantum dots but was so far only demonstrated on PbS quantum dots [87]. To the best of our knowledge, three-quantum 2D spectroscopy has not been reported on any colloidal quantum dot sample.

In this work, we employ multiple-quantum 2D fluorescence spectroscopy to measure biexciton and triexciton spectra directly and to observe multiexciton correlations in colloidal quantum dots. We choose a fluorescent core/shell quantum dot system, $CdSe_{1-x}S_x/ZnS$, in which several excitonic transitions can be simultaneously excited by our broadband laser spectrum. We carry out a three-pulse 2D experiment with which we simultaneously acquire one-quantum–two-quantum (1Q–2Q) and one-quantum–three-quantum (1Q–3Q) 2D spectra that reveal biexciton and triexciton states of the system, respectively. We show that our measurements are sensitive to multiexciton correlations and help to characterize highly excited states in colloidal quantum dots.

3.2 Results and Discussion

In Fig. 3.1, we review the linear exciton properties of the $CdSe_{1-x}S_x/ZnS$ quantum dots. These are capped with oleic acid ligands to be soluble in toluene (Fig. 3.1a). Their linear absorption is shown in Figure 3.1b. Because of the absorption profile being close in shape to the one of pure CdSe, the percentage of sulfur in the core alloy can be roughly estimated to be below 20% [159, 160]. Because ZnS and oleic acid both absorb in the UV [161, 162], the first five exciton transitions can be assigned to those of the core. We employ multi-Gaussian fitting according to established procedures in the literature to determine the amplitudes and energetic positions of the underlying exciton transitions [131, 138, 154, 163]. We use a cubic background function according to Norris and Bawendi [163]. From the fit, we obtain the energies of the first five exciton transitions: $E(X_1) = 1.865$ eV, $E(X_2) = 1.898$ eV, $E(X_3) = 1.973$ eV, $E(X_4) = 2.081$ eV, and $E(X_5) = 2.207$ eV. The bandwidth of these peaks increases as transition energy increases, which is in agreement with previous work [131, 138, 141, 154, 163]. Because of a comparably large average quantum dot diameter of 6 nm, the exciton progression is energetically dense such that the shown exciton bands overlap significantly [129]. We assign the extracted peaks to specific transitions between electron–hole levels considering CdSe as the host lattice (Fig. 3.1c, left) [131, 164]. It is important to separate the electron–hole basis and the exciton basis. While the electron–hole basis is useful to descriptively explain quantum dot properties, the exciton basis is the energy eigenbasis of the system and thus a suitable basis to discuss the spectroscopic properties of quantum dots [138]. For the remainder, we will use the exciton basis (Fig. 3.1c, right)

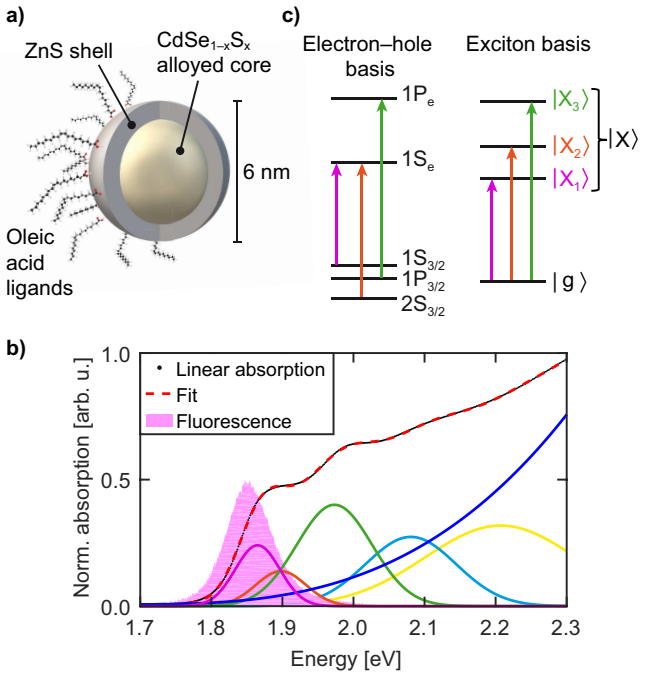

Figure 3.1. Single-exciton properties of the quantum dot system measured in this work. (a) Schematic representation of a $CdSe_{1-x}S_x$/ZnS alloyed core/shell quantum dot. The quantum dots are capped with oleic acid and dispersed in toluene. (b) Linear absorption (black line, normalized to 1.0) and emission spectrum (pink shaded, normalized to 0.5) of $CdSe_{1-x}S_x$/ZnS quantum dots in toluene. Individual excitonic transitions into single-exciton states $|X_1\rangle$ (purple line), $|X_2\rangle$ (orange), $|X_3\rangle$ (green), $|X_4\rangle$ (light blue), and $|X_5\rangle$ (yellow) can be inferred from multi-Gaussian fitting (red dashed), with the dark blue curve representing a cubic background. (c) Energy level scheme of the first three excitations in the electron–hole basis (left) and the exciton basis (right), with the color code of the arrows corresponding to panel b. Note that the "ket" notation indicates the eigenbasis of the system. The manifold of single-exciton statesis denoted as $|X\rangle$. Reprinted with permission from Ref. [1]. Copyright © (2021) American Chemical Society.

and mainly consider the first three excitons, $|X_1\rangle$ $\left(1S_{3/2} \rightarrow 1S_e\right)$, $|X_2\rangle$ $\left(2S_{3/2} \rightarrow 1S_e\right)$, and $|X_3\rangle$ $\left(1P_{3/2} \rightarrow 1P_e\right)$, because these are the ones that we predominantly cover with our fs laser excitation spectrum (see below for more details). Note the comparably small amplitude of the $|X_2\rangle$ peak (Figure 1b, orange), which can be explained by the smaller overlap between the $2S_{3/2}$ hole with the $1S_e$ electron wave function, compared to the overlap of the $1S_{3/2}$ hole with the $1S_e$ electron wave function, resulting in a transition dipole moment smaller than for the $|X_1\rangle$ transition [165, 166]. The fluorescence probed in our experiments (Fig. 3.1b, pink shaded area) originates from the band-edge exciton (Fig. 3.1b, purple line). We discuss separately acquired 1Q–1Q 2D spectra in Sec. 3.5.1 in the Supporting Information. These 2D spectra feature coherent phonon oscillations that can be attributed to the longitudinal optical (LO) phonons of CdSe

[139, 148, 152, 153, 155] and the ZnS shell [167], in agreement with previous reports.

Having determined some single-exciton characteristics, we turn now to probing properties of multiexcitonic states. Let us first focus on biexciton states $|X_nX_m\rangle$. Coulomb interactions between the constituent charge carriers lead to a shift of the energy of the biexciton state $E(X_nX_m)$ with respect to the sum of the resonance energies of the two independent single-exciton transitions $E(X_n)$ and $E(X_m)$ that comprise the biexciton. This shift is quantified by the biexciton binding energy $\Delta(X_nX_m)$, which we define as $\Delta(X_nX_m) = E(X_n) + E(X_m) - E(X_nX_m)$. The biexciton binding energy is an important quantity as it provides a measure for the interaction strength between correlated single excitons. Usually, the biexciton is a bound state, which can be characterized by a positive binding energy [128, 168]. In some cases, negative binding energies were also observed [119, 169]. Because the biexciton consists of a manifold of fine-structure states, a distinction is further made between absorptive and emissive biexciton binding energies [170]. These binding energies relate to spectroscopic transitions into the absorbing and transitions from the emitting biexciton fine-structure states, respectively, which are in turn spectrally separated by a biexciton Stokes shift. Absorptive and emissive biexciton binding energies can be distinguished experimentally, because, for example, transient absorption measures absorptive transitions, whereas time-resolved photoluminescence measures emissive ones [138]. However, since we time-integrate our fluorescence signal in our experiments below, all the biexciton binding energies we determine are considered as absorptive. The most prominent biexciton in CdSe quantum dots, typically measured in time-resolved fluorescence experiments, is the ground-state biexciton $|X_1X_1\rangle$, where both underlying single-exciton transitions correspond to the $1S_{3/2} \rightarrow 1S_e$ band-edge transition [168, 171].

In our experiment, we measure the biexciton spectra by projecting the biexciton states onto the single-exciton states. Technically, this is realized by encoding coherent superpositions of both single-exciton states and biexciton states with the ground state (Fig. 3.2a) into a phase-coherent pulse sequence (Fig. 3.2b). For that purpose, we employed three-pulse sequences scanning interpulse delays τ and t, and 36-fold phase cycling. As we demonstrated recently [3],[1] this phase-cycling protocol also enables us to access the triexciton manifold, which we will discuss later. In Fig. 3.2b, the first pulse creates the ground–exciton 1Q coherence that oscillates over τ (gray line), which is subsequently converted into a ground–biexciton 2Q coherence, evolving over t, by the second pulse (blue line). This 2Q coherence is then converted into a single-exciton population that leads to fluorescence being emitted over t' over which we time-integrate.

[1] See Chapter 2.

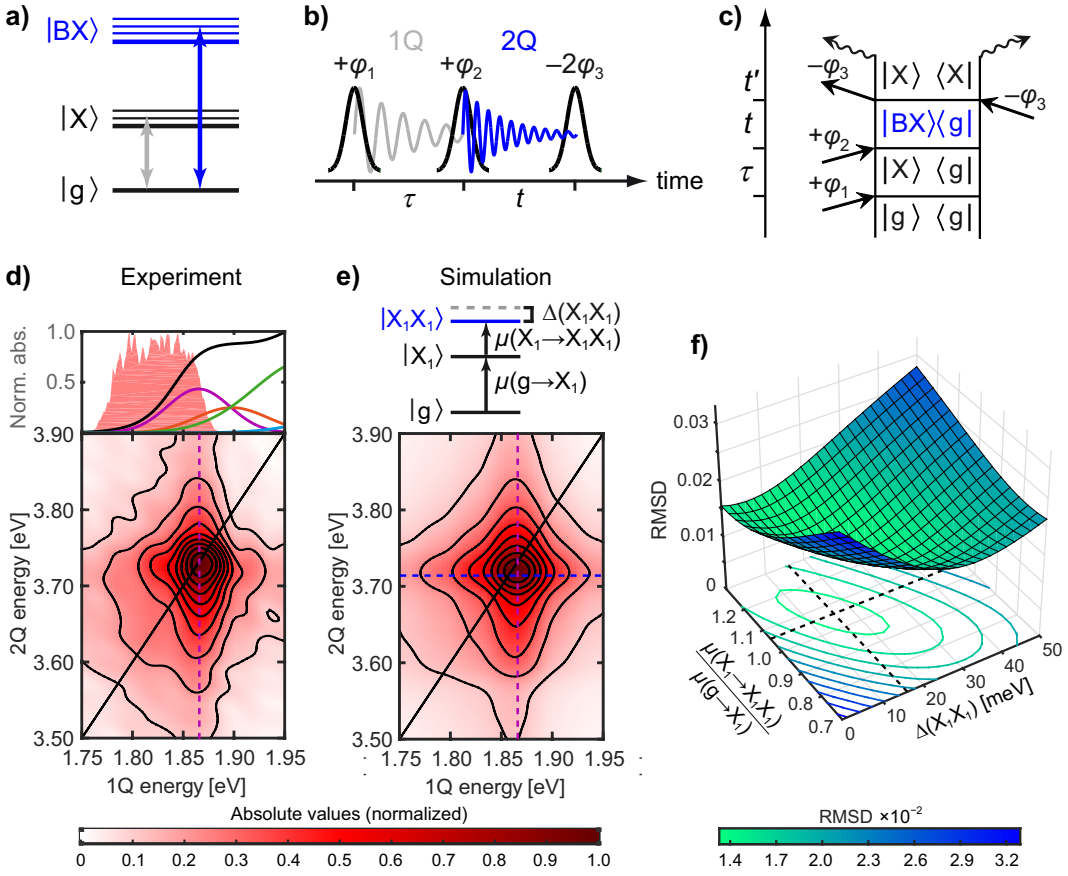

Figure 3.2. Measuring the ground-state biexciton by 1Q–2Q 2D fluorescence spectroscopy. (a) Energy scheme of exciton ($|X\rangle$) and biexciton ($|BX\rangle$) manifolds. (b) Pulse sequence corresponding to the 1Q–2Q contribution. (c) Double-sided Feynman diagram that contributes to the 1Q–2Q 2D spectrum. Fluorescence emission over the detection time t' is denoted by wavy arrows. (d) Top: overlay of the laser spectrum (red shaded area) with the linear absorption spectrum of $CdSe_{1-x}S_x/ZnS$ quantum dots in toluene (black line, with individual excitonic transitions in the same color code as in Fig. 3.1b). Bottom: experimental 1Q–2Q 2D spectrum of the ground-state biexciton (absolute magnitude, normalized). The black diagonal line is drawn where the 2Q energy corresponds to twice the 1Q energy. The purple dashed line indicates the energy of the band-edge exciton state $|X_1\rangle$. (e) Top: energy-level scheme used to simulate the 1Q–2Q 2D spectrum of the ground-state biexciton (bottom, absolute magnitude, normalized), with individual transition dipole moments $\mu(g \rightarrow X_1)$ and $\mu(X_1 \rightarrow X_1X_1)$, and the biexciton binding energy $\Delta(X_1X_1)$. The blue dashed line indicates the energy of the ground-state biexciton that is employed in the simulation and the purple dashed line again the energy of the band-edge exciton state $|X_1\rangle$. (f) Fitness landscape for the determination of $\mu(X_1 \rightarrow X_1X_1)$ and $\Delta(X_1X_1)$. The lowest root–mean–squared deviation (RMSD) between experiment and simulation is obtained for $\Delta(X_1X_1) = 16$ meV and $\mu(X_1 \rightarrow X_1X_1) = 1.06\ \mu(g \rightarrow X_1)$, as indicated by the black dashed lines. Reprinted with permission from Ref. [1]. Copyright © (2021) American Chemical Society.

By appropriate weighting of the experimental data using the phase signature shown in Fig. 3.2b (see also Sec. 3.4) [3, 29], we isolate this so-called nonrephasing 1Q–2Q contri-

bution, which corresponds to a fourth-order nonlinear process. The action of the pulse phases corresponding to this phase signature is depicted as a double-sided Feynman diagram in Fig. 3.2c [19], which remains after pathway cancellation (see also Sec. 3.5.3 in the Supporting Information) [3, 87], showing that in principle the whole biexciton manifold can be probed as $|\mathrm{BX}\rangle\langle\mathrm{g}|$ 2Q coherences. By performing a 2D Fourier transformation of the 1Q–2Q signal with respect to τ and t, we encode spectral correlations among excitons and biexcitons onto a 2D frequency grid. Note that because the 1Q–2Q signal (and also the 1Q–3Q signal, which we discuss later) is a nonrephasing signal, it contains both the absorptive and the dispersive components of the complex-valued nonlinear response, leading to phase-twisted peaks in the real part of the resulting 2D spectrum, which are difficult to interpret. We thus choose magnitude spectra in the following to avoid the phase-twisted representation [17]. Dispersive components can in principle be eliminated by summing the real parts of both rephasing and nonrephasing 2Q contributions, leading to purely absorptive 2Q spectra, which necessitates the measurement of higher-order processes [2, 52].

In the experiment shown in Fig. 3.2d, we chose our excitation spectrum (top, red shaded area) to selectively excite $|\mathrm{X}_1\rangle$ (purple), which in turn leads to the formation of the ground-state biexciton $|\mathrm{X}_1\rangle$ through double excitation. The resulting 1Q–2Q 2D spectrum (bottom) thus shows a single feature at the resonance energy of $|\mathrm{X}_1\rangle$ (purple dashed line) along the 1Q energy axis, being slightly shifted below the diagonal as is typical for a bound biexciton. Apart from the biexciton binding energy, another important quantity that is otherwise difficult to access experimentally is the transition dipole moment from $|\mathrm{X}_1\rangle$ into $|\mathrm{X}_1\mathrm{X}_1\rangle$, $\mu(\mathrm{X}_1 \rightarrow \mathrm{X}_1\mathrm{X}_1)$. In the first approximation, it was previously considered that $\mu(\mathrm{X}_1 \rightarrow \mathrm{X}_1\mathrm{X}_1)$ is equal to the transition dipole moment from the ground state to $|\mathrm{X}_1\rangle$, $\mu(\mathrm{g} \rightarrow \mathrm{X}_1)$ [137, 172]. By systematic simulation of our experimental 2D spectrum (Fig. 3.2e, see Sec. 3.5.2 in the Supporting Information for details), we verified that such an assignment is indeed valid in the present system. To determine $\Delta(\mathrm{X}_1\mathrm{X}_1)$ and $\mu(\mathrm{X}_1 \rightarrow \mathrm{X}_1\mathrm{X}_1)$, we conducted a series of simulations, simultaneously varying both quantities, and compared the root–mean–squared deviation (RMSD), which describes the pixel-by-pixel deviation in the 2D spectra, between experiment and simulation. The resulting fitness landscape (Fig. 3.2f) shows a global minimum at $\mu(\mathrm{X}_1 \rightarrow \mathrm{X}_1\mathrm{X}_1) = 1.06\ \mu(\mathrm{g} \rightarrow \mathrm{X}_1)$ and $\Delta(\mathrm{X}_1\mathrm{X}_1) = 16$ meV. Consequently, the energy of the ground-state biexciton is determined to be 3.714 eV (blue dashed line in Fig. 3.2e). The value for $\Delta(\mathrm{X}_1\mathrm{X}_1)$ is in excellent agreement with previous observations on CdSe quantum dots of similar radii [126, 173]. Further, this finding indicates that alloying the core with sulfur does not lead to strong changes of Coulomb interac-

tions between the charge carriers constituting the ground-state biexciton, compared to CdSe quantum dots. The simulation result using the optimized parameters is shown in Fig. 3.2e and shows excellent agreement with experiment.

It was also shown that, similar to the single-exciton manifold, there is a manifold of biexciton states, that is, having a spectrum that results from exciting different combinations of excitons [126, 128, 138]. Because of the transient nature of excited multiexcitons, however, it is difficult to observe these species. In experiments with coherent signal detection, one can reveal information about excited biexcitons by modeling excited-state absorption features with a series of Gaussians at pump energies moderately above the band-edge exciton energy [126, 131, 138]. However, these features may strongly overlap with other single-excitonic resonances, complicating the interpretation. The particular strength of our technique is that it is free of overlapping features because it directly spectrally resolves the energies of the biexciton states along the 2Q axis. To access the manifold of excited biexcitons, we conducted a second experiment by shifting the excitation laser spectrum to higher energies. Thus, the laser acquires substantial overlap with the $|\mathrm{g}\rangle \rightarrow |\mathrm{X}_2\rangle$ and $|\mathrm{g}\rangle \rightarrow |\mathrm{X}_3\rangle$ transitions, and the 1Q–2Q spectrum becomes clearly dominated by excited biexcitons (Fig. 3.3a).

Because of the comparably large oscillator strength of the $|\mathrm{g}\rangle \rightarrow |\mathrm{X}_3\rangle$ transition, the most prominent features mainly originate from the $|\mathrm{X}_3\rangle$-associated biexciton states, that is, $|\mathrm{X}_1\mathrm{X}_3\rangle$, $|\mathrm{X}_2\mathrm{X}_3\rangle$, and $|\mathrm{X}_3\mathrm{X}_3\rangle$. Simulating the 1Q–2Q spectrum (Fig. 3.3b), however, we conclude that the pattern of features indeed results from many overlapping biexciton states as depicted in Fig. 3.3c (for simulation details, see Sec. 3.5.2 in the Supporting Information). We aimed for a minimal model description and hence only included the states with largest spectral overlap with the laser spectrum, $|\mathrm{X}_1\rangle$, $|\mathrm{X}_2\rangle$, $|\mathrm{X}_3\rangle$, and the corresponding biexciton states, leading to a very good reproduction of the experimental spectrum. Note that we rationalize our results in terms of effective mass theory states and thus use a rather simplistic picture featuring a coarse manifold of discrete biexciton states. Indeed, theoretical treatment using the atomistic approach delivers a more realistic description of the electronic structure of quantum dots [139, 174]. However, atomistic calculations predict a complicated quasi-continuum of fine-structure electron and hole states. On the other hand, at least for the lowest exciton states, both atomistic and effective mass theory yield comparable results [138, 175, 176]. Epecially for well-passivated quantum dots with a ZnS shell like in our case, it turns out that lowest electron and hole levels are well separated [175], which justifies the use of a model with the first three single-exciton states (and the biexciton states resulting from these states) as discrete states. Small deviations between experiment and simulation in the

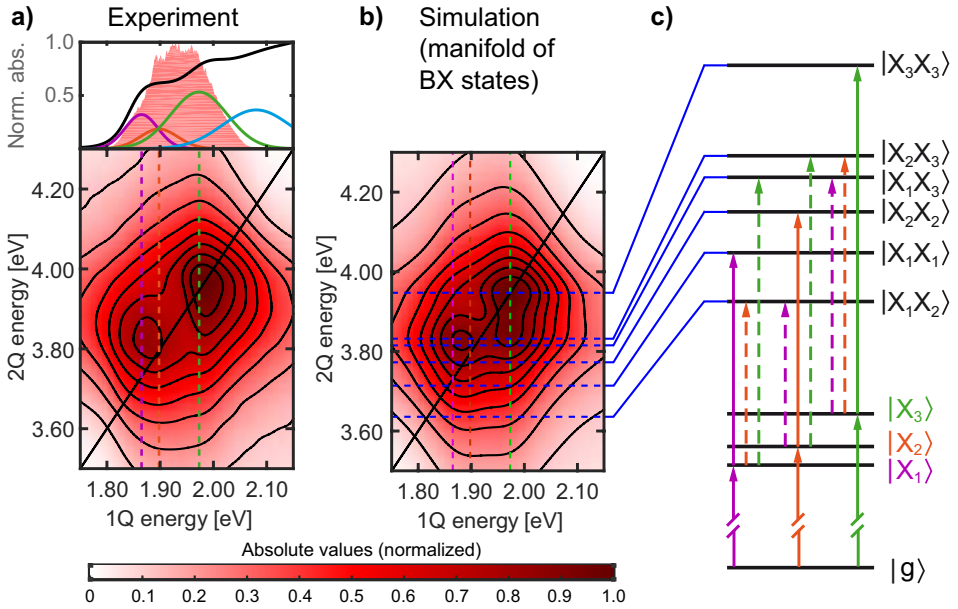

Figure 3.3. Measuring excited biexciton spectra by 1Q–2Q 2D fluorescence spectroscopy. (a) Top: overlay of the laser spectrum (red shaded area) with the linear absorption spectrum of $CdSe_{1-x}S_x/ZnS$ quantum dots in toluene (black line, with individual excitonic transitions in the same color code as in Fig. 3.1b). Bottom: experimental 1Q–2Q 2D spectrum of excited biexcitons (absolute magnitude, normalized). The resonance energies of the first three single-exciton transitions are indicated as colored dashed lines. The black diagonal line is drawn where the 2Q energy corresponds to twice the 1Q energy. (b) Simulated 1Q–2Q 2D spectrum of excited biexcitons (absolute magnitude, normalized). The blue dashed lines indicate the energies of the biexciton states employed in the simulation and the other colored lines again the energies of the first three single-exciton transitions. (c) Energy level scheme used in the simulation including all possible biexciton states that can be constructed from $|X_1\rangle$, $|X_2\rangle$, and $|X_3\rangle$. Solid arrows signify that the transition dipole moments for the $|X\rangle \rightarrow |BX\rangle$ transitions are equal to the dipole moments of the respective $|g\rangle \rightarrow |X\rangle$ transitions; dashed arrows into several biexciton states represent 60% magnitude of the transition dipole moments of the $|X\rangle \rightarrow |BX\rangle$ transitions relative to those of the respective $|g\rangle \rightarrow |X\rangle$ transitions. Reprinted with permission from Ref. [1]. Copyright © (2021) American Chemical Society.

high-energy region along both 1Q and 2Q dimensions can be explained by a contribution of $|X_4\rangle$ (and possibly $|X_4\rangle$-associated biexcitons) to the observed signal since there is at least a small overlap of the laser with the $|X_4\rangle$ band (Fig. 3.3a, top panel). Note that in Fig. 3.3a, the ground-state biexciton is not visible as a clear resonance such as in Fig. 3.2d. Instead, due to the large contribution of the excited biexcitons, the ground-state biexciton now merely contributes to the shoulder of the 1Q–2Q spectrum at lower 2Q energies.

We were able to obtain a good agreement to the experimental 1Q–2Q spectrum (RMSD ~ 0.03) by systematic variation of the individual binding energies $\Delta(X_nX_m)$

for each state of the biexciton manifold, and by scaling the dipole moments of the transitions into the mixed biexciton states ($(|X_n\rangle \rightarrow |X_nX_m\rangle$, with $n \neq m$) by 0.6 (Fig. 3.3c, dashed arrows). We show the root–mean–squared deviations for other scaling values in Fig. 3.7c in Sec. 3.5.2 in the Supporting Information, demonstrating the sensitivity of 1Q–2Q 2D spectra toward the dipole moments of the biexciton transitions. In contrast to biexcitons that involve a double excitation of the same single exciton (e.g., $|g\rangle \rightarrow |X_1\rangle \rightarrow |X_1X_1\rangle$), there are always two excitation pathways that lead to a mixed biexciton. The mixed biexciton $|X_1X_3\rangle$, for example, can be accessed by the two excitation pathways $|g\rangle \rightarrow |X_1\rangle \rightarrow |X_1X_3\rangle$ and $|g\rangle \rightarrow |X_3\rangle \rightarrow |X_1X_3\rangle$. Because of the occurrence of these two possibilities, one expects the transition dipole moments between the single-exciton states and the respective mixed biexciton states to be only half as large as those to the nonmixed biexciton states, at least in the case that the first transition step does not influence the second one. This is close to our finding, from the simulation, of a scaling value of 0.6 for the exciton-to-biexciton transition dipole moment.

Concerning the biexciton binding energies, our estimates of $\Delta(|X_1X_2\rangle) = 127$ meV and $\Delta(|X_1X_3\rangle) = 23$ meV are significantly larger than the ground-state biexciton binding energy (16 meV), which reproduces a trend in accordance with previous observations on CdSe quantum dots [126–128, 138]. For the other excited biexcitons, the simulation yields $\Delta(|X_2X_2\rangle) = 23$ meV, $\Delta(|X_2X_3\rangle) = 39$ meV, and $\Delta(|X_3X_3\rangle) = -1$ meV. Hence, our results indicate that biexcitons that comprise the same exciton types, that is, with similar electron and hole wave functions involved, have a smaller binding energy than mixed biexcitons. The uncertainties of the biexciton binding energies can be estimated from their RMSD curves in Fig. 3.7 in the Supporting Information. Note that the parameters determined here may not necessarily represent the ones that correspond to the global RMSD minimum. As indicated in the example above concerning the determination of the binding energy of the ground-state biexciton and the dipole moment into the ground-state biexciton, it is not straightforward to find the global minimum of the deviation between experiment and simulation because binding energies and transition dipole moments are not independent of each other with regard to the precise amplitude distribution of the 1Q–2Q 2D spectrum. The problem of the mutual optimization of transition dipole moments and binding energies of excited biexcitons should be treated, in principle, in a hyper-dimensional parameter space, which is, however, computationally intractable within our simulation framework. (Note further that our simulations include pulse-shape effects, which are crucial for the accurate reproduction of peak shapes, but enormously increase computational cost.) The parameters we determined could represent a local minimum on the RMSD hypersurface and possibly reflect a trend

rather than explicit binding energies. Moreover, we emphasize that our model uses a minimal number of exciton states so that fine-structure biexciton states and higher biexciton states are neglected. In particular, the almost negligible binding energy of $|X_3X_3\rangle$ could be the result of the presence of the $|X_4\rangle$-associated biexcitons mentioned above, which are expected in the energetic vicinity of $|X_3X_3\rangle$. Nevertheless, our results strongly suggest that the peak pattern observed in the 1Q–2Q 2D spectrum of excited biexcitons is the result of the interplay of many overlapping discrete biexciton states, which have distinct binding energies and transition dipole moments.

As mentioned above, our phase-cycling scheme also grants us access to a sixth-order nonlinear signal, which projects the triexciton states onto the single-exciton states (Fig. 3.4a) [3]. We can extract this signal from the same data set of the three-pulse experiment by weighting with the 1Q–3Q signal-specific phase signature, as depicted in Fig. 3.4b. The 1Q–3Q signal has the phase-specific interaction pattern shown in the Feynman diagram in Fig. 3.4c, which is the one that remains after pathway cancellation due to Auger relaxation of the multiexcitons (see Sec. 3.5.3 in the Supporting Information).

Upon first inspection of the experimental 1Q–3Q 2D spectrum in Fig. 3.4d, it is apparent that it is dominated by excited triexcitons. The ground-state triexciton $|X_1X_1X_3\rangle$ [177, 178], which is, under the assumption of a binding energy of ~100 meV [138], expected at a 3Q energy of ~5.6 eV, does not appear as a clear resonance. The peak of the largest-magnitude feature at a 3Q energy of ~5.9 eV is somewhat shifted away from the $|X_3\rangle$ 1Q energy (green dashed line in Fig. 3.4d), which might be an indication for a non-negligible contribution of the $|X_4\rangle$ exciton (and $|X_4\rangle$-associated triexcitons).

The most striking features of the 1Q–3Q spectrum are the significantly negatively tilted peak shapes as indicated by the white line for the higher-energy feature in Fig.3.4d. While positive peak tilts were previously observed in 2Q spectra [179] of semiconductor quantum wells [99] and a laser dye [56], we here observe, in contrast, a negative peak tilt in 3Q 2D spectra. One of the great strengths of 2D spectroscopy, which we want to exploit in the following, is its ability to probe frequency–frequency correlation functions [180–182]. We sought to model the origin of this peak tilt by a simple response-function calculation (Fig. 3.4e). For the sake of simplicity, we only modeled the feature with the largest magnitude in the 1Q–3Q spectrum, which we mainly attribute to the excited triexciton $|X_3X_3X_3\rangle$. We estimate a binding energy of $\Delta(|X_3X_3X_3\rangle) \approx 50$ meV. Following a similar modeling strategy as described in the literature [67], we modeled (anti)correlated transition energy fluctuations (see Sec. 3.4) and assumed that fluctuation bandwidths associated with biexciton and triexciton states are two- and three-times

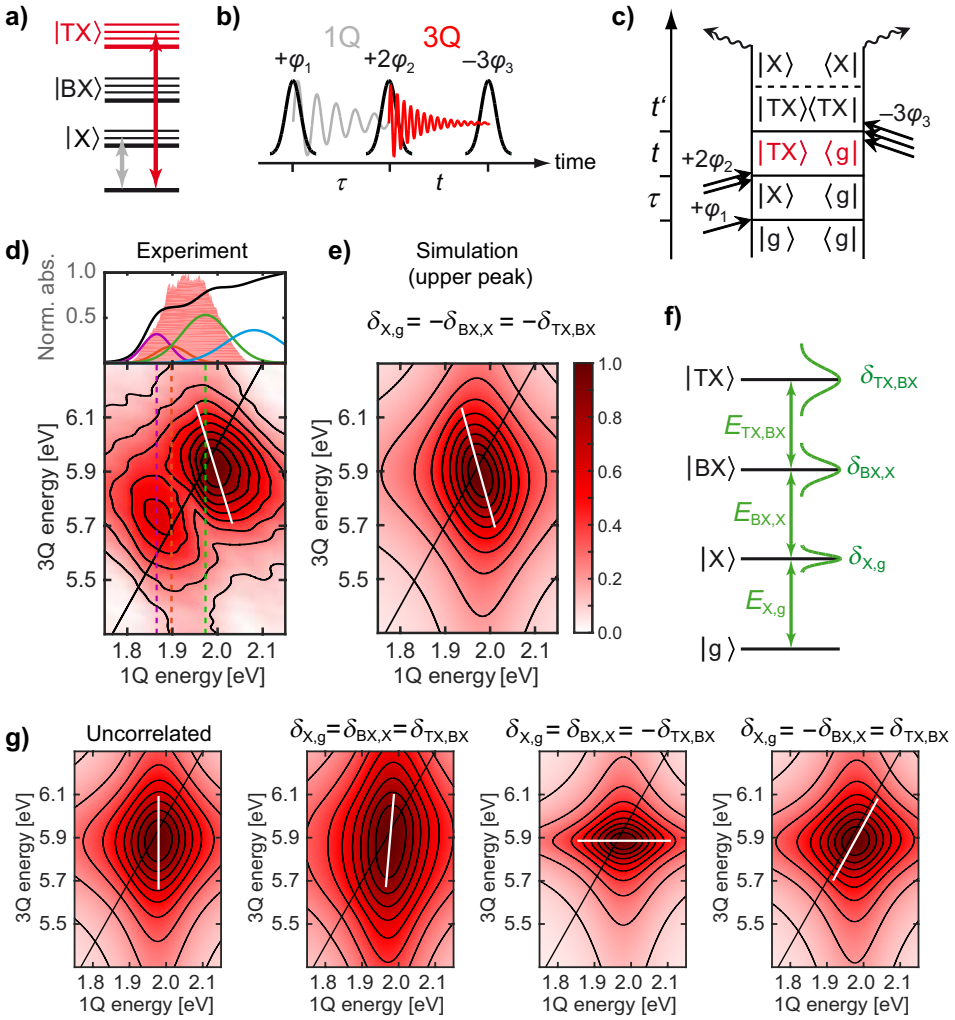

Figure 3.4. Measuring triexciton spectra by 1Q–3Q 2D fluorescence spectroscopy. (a) Energy level scheme of exciton ($|X\rangle$), biexciton ($|BX\rangle$), and triexciton ($|TX\rangle$) manifolds. (b) Pulse sequence of the 1Q–3Q process. (c) Double-sided Feynman diagram contributing to the 1Q–3Q process. (d) Top: overlay of the laser spectrum (red shaded area) with the linear absorption spectrum of $CdSe_{1-x}S_x/ZnS$ quantum dots in toluene (black line, with individual excitonic transitions in the same color code as in Fig. 3.1b). Bottom: experimental 1Q–3Q 2D fluorescence spectrum. The first three single-excitonic transitions are indicated as colored dashed lines. (e) Response-function calculation of the higher-energy feature only. (f) Energy level scheme displaying transition energy fluctuations with Gaussian bandwidths $\delta_{X,g}$, $\delta_{BX,X}$, and $\delta_{TX,BX}$. (g) Response-function calculations of the higher-energy feature only, for uncorrelated (left) and various other scenarios of (anti)correlated transition-energy fluctuations as labeled on the top. In panels d, e, and g, the black diagonal line is drawn where the 3Q energy corresponds to three-times the 1Q energy, whereas white solid lines indicate the line-shape tilt. All 2D spectra are shown in normalized absolute magnitudes. Reprinted with permission from Ref. [1]. Copyright © (2021) American Chemical Society.

larger, respectively, than the ground-state to single-exciton transition fluctuation bandwidth $\delta_{X,g}$ (Fig. 3.4f). If two transition energy fluctuations are correlated (positive

sign), then both transition energies are blue- or red-shifted. In the anticorrelated case (negative sign), the red-shift of one of the transitions causes a blue-shift of the other transition and vice versa. We tested and plot in Fig. 3.4g, from left to right, different scenarios of uncorrelated, fully correlated, and two alternatives of anticorrelated fluctuations and found that the peak tilt observed in the experiment is only reproduced by setting $\delta_{\mathrm{X,g}} = -\delta_{\mathrm{BX,X}} = -\delta_{\mathrm{TX,BX}}$ (Fig. 3.4e). In all other cases as shown in Fig. 3.4g, the direction of the tilt is wrong. Thus, we deduce a pattern of anticorrelated fluctuations to be the most accurate description. Indeed, strongly (anti)correlated behavior can be expected regarding the fact that all (multi)excitons are confined over the same core volume. In particular, the anticorrelation between $\delta_{\mathrm{X,g}}$ and $\delta_{\mathrm{BX,X}}$ as well as between $\delta_{\mathrm{X,g}}$ and $\delta_{\mathrm{TX,BX}}$ can be viewed as an intrinsic feature of the quantum dot to adapt to bath-induced transition energy fluctuations. In other words, every transition energy fluctuation of the single exciton will directly affect the energies of the states of the multiexciton manifolds. These fluctuations result from local changes in the dielectric constant or the local electric field and thus modify the Coulomb interactions between the charge carriers of each exciton. In turn, the fluctuation pattern we observe indicates that, depending on the amplitude of the single-exciton transition energy fluctuation $\delta_{\mathrm{X,g}}$, the corresponding multiexciton is stabilized (increased binding energy) or destabilized (decreased binding energy or even repulsive interaction energy). Interestingly, we here observe correlations between multiexcitons. Stabilizing (or destabilizing) the biexciton causes a stabilization (or destabilization) of the corresponding triexciton as well. One potential mechanism that could induce this type of dependence is the quantum confined Stark effect. Under the effect of an external electric field, there is an increase (or decrease) in the Coulomb repulsion of all multiexcitonic states if the electric field is directed along (or against) the permanent dipole of the excited single exciton [183, 184].

3.3 Conclusion

We have demonstrated that multiple-quantum two-dimensional (2D) fluorescence spectroscopy gives direct access to the spectra of biexciton and triexciton states in colloidal semiconductor quantum dots. Our method directly resolves the energies of the biexciton and triexciton states without further overlapping features or solvent contributions. This represents an advantage for probing multiexciton correlations compared to time-resolved photoluminescence, transient absorption, or one-quantum–one-quantum 2D spectroscopy. On the example of alloyed $\mathrm{CdSe_{1-x}S_x/ZnS}$ core/shell quantum dots, signatures of multiexciton correlations were observed as resonances in one-quantum–

two-quantum (1Q–2Q) and one-quantum–three-quantum (1Q–3Q) 2D spectra. While the 1Q–2Q 2D experiment revealed correlations between single excitons in terms of biexciton binding energies, in the 1Q–3Q 2D experiment, significant correlations between biexcitons and triexcitons manifested as correlated transition energy fluctuations.

We showed that upon broadband excitation of the first three single-exciton transitions, the 1Q–2Q and 1Q–3Q 2D spectra become dominated by many overlapping peaks stemming from various excited multiexciton states. By analyzing 1Q–2Q 2D spectra with different laser spectra, we determined the binding energy of the lowest biexciton to be 16 meV and estimated the binding energies of the first five excited biexcitons. Our results indicate that mixed biexcitons, in which the electrons and holes occupy states of different symmetry, have the largest binding energies. Through simulation of the obtained spectra, we also determined relative exciton-to-biexciton transition dipole moments. We found that biexciton states that do not involve a double excitation of the same excitonic transition have a significantly lower exciton-to-biexciton dipole moment than biexciton states involving a double excitation of the same exciton transition.

Results from 3Q 2D spectroscopy revealed triexciton excited states with significant peak tilts with negative sign. We interpreted these tilts as a signature of strongly anticorrelated transition energy fluctuations, being a consequence of interparticle Coulomb interactions between the charge carriers that constitute the multiexcitons. Altogether, we demonstrated that our technique elucidates the highly correlated character of excitons across various multiexciton states. We believe that the technique can be applied to many other fluorescent nanomaterials as well, and knowledge gained from these experiments will help to manipulate and tailor multiexciton correlations, which is essential for the development of the next generation of quantum dot devices.

3.4 Methods

Experimental Setup and Data Processing

All experiments were conducted at room temperature. The experimental implementation of the setup was described in detail previously [3, 4]. Briefly, we used a Ti:Sa chirped-pulse amplifier system (Spitfire Pro, Spectra-Physics, 800 nm, 35 fs) at 1 kHz. We generated a white-light continuum by a hollow-core fiber (Ultrafast Innovations GmbH) filled with 1.1–1.4 bar of argon. The white light was shaped by an acousto-optical programmable dispersive filter (AOPDF, Dazzler, Fastlite) to produce phase-cycled three- and four-pulse sequences (for the measurements reported in the Supporting Information) on a shot-to-shot basis. Dispersion management was done by a dual

grism compressor (Fastlite) and the AOPDF. The output beam was focused into a capillary flow cuvette with square cross-section of $(250\ \mu\mathrm{m})^2$ (131.310-QS, Hellma), through which the sample volume (10 mL) was continuously pumped by a microannular gear pump (mzr-2942-cy, HNP Mikrosysteme GmbH) to suppress photocharging effects. The sample was commercially purchased from Sigma-Aldrich and consisted of a 1 mg/mL solution of $CdSe_{1-x}S_x$/ZnS alloyed core/shell quantum dots with an average diameter of 6 nm, functionalized with (9Z)-octadec-9-enoic acid ligands (oleic acid) and dispersed in toluene. In all experiments, the fluorescence signal was attenuated to a linear detector response level by neutral density filters (Newport) and detected via an avalanche photodiode (APD410A2, Thorlabs) with aid of a pair of microscope objectives (04OAS010, CVI Melles Griot). Potential scattering contributions of the excitation pulses were prevented by detecting the fluorescence at an angle of 90° with respect to the excitation beam while using an excitation polarization that points into the detection direction [72], and by employing an RG645 color filter. The 2D experiments were carried out on different sample batches on different days to ensure reproducibility. For the three-pulse 2D experiment that probed the ground-state biexciton, we scanned both coherence times τ and t from 0 to 120 fs in 4 fs steps in a fully rotating frame of 441 THz (1.82 eV). The pulse duration was <33 fs (intensity fwhm) and the excitation energy was 60 nJ (at maximum pulse overlap). For the experiment that measured the manifolds of biexcitons and triexcitons, the reference frequency was changed to 468 THz (1.94 eV) whereas the pulse duration was <18 fs and the excitation energy was 180 nJ. For all three-pulse experiments, we employed 36-fold (1×6×6) phase cycling. Averaging was performed to increase data quality, leading to a normalized standard deviation of the maximal signal magnitudes of the 1Q–2Q signal of the ground-state biexciton 2D measurement of 4.5%. In case of the 2D experiment probing of the biexciton and triexciton manifolds, the normalized standard deviations of the 1Q–2Q and 1Q–3Q signals are 2.5% and 4.5%, respectively. For each 2D experiment, a control measurement was further carried out to check for unwanted signals arising from detector or pulse-shaper nonlinearities. These control measurements were conducted as a full 2D measurement over several averages without a quantum dot sample but direct focusing of the excitation pulse trains on the APD. The same APD signal level as in case of fluorescence detection of the quantum dots was adjusted by using neutral density filters. For details, see Sec. 3.5.4 in the SI.

After the 2D experiments, we isolated the complex-valued contributions $\tilde{p}^{1\mathrm{Q}\text{–}N\mathrm{Q}}$ with $N = 2, 3$ from the same raw data set by using

$$\tilde{p}^{1\mathrm{Q}\text{–}N\mathrm{Q}}(\tau, t, \beta, \gamma) = \frac{1}{36} \sum_{l=0}^{5} \sum_{m=0}^{5} p(\tau, t, l\Delta\varphi_{21}, m\Delta\varphi_{31})\, \mathrm{e}^{-\mathrm{i}l\beta\Delta\varphi_{21}} \mathrm{e}^{-\mathrm{i}m\gamma\Delta\varphi_{31}} \tag{3.1}$$

where we set $\beta = +1, \gamma = -2$ for the extraction of the 1Q–2Q contribution [29], and $\beta = +2, \gamma = -3$ for the 1Q–3Q contribution [3].

Response-Function Calculations

For modeling the line shape tilt in the 1Q–3Q 2D spectra, we calculated the sixth-order 1Q–3Q response function in the impulsive limit based on the Feynman diagram shown in Fig. 3.4c, which can be expressed as a 2D Lorentzian function in frequency domain:

$$\tilde{Q}^{1Q-3Q}(\hbar\omega_\tau, \hbar\omega_t) = \frac{\mu^2_{TX,BX}\mu^2_{BX,X}\mu^2_{X,g}}{\hbar(\omega_\tau - \omega'_{X,g}) + i\Gamma_X} \times \frac{1}{\hbar(\omega_t - \omega'_{TX,g}) + i\Gamma_{TX}} \tag{3.2}$$

where $\omega'_{X,g}$ and $\omega'_{TX,g}$ are the modified frequencies of the exciton and triexciton state, respectively. We set all transition dipole moments $\mu_{n,m}$ between the exciton states to one (arbitrary units) for simplicity and estimated the line widths to be $\Gamma_X = 50$ meV and $\Gamma_{TX} = 80$ meV. The modified transition frequencies are defined as $\omega'_{X,g} = \omega_{X,g} + \delta_{X,g}/\hbar$ and $\omega'_{TX,g} = \omega_{TX,g} + \delta_{TX,g}/\hbar$, thus arising from energy offsets $\delta_{n,m}$, which we modeled in the following way. Over the course of 2000 iterations, we sampled random offsets δ_1, δ_2, and δ_3 from a Gaussian distribution and employed two correlation parameters a and b that describe the degree of correlation between the transition energies. In terms of correlated transition energy fluctuations, we obtain the following set of equations:

$$\delta_{X,g} = \delta_1 \tag{3.3}$$

$$\delta_{BX,X} = 2\left[a\delta_1 + (1 - |a|)\,\delta_2\right] \tag{3.4}$$

$$\delta_{BX,g} = \delta_1 + \delta_{BX,X} \tag{3.5}$$

$$\delta_{TX,BX} = \frac{3}{2}\left[b\delta_{BX,X} + (1 - |b|)\,\delta_3\right] \tag{3.6}$$

$$\delta_{TX,g} = \delta_1 + \delta_{BX,X} + \delta_{TX,BX} \tag{3.7}$$

where we set a fluctuation bandwidth of 50 meV (fwhm) for $\delta_{X,g}$ and further assumed that the fluctuation bandwidth of the exciton–biexciton transition and biexciton–triexciton transition were two- and three-times larger than $\delta_{X,g}$, respectively. In Eqs. (3.3)–(3.7), a controls the degree of correlation between the transition energy fluctuations $\delta_{X,g}$ and $\delta_{BX,X}$, whereas b controls the respective degree between $\delta_{BX,X}$ and $\delta_{TX,X}$. The parameters a and b were both chosen to be 0 (uncorrelated) or different combinations of 1 (fully correlated) and -1 (fully anticorrelated) to produce the 2D spectra corresponding to the scenarios that are shown in Fig. 3.4. The displayed calculated 2D spectra correspond to the average over the response functions from all 2000 iterations.

3.5 Supporting Information

3.5.1 1Q–1Q 2D Fluorescence Spectroscopy

In this section we describe a fourth-order 1Q–1Q 2D experiment that is employed to measure phonon coherences in $CdSe_{1-x}S_x/ZnS$ quantum dots. We use a four-pulse sequence scanning interpulse delays τ, T, and t and 27-fold phase cycling to extract the rephasing and nonrephasing 1Q–0Q–1Q nonlinear signal [29]. The pulse sequence is schematically shown in Fig. 3.5a. The first pulse creates a ground–exciton 1Q coherence that oscillates over τ (gray line), which is then converted into a population or a 0Q coherence (red line) by the second pulse. The 0Q coherence evolves over the delay T before it is again transformed into a 1Q coherence by the third pulse (gray line). The fourth pulse converts this coherence into a population that leads to fluorescence over which we integrate in time.

In the experiment, we employed compressed pulses with 15 fs duration (intensity fwhm, determined by collinear frequency-resolved optical gating). At maximum pulse overlap, the excitation energy is 170 nJ. The delays τ and t are scanned from 0 to 84 fs in 15 steps while operating in a fully rotating frame of 468 THz. The delay T is scanned from 0 to 400 fs in 21 steps. Potential artifacts in the rephasing signal, which might originate from pulse shaper nonlinearities, are corrected by applying scaling factors to the radio-frequency signal amplitude of the acousto-optical programmable dispersive filter for each pulse sequence. These scaling values are determined by previous separate measurements of the output powers of all pulse sequence configurations directly on the avalanche photodiode. In particular, the scaling value for each pulse shape configuration is determined by the ratio of the respective powers measured in the nonlinear to those in the linear pulse-shaper operation regime [185]. After the experiment, the complex-valued 1Q–0Q–1Q signals $\tilde{p}(\tau, T, t, \beta, \gamma, \delta)$ are isolated from the raw data $p(\tau, T, t, l\Delta\varphi_{21}, m\Delta\varphi_{31}, n\Delta\varphi_{41})$ via

$$\tilde{p}(\tau, T, t, \beta, \gamma, \delta) = \frac{1}{27} \sum_{l=0}^{2} \sum_{m=0}^{2} \sum_{n=0}^{2} p(\tau, T, t, l\Delta\varphi_{21}, m\Delta\varphi_{31}, n\Delta\varphi_{41}) \times \mathrm{e}^{-\mathrm{i}l\beta\Delta\varphi_{21}} \mathrm{e}^{-\mathrm{i}m\gamma\Delta\varphi_{31}} \mathrm{e}^{-\mathrm{i}n\delta\Delta\varphi_{41}}, \tag{3.8}$$

where we employed contribution-specific weights $\beta = +1$, $\gamma = +1$, $\delta = -1$ for the rephasing and $\beta = -1$, $\gamma = +1$, $\delta = -1$ for the nonrephasing contribution. The absorptive 1Q–0Q–1Q signal is then obtained by adding the nonrephasing to the rephasing signal [29]. By performing a 2D Fourier transformation of the absorptive signal with respect to τ and t, we encode the 0Q coherences along T onto a 1Q–1Q 2D frequency

grid which maps spectral correlations among the single excitons.

The first three exciton bands are well covered by the employed laser spectrum, having largest overlap with the $|X_3\rangle$ band and partial overlap with the broad $|X_4\rangle$ band (Fig. 3.5b, top). The absorptive 1Q–1Q 2D spectrum at $T = 20$ fs is shown in Fig. 3.5b, bottom. As a reference, we plot the linear absorption spectrum with an overlay of the laser spectrum on the top of the 2D spectrum and further indicate the excitonic resonance energies by dashed lines as a guide for the eye. The individual colored excitonic transitions are depicted as the Gaussian components that have been obtained from fitting the linear absorption spectrum, as discussed in the main manuscript (Fig. 3.1b). The absorptive 1Q–1Q 2D spectrum features a rectangular shape, being a result of the superposition of several overlapping diagonal and cross peaks. Cross peaks emerge because the exciton eigenstates are coupled to their common ground state.

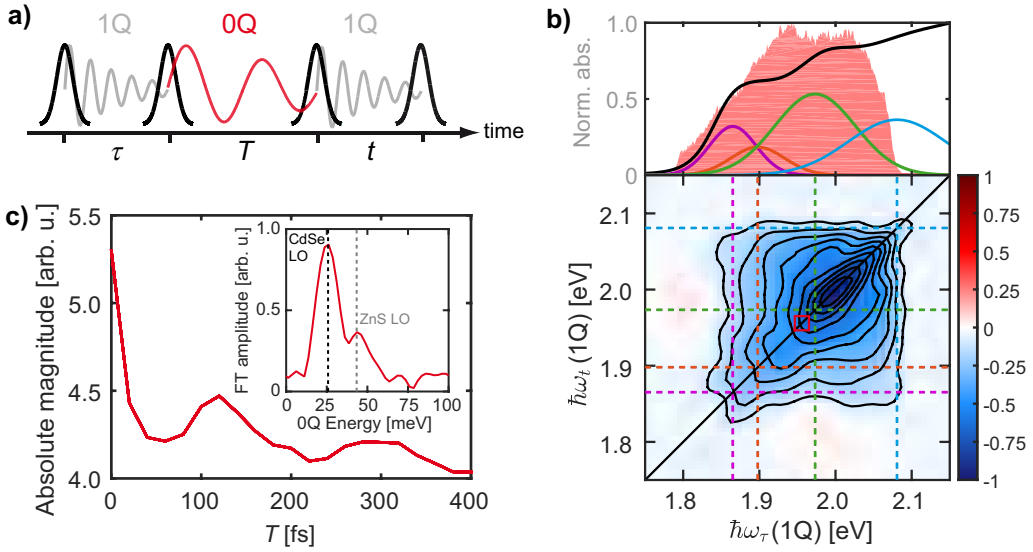

Figure 3.5. Phonon coherences in 1Q–1Q 2D spectroscopy of $CdSe_{1-x}S_x$/ZnS quantum dots in toluene. (a) Scheme of a four-pulse sequence corresponding to the 1Q–0Q–1Q-type signal contributions, with electronic coherences in gray and phonon 0Q coherence highlighted in red. (b) Top: linear absorption spectrum of $CdSe_{1-x}S_x$/ZnS quantum dots in toluene (black line). The individual excitonic transitions, which were obtained from the fit of the linear absorption spectrum as described in the manuscript, are indicated by colored lines. The employed laser spectrum is shown as a red dashed area. Bottom: experimental 1Q–1Q 2D spectrum at $T = 20$ fs (normalized to its highest absolute value), obtained after 2D Fourier transformation of the absorptive 1Q–0Q–1Q signal with respect to the delays τ and t. The resonance energies of the individual excitonic transitions are indicated as dashed lines. The solid diagonal line is drawn along $\hbar\omega_\tau = \hbar\omega_t$. The red square marks the region of interest (ROI) chosen to monitor oscillations over T. (c) Absolute magnitude of the oscillatory trace resulting from integration of the ROI for each population time step. The Fourier transformation of this trace after removal of incoherent population dynamics is shown in the inset. Reprinted with permission from Ref. [1]. Copyright © (2021) American Chemical Society.

In Fig. 3.5c, we show an oscillatory trace taken at a diagonal peak position (red square in Fig. 3.5b) that can be attributed to coupling to coherent phonons. We remove the incoherent population decay by subtracting a bi-exponential fit and Fourier transforming the result (using a Tukey window to suppress truncation artifacts) to obtain the beating spectrum shown in the inset of Fig. 3.5c. We find a strong peak at 25.8 meV, which can be attributed to the well-known longitudinal optical (LO) phonon of CdSe [139, 148, 152, 153, 155], and a weaker peak at 43.4 meV, which corresponds to the LO phonon of the ZnS shell [167]. Potential CdS LO phonon bands could not be resolved. Due to the fluorescence detection, the assignment of 0Q coherence peaks is not perturbed by solvent background (note that toluene also has Raman active modes within 0–100 meV that may complicate the analysis [186]).

3.5.2 Simulation Details

General

We calculate the dynamical evolution of the density matrix $\rho(t')$ by the master equation in the Lindblad formalism [21], as we employed on other model systems previously [3, 4]. The master equation is

$$\frac{\partial}{\partial t'}\rho(t') = -\frac{\mathrm{i}}{\hbar}[H(t'), \rho(t')] + \sum_j \frac{1}{T_j}\left(\mathcal{L}_j\rho(t')\mathcal{L}_j^\dagger - \frac{1}{2}\mathcal{L}_j^\dagger\mathcal{L}_j\rho(t') - \frac{1}{2}\rho(t')\mathcal{L}_j^\dagger\mathcal{L}_j\right), \quad (3.9)$$

where the Lindbladians $\mathcal{L}_j$ describe the relaxation processes, that is, population relaxation $\mathcal{L}_j^{\mathrm{rel}}$ and pure dephasing $\mathcal{L}_j^{\mathrm{deph}}$ which are induced by coupling to the bath. These processes are associated with respective times T_j. Population relaxation and pure dephasing can be expressed by $\mathcal{L}_j^{\mathrm{rel}} = a_n^\dagger a_m$ $(n \neq m)$ and $\mathcal{L}_j^{\mathrm{deph}} = a_n^\dagger a_n$ by using the creation and annihilation operators $a^\dagger$ and a, respectively. In Eq. (3.9), the excitonic Hamiltonian corresponding to N states is defined as

$$H(t') = \hbar\omega_n \sum_{n=1}^{N} |n\rangle\langle n| \; + \; \gamma_{\mathrm{ext}} E(t') \sum_{n\neq m} \mu_{nm}\left(|n\rangle\langle m| + |m\rangle\langle n|\right), \quad (3.10)$$

where the first, time-independent, term contains the eigenstates $|n\rangle$ with state energies $\hbar\omega_n$ and the second, time-dependent, term describes the interaction of the system with the (normalized) external electric field $E(t')$, where μ_{nm} are the transition dipole moments and γ_{ext} is the external field amplitude. The electric fields are expressed as three-pulse sequences, in the case of the experiments discussed in the main manuscript, with time delay τ between the first two pulses and delay t between the second and the last

pulse, where each pulse has the pulse duration τ_p and individual phase φ_i ($i = 1, 2, 3$),

$$\begin{aligned} E(t') = {} & E_0(t' - t_0)\exp\left(\mathrm{i}\omega_0(t' - \gamma_0 t_0) - \mathrm{i}\varphi_1\right) \\ & + E_0(t' - t_0 + \tau)\exp\left(\mathrm{i}\omega_0(t' - \gamma_0(t_0 + \tau)) - \mathrm{i}\varphi_2\right) \\ & + E_0(t' - t_0 + \tau + t)\exp\left(\mathrm{i}\omega_0(t' - \gamma_0(t_0 + \tau + t)) - \mathrm{i}\varphi_3\right), \end{aligned} \tag{3.11}$$

with E_0 being an envelope function. In Eq. (3.11), the value of γ_0 is chosen to be zero (fully rotating frame) in all simulations, whereas ω_0 is set to the laser reference frequency of the respective experiment that shall be simulated. The temporal offset of the first pulse of the sequence, t_0, is set to 100 fs in all simulations. The pulse duration τ_p is set to the respective experimental value. In order to save computation time, we employ a 16-fold (1×4×4) phase-cycling scheme, i.e., the phases φ_2 and φ_3 are cycled four times each, which was previously shown to be sufficient to isolate the 1Q–2Q nonlinear signal contribution [29]. (Note, however, that in the experiment we employed 36-fold phase cycling to additionally resolve the 1Q–3Q signal.) The sampling steps for the coherence times τ and t (0–120 fs with a step size of 4 fs in a fully rotating frame of the laser reference frequency) are set identically to the experiment. The time-dependent interaction of the external electric fields with the system is calculated within the rotating-wave approximation. The detection of fluorescence is simulated by time-integrating over the population density matrix elements according to $\mathrm{Tr}\{\Pi\rho(t')\}$, where Π is a projection operator onto the excited population density matrix elements.

Simulation of the 1Q–2Q 2D Spectrum of the Ground-State Biexciton

We now describe in detail how we determined the transition dipole moment from the band-edge exciton state $|\mathrm{X}_1\rangle$ to the ground-state biexciton $|\mathrm{X}_1\mathrm{X}_1\rangle$, $\mu(\mathrm{X}_1 \rightarrow \mathrm{X}_1\mathrm{X}_1)$, as well as the binding energy of the ground-state biexciton $\Delta(\mathrm{X}_1\mathrm{X}_1)$. For that purpose, we simulated the experimental 1Q–2Q 2D spectrum of the ground-state biexciton (Fig. 3.2d in the paper). As a minimal basis for the simulation, we incorporated a three-level Hamiltonian with ground, exciton and biexciton states into Eq. 3.10. A corresponding energy level scheme is shown in Fig. 3.6a.

The energy of $|\mathrm{X}_1\rangle$ was set to the value determined by the fit of the linear absorption spectrum [$E(\mathrm{X}_1) = 1.865$ eV] (Fig. 3.1b in the paper). In order to fit the experimental line shape, we set the pure dephasing time of the 1Q coherences to be 100 fs and the 2Q coherence to be 70 fs. The population relaxation times of $|\mathrm{X}_1\rangle$ and $|\mathrm{X}_1\mathrm{X}_1\rangle$ were set to 10 ns and 140 ps, respectively, according to the lifetimes of these states from the literature [187]. In the experiment, we employed super-Gaussian amplitude modulation by the pulse shaper in order to selectively excite the $|\mathrm{X}_1\rangle$ band (Fig. 3.6b, red curve).

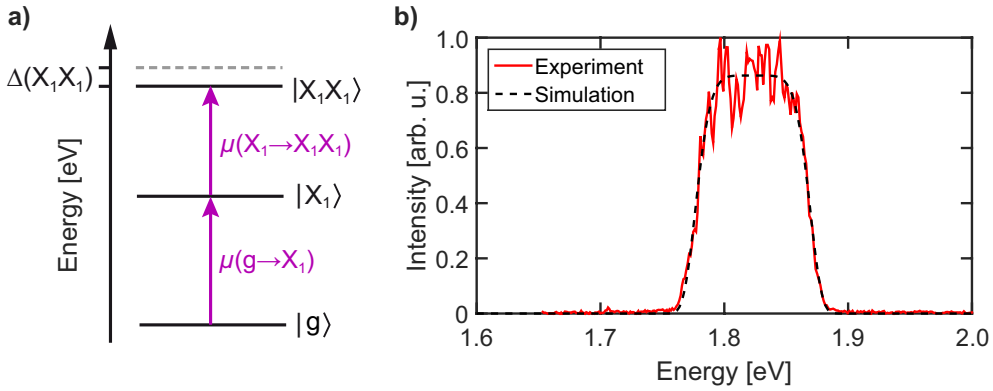

Figure 3.6. Energy-level scheme and excitation spectrum used for simulating the 1Q–2Q 2D spectrum of the ground-state biexciton. (a) Energy scheme for a three-level system consisting of a ground state ($|g\rangle$), single-exciton state ($|X_1\rangle$) and ground-state biexciton state ($|X_1X_1\rangle$) with individual transition dipole moments μ (purple). The biexciton binding energy, $\Delta(X_1X_1)$, is denoted as the energy shift of the biexciton state with respect to twice the single-exciton energy, whereas the latter is denoted as a gray dashed line. (b) Experimental laser spectrum (red, normalized), fitted with a super-Gaussian function (black dashed) which is used in the simulation. Reprinted with permission from Ref. [1]. Copyright © (2021) American Chemical Society.

Hence, in the simulation, the temporal excitation electric field envelopes of Eq. (3.11) were constructed to correspond to the Fourier transform of the spectral electric field that was calculated from a super-Gaussian fit of the excitation spectrum (Fig. 3.6b, black dashed curve). The external field amplitude was set to $\gamma_{\text{ext}} = 0.3 \times 10^{-3}$.

The position of a peak in a 1Q–2Q 2D spectrum gives access to the energy of a biexciton state and thus information about the biexciton binding energy. In our simulations, we noticed that the deviation between experimental and simulated 1Q–2Q 2D spectrum mainly depended on the actual binding energy, while the value for the transition dipole moment $\mu(X_1 \rightarrow X_1X_1)$ also influenced both the peak position and its shape. Hence, we conducted a series of simulations in which we varied systematically the magnitude of $\mu(X_1 \rightarrow X_1X_1)$ and the value of $\Delta(X_1X_1)$. For each simulation, we calculated the root–mean–squared deviation of the 2D spectra between simulation and experiment. The values for $\mu(X_1 \rightarrow X_1X_1)$ were varied from 0.7 to 1.3 in steps of 0.04 [in units of $\mu(g \rightarrow X_1)$], whereas $\Delta(X_1X_1)$ was varied from 0 to 50 meV in steps of 2 meV, thus leading to 416 simulations for the total fitness landscape. This landscape is presented as Fig. 3.2f in the main paper.

Simulation of the 1Q–2Q 2D Spectrum of the Biexciton Manifold

In order to simulate the 1Q–2Q 2D spectrum that maps the biexciton manifold (Fig. 3.3a in the paper), we employed a ten-level Hamiltonian corresponding to the energy-level scheme shown in Fig. 3.7a. We incorporated all possible biexciton states that can be

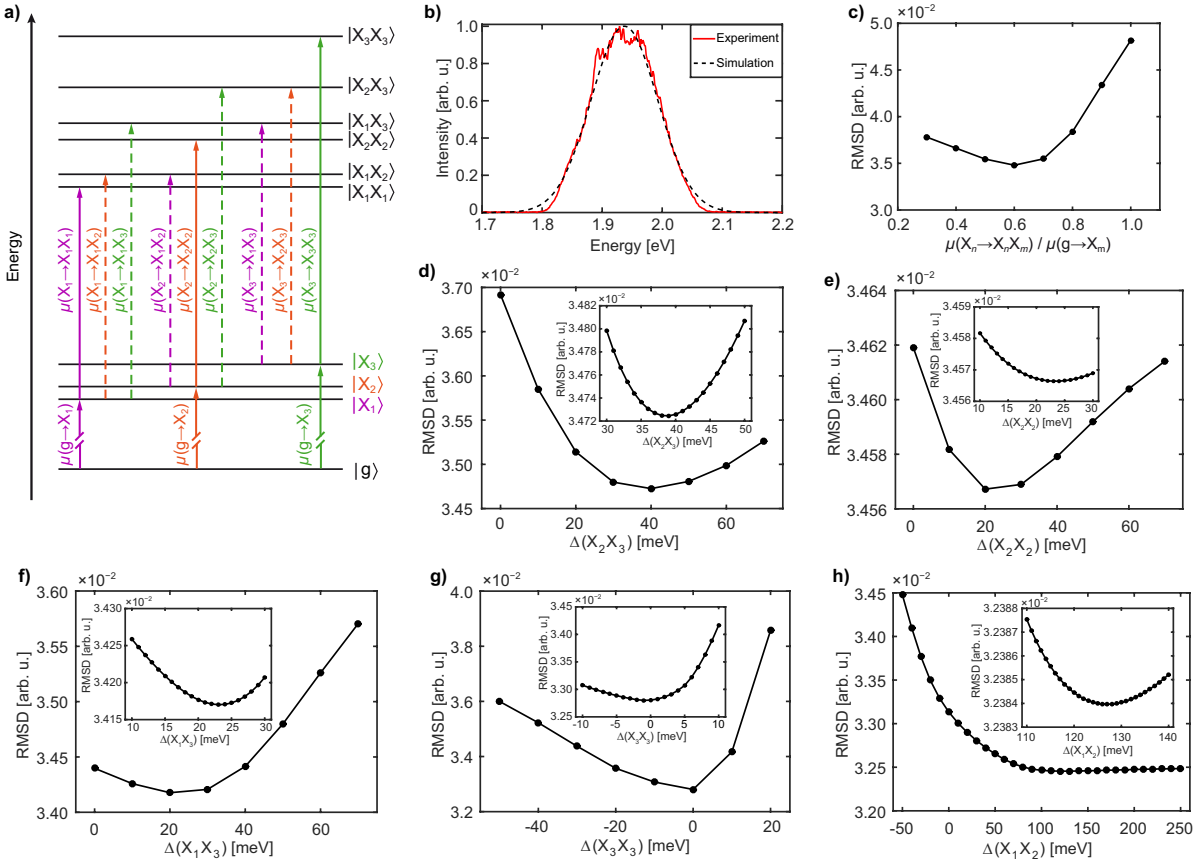

Figure 3.7. Simulation of the 1Q–2Q 2D spectrum of excited biexciton states. (a) Energy scheme for a ten-level system consisting of one ground state ($|\mathrm{g}\rangle$), three single-exciton states ($|\mathrm{X}_n\rangle$) and six biexciton states ($|\mathrm{X}_n\mathrm{X}_m\rangle$) with individual transition dipole moments μ. Excitonic transitions between the states have the same color code as in Fig. 3.1b of the paper. Solid arrows signify that the transition dipole moments $\mu(\mathrm{X}_n \rightarrow \mathrm{X}_n\mathrm{X}_n)$ are equal to the dipole moments $\mu(\mathrm{g} \rightarrow \mathrm{X}_n)$; dashed arrows into several biexciton states indicate scaled transition dipole moments into mixed biexciton states [$\mu(\mathrm{X}_n \rightarrow \mathrm{X}_n\mathrm{X}_m)$, where $n \neq m$]. (b) Experimental laser spectrum (red, normalized), fitted with a Gaussian function (black dashed) which is used in the simulation. (c) Root–mean–squared deviation (RMSD) between experimental and simulated normalized absolute magnitude spectra for various scaling values of the transition dipole moments into mixed biexciton states. (d)–(h) RMSD values with respect to the variation of the binding energies of the biexciton states (d) $\Delta(\mathrm{X}_2\mathrm{X}_3)$, (e) $\Delta(\mathrm{X}_2\mathrm{X}_2)$, (f) $\Delta(\mathrm{X}_1\mathrm{X}_3)$, (g) $\Delta(\mathrm{X}_3\mathrm{X}_3)$, and (h) $\Delta(\mathrm{X}_1\mathrm{X}_2)$ in coarse steps of 10 meV. The insets show the respective RMSD values for a variation in steps of 1 meV around the minimum of each coarse scan. Reprinted with permission from Ref. [1]. Copyright © (2021) American Chemical Society.

constructed from the exciton states $|X_1\rangle$, $|X_2\rangle$, and $|X_3\rangle$, giving rise to a total of six different biexciton states. For the simulation, the single-exciton parameters were taken from the fit of the linear absorption spectrum (Fig. 3.1b in the paper). In particular, we took the square root of the individual Gaussian amplitudes obtained from the multi-Gaussian fit as the values for transition dipole moments into the single-exciton states (Table 3.1). The single-exciton transition energies were taken as the energies at the maxima of the respective Gaussian components of the linear absorption fit. The laser excitation fields employed in the simulation corresponded to the Fourier transform of the spectral electric field that was calculated from a Gaussian fit of the experimental laser spectrum (Fig. 3.7b).

Since we experimentally operate in a regime with high excitation energy where exciton and biexciton populations are near equilibrium [138], we adjusted the external field amplitude to $\gamma_{\text{ext}} = 10^{-3}$. At such a high excitation energy regime like in our experiment, one has to consider contaminations by signals which are of higher nonlinear orders and cannot be separated from the desired signal via phase cycling [188]. Note, however, that our nonperturbative treatment inherently captures effects caused by such contaminations with higher nonlinear orders.

Charge cooling was modeled as a population relaxation process with an estimated time constant of 300 fs. We assumed the same times of charge cooling for each downward transition within the single-exciton and biexciton manifolds. The lifetimes of $|X_1\rangle$ and $|X_1X_1\rangle$ were set to 10 ns and 140 ps, respectively. The pure dephasing times of the $|X_1\rangle\langle g|$, $|X_2\rangle\langle g|$, and $|X_3\rangle\langle g|$ coherences were set to 100, 90, and 80 fs, respectively, and all pure dephasing times related to the biexciton manifold were set to 70 fs, to fit the observed line shapes. Note that the values set for the pure dephasing times do not inevitably represent the actual pure dephasing times. The necessity to use the values above might be a result of line-shape effects due to correlated transition energy fluctuations, as discussed for the 1Q–3Q 2D spectra in the main paper. We did not explicitly incorporate these fluctuation effects here because we rather focused on a reproduction of the shape of the 1Q–2Q 2D spectrum in terms of energy shifts of the various states of the biexciton manifold and transition dipole moments from the exciton to the biexciton manifold. Incorporating correlated transition energy fluctuations would have made the simulation intractable. Thus, the pure dephasing times we employed in the simulations have to be viewed as phenomenological. The same holds for the simulation of the 1Q–2Q 2D spectrum of the ground-state biexciton.

Our model neglects potential effects related to multi-exciton generation (MEG). The presence of MEG would presuppose interaction between high-lying states of single-

exciton manifold with energetically close biexciton states. However, MEG has an energy threshold of 2.5 times the bandgap energy in CdSe [121], which would be outside the energy range of the biexciton states we probe in our experiment. More importantly, the MEG efficiency in CdSe (and CdSe/ZnS) quantum dots was found to be extremely low [189], giving rise to MEG rates in the order of several ps. Hence, due to its low efficiency, MEG does not have a disturbing influence on our 1Q–2Q 2D spectra. Note further that the timescale of our experiment is much shorter than the timescale of MEG. In our experiment, we excite the quantum dots with a three-pulse sequence with maximum interpulse delays of 120 fs. Thus, the perturbation by the excitation pulses is carried out within a window of 240 fs, meaning that probing coherent dynamics is already accomplished before MEG contributes significantly. Nonetheless, if there were interaction and thus mixing between high-lying single-exciton states and biexciton states, one would expect additional broadening and distortion along the 2Q energy axis, which would perturb the assignment of individual biexciton states and in turn exacerbate the determination of state-specific binding energies.

In order to find optimal parameters for the simulated 1Q–2Q 2D spectrum, we follow the general strategy of optimizing one parameter after another. Whenever we find an optimal value for a specific parameter, we incorporate it into the model before varying the next one. We started with a model in which all exciton-to-exciton transition dipole moments are equal to the respective ground-to-exciton dipole moments, which is based on our finding from the simulation of the 1Q–2Q 2D spectrum of the ground-state biexciton. Further, we employed biexciton binding energies of $\Delta(X_1X_1) = 16$ meV, $\Delta(X_1X_2) = 30$ meV, $\Delta(X_2X_2) = 16$ meV, $\Delta(X_1X_3) = 50$ meV, $\Delta(X_2X_3) = 30$ meV, and $\Delta(X_3X_3) = 10$ meV as an initial guess. Based on these parameters, we first simulated the 1Q–2Q 2D spectrum with different scaling values for the transition dipole moments into mixed biexciton states, $\mu(X_n \rightarrow X_nX_m)$ (where $n \neq m$) and calculated the root–mean–squared deviation (RMSD) between experiment and simulation for each scaling value (Fig. 3.7c). The resulting curve demonstrates that the similarity between simulated and experimental spectra increases significantly if one scales the transition dipole moments into mixed biexciton states by 0.6.

Next, we varied each binding energy separately, while leaving the others constant. Whenever an optimal parameter was found, it was incorporated into the model before varying the next parameter. As the binding energy of $|X_1X_1\rangle$ was determined through the simulation of a separate experiment (see above), we set $\Delta(X_1X_1) = 16$ meV constant throughout. For the determination of the other biexciton binding energies, we first performed a coarse scan of each binding energy in 10 meV steps followed by a scan

with 1 meV steps around the RMSD minimum (Fig. 3.7d–h). The resulting simulation parameters for the 2D spectrum of Fig. 3.3b in the paper are summarized in Table 3.1.

Table 3.1. Simulation parameters for the energies of the single-exciton and biexciton states as well as transition dipole moments and binding energies used to produce the simulated 1Q–2Q 2D spectrum shown in Fig. 3.3b of the paper. Reproduced from Ref. [1].

Quantity		**Value**
Energies of the single-exciton states (eV)	$E(\mathrm{X}_1)$	1.865
	$E(\mathrm{X}_2)$	1.898
	$E(\mathrm{X}_3)$	1.973
Energies of the biexciton states (eV)	$E(\mathrm{X}_1\mathrm{X}_1)$	3.714
	$E(\mathrm{X}_1\mathrm{X}_2)$	3.636
	$E(\mathrm{X}_2\mathrm{X}_2)$	3.773
	$E(\mathrm{X}_1\mathrm{X}_3)$	3.815
	$E(\mathrm{X}_2\mathrm{X}_3)$	3.832
	$E(\mathrm{X}_3\mathrm{X}_3)$	3.947
Ground-state-to-exction transition dipole moments (arb. u.)	$\mu(\mathrm{g}\rightarrow\mathrm{X}_1)$	0.491
	$\mu(\mathrm{g}\rightarrow\mathrm{X}_2)$	0.372
	$\mu(\mathrm{g}\rightarrow\mathrm{X}_3)$	0.633
Exction-to-biexciton transition dipole moments (arb. u.)	$\mu(\mathrm{X}_1\rightarrow\mathrm{X}_1\mathrm{X}_1)$	0.491
	$\mu(\mathrm{X}_1\rightarrow\mathrm{X}_1\mathrm{X}_2)$	0.223
	$\mu(\mathrm{X}_1\rightarrow\mathrm{X}_1\mathrm{X}_3)$	0.380
	$\mu(\mathrm{X}_2\rightarrow\mathrm{X}_1\mathrm{X}_2)$	0.294
	$\mu(\mathrm{X}_2\rightarrow\mathrm{X}_2\mathrm{X}_2)$	0.372
	$\mu(\mathrm{X}_2\rightarrow\mathrm{X}_2\mathrm{X}_3)$	0.380
	$\mu(\mathrm{X}_3\rightarrow\mathrm{X}_1\mathrm{X}_3)$	0.294
	$\mu(\mathrm{X}_3\rightarrow\mathrm{X}_2\mathrm{X}_3)$	0.223
	$\mu(\mathrm{X}_3\rightarrow\mathrm{X}_3\mathrm{X}_3)$	0.633
Biexciton binding energies (meV)	$\Delta(\mathrm{X}_1\mathrm{X}_1)$	16
	$\Delta(\mathrm{X}_1\mathrm{X}_2)$	127
	$\Delta(\mathrm{X}_2\mathrm{X}_2)$	23
	$\Delta(\mathrm{X}_1\mathrm{X}_3)$	23
	$\Delta(\mathrm{X}_2\mathrm{X}_3)$	39
	$\Delta(\mathrm{X}_3\mathrm{X}_3)$	-1

3.5.3 Double-Sided Feynman Diagrams of the 1Q–2Q and 1Q–3Q Signals

We provide all possible double-sided Feynman diagrams [19] corresponding to Liouville pathways contributing to the nonrephasing 1Q–2Q and 1Q–3Q signals in Fig. 3.8. For simplicity, we formulate the diagrams for a system in the manifold picture, where $|\mathrm{g}\rangle$ denotes the ground state, $|\mathrm{X}\rangle$ the single-exciton manifold, $|\mathrm{BX}\rangle$ the biexciton manifold, and $|\mathrm{TX}\rangle$ the triexciton manifold. These diagrams display particular elements of the density matrix which evolve over certain time intervals. Time is running from bottom to top, where the delay between the first two pulses is denoted by τ, the delay between the second and the third pulse by t, and the fluorescence detection time by t'. The interaction of a specific coherent light field m ($m = 1, 2, 3$) is denoted by solid arrows,

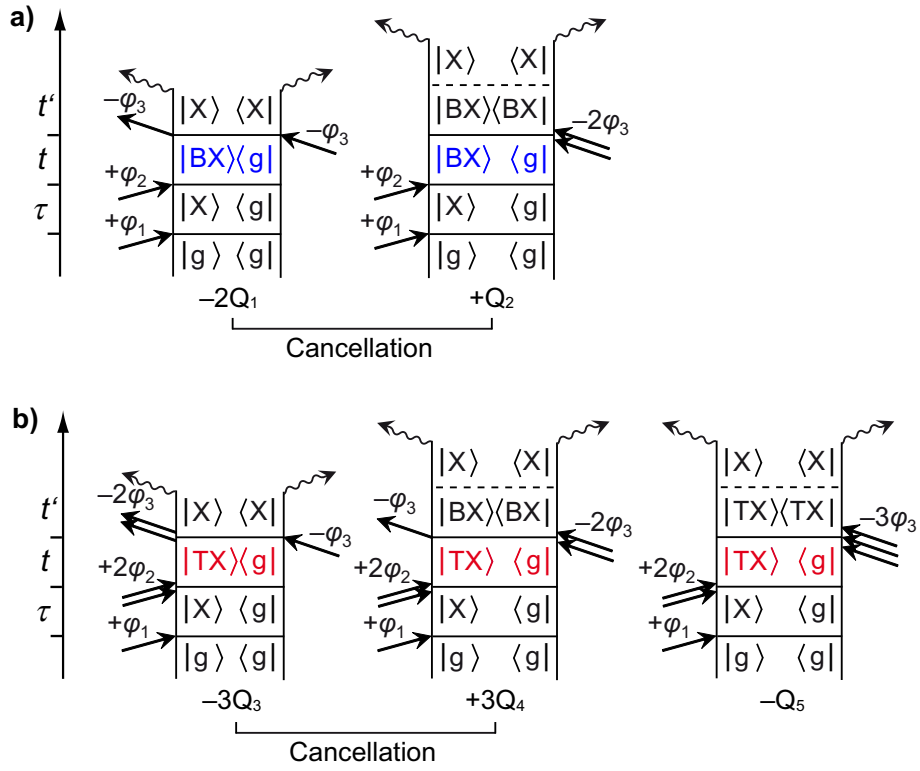

Figure 3.8. Complete set of double-sided Feynman diagrams for (a) the fourth-order 1Q–2Q contribution and (b) the sixth-order 1Q–3Q contribution on the basis of a ground state $|\mathrm{g}\rangle$, the single-exciton manifold $|\mathrm{X}\rangle$, the biexciton manifold $|\mathrm{BX}\rangle$ and the triexciton manifold $|\mathrm{TX}\rangle$. Time delays between the pulses are denoted as τ and t, whereas t' is the detection time. Each diagram is labeled according to its sign (note that the i^n prefactor, where n is the order of nonlinearity, is excluded) and its weight due to time ordering. Incident coherent light fields are represented by solid arrows whereas incoherent emission is denoted by wavy arrows. Dashed lines between population density matrix elements signify nonradiative relaxation. Reprinted with permission from Ref. [1]. Copyright © (2021) American Chemical Society.

where an arrow pointing to the right (left) corresponds to a phase of $+\varphi_m$ $(-\varphi_m)$. Incoherent fluorescence emission is denoted as wavy arrows. Each diagram is labeled with its sign determined by the number of coherent interactions occurring on the right side of the diagram. Note that we omit the prefactor of i^n, where n is the total number of interactions for a given signal contribution.

In addition, each diagram is labeled with an integer denoting its weight due to time ordering. Because the multiexciton populations decay via Auger relaxation into the $|\mathrm{X}\rangle$ manifold, each diagram is further considered to yield the same fluorescence yield.

The manifold representation gives rise to two diagrams for the 1Q–2Q signal (Fig. 3.8a) and three diagrams for the 1Q–3Q signal (Fig. 3.8b). Due to the different signs of the diagrams, cancellation effects occur. For example, diagram $+Q_2$ is cancelled by $-2Q_1$, leaving $-Q_1$ as the sole contribution to the 1Q–2Q signal. In case of the 1Q–3Q signal, diagrams $-Q_3$ and $+Q_4$ completely cancel, leading to diagram $-Q_5$ as the remaining one.

3.5.4 Control 2D Measurement

In order to exclude signal contaminations by contributions arising from potential nonlinearities of the experimental setup, such as detector and/or pulse-shaper nonlinearities, we performed control measurements of the complete pulse sequence of the 2D measurements (that is, without any sample). For that purpose, we directly focus the excitation beam on the avalanche photodiode at a signal level that is analogous to the case of fluorescence detection using identical sampling parameters as in the actual 2D experiment performed on the quantum dot sample. After the measurement of the pulse sequences, we then process the data analogous to the experiment, that is weighting the raw data by phase factors that are unique for each nonlinear signal contribution of interest. If there were any detector nonlinearity contributing, distinct signals would appear after this weighting procedure. Assuming perfect detector linearity at the employed maximal detector signal level, only noise is expected. Since no detector has perfect linearity, it is important to ensure that the signal strength arising from potential detector nonlinearity is at least on the order of magnitude of the noise level. Otherwise, the 2D measurements on the sample could indeed be perturbed by such unwanted nonlinear signals.

As we carried out two separate multiple-quantum 2D measurements with different laser spectra (compare Fig. 3.2d and Fig. 3.3a in the manuscript), we performed two separate control measurements. The 1Q–2Q 2D spectrum of the control measurement for Figure 3.2d is thus shown in Fig. 3.9a, whereas the 1Q–2Q and 1Q–3Q 2D spectra of the control measurement for Figs. 3.3a and 3.4d are presented in Figs. 3.9b and 3.9c,

respectively.

The resulting 2D spectra all show noise and no significant signals above the noise floor. In relation to the respective 2D measurements performed on the quantum dot sample, the absolute maximal signal levels of the control 2D spectra are lower by factors of 13.8 (Fig. 3.9a), 24.9 (Fig. 3.9b), and 15.7 (Fig. 3.9c). We thus conclude that detector nonlinearities significantly do not contaminate the nonlinear signals of the quantum dot sample.

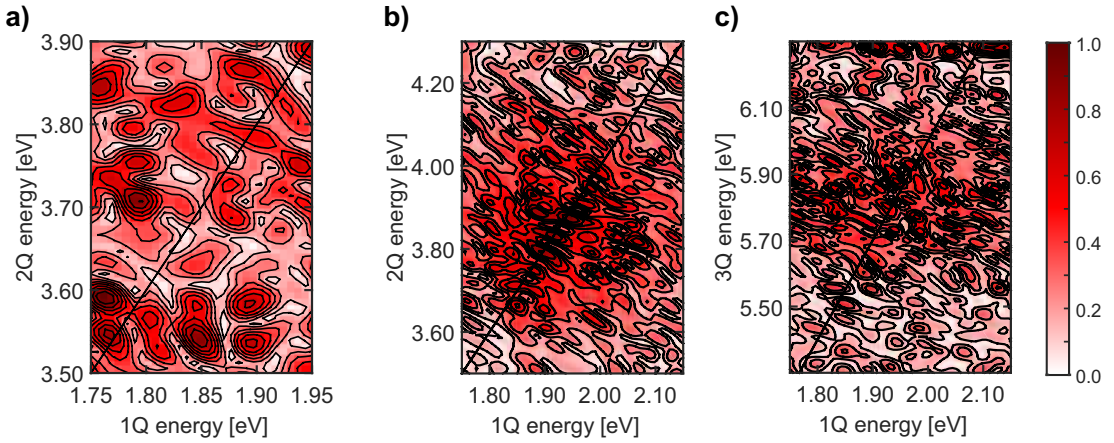

Figure 3.9. Absolute-valued control 2D spectra obtained by direct focusing of the excitation pulse sequences on the employed avalanche photodiode (APD), normalized to their respective highest absolute values. The signal level on the APD was adjusted to the signal level of an actual 2D experiment with fluorescence detection. a) Control 1Q–2Q 2D spectrum for the measurement of Fig. 3.2d in the manuscript. b) 1Q–2Q and c) 1Q–3Q 2D control spectra for the measurements reported in the manuscript in Figs. 3.3a and 3.4d, respectively. Reprinted with permission from Ref. [1]. Copyright © (2021) American Chemical Society.

Chapter 4

Rapid Multiple-Quantum Three-Dimensional Fluorescence Spectroscopy Disentangles Quantum Pathways

Coherent two-dimensional spectroscopy is a powerful tool for probing ultrafast quantum dynamics in complex systems. Several variants offer different types of information but typically require distinct beam geometries. Here we introduce population-based three-dimensional (3D) electronic spectroscopy and demonstrate the extraction of all fourth- and multiple sixth-order nonlinear signal contributions by employing 125-fold (1×5×5×5) phase cycling of a four-pulse sequence. Utilizing fluorescence detection and shot-to-shot pulse shaping in single-beam geometry, we obtain various 3D spectra of the dianion of TIPS-tetraazapentacene, a fluorophore with limited stability at ambient conditions. From this, we recover previously unknown characteristics of its electronic two-photon state. Rephasing and nonrephasing sixth-order contributions are measured without additional phasing that hampered previous attempts using noncollinear geometries. We systematically resolve all nonlinear signals from the same dataset that can be acquired in 8 min. The approach is generalizable to other incoherent observables such as external photoelectrons, photocurrents, or photoions.

4.1 Introduction

Inspired by multidimensional nuclear magnetic resonance (NMR) experiments that give extraordinary insight into chemical structure, optical multidimensional spectroscopic techniques reveal vibrational and electronic structure and dynamics employing sequences of ultrashort laser pulses. The enhanced dimensionality within these experiments enables the observation of cross peaks in the spectral domain. These may represent signatures of coupling phenomena, energy or charge transfer [84, 190–192], photochemical reactions [193, 194], vibrational or electronic coherences [195–201], or many-body interactions [40, 53, 81, 98]. The great versatility of multidimensional techniques results from their ability to distinguish between specific nonlinear signal contributions. These contributions correspond to different subsets of optically driven quantum pathways through the excited-state manifold of a system.

In a two-dimensional (2D) experiment, a first laser pulse creates a coherence that evolves during the coherence time τ. In one exemplary pathway, the interaction with a second pulse can lead to a population evolving during population time T, and the interaction with a third pulse to another coherence. The latter gives rise to a macroscopic polarization that emits a coherent electric field during the final time t. In the most common approach, this coherent field is heterodyne detected with a reference pulse to yield the amplitude-resolved and phase-resolved nonlinear optical signal. 2D Fourier transformation with respect to τ and t results in a 2D spectrum as a function of frequencies ω_τ and ω_t, respectively, retaining a parametric dependence on T. This approach has been used extensively to investigate one-quantum (1Q) coherences, that is, coherent superpositions between states which oscillate at a frequency covered by the employed laser spectrum, and to decipher energy transfer mechanisms [85, 202–204]. Broadband excitation in the visible may also generate superpositions of energetically close-lying states within one electronic manifold, also called zero-quantum (0Q) coherences, which are observed as oscillations as a function of T. In molecules, this often signifies nuclear wavepacket dynamics, oscillating on ground-state or excited-state electronic potential energy surfaces [195, 205]. It is challenging to identify uniquely the origin of all oscillatory signals due to their spectral overlap. Using a third dimension may resolve some of the peaks [42, 206–208]. Thus, one can distinguish vibrational coherence in ground and excited electronic states in molecules [205], unravel hidden vibrational couplings [63], or study ultrafast photochemistry [194]. Such 3D spectra may be used to isolate quantum coherence selectively, allowing for the possibility to reconstruct the Hamiltonian of a system [41, 209].

Apart from higher dimensionality, higher orders of nonlinearity unveil further details that cannot directly be ascertained from lower-order signals. For instance, nonlinear signals that are of higher than third order in the interaction with the electric field enabled studying intricate details about electronic correlations in semiconductor nanostructures [53], tracking multistep energy transfer in light-harvesting complexes [210], and observing exciton–exciton annihilation in molecular aggregates [102]. While useful, it is challenging to capture all contributions with conventional noncollinear techniques because one must ensure phase stability between various optical beams. In addition, each signal contribution has to be measured separately by choosing the corresponding phase-matching condition, and scattering of excitation pulses as well as the nonresonant response from the environment leads to artifacts [56]. In this context, it was previously shown that a partially collinear pump–probe geometry offers many advantages due to its inherent phase stability, and the capability to isolate several, directly phased signals at once [50, 211–214]. As another alternative that also preserves these advantages, one can employ phase modulation or phase cycling with fluorescence detection [48, 51, 69, 71, 75, 86, 158, 215–217]. Fluorescence detection reveals features that would be hidden with coherent detection [75, 218]. Another key feature of fluorescence-based detection is the excellent sensitivity for higher-order signal contributions [107], since scattered excitation light does not contribute. Most fluorescence-based multidimensional experiments focus on fourth-order nonlinear signals, while studies of high-order population-based spectroscopy are scarce [78, 106, 107]. Apart from that, it is desirable to design a versatile and convenient approach to gain maximum nonlinear information content from a single data set in order to investigate systems with limited (photo)chemical stability without the need to carry out separate multi-dimensional experiments for each signal contribution. Such an approach should offer direct comparability between different signal contributions that is beneficial for interpretation purposes, especially because nonlinear signals show a strong dependence on the employed excitation conditions that might not be identical throughout separate measurements.

In this work, we address the aspect of gaining multiple nonlinear signals from a single rapid measurement and demonstrate this by recording a variety of multiple-quantum, fourth- and sixth-order 3D spectra simultaneously. This allows us to extract certain sets out of a vast manifold of quantum pathways where each set provides rich and selective information about correlations between excited states, vibrational coherences, and excited-state dynamics. We show how to obtain the information systematically from only one raw data set by appropriate weighting with Liouville pathway-specific phase factors. Thus we can assign 0Q, 1Q, and two-quantum (2Q) coherence dynamics to the

three conjugate time delays employed in the experiment. For demonstration, we choose the dianion of the bis(triisopropylsilyl)ethynyl-substituted symmetric tetraazapentacene TIPS–TAP^{2-} [219, 220], dissolved in tetrahydrofuran (THF), which nicely illustrates the application potential of the technique because the highly reduced compound is extremely sensitive toward traces of oxygen and moisture, thus having limited stability at ambient conditions, and all data from two different orders of nonlinearity are obtained within only a few minutes of measurement time. The TIPS–TAP compound and related species are of considerable interest for use in organic field effect transistors (OFETs) due to their ability to serve as efficient negative charge carriers. In addition, and of specific relevance to this study, the TIPS–TAP dianion, formed by two-electron reduction of the neutral compound, has a remarkably high fluorescence quantum yield of 95% in Et_2O solution [219, 220].

4.2 Results

4.2.1 Method Development

We employ a single-beam geometry and thus cannot use phase matching to distinguish between various signal contributions. Instead, we employ phase cycling (Fig. 4.1) [29, 48, 50, 51, 71, 72, 214]. The key idea is to vary the phases of the excitation pulses with step sizes fine enough to resolve different signal contributions without aliasing. Because the laser is not carrier-envelope phase-stabilized, it is adequate to operate with

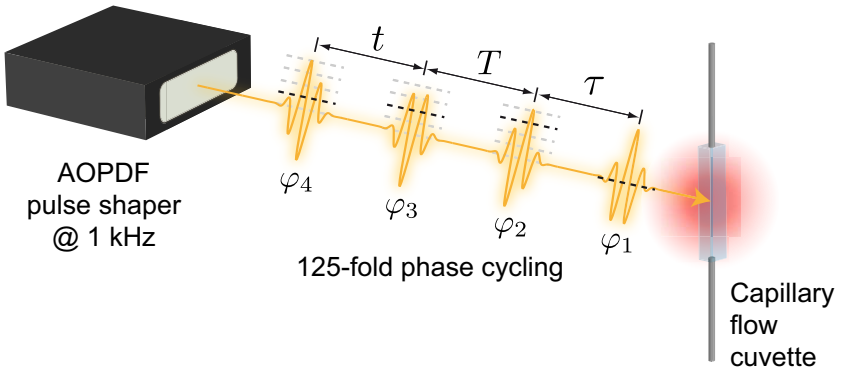

Figure 4.1. Scheme of the experiment. An acousto-optic programmable dispersive filter (AOPDF) creates a phase-coherent pulse sequence with individual pulse phases φ_i ($i = 1, 2, 3, 4$) that is employed in the multidimensional experiment. Besides scanning the interpulse delays τ, T, and t, we further sample the phases of the second, third, and fourth pulse five times each and finally detect the integrated fluorescence intensity from the sample as a function of these excitation pulse sequence parameters. Reproduced from Ref. [4].

interpulse phases $\Delta\varphi_{i1}$ ($i = 1, 2, 3$) that are cycled in discrete steps between 0 and 2π with a pulse shaper (DAZZLER, Fastlite). Thus, the raw data matrix p obtained from the experiment represents integrated fluorescence intensities as a function of sampled time delays and interpulse phases. Various phase-cycling schemes for fourth-order population-based 2D spectroscopy were discussed in the literature, aiming to preserve an experimentally manageable amount of phase steps [29]. Phase-cycling protocols employing an increased number of phase steps generate a denser grid in phase space resolving more nonlinear signal contributions within a single experiment. The associated significant increase in acquisition time can be compensated by our rapid-scan approach [72]. In our experiment, we sampled, in addition to the time delays τ, T, and t between the pulses, the interpulse delays by means of a 125-fold (1×5×5×5) phase-cycling scheme (Fig. 4.1), where the phases of the second, third, and fourth pulse were sampled in five steps each. A detailed schematic of the experimental setup is given in Supplementary Fig. 4.7 and described in Supplementary Sec. 4.5.1.

After the experiment, the raw data p is decoded by weighting it with phase factors which recover complex-valued nonlinear signal contributions $\tilde{p}$ by using

$$\begin{aligned}\tilde{p}\left(\tau, T, t, \beta, \gamma, \delta\right) = \frac{1}{125} \sum_{l=0}^{4} \sum_{m=0}^{4} \sum_{n=0}^{4} p\left(\tau, t, T, l\Delta\varphi_{21}, m\Delta\varphi_{31}, n\Delta\varphi_{41}\right) \\ \times \exp\left(-\mathrm{i}l\beta\Delta\varphi_{21}\right) \exp\left(-\mathrm{i}m\gamma\Delta\varphi_{31}\right) \exp\left(-\mathrm{i}n\delta\Delta\varphi_{41}\right),\end{aligned} \tag{4.1}$$

where $\Delta\varphi_{ij}$ denotes interpulse phases between pulses i and j, and β, γ, and δ are the weighting parameters [29]. According to phase-cycling theory and double-sided Feynman diagram analysis (see Supplementary Sec. 4.5.2) [19, 29], we identified that this scheme is able to resolve and distinguish between three fourth-order and twelve sixth-order contributions (Table 4.1), all of them simultaneously, i.e., from the same raw data set. With 125-fold phase cycling, five-step phase sampling ensures discrimination between integer values ranging from -2 to $+2$ for β, γ, and δ so that all listed fourth-order and sixth-order contributions are obtained simultaneously, but can be resolved individually. Besides the fourth-order contributions, the selection of the sixth-order contributions is dictated by choosing the weights of β, γ, and δ themselves because at the moment one of the factors is set to ± 2, the weighting will uniquely pick a contribution which originates from a pulse sequence in which two of the four pulses interact twice, resulting in six interactions in total. Performing 3D Fourier transforms of each contribution with respect to τ, T, and t generates 3D spectra as will be shown below using our experimental data.

All contributions are inherently phased correctly with respect to each other. This

Table 4.1. Summary of fourth-order and sixth-order nonlinear signal contributions. The signal contributions listed here can be resolved and isolated from a 125-fold (1×5×5×5) phase-cycling scheme using incoherent detection. The first four columns on the left give the label of the nonlinear signal contribution that probes specific types of quantum coherence over the three temporal dimensions τ, T, and t. Their respective weight factors β, γ, and δ are listed on the right. All contributions can further be classified as either fully nonrephasing (NR, no phase conjugation between coherences) or rephasing (R), whereas for the latter the superscripts denote which particular dimensions hold the phase conjugation that is introduced during a rephasing pulse sequence; a: between τ and t, b: between τ and T, c: between T and t. Reproduced from Ref. [4].

Fourth-order contributions $\tilde{p}^{(4)}$				**Weights**		
	τ	T	t	β	γ	δ
R^{a}	1Q	0Q	1Q	+1	+1	−1
NR	1Q	0Q	1Q	−1	+1	−1
NR	1Q	2Q	1Q	+1	−1	−1
Sixth-order contributions $\tilde{p}^{(6)}$						
$R^{b,c}$	1Q	1Q	1Q	+2	−2	+1
R^{a}	2Q	0Q	1Q	+2	+1	−1
NR	2Q	0Q	1Q	−2	+1	−1
R^{a}	1Q	0Q	2Q	+1	+2	−2
NR	1Q	0Q	2Q	−1	+2	−2
$R^{a,c}$	2Q	1Q	1Q	+1	+2	−1
$R^{a,b}$	1Q	1Q	2Q	+2	+1	−2
NR	2Q	1Q	2Q	−1	+1	−2
NR	1Q	3Q	1Q	+2	−2	−1
NR	2Q	3Q	1Q	+1	−2	−1
NR	1Q	3Q	2Q	+2	−1	−2
NR	2Q	3Q	2Q	+1	−1	−2

is an advantage compared with noncollinear coherence-detected multidimensional spectroscopy, for which one must usually perform an auxiliary procedure, such as an additional pump–probe experiment, in order to assign the correct phase information [39]. However, analogously to coherently detected experiments [102], if the excitation density is high enough to generate sixth-order signals, these may also contaminate the fourth-order ones. Hence, whenever we use the term fourth-order signal, we mean a nonlinear signal that is predominantly of fourth order (see Supplementary Sec. 4.5.3). Apart from

that, an advantage of our technique is that we are able to simultaneously isolate the higher-order contribution by appropriate phase cycling.

We sampled every temporal dimension in steps of 6 fs utilizing the fully rotating frame of the pulse shaper's reference frequency of 508.1 THz (2.1 eV) in order to find a compromise regarding acquisition time with respect to the limited sample stability. In total, $15\times15\times15\times125 = 421,875$ different pulse trains were streamed in order to acquire a full 3D data set. At the 1 kHz repetition rate of our setup, the pure acquisition time for the full multidimensional data set is only 8 min (without averaging). In our sampling protocol, we first sample through all phase-cycling steps for fixed interpulse delays to prevent errors in reconstructing the phase-sensitive nonlinear signal contributions by Eq. (4.1) (for further details see Supplementary Sec. 4.5.1). With the broad spectral bandwidth (70 nm) of the employed laser pulses, we resolve high-frequency vibrational coherence in the 0Q domain, 1Q coherence between ground- and singly-excited electronic states as well as between singly- and higher-excited states, and 2Q coherences between ground- and higher-excited electronic states via multiphoton processes. Li et al. previously introduced multiphoton 2D fluorescence spectroscopy, where signatures of one-photon and two-photon transitions into the same electronic state could be obtained [221]. In this work, however, we will consider one-photon and two-photon transitions into different electronic states. Probing 3Q coherences would lead to aliasing artifacts in the present example. Therefore, we will restrict the discussion below to the signal contributions that did not involve any 3Q coherence. However, using more temporal sampling steps would allow the unique recovery of 3Q contributions as well with the same setup, again within one unified measurement protocol.

Our technique is currently limited to a maximum temporal shaping window of 8 ps for every pulse sequence according to the length of the chosen AOPDF crystal. At such delays, one can measure electronic and vibrational coherence dynamics of dissolved molecular systems that proceed on time scales up to several picoseconds. In cases of much slower dephasing, such as in some semiconductor nanostructures [40, 53, 57], measurements of all relevant dynamics becomes challenging. Another example of slow dynamics proceeding at the 10 to 100 ps time scale is exciton diffusion dynamics in some molecular aggregates [102]. Nevertheless, because of the absence of spurious coherent artifacts for early population times, our technique has great application potential to study ultrafast processes such as rapid exciton–exciton annihilation in many classes of molecular aggregates,[1] and the single-beam geometry provides a compact, stable, and convenient access.

[1] See Chapter 5.

4.2.2 Fourth-Order 3D Spectra

The linear absorption [220] and fluorescence spectra of TIPS–TAP^{2-} are shown in Fig. 4.2a together with the laser spectrum. The dianion features well-resolved peaks in both absorption and fluorescence spectra together with a small Stokes shift. The main band of the $S_0 \rightarrow S_1$ π–π^* transition [219] at 2.06 eV is well covered by the laser spectrum, having further very small amplitude in the region of the main vibrational progression band, which is located at 2.23 eV. This progression is assigned to a ≈1400 cm^{-1} (≈0.17 eV) vibrational mode of the conjugated system [220]. Based on that and on experimental observations, we construct an energy-level scheme depicted in Fig. 4.2b, incorporating the single 0.17 eV mode being coupled to the electronic singlet states S_0, S_1 as well as to a highly excited two-photon singlet state S_x with different displacements along the vibrational coordinate (see also below). For the following, we use the labels $|g_v\rangle$, $|e_v\rangle$, and $|f_v\rangle$ to denote electronic ground-, first excited, and doubly excited states, respectively, where the subscript v denotes the quantum of vibrational excitation.

In Fig. 4.3a (left), we present the experimental absolute-valued rephasing 1Q–0Q–1Q 3D spectrum, which we extracted from the raw data by using the weights from Table 4.1 according to its phase signature [29] of $\varphi_{\mathrm{R1Q0Q1Q}} = -\varphi_1 + \varphi_2 + \varphi_3 - \varphi_4$. Throughout this

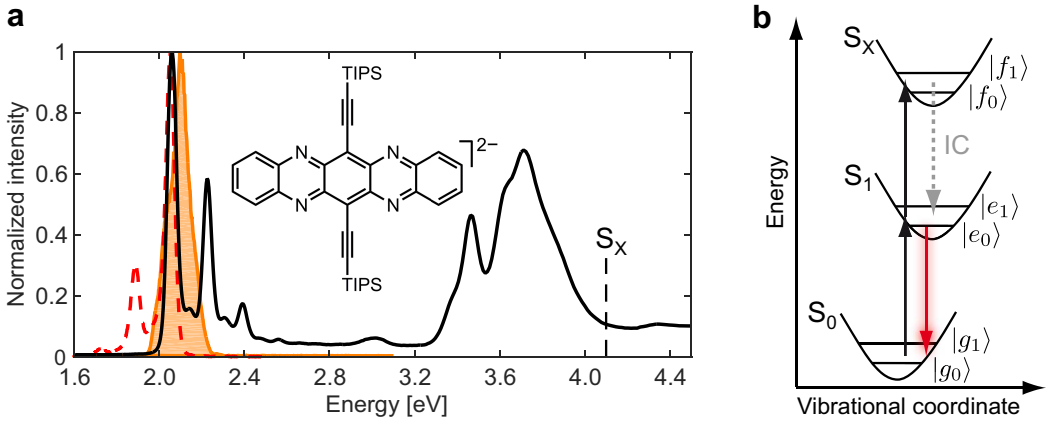

Figure 4.2. Sample spectra and energy scheme. (a) Linear absorption (black, determined via spectroelectrochemistry in THF/N(n-Bu)$_4$PF$_6$ of TIPS–TAP^{2-} (molecular structure shown in the inset). The laser spectrum employed in the multidimensional experiment is displayed as an orange shaded area. The emission spectrum of TIPS–TAP^{2-} in THF, which was acquired immediately before the multidimensional experiment, is shown as a red dashed line. Absorption and emission spectra are normalized to their respective maximum value. The black dashed line at 4.1 eV marks the energy of the doubly excited state S_x. (b) Energy-level scheme used for interpreting the 3D spectra with the dashed gray arrow denoting internal conversion (IC) and the red arrow the observed fluorescence. Reproduced from Ref. [4].

section, we display the 3D spectral solids with three isosurfaces of varying transparency, visualizing the signal amplitude. In addition, we project the solid onto 2D frequency planes, which are represented as contour plots that are normalized to the highest absolute value each. Thus, different types of 2D spectra can be extracted as well. In case of the rephasing 1Q–0Q–1Q spectrum, the 2D projections deliver the photon-echo (1Q–1Q) spectrum for $T = 0$ on the bottom $(\hbar\omega_\tau, \hbar\omega_t)$ plane, the 1Q–0Q spectrum at $t = 0$ on the $(\hbar\omega_\tau, \Delta\hbar\omega_T)$ plane, and the 0Q–1Q spectrum at $\tau = 0$ on the $(\hbar\omega_t, \Delta\hbar\omega_T)$ plane. The 3D solid displays a dominating feature centered around a coordinate of $(\hbar\omega_\tau, \Delta\hbar\omega_T, \hbar\omega_t) = (2.06, 0, 2.06)$ eV that exhibits a characteristic star-shaped lineshape [41, 43]. This peak coordinate corresponds exactly to the maximum of the linear absorption spectrum, which is attributed to the transition from state $|g_0\rangle$ to $|e_0\rangle$ in the model (Fig. 4.2b). It is accompanied by a much weaker feature at $(2.23, 0, 2.23)$ eV, which corresponds to the transition from $|g_0\rangle$ to $|e_1\rangle$. The overall amplitude of the 3D solid is determined by the multiplication of $|e_0\rangle$ and $|e_1\rangle$ with the laser spectrum. The solid is elongated toward higher 1Q energies which reflects coupling to the progression band $|e_1\rangle$ at 2.23 eV, mediated by the common ground state $|g_0\rangle$. Mediation by a hot ground state $|g_1\rangle$ can be excluded because this would involve an $|e_0\rangle \rightarrow |g_1\rangle$ transition with a transition energy of 1.89 eV, where the laser spectrum has no intensity. As further shown in Supplementary Sec. 4.5.5 and Supplementary Fig. 4.13 and discussed in a similar scenario [222], the filtering effect by the laser spectrum removes from the complete manifold a number of pathways that involve the transition between $|e_0\rangle$ and $|g_1\rangle$, also in the nonrephasing 1Q–0Q–1Q contribution. This simplifies the interpretation.

Apart from these features being located within the $\Delta\hbar\omega_T = 0$ plane, which reflects the fact that the system evolves in a population state during T, we observe two additional weak cross peaks A and B. In order to separate them from the dominating peaks, we isolate the voxels within the spectral volumes that span the regions in the vicinity of peak A and B, which is indicated by red and blue cuboids, respectively (Fig. 4.3a, right). By determining the coordinates of the maximum amplitude of each isolated cross peak, we find that these are shifted along the $\Delta\hbar\omega_T$ axis by +188 meV (A) and −172 meV (B). In view of the effective spectral resolution (15.7 meV), these values are in fair agreement with the energy spacing $\hbar\omega_{0Q} \approx 0.17$ eV between vibrational levels within S_0 and S_1, and thus they originate from vibrational coherence. These cross peaks can be described by double-sided Feynman diagrams [19] (Fig. 4.3b), where the wavy arrows pointing to the right (left) denote the laser fields, interacting with a phase of $+\varphi$ $(-\varphi)$. The sign of the 0Q coherence frequency determines whether the coherence oscillates positively, e.g., $|e_1\rangle\langle e_0| \propto \exp(-\mathrm{i}\omega_{0Q}T)$, or negatively with $|e_0\rangle\langle e_1| \propto \exp(+\mathrm{i}\omega_{0Q}T)$ [41, 222]. As

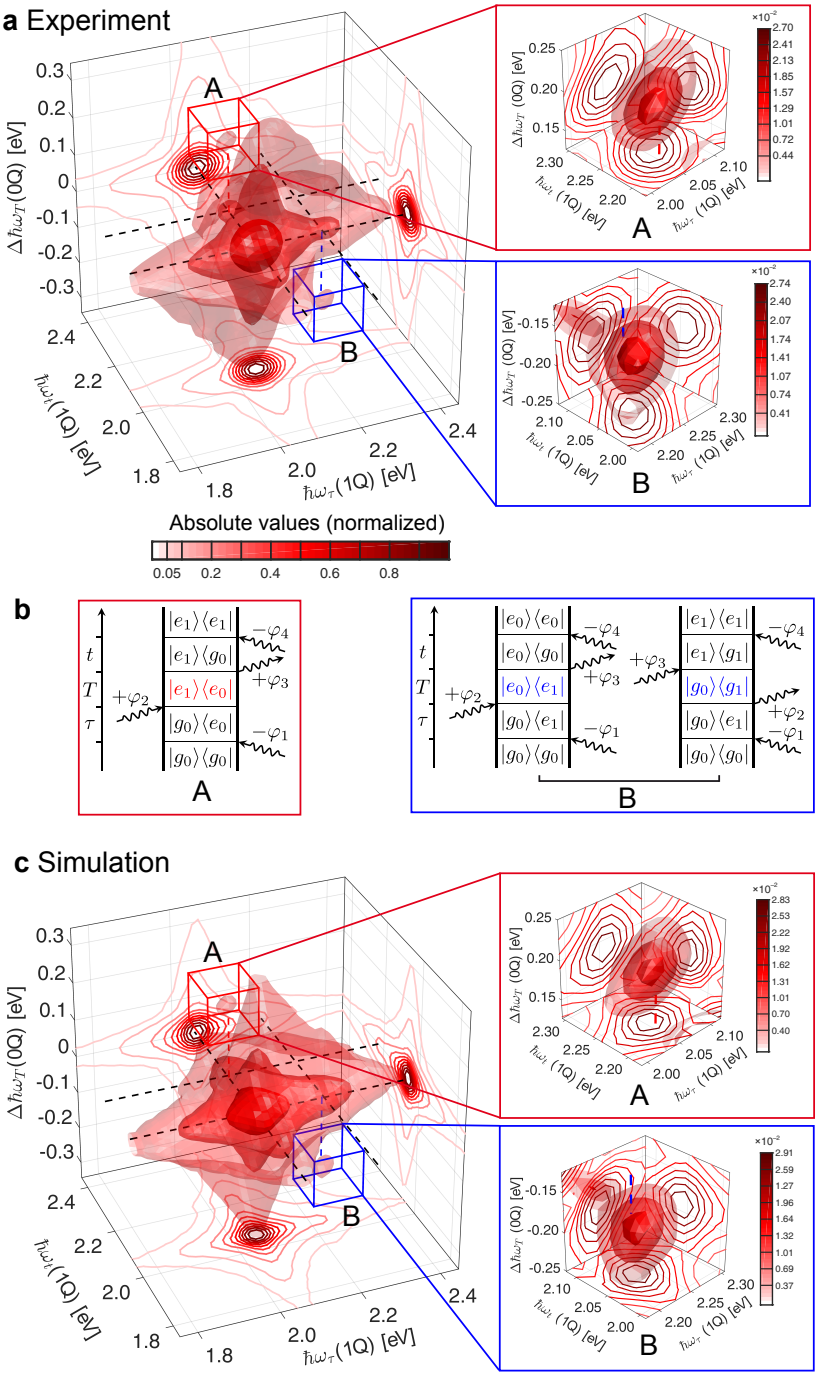

Figure 4.3. Fourth-order rephasing 1Q–0Q–1Q 3D spectrum of TIPS–TAP^{2-} in THF. (a) Experimental and (c) simulated rephasing 1Q–0Q–1Q 3D spectra, shown in absolute values. The energies of the main absorption band at 2.06 eV and the progression band at 2.23 eV are indicated as dashed black lines in the $\Delta\hbar\omega_T = 0$ plane as a guide for the eye. Red and blue dashed vertical lines mark positive and negative shifts of 0.17 eV, respectively, along the 0Q axis $\Delta\hbar\omega_T$. Isosurfaces are drawn at 2.3, 9.0, and 35% of the maximal signal amplitude. Contour lines of the 2D projections of the spectral solids

are drawn at linearly spaced levels of the normalized signal amplitude with an additional contour line at 0.05. The spectral volumes inside the red and blue cuboids, which are centered around peaks A and B are isolated and shown on the right. There, isosurfaces are drawn at 50, 70, and 90% of the isolated maximal signal amplitudes whereas the color bars indicate the signal levels (normalized to the highest absolute value of the respective full 3D spectrum) for each contour line. (b) Double-sided Feynman diagrams that describe the peaks A (red) and B (blue). Reproduced from Ref. [4].

previously demonstrated, analyzing these oppositely signed signatures has proven to be a powerful tool to decipher the origin of the underlying quantum coherences [223, 224].

Peak A is described by a single Feynman diagram involving vibrational coherence in the first excited electronic state that oscillates with a positive frequency. In contrast, Peak B can be described by two diagrams that include vibrational wavepacket evolutions oscillating with a negative frequency within both the ground and the first excited electronic state. There is no way to construct a diagram in which a positively oscillating $|g_1\rangle\langle g_0|$ coherence is created, except if one assumes that the system is initially in a vibrationally excited electronic ground state which is unlikely because the amount of thermal energy that was present at the experiment (≈26 meV) is much less than the 0Q energy (≈170 meV). Interestingly, although two pathways could contribute to peak B in principle, its amplitude is nearly identical to peak A (Fig. 4.3a, right), indicating that only one of the two pathways for peak B contributes significantly. Taking into account the Huang–Rhys factor of the ≈170 meV mode, which we estimated to be S_{HR} ≈0.6 from linear absorption, leads to a low transition strength for the $|g_1\rangle \rightarrow |e_1\rangle$ transition that is involved twice in the right B pathway in Fig. 4.3b, strongly diminishing its contribution to the peak. Thus, while peak A represents an isolated single Liouville pathway, peak B predominantly bears the signature of the excited-state vibrational coherence over T. As evident from Fig. 4.3, the experimental results (Fig. 4.3a) can be very well reproduced by simulations (Fig. 4.3c) using Lindblad theory [21], in terms of peak positions as well as their shapes and amplitudes, even for the peaks A and B (for details about the simulation model see below and Supplementary Sec. 4.5.6). Overall, this successfully demonstrates the decongestion that 3D spectroscopy offers, yielding a separation of population and wavepacket contributions in the studied molecule which in turn enables us to isolate signatures of vibrational coherence in the excited electronic state and distinguish them from vibrations in the electronic ground state.

While 1Q–0Q–1Q spectra give extensive information about the manifold of singly excited states, it is difficult to reveal direct signatures involving higher excited states which could be accessed via excited-state absorption (ESA). This issue is a complication for

interpreting any type of third-order spectroscopy, be it pump–probe transient absorption or conventional electronic 2D spectroscopy, i.e., it is challenging to assess the influence of higher excited states on the observed transient spectra because, typically, not much is known about them. Thus, it is desirable to design nonlinear spectroscopy experiments that specifically address these higher lying states. We will turn to such experiments now and implement 1Q–2Q–1Q 3D spectroscopy. The results obtained therein will also justify why, while discussing the 1Q–0Q–1Q spectra, we neglected any ESA signatures that could potentially contribute to the 1Q–0Q–1Q signals. (However, we already incorporated the higher excited state into the simulation model, but the 1Q–0Q–1Q ESA pathways cancel in pairs, as also discussed in Supplementary Sec. 4.5.4.)

In order to probe highly excited states, it is necessary to prepare them as a 2Q coherence via an interaction phase $\pm 2\varphi$ by a single laser pulse [9, 29] or by $\pm\varphi$ from two pulses each [225]. Concerning the latter, applying the weights that correspond to the phase signature $\varphi_{1Q2Q1Q} = +\varphi_1 + \varphi_2 - \varphi_3 - \varphi_4$ (Table 4.1) extracts all nonrephasing fourth-order pathways in which a 2Q coherence evolves during T and that can be visualized as the experimental 1Q–2Q–1Q 3D spectrum (Fig. 4.4a).

Now, the $\hbar\omega_T$ axis contains information about electronic states that lie within two quanta of the excitation laser spectrum so that one can probe how these states are coupled to the manifold of singly excited states. The 3D signal peaks at 4.10 eV along the 2Q axis, indicating the presence of a higher-excited electronic state S_x. The solid shows further a vibrational shoulder along $\hbar\omega_T$ with a higher magnitude compared with the 1Q progression band, resulting from the multiplication with the laser spectrum which has its maximum at ≈4.20 eV in the 2Q domain. The linear absorption spectrum in the UV range (see Fig. 4.2a) does not exhibit a significant absorption band at 4.10 eV, suggesting that the probed 2Q state is a two-photon allowed (but one-photon forbidden) state, which is reasonable considering the inversion symmetry of the molecule. Time-dependent density-functional theory calculations (TD–DFT) also support such a two-photon state which can be attributed to S_{74} and that is accessed by two consecutive nearly degenerate one-photon transitions $S_0 \rightarrow S_1$ and $S_1 \rightarrow S_{74}$, respectively, both having high oscillator strengths, whereas the direct $S_0 \rightarrow S_{74}$ transition has zero oscillator strength (see Supplementary Sec. 4.5.7 and Figs. 4.14 and 4.15). We sought a separate experimental signature of the 2Q state by performing a two-photon absorption (2PA) measurement. The strong one-photon absorption, however, superimposes any potential 2PA signal so that it is impossible to extract the 2PA spectrum of this compound by conventional 2PA techniques. Nevertheless, this underlines the significant advantage of the use of phase cycling and two-quantum 3D spectroscopy, because here the desired

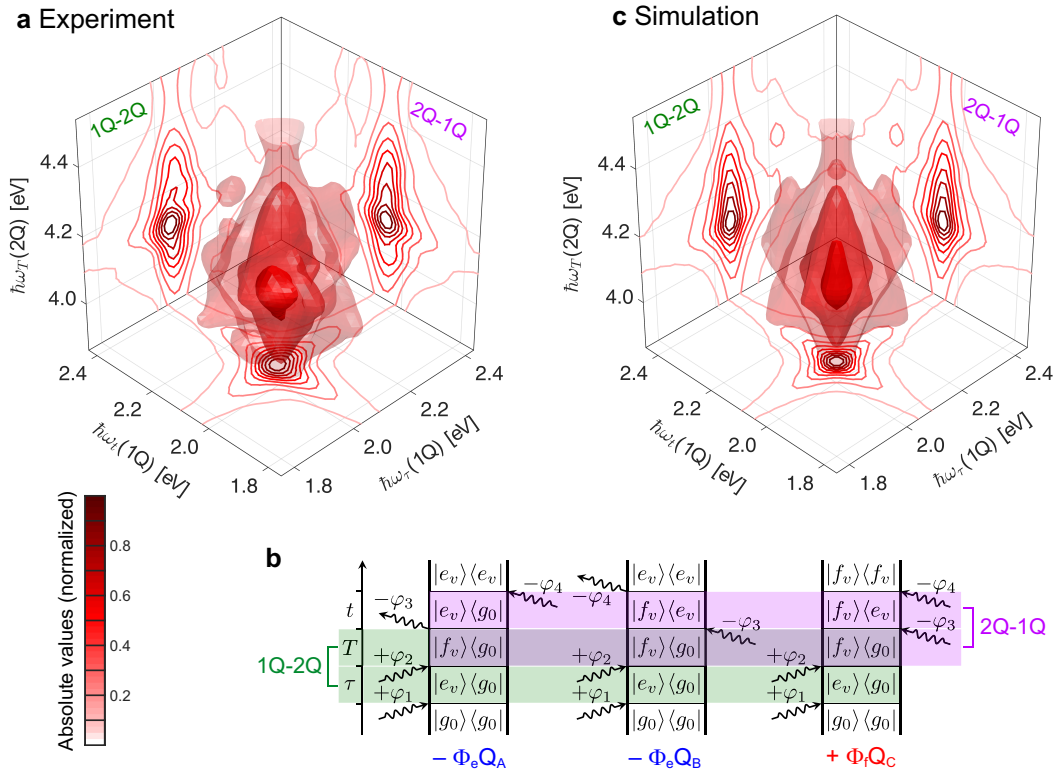

Figure 4.4. Fourth-order three-dimensional 1Q–2Q–1Q spectrum of TIPS–TAP^{2-} in THF. (a) Experimental and (c) simulated 3D spectra, both shown in absolute values. Isosurfaces are drawn at 11, 25, and 60% of the maximal signal. Contour lines of the 2D projections are drawn at linearly spaced levels of each normalized projection. (b) Double-sided Feynman diagrams that correspond to the 1Q–2Q–1Q process, highlighting the coherence density matrix elements that are relevant for 1Q–2Q and 2Q–1Q 2D spectra in green and pink, respectively. Each pathway is labeled according to its sign, where Φ denotes the pathway-specific fluorescence quantum yield that is dependent on the finally prepared population state (marked by the index). Reproduced from Ref. [4].

nonlinear signal is isolated unambiguously by its unique phase signature.

The 1Q–2Q–1Q spectral solid can be projected onto the three 2D planes to extract a nonrephasing 1Q–1Q spectrum at $T = 0$ along $(\hbar\omega_\tau, \hbar\omega_t)$, the 2Q–1Q spectrum along $(\hbar\omega_T, \hbar\omega_t)$, and the 1Q–2Q spectrum along $(\hbar\omega_\tau, \hbar\omega_T)$ [206]. Fluorescence-detected 2Q spectroscopy is sensitive to relaxation channels of highly excited states because all relaxation processes that happen after the perturbation by the light fields until the final emission of fluorescence in fact matter, which is in contrast to coherently detected multidimensional spectroscopy [27, 218]. In that sense, a cross check between the 2Q–1Q and 1Q–2Q 2D spectra offers the ability to draw conclusions about the relaxation pathways of the 2Q manifold [9]. From Fig. 4.4a, it is apparent that these 2D projections are

nearly identical in relative signal amplitude, which is an indication of highly efficient internal conversion from S_x to S_1 as expected for a system with such a high fluorescence quantum yield (95% in Et_2O [219, 220]). The double-sided Feynman diagrams in Fig. 4.4b explain that the equality of both projections results from a total cancellation of the opposite-signed excited-state absorption pathways Q_B and Q_C. Due to a complete nonradiative population transfer from $|f_v\rangle\langle f_v|$ to $|e_v\rangle\langle e_v|$, the pathway-specific quantum yield [26] Φ_f is equal to Φ_e. This erases any signal stemming from $|f_v\rangle\langle e_v|$ coherences so that both 2D projections only feature $|e_v\rangle\langle g_0|$ coherence signals along their respective 1Q axes. Contributions from $|f_v\rangle\langle e_v|$ coherences would lead to an asymmetry of the 3D solid. Consequently, the whole 3D spectrum can be described by pathway type Q_A only. Thus, the 1Q–2Q–1Q 3D spectrum delivers detailed information on the highly excited 2Q state and its relaxation dynamics.

The simulated 1Q–2Q–1Q spectrum (Fig. 4.4c) reproduces well the overall symmetric shape of the solid, reflecting identical 2Q–1Q and 1Q–2Q projections, where we estimated an internal conversion time constant of 100 fs. In the simulation model, we derived the transition strengths into the S_x state with the aid of TD–DFT calculations (see Supplementary Sec. 4.5.6). In addition, by performing simulations with varying Huang–Rhys factor of the ≈0.17 eV mode between S_1 and S_x, we found that a S_{HR} of ≈0.05 best reproduces the experiment (especially the lineshape along the 2Q axis). This reflects a much smaller displacement between the two-photon and the first excited state compared with that between first excited state and ground state. Furthermore, a pure dephasing time for all $|f_v\rangle\langle e_v|$ coherences of 300 fs yields good reproduction, which is much higher than those of the $|e_v\rangle\langle g_v|$ coherences (90 fs), thus indicating a lower transition energy fluctuation between S_1 and S_x compared with S_0 and S_1. It is also worth noting that in coherently detected 2Q spectroscopy, when $|e_v\rangle\langle g_v|$ and $|f_v\rangle\langle e_v|$ coherence energies are nearly degenerate as in the present system, the signal would vanish due to destructive interference of the involved pathways [36]. In contrast, the 2Q-associated pathways in population-based detection differ due to the additional order in perturbation, so that the signal is preserved by a single pathway type [26]. In the present case, this is an advantage because one can then analyze the signal, whereas the vanishing signal of coherently detected 2Q spectra obviously could not be analyzed. To conclude, these results demonstrate that our approach provides rich information about the electronic structure of the system that can otherwise be obscured in other methods.

4.2.3 Sixth-Order 3D Spectra

While the previous discussion involved responses from fourth-order nonlinear processes, in which each pulse interacts once with the system, the employed phase cycling also selectively captures processes in which six light-field interactions are distributed over four pulses. For the following, we want to focus on sixth-order processes that probe 0Q, 1Q, and 2Q coherences simultaneously, such as the rephasing 2Q–0Q–1Q contribution. Compared with the fourth-order 1Q–2Q–1Q process, in a sixth-order process the generation of the 2Q coherence results from a double interaction of a single laser pulse. The overall six-fold interaction pattern allows us to rephase a 2Q coherence by means of a 1Q coherence, thus the homogeneous linewidth of both 1Q and 2Q coherences contribute to the spectral response. Therefore, this sixth-order sequence is analogous to the coherently detected fifth-order rephasing 2Q sequence, which was first designed by Fulmer, Ding, and Zanni for 2D IR spectroscopy [64, 94], but here carried out using fluorescence. There are also other coherently detected signal variants that employ this process in the optical regime [57, 102]. However, extending the earlier work we are able to isolate both rephasing and nonrephasing 2Q–0Q–1Q as well as 1Q–0Q–2Q contributions directly in amplitude and phase without the need of additional phasing. Analogous to the common procedure for lower-order 2D spectra, adding the real parts of the properly rotated rephasing and nonrephasing 2Q–0Q–1Q contributions with phase signatures $\varphi_{\mathrm{R2Q0Q1Q}} = -2\varphi_1 + 2\varphi_2 + \varphi_3 - \varphi_4$ and $\varphi_{\mathrm{NR2Q0Q1Q}} = +2\varphi_1 - 2\varphi_2 + \varphi_3 - \varphi_4$, respectively, enables us to receive purely absorptive 2Q–1Q spectra. The 2Q–1Q spectrum at $T = 0$ can be extracted by taking the bottom projection of the 3D spectrum in Fig. 4.5.

As is typical for a higher-order nonlinear signal, the overall signal amplitude is much lower than in the fourth-order spectra, which manifests as increased noise compared with the fourth-order spectra. Still, the signal quality is quite good due to the use of fluorescence as an observable that excludes artifacts from nonresonant solvent contributions and scattered excitation light, and also to the shot-to-shot rapid scanning implementation. Thus, even this sixth-order signal shows a remarkable agreement with the theoretical prediction (Fig. 4.5b).

We observe features at positions A and C signifying that $|e_0\rangle$ and $|e_1\rangle$ are coupled to the lowest level of the doubly excited manifold, $|f_0\rangle$, whereas features B and D indicate that the singly excited manifold is coupled to $|f_1\rangle$ as well. This leads to a rectangular arrangement of features in the $\Delta\hbar\omega_T = 0$ plane which is also well reproduced by the simulation (Fig. 4.5b), further verifying the absence of lower-order cascaded contributions. Additional unwanted signals, such as those originating from many-particle excitations of noninteracting molecules [79] are not present in our experiment (for a detailed discussion

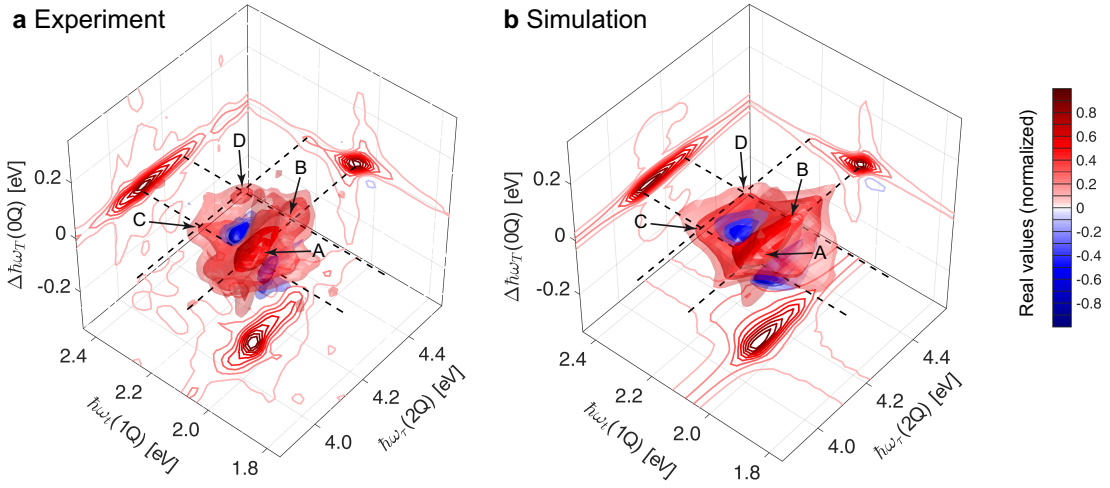

Figure 4.5. Sixth-order 2Q–0Q–1Q three-dimensional (3D) spectrum (real part) of TIPS–TAP^{2-} in THF. The 3D spectra shown are obtained by the sum of the rephasing and nonrephasing 2Q–0Q–1Q contributions. (a) Experimental and (b) simulated 3D spectra. Isosurfaces are drawn at −12, −10, −7, 7, 11, and 35% of the normalized signal amplitude. Contour lines are drawn at 0.1 steps as indicated by the color bar. The bottom projections of the solids show the purely absorptive 2Q–1Q 2D spectrum at $T = 0$ fs. The dashed lines in the $\Delta\hbar\omega_T = 0$ plane denote the energies of the main absorption band at 2.06 eV and the progression band at 2.23 eV along $\hbar\omega_t$ and the energies of the 2Q levels at 4.10 and 4.27 eV along $\hbar\omega_\tau$. The letters A, B, C, D mark peaks, which are discussed in the text. Reproduced from Ref. [4].

see Supplementary Sec. 4.5.9). Another source for unwanted signals is so-called incoherent population mixing, that is, signals arising from interacting excited-state populations, as discussed by Grégoire et al., which was observed in solid-state semiconductors under high excitation densities [74]. In our experiment, we determined the number of absorbed photons per molecule [102] to be 0.26, which would in principle facilitate the generation of such incoherent signals by bimolecular processes. Considering the relevance of this value for multiparticle interactions, however, we have to take into account the relative distance of chromophores because for systems that do not form aggregates (such as in the present case), the probability of bimolecular processes is generally low. According to the suggestion of Tiwari et al., we have estimated the effect of multiparticle interactions for the present sample using Förster resonance energy transfer (FRET) as a crucial step that would facilitate the interaction of populations of two distinct molecules by subsequent exciton–exciton annihilation [216]. We calculated the Förster critical concentration [226, 227] for this effect to be 0.54 mM, which is above our concentration (0.40 mM) so that we expect such contributions in our experiment not to be present.

Besides the inverted sign in the 3D solid compared with fourth-order contributions (see also Supplementary Sec. 4.5.8), strong evidence for the isolation of sixth-order signals is presented in Fig. 4.6, where we compare transients over T of the rephasing fourth-order 1Q–0Q–1Q (Fig. 4.6a) and the rephasing sixth-order 2Q–0Q–1Q contributions (Fig. 4.6b), taken at above-diagonal cross-peak positions. The respective Liouville pathways (Fig. 4.6c, d) that contain these 0Q coherences only differ in the type of electronic quantum coherence that evolves during τ, but the coherence evolution during T is the same (marked in blue and red, respectively). The 0Q oscillation period (≈24 fs) corresponds well to the 0.17 eV vibrational mode in both cases. In principle, sixth-order 2Q–0Q–1Q processes are capable of tracking 0Q coherence dynamics within higher-excited electronic states. This is impossible to see with lower-order spectroscopic techniques. However, we attribute the present oscillation to 0Q coherence within the S_1 state because all pathways that bear possible 0Q coherence in S_x cancel due to internal conversion (see Supplementary Sec. 4.5.10 and Fig. 4.18). Importantly, we observe a phase shift of exactly π between Fig. 4.6a, b. This demonstrates the isolation of the sixth-order nonlinear signal from unwanted lower-order contributions such as cascade processes [101]. The phase shift results from the different prefactors of the perturbative expansion, i.e., $i^4 = 1$ versus $i^6 = -1$. This finding is also in excellent agreement with the

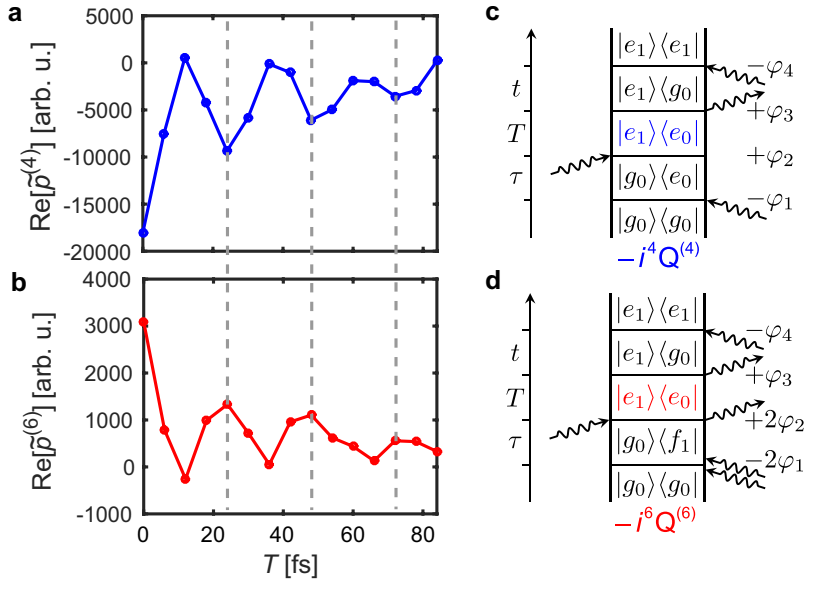

Figure 4.6. Comparison of fourth- and sixth-order 0Q coherence signatures of TIPS–TAP^{2-} in THF. (a) Real part of a cross-peak transient of the rephasing 1Q–0Q–1Q contribution $\left(\tilde{p}^{(4)}\right)$ at $(\hbar\omega_\tau, \hbar\omega_t) = (2.06, 2.23)$ eV, along with (c) a respective double-sided Feynman diagram. (b) Real part of a cross-peak transient of the rephasing 2Q–0Q–1Q contribution $\left(\tilde{p}^{(6)}\right)$ at $(\hbar\omega_\tau, \hbar\omega_t) = (4.27, 2.23)$ eV with (d) a respective double-sided Feynman diagram. Reproduced from Ref. [4].

simulations using identical parameters with the same model as above (see Supplementary Sec. 4.5.11 and Fig. 4.19).

We further note that the rephasing and nonrephasing 2Q–0Q–1Q signals represent the direct population-based analogues of the coherently detected signals employed in the recently introduced exciton–exciton-interaction (EEI) 2D spectroscopy [102]. Thus, we deem that these sixth-order signals are also susceptible to exciton–exciton annihilation dynamics over T for excitonic systems.[2]

4.3 Conclusion

We introduced three-dimensional (3D) fluorescence-detected coherent spectroscopy and demonstrated the potential of the technique on a dianionic molecule in solution. By using shot-to-shot pulse shaping in a fully collinear single-beam setup, nearly half a million pulse trains were streamed in just 8 min. This time scale is short enough to capture rich information about a molecular system with limited chemical stability. A 125-fold phase-cycling procedure enabled us systematically and simultaneously to acquire multiple fourth- and sixth-order 3D spectra that were encoded into the monitored fluorescence signal, offering access to various kinds of high-order nonlinear signal contributions. From these, we obtained the characteristics of a two-photon allowed state, such as its energy, vibrational displacement, and highly efficient internal conversion to S_1. We also find a significantly longer dephasing time of 1Q coherences between the first and the two-photon excited state, reflecting a degree of correlation between the energy fluctuations of these two excited states, relative to the ground state. In addition, the simultaneous acquisition of rephasing and nonrephasing sixth-order signal contributions allowed us to obtain purely absorptive 2Q spectra from the same measurement. Our approach does not necessitate changing any physical setup component in order to obtain a certain nonlinear signal contribution, and can readily be upscaled in terms of even further extended phase cycling and dimensionality. The possibility to acquire multiple-quantum signals in a systematic fashion by phase cycling underlines the enormous versatility of this technique which can also be employed for other incoherent detection modes such as the detection of electrons or ions [228, 229]. From a total of 15 different signal contributions for the phase-cycling scheme illustrated herein, some of the nonlinear signals may prove useful, especially in excitonic systems, to decipher multiexcitonic coupling patterns, to determine bi- and triexciton binding energies, or to track selectively exciton–exciton annihilation, all from a single measurement.

[2]This aspect is discussed in detail in Chapter 5.

4.4 Methods

Sample Preparation and Handling

The sample is a 0.4 mM solution of the potassium salt of the dianion of 6,13-bis((triisopropylsilyl)ethynyl)quinoxalino[2,3-b]phenazine (TIPS–TAP^{2-}) in THF. The compound was synthesized by reducing the respective neutral species with two equivalents of [K(18-crown-6)(THF)$_2$] anthracenide, as previously described [219, 220]. The preparation was conducted in an argon-filled glove box. THF was stored over NaK inside the glove box and filtered several times through alumina. After preparation, the dark-red solution of TIPS–TAP^{2-} was transferred into a home-built sealed tubing system under inert conditions. During the multidimensional experiment, the sample was continuously pumped through a capillary flow cuvette with (250 µm)^2 cross-section (131.310-QS, Hellma) by a peristaltic pump (Masterflex L/S model 7518-00). Fluorescence spectra were recorded immediately before and after the multidimensional experiment, confirming that no possible decay products contaminated the nonlinear signals (see also Supplementary Sec. 4.5.1 and Fig. 4.9).

Experimental Procedure and Data Processing

The experimental setup for single-beam shot-to-shot multidimensional fluorescence spectroscopy has been reported elsewhere [9, 72]. For a detailed schematic, see Fig. 4.7 in Supplementary Sec. 4.5.1. Briefly, an argon-filled (1.3 bar absolute pressure) hollow-core fiber was used in combination with an acousto-optical programmable dispersive filter (DAZZLER, Fastlite) to produce broadband phase-modulated four-pulse sequences with variable time delays and variable phases between all four pulses. We used a dual grism compressor for dispersion compensation. Collinear frequency-resolved optical gating (cFROG) [230] yielded a temporal pulse duration of <21 fs (intensity FWHM), whereas the excitation energy is 200 nJ (determined at maximum temporal overlap and complete constructive interference of all four excitation pulses). In the multidimensional experiment we employed 125-fold phase cycling, allowing us to extract the various signal contributions out of the raw data by employing interpulse phase weights as described in the Results section. The excitation pulse trains were focused into the sample cuvette via a $f = -150$ mm focusing mirror. Fluorescence was collected perpendicular to the direction of the incoming laser beam by two 0.25-NA microscope objectives which were coupled to an avalanche photodiode (APD) via a 400-µm core-diameter multi-mode fiber. In order to avoid nonlinear contributions from the APD, the fluorescence signal was attenuated to a signal level within the linear detection regime via neutral density

filters. To improve data quality, we averaged over four raw data sets. Each signal contribution was extracted by employing phase weights according to Eq. (4.1) and Table 4.1. In order to avoid truncation artifacts stemming from long-lived dynamics that evolve during T, the respective signal contribution was first apodized with a Hanning window. Before 3D Fourier transformation, the initial time-domain values of all temporal dimensions were scaled by a factor of 0.5 to suppress spurious peak-shape artifacts [231] and further three-fold zero-padded in every temporal dimension.

4.5 Supplementary Information

4.5.1 Details of the Experiment

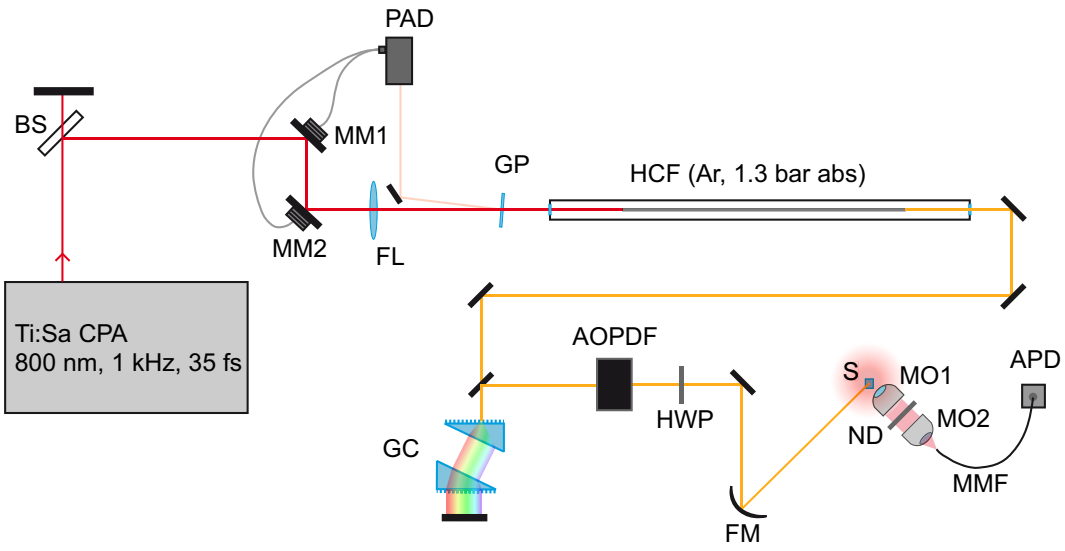

Figure 4.7. Schematic of shot-to-shot single-beam multidimensional fluorescence spectroscopy. CPA: chirped-pulse amplifier; BS: beam splitter; MM1, MM2: motorized mirrors; FL: fused-silica focusing lens ($f = 120$ cm); PAD: position and angle detector; GP: fused-silica glass plate; HCF: hollow-core fiber (filled with argon); GC: dual grism compressor; AOPDF: acousto-optic programmable dispersive filter; HWP: half-wave plate; FM: focusing mirror ($f = -15$ cm); S: sample, being pumped through a capillary flow cuvette; MO1, MO2: microscope objectives, ND: neutral density filter; MMF: multimode fiber; APD: avalanche photodiode. Reproduced from Ref. [4].

The schematic layout of our experimental apparatus is shown in Fig. 4.7. We guide a fraction (0.4 mJ) of the 35 fs pulses (as confirmed by intensity autocorrelation) of a commercial Ti:Sa chirped-pulse amplifier laser system (Spitfire Pro, Spectra Physics) with 1 kHz repetition rate through a beam-stabilization system (Aligna, TEM Messtechnik GmbH). The latter consists of two motorized mirrors which are controlled via a feedback from a combined angle and position detector. This detector tracks the spatial properties

of a weak reflection of the fundamental beam that is produced by a fused-silica glass plate and led into the detection unit. With that, a stabilized beam pointing into the argon-filled fused-silica hollow-core fiber with a length of 110 cm and an inner diameter of 250 µm (HCF, Ultrafast Innovations GmbH) via a lens with $f = 120$ cm is ensured, providing long-term stability of the fiber output. The argon pressure inside the fiber is kept constant at 1.3 bar (absolute). Dispersion management is provided by a dual grism compressor (Fastlite), especially in order to pre-compensate the dispersion which is introduced by the 2.5 cm long TeO_2 crystal of the pulse shaper. The pulse shaper is an acousto-optic programmable dispersive filter (AOPDF, DAZZLER, Fastlite) which operates directly at the repetition rate of the laser on a shot-to-shot basis. With that, we generate collinear four-pulse trains which are then focused via a focusing mirror ($f = -15$ cm) into the sample. The sample is pumped through a capillary-type flow cell with square cross section of $(250\ \mu m)^2$ (131.130-QS, Hellma), which is placed vertically into the focus position. We use a peristaltic pump (Masterflex L/S model 7518-00). The tubing circuit is connected to a reservoir with ~25 mL sample volume, where the concentration of 6,13-bis((triisopropylsilyl)ethynyl)quinoxalino[2,3-b]phenazine (TIPS–TAP^{2-}) in THF is 0.4 mM. Filling the reservoir and sealing the tubing circuit is conducted inside an argon-filled glove box. The excitation energy is 200 nJ at maximum temporal overlap and complete interference of all four excitation pulses. At an angle of 90° with respect to the excitation direction, two microscope objectives with 0.25-NA (04OAS010, CVI MellesGriot) collect the fluorescence light which is then guided into a 0.22-NA multimode glass fiber (QP400-2-SR, Ocean Optics, core diameter 400 µm). The detection of stray light is efficiently avoided by utilizing the 90° detection geometry in combination with a horizontal excitation beam polarization which is generated via a half-wave plate after the AOPDF. For the detection of fluorescence spectra and confirmation of the absence of any stray light (see also Fig. 4.9), we plug the fiber into a spectrometer (HR 4000, Ocean Optics, not shown in Fig. 4.7). In order to perform multidimensional experiments, the fiber is plugged into an avalanche photodiode (APD410x, Thorlabs). The fluorescence is attenuated by an absorptive neutral density filter (FS-3R, Newport) with OD = 1.8 to a suitable signal level to avoid artifacts stemming from saturation of the APD. The analog fluorescence signal is finally digitized by a 14 bit 1 GS/s digitizer card (ADQ14, Signal Processing Devices Sweden AB). The data presented in the manuscript were averaged over four complete datasets. In Fig. 4.8, we show exemplarily the fourth-order 1Q–0Q–1Q and the sixth-order 2Q–0Q–1Q 3D spectra resulting from a single data set without averaging. The same plotting parameters were used as those described in the captions of manuscript Figs. 4.3 and 4.5, respectively.

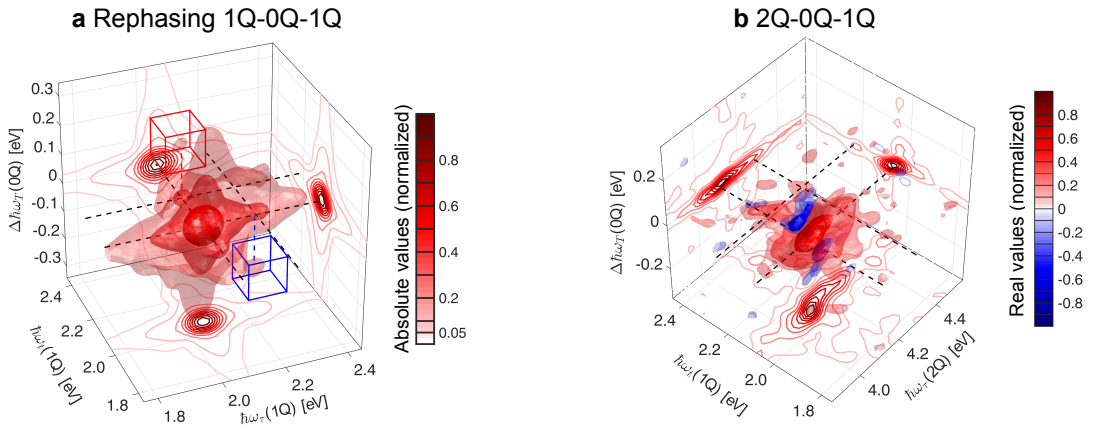

Figure 4.8. 3D spectra obtained after a single measurement without averaging. (a) Rephasing 1Q–0Q–1Q and (b) 2Q–0Q–1Q 3D spectra, generated by the sum of real-valued rephasing and nonrephasing 2Q–0Q–1Q contributions. Reproduced from Ref. [4].

It is evident that an excellent signal-to-noise ratio is achieved for the fourth-order 3D spectrum after only a single run, i.e., without any averaging. For the sixth-order contribution that is much weaker, the noise is significantly higher compared to the four-times averaged data in Fig. 4.5 of the manuscript. Nevertheless, relevant signal features are already visible. This shows that it is indeed possible to obtain all fourth-order signals in 8 min, while for the sixth-order signals additional averaging is helpful.

We want to turn now to a discussion regarding the sample stability and the effect of its degradation on the acquired data. As a dianionic compound, TIPS–TAP^{2-} is extremely sensitive towards even traces of oxygen and moisture. Although care was taken during preparation, i.e., flame-drying of the sample reservoir flask and assembly of the tubing circuit inside the glove box, it was not possible to achieve stability of the compound within the tubing circuit over several hours. We believe that either residual traces of oxygen and moisture inside the tubing circuit or an insufficient sealing of the latter caused the sample decay. Fluorescence spectra of TIPS–TAP^{2-} in THF, taken immediately before and after the multidimensional experiment and normalized to the maximal value of the former are presented in Fig. 4.9. Both spectra are acquired by using the same excitation energy. The fluorescence peaks at 603 nm and 656 nm feature a well-resolved vibrational progression. We do not observe any scattered light of the excitation spectrum which spans the region between 550 and 635 nm, peaking at 590 nm, nor any additional fluorescence bands of possible decay products. Moreover, we do not observe any additional peaks that do not belong to the dianionic species in all three-dimensional (3D) spectra. Thus, we conclude that we measured the nonlinear response

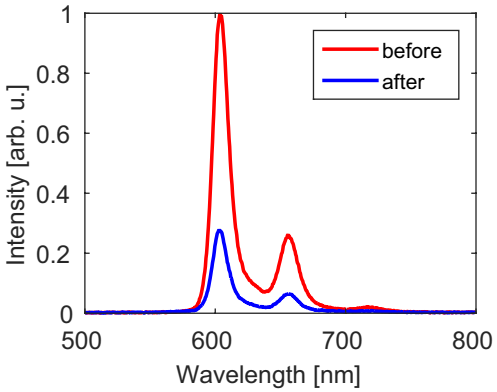

Figure 4.9. Fluorescence spectra of TIPS–TAP^{2-} in THF. The spectra shown are measured immediately before (red) and after (blue) the three-dimensional experiment with the same excitation power and normalized to the maximal value of the red curve. Reproduced from Ref. [4].

of TIPS–TAP^{2-} selectively in our 3D experiment. We note further that fluorescence detection here selectively captures the nonlinear signals from the highly-fluorescent dianion only, while in an approach using coherence detection, one cannot exclude signals from non-fluorescent decay products.

The question arises if the sample degradation would affect the reconstruction of nonlinear signals. We will now discuss why our sampling scheme avoids to first order those errors that might be connected with sample decay.

The most crucial criterion for extracting nonlinear contributions according to their phase signatures by Eq. (4.1) in the manuscript is that the signal level should not drop dramatically within the phase-cycling procedure for any particular given setting of time delays. Hence, it would be detrimental if we had sampled the phase-cycling steps after scanning the complete manifold of interpulse time delays. In our sampling scheme, however, we first acquire all the phase-cycling steps for any given combination of interpulse delays before we change the latter to different settings. Due to the availability of shot-to-shot pulse-shape modulation, acquiring a 125-step phase-cycling set takes 125 ms at 1 kHz repetition rate. This time scale is significantly smaller than the time scale on which the sample degrades, so that the phase-cycling procedure is not compromised by sample degradation.

We characterize the sample degradation during the measurement by recording several "reference" data points, consisting of a repetition (for averaging) of a single, compressed, but otherwise unshaped laser pulse. This reference measurement corresponds effectively to setting all interpulse time delays and interpulse phase differences to zero. These reference data are acquired at the beginning and the end of the full dataset as well as before any population time increment. Thus, between two averaged reference data

measurements, the 125-step phase cycling is conducted for all delay increments of τ and t at a given, fixed T. The resulting reference data points are shown in Fig. 4.10.

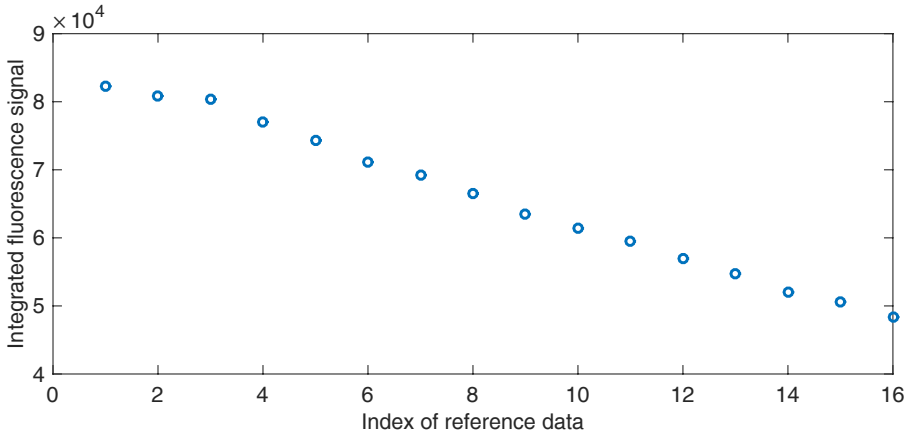

Figure 4.10. Reference measurements. The plot shows time-integrated fluorescence signals that were acquired as reference data (by averaging over a repetition of a single laser pulse) during the multidimensional experiment. Between any two reference points, 125 different phase-cycled data points for each τ and t delay are acquired (not shown). Reproduced from Ref. [4].

In our specific case, analyzing the decay of the reference measurements, we find that the signal changes on average by 3.5% between two reference measurements, so that the claim of constant intensity for any given phase-cycling set is fulfilled up to that precision throughout all τ and t combinations for any T, and the intensity decreases by less than 0.02% for a 125-step phase cycling protocol at any fixed τ and t combination.

The signal decays for instable samples throughout the sampling of T steps because these are sampled last. The degradation acts then as an additional damping of the actual dephasing dynamics of coherences that evolve during T. This has most effects on the 0Q coherence dynamics which usually dephase within several picoseconds. The sample decay then manifests as an additional broadening of the 3D line shapes along the ω_T axis in the 3D spectra. However, a broadening along ω_T for 0Q coherences is introduced anyway by the Hann window we applied in order to avoid truncation artifacts from Fourier transform. Hence, this additional broadening by sample decay might be present but it does not change the spectral position of 0Q features.

Finally, we point out that a sample decay over the course of the acquisition time is not particular in any way to the present technique, but would rather occur with any other approach. On the contrary, using the present shot-to-shot modulation technique, the effect of sample degradation can be reduced as far as possible and thus facilitates measurement of unstable species that are not amenable to analysis with conventional means.

4.5.2 Liouville Pathways Accessible by 125-fold Phase Cycling

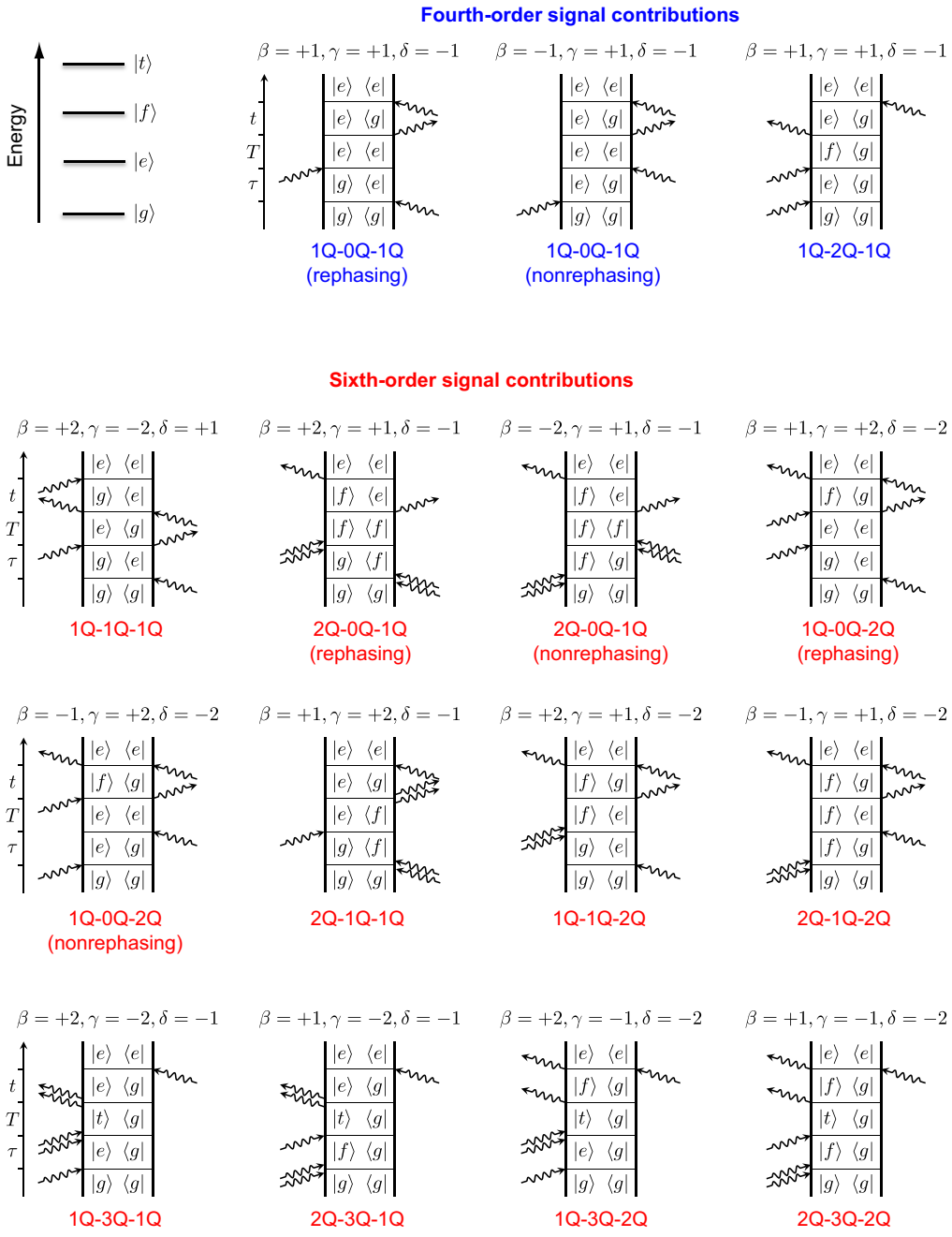

Figure 4.11. Double-sided Feynman diagrams for all signal contributions that can be accessed via 125-fold phase cycling. On the basis of a four-level system (top left), one exemplary diagram for each fourth- and sixth-order nonlinear signal contribution is shown. The respective weighting factors β, γ, and δ are denoted on the top of each diagram. Reproduced from Ref. [4].

We list double-sided Feynman diagrams [19] corresponding to Liouville pathways that can be accessed by (1×5×5×5)-fold phase cycling in Fig. 4.11. For the sake of simplicity,

we only show one exemplary diagram per nonlinear signal contribution that leaves the system in an $|e\rangle\langle e|$ population state after the final laser-field interaction. For that purpose, we consider a simple four-level electronic system consisting of a ground state $|g\rangle$, a one-quantum state (1Q) $|e\rangle$, a two-quantum state (2Q) $|f\rangle$, and a three-quantum state (3Q) $|t\rangle$ (top left in Fig. 4.11). Each diagram is labeled at the top with the weighting parameters β, γ, and δ which are needed for its extraction from the raw data (via Eq. (4.1) of the main manuscript). Although all shown pathways exhibit a negative sign according to the Feynman diagram rules [19], the real part of all sixth-order signals is predominantly positive (with weak negative phase twists, see also Fig. 4.16). This is due to the additional factor i^2 from the perturbative expansion that must be multiplied with each sixth-order diagram, as noted in the main manuscript.

We now point out some benefits of particular signals. With 125-fold phase cycling, one is able to generate purely absorptive sixth-order 2Q–1Q (Fig. 4.5 in the main manuscript) and 1Q–2Q 2D spectra (by adding the real parts of rephasing and nonrephasing contributions), where 2Q population dynamics as well as 0Q coherence between 2Q states can in principle be observed over T. Similarly as in the fourth-order regime, the sixth-order 1Q–2Q 2D spectrum may be less congested because the generation of 1Q coherences is restricted to superpositions between the ground and the first electronic excited state [29]. Sixth-order contributions may further probe 3Q coherences and how they couple to other states of the excited-state manifold by the sixth-order 1Q–3Q–1Q, 2Q–3Q–1Q, 1Q–3Q–2Q, and 2Q–3Q–2Q contributions.[3] In the latter one, as well as in the sixth-order 2Q–1Q–2Q 3D spectrum, the bottom projection of the 3D solid yields the nonrephasing 2Q–2Q 2D correlation spectrum that may indicate coupling within the 2Q manifold by means of cross peaks.

4.5.3 Contamination of Fourth-Order Signals

A common fundamental assumption in third-order nonlinear spectroscopic experiments employing coherent detection is that the third-order signals dominate over the higher nonlinear orders (e.g., fifth-order signals). However, once fifth-order signals are present, these contaminate the third-order signals. This results from the emission of the signal of both nonlinear orders into the same phase matched direction, because one can in principle add zero to the wave vector of any of the incident beams (e.g., $0 = \mathbf{k}_1 – \mathbf{k}_1$). Due to the similar nature of phase matching and phase cycling, this effect is also expected in our experiment, meaning that for any pulse, interaction phases of, e.g., $0 = \varphi_1 - \varphi_1$

[3] The sixth-order contributions discussed in Chapter 2 correspond in principle to various 2D projections of such 3D multiple-quantum response signals.

can be added. As a result, fourth-order signals can be contaminated by sixth-order signals, analogously to the case that third-order signals can be contaminated by fifth-order ones. We have discussed the latter previously in the context of our development of exciton–exciton-interaction 2D (EEI2D) spectroscopy [102]. In that work, we showed that the contamination of third-order signals, due to exciton–exciton annihilation, for example, can be characterized by separately and simultaneously measuring a fifth-order EEI2D signal.

In the present work, we compare the absolute-valued signal magnitudes of the fourth-order rephasing 1Q–0Q–1Q and sixth-order rephasing 2Q–0Q–1Q signals that we also simultaneously measure and find that the sixth-order signal has only 4.96% of the magnitude of the fourth-order one. Hence, because the sixth-order signal is over one magnitude weaker than the fourth-order one, any possible distortion would be at the 5% level or lower.

Considering all the evidence enables us to assign the nominally labeled "fourth-order spectra" indeed to result predominantly from the fourth-order nonlinear response.

4.5.4 Pathway Cancellation in the Fourth-Order Rephasing 1Q–0Q–1Q 3D Spectrum

The rephasing 1Q–0Q–1Q signal can in essence be described by depicting the response by double-sided Feynman diagrams which are shown in Fig. 4.12. Considering the phase signature of the signal, $\varphi_{\mathrm{R1Q0Q1Q}} = -\varphi_1 + \varphi_2 + \varphi_3 - \varphi_4$, there are four pathway types Q_1, Q_2, Q_3, and Q_4 that can be constructed.

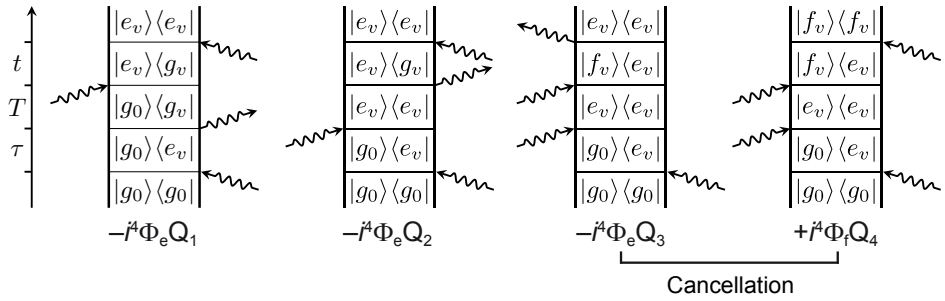

Figure 4.12. Double-sided Feynman diagrams describing rephasing 1Q–0Q–1Q Liouville pathways. Each diagram is labeled according to its sign, where Φ denotes the pathway-specific fluorescence quantum yield that depends on the finally-prepared population state (subscript e or f). Reproduced from Ref. [4].

Here, the subscript "v" in the bra's and ket's denotes the quantum of vibrational excitation, so that these pathway types can either be static (same vibrational quanta

over the population time T) or oscillating (different sets of vibrational quanta over T). The pathway types Q_1 and Q_2, both having a negative sign, end in a $|e_v\rangle\langle e_v|$ population and contain the $|e_v\rangle\langle g_v|$ coherences that evolve over t. In contrast, pathway Q_3 and Q_4 probe the $|f_v\rangle\langle e_v|$ coherence dynamics over t. Hence, Q_3 and Q_4 would principally manifest as excited-state absorption (ESA) contributions along ω_t in a respective 3D spectrum. However, these two pathways are opposite in sign. In the present case, fast internal conversion (IC) leads to identical weights Φ_e and Φ_f of pathways Q_3 and Q_4, respectively, because, if the system is left in a $|f_v\rangle\langle f_v|$ population, also one photon is emitted in the downward decay pathway $|f_v\rangle \rightarrow |e_v\rangle \rightarrow |g_v\rangle$. Thus, ESA contributions cannot be observed because of complete pathway cancellation. A similar situation is also evident regarding the 1Q–2Q–1Q pathways in Fig. 4.4b of the main manuscript. Consequently, pathways Q_1 and Q_2, to which the pathways in Fig. 4.3 of the manuscript also belong, represent the pathway types that entirely express the signal.

4.5.5 Experimental and Simulated Fourth-Order Nonrephasing 1Q–0Q–1Q 3D Spectra

We provide an exemplary detailed pathway analysis on the fourth-order nonrephasing 1Q–0Q–1Q 3D spectrum in Fig. 4.13. In principle, this kind of analysis can be conducted for every signal contribution that can be extracted from the raw dataset. Such a full analysis of all signal contributions is, however, beyond the scope of this work. We extract the nonrephasing 1Q–0Q–1Q signal contribution from the raw data by employing weights corresponding to its phase signature [29] of $\varphi_{\mathrm{NR1Q0Q1Q}} = +\varphi_1 - \varphi_2 + \varphi_3 - \varphi_4$. In order to discuss its peak positions, we choose the absolute-valued representation. The experimental and simulated 3D spectra are displayed in Fig. 4.13a and b, respectively, whereas corresponding double-sided Feynman diagrams are shown in Fig. 4.13c. We do not consider diagrams involving the higher excited state because every negatively signed excited-state absorption (ESA) pathway has a positively signed analogue [26] which leads to destructive interference of these pathways due to the high internal conversion rate as employed in the model. A similar situation is evident in the rephasing 1Q–0Q–1Q spectra (see also Sec. 4.5.4). In general, the 1Q–0Q–1Q pathways can further be classified as either “static” or “beating”, depending on whether the dynamic evolution of a population density matrix element (highlighted in green) or a 0Q coherence density matrix element (red and blue, corresponding to positive and negative frequency shift, respectively) is probed over T.

Overall, the nonrephasing 1Q–0Q–1Q 3D spectrum shows a similar peak arrangement as its rephasing analogue (Fig. 4.3 in the main manuscript). It features two diagonal

(A, D) and two cross peaks (B, C) in the $\Delta\hbar\omega_T = 0$ plane. In contrast to the positively and negatively shifted 0Q peaks in the rephasing 1Q–0Q–1Q 3D spectrum of the main manuscript (Fig. 4.3), in the nonrephasing 1Q–0Q–1Q 3D spectrum, a peak E that is shifted by +0.17 eV on the 0Q axis appears above the diagonal peak D in the $(\hbar\omega_\tau, \Delta\hbar\omega_T, \hbar\omega_t)$ plane. However, it is so weak in magnitude that it can only be

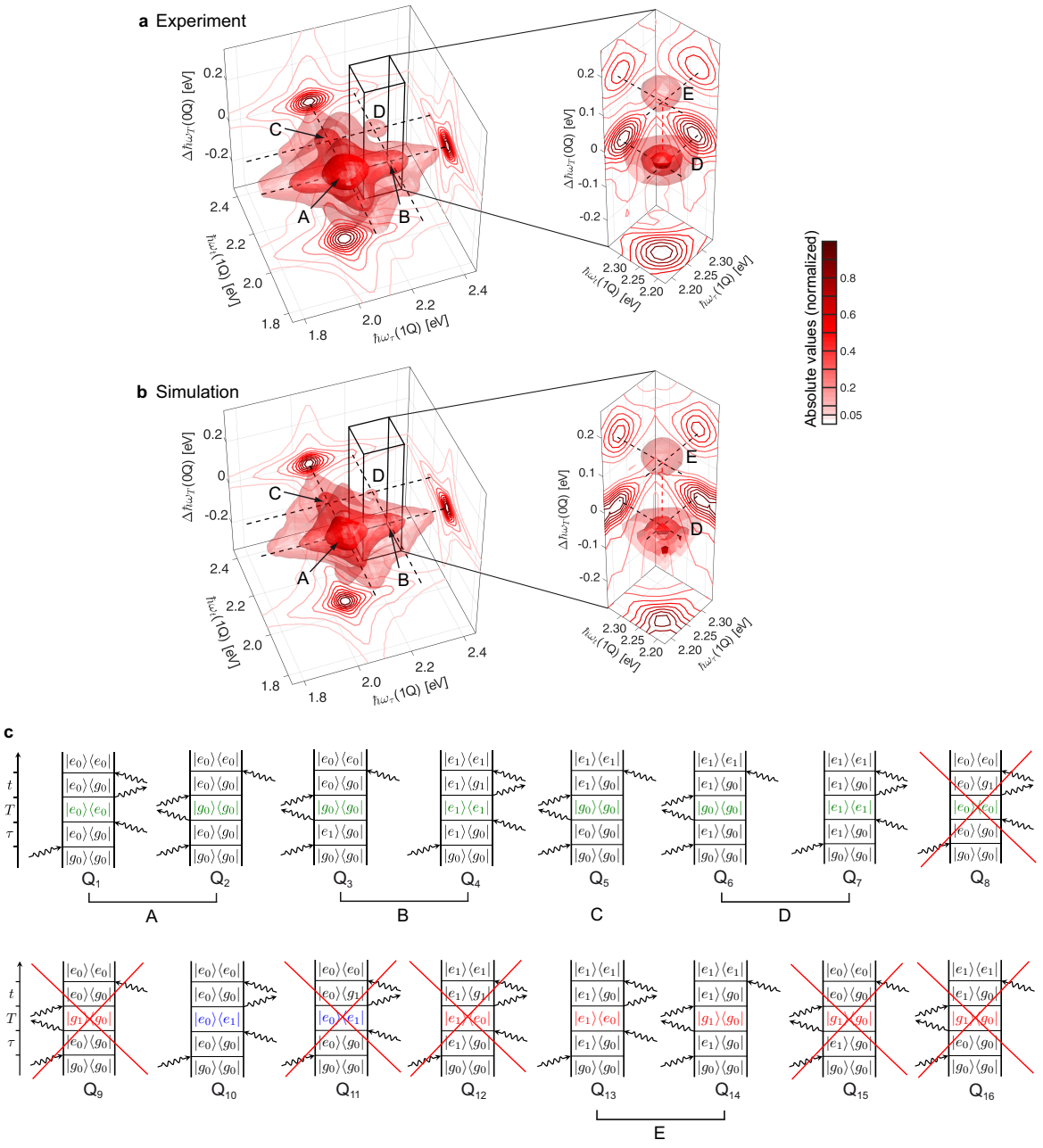

Figure 4.13. Fourth-order nonrephasing 1Q–0Q–1Q 3D spectrum of TIPS–TAP^{2-} in THF. (a) Experimental 3D spectrum shown along with (b) the simulated 3D spectrum. Within both experimental

and simulated 3D spectra, the energies of the levels $|e_0\rangle$ (2.06 eV) and $|e_1\rangle$ (2.23 eV) are indicated by dashed black lines. Isosurfaces are drawn at 3.9, 12, and 35% of the maximal signal amplitude. Contour lines of the 2D projections of the spectral solids are drawn at linearly spaced levels of the normalized signal amplitude with an additional contour line at 0.05. The spectral volume inside the black cuboid, which is centered around peak D, is isolated and shown on the right. There, isosurfaces are drawn at 40, 70, and 90% of the isolated maximal signal amplitude and the red dashed line denotes an energy shift of +0.17 eV. (c) Possible double-sided Feynman diagrams that contribute to the signal. Non-oscillatory density matrix elements are highlighted in green whereas oscillatory 0Q coherence is highlighted in red and blue, according to positive and negative oscillation frequency, respectively. Certain pathways are grouped under the letters A to E in order to label the respective features observed in the 3D spectra. Non-contributing pathways, which involve a transition between $|e_0\rangle$ and $|g_1\rangle$, are crossed out. Reproduced from Ref. [4].

visualized if we mask out the strong feature A at lower 1Q energies. Thus, we isolate the voxels within the spectral volume that spans the region in the vicinity of peak D (Fig. 4.13a and b, right) to make peak E visible. The latter reflects a superposition of two pathways that probe 0Q coherence both in S_0 and S_1 (see diagrams Q_{13} and Q_{14} in Fig. 4.13c). The amplitude of this peak is so low because the energies of the involved electronic transitions are only poorly covered by the employed laser spectrum. Diagram Q_{10} corresponds to an additional 3D peak which is expected to appear at a coordinate of $(\hbar\omega_\tau, \Delta\hbar\omega_T, \hbar\omega_t) = (2.06, -0.17, 2.06)$ eV, where the negative 0Q coherence shift corresponds to excited-state vibrational coherence. However, it is masked by the lineshape of the dominating peak A.

Spectral filtering was shown to be a useful method to eliminate certain Liouville pathways [222]. In our experiments, we did not utilize it on purpose. However, because the laser spectrum is blue-shifted from the main absorption band, some pathways are also eliminated. This means, because the laser spectrum does not cover the energy of the transition between $|e_0\rangle$ and $|g_1\rangle$ (1.89 eV), pathways that involve this transition do not contribute to the signal. Apparently, this mostly affects beating pathways. We indicate this by red crosses in Fig. 4.13c.

4.5.6 Description of the Simulation Model

For simulations, we solve the Lindblad master equation [21], which can be written in a superoperator form,

$$\frac{\partial}{\partial t'}\rho(t') = -\mathrm{i}\mathcal{L}_0\rho(t') - \mathcal{L}_{\mathrm{SO}}\rho(t'). \tag{4.2}$$

In terms of the density matrix $\rho(t')$, the first term on the right side of Eq. (4.2) is

$$\mathcal{L}_0\rho(t') = \frac{1}{\hbar}\left[H(t'), \rho(t')\right], \tag{4.3}$$

and the second term reads

$$\mathcal{L}_{\mathrm{SO}}\rho(t') = \sum_j \frac{1}{T_j}\mathcal{L}_j\rho(t')\mathcal{L}_j^\dagger - \frac{1}{2}\mathcal{L}_j^\dagger\mathcal{L}_j\rho(t') - \frac{1}{2}\rho(t')\mathcal{L}_j^\dagger\mathcal{L}_j, \tag{4.4}$$

with T_j as the time being associated with a dissipation process that induces decoherence by pure dephasing and population relaxation. The Lindblad operators $\mathcal{L}_j$ are defined as $\mathcal{L}_j = a_n^\dagger a_n$ for pure dephasing and $\mathcal{L}_j = a_n^\dagger a_m$ with $n \neq m$ for a population relaxation process, where $a^\dagger$ and a denote the creation and annihilation operators, respectively [89, 225]. The superoperator formulation leads to a reduction of computational cost of calculations with a large amount of external light fields, which is 421875 in the present case.

The Hamiltonian $H(t')$ in Eq. (4.3) is given by

$$H(t') = H_0 + H_I(t'), \tag{4.5}$$

where the time-independent Hamiltonian H_0 is

$$H_0 = \hbar\omega_n \sum_n^N |n\rangle\langle n| \tag{4.6}$$

with energy eigenstates $|n\rangle$ and associated frequencies ω_n. The interaction Hamiltonian $H_I(t')$ is

$$H_I(t') = \gamma_{\mathrm{ext}} E(t') \sum_{n\neq m} \mu_{nm}\left(|n\rangle\langle m| + |m\rangle\langle n|\right), \tag{4.7}$$

with the external field coupling strength $\gamma_{\mathrm{ext}} = 0.3{\times}10^{-3}$ and transition dipole moments μ_{nm} between states $|n\rangle$ and $|m\rangle$. In Eq. (4.7), the external light fields $E(t')$ are four-pulse sequences with pulse-specific phases φ_k and defined as

$$\begin{aligned}
E(t') = {} & \exp\left(-\frac{4\ln 2}{\tau_p^2}(t'-t_0)^2\right)\exp\left(\mathrm{i}\omega_0(t'-\gamma_0 t_0) - \mathrm{i}\varphi_1\right) \\
& + \exp\left(-\frac{4\ln 2}{\tau_p^2}(t'-t_0+\tau)^2\right)\exp\left(\mathrm{i}\omega_0(t'-\gamma_0(t_0+\tau)) - \mathrm{i}\varphi_2\right) \\
& + \exp\left(-\frac{4\ln 2}{\tau_p^2}(t'-t_0+\tau+T)^2\right)\exp\left(\mathrm{i}\omega_0(t'-\gamma_0(t_0+\tau+T)) - \mathrm{i}\varphi_3\right) \\
& + \exp\left(-\frac{4\ln 2}{\tau_p^2}(t'-t_0+\tau+T+t)^2\right)\exp\left(\mathrm{i}\omega_0(t'-\gamma_0(t_0+\tau+T+t)) - \mathrm{i}\varphi_4\right),
\end{aligned} \tag{4.8}$$

where t_0 is an offset (set to 100 fs), τ, T, and t are the interpulse delays, which are sampled identical to the experimental parameters, ω_0 is the central frequency (3.19 rad/fs, corresponding to 2.10 eV), and τ_p is the pulse duration given by the intensity full width at half maximum, which is set to 17 fs. The parameter γ_0 is set to zero (fully rotating frame), allowing to take larger sampling steps like in the experiment. We employ a six-level energy level scheme, representing a model with three electronic states, where each state is coupled to a single vibrational mode with an energy of 0.17 eV, assuming equal vibrational frequencies in all electronic states (see Fig. 4.2b in the main manuscript). The model neglects solvent and dynamic Stokes shift effects as well as possible singlet fission mechanisms. It was previously reported that TIPS-pentacene exhibits singlet fission in highly concentrated solutions [232]; however, even if we assume that such a process could be present in the dianionic tetraaza-compound, it is improbable regarding the comparably low concentration regime (0.4 mM) we used in our experiment.

For calculating the transition dipole moments, we estimate the Huang–Rhys factor S_{HR} of the 0.17 eV mode that is coupled to the $S_0 \rightarrow S_1$ transition to be 0.6 from linear absorption data. The transition dipole moments μ_{nm} between electronic level pairs $|a_n\rangle$ and $|b_m\rangle$ with vibrational quanta n and m are thereby defined as [233]

$$\mu_{b_0 a_0} = \mu \, \exp\left(-S_{\mathrm{HR}}/2\right), \tag{4.9}$$

$$\mu_{b_1 a_0} = \mu_{b_0 a_1} = \sqrt{S_{\mathrm{HR}}}\mu \, \exp\left(-S_{\mathrm{HR}}/2\right), \tag{4.10}$$

$$\mu_{b_1 a_1} = \left(1 - S_{\mathrm{HR}}\right) \mu \, \exp\left(-S_{\mathrm{HR}}/2\right), \tag{4.11}$$

with an "overall" transition dipole moment μ. In order to estimate S_{HR} of the same mode coupled to the $S_1 \rightarrow S_{74}$ transition, we carry out a screening of S_{HR} until best agreement between the experimental and the simulated 1Q–2Q–1Q 3D spectrum is achieved, where we vary S_{HR} from 0.6 to 0.05 in steps of 0.05. A S_{HR} of 0.05 reproduces the 3D solid best, especially the amplitude of the shoulder above 4.10 eV along the 2Q axis (see Fig. 4.4 in the main manuscript). Further, we scale the strengths of the $|e_n\rangle \rightarrow |f_n\rangle$ transitions relative to the $|g_n\rangle \rightarrow |e_n\rangle$ transitions according to the ratio of oscillator strengths f as received from the TD–DFT calculation (see Sec. 4.5.7),

$$\frac{f_{S_0 \rightarrow S_1}}{f_{S_1 \rightarrow S_{74}}} = \frac{|\mu_{eg}|^2}{|\mu_{fe}|^2}, \tag{4.12}$$

which leads to $\mu_{fe} = 0.64 \; \mu_{eg}$. The resulting transition moments are summarized in Table 4.2.

We employ a ladder-type population relaxation down to the global ground state $|g_0\rangle$, where we set the relaxation constant of $|e_0\rangle$ to lower states to 6.1 ns according to the

experimentally determined fluorescence lifetime of the molecule [220]. For internal conversion, we assume a 100 fs relaxation time where we further estimate a 6 ps relaxation time for vibrationally excited populations in each electronic state.

The general procedure for estimating the pure dephasing times is as follows. First, a minimal four-level system with the levels $|g_0\rangle$, $|g_1\rangle$, $|e_0\rangle$, and $|e_1\rangle$ is considered and the rephasing and nonrephasing 1Q–0Q–1Q signals are simulated and compared to the experimental result. A manual adjustment of the pure 1Q dephasing time in steps of 10 fs is then performed until best agreement with experimental data. This value is also used as a starting value for the dephasing time of coherences between the $|e_n\rangle$ and $|f_n\rangle$ as well as the $|g_n\rangle$ and $|f_n\rangle$ manifold. Then, a comparison between experimental and simulated 1Q–2Q–1Q 3D spectra is used as an additional feedback for the iterative manual refinement of the $|f_n\rangle\langle e_n|$ and $|f_n\rangle\langle g_n|$ dephasing times, leading to the parameters given in Table 4.2. All calculations were conducted on a CPU cluster with 72 cores and 1 TB RAM using the parallel computing toolbox in MatLab R2018a, where the calculation for each pulse sequence is conducted separately on a single core, so that a full simulation dataset is generated in approximately 2 hours.

Table 4.2. Simulation parameters. Table showing transition moments and pure dephasing times between the states employed in the model. Reproduced from Ref. [4].

Transition moments					
$S_0 \rightarrow S_1$		$S_1 \rightarrow S_{74}$		$S_0 \rightarrow S_{74}$	
$\mu_{e_0g_0}$	0.74	$\mu_{f_0e_0}$	0.62	$\mu_{f_0g_0}$	0
$\mu_{e_1g_0}$	0.57	$\mu_{f_1e_0}$	0.14	$\mu_{f_1g_0}$	0
$\mu_{e_0g_1}$	0.57	$\mu_{f_0e_1}$	0.14	$\mu_{f_0g_1}$	0
$\mu_{e_1g_1}$	0.27	$\mu_{f_1e_1}$	0.59	$\mu_{f_1g_1}$	0
Pure dephasing time constants					
$\|e_n\rangle\langle g_n\|$	90 fs	$\|f_n\rangle\langle e_n\|$	300 fs	$\|f_n\rangle\langle g_n\|$	100 fs

4.5.7 Quantum-Chemical Calculations

In order to evaluate the origin of the two-quantum (2Q) resonance at 4.10 eV in the 2Q-associated 3D spectra, we performed quantum chemical calculations by using density functional theory (DFT) and time-dependent density functional theory (TD–DFT). All calculations were carried out with the Gaussian program package [234]. The ground state

equilibrium structure of TIPS–TAP^{2-} was optimized with DFT/CAM-B3LYP/6-311G** and employing a polarizable continuum solvent model for tetrahydrofuran (THF) solvation. TD–DFT calculations were performed on the optimized structure with BLYP functional and 6-31+G* basis set for the first 100 vertical transitions ($S_0 \rightarrow S_n$). Subsequently, $S_1 \rightarrow S_n$ transitions were obtained by computing transition dipole moments between excited states. In the $S_0 \rightarrow S_n$ spectrum (Fig. 4.14), the $S_0 \rightarrow S_1$ transition energy (590 nm, 2.10 eV) is in good agreement with the experimentally observed peak (602 nm, 2.06 eV). There are some higher excited states with nonzero oscillator strength. However, at nearly twice the energy of the $S_0 \rightarrow S_1$ transition (295 nm, 4.20 eV) there is no transition with significant oscillator strength present in the calculation which is analogous to experimental observations. Thus, this reflects that the experimentally observed 2Q state at 4.10 eV is unlikely to be excited via a single one-photon transition due to inversion symmetry of the molecule.

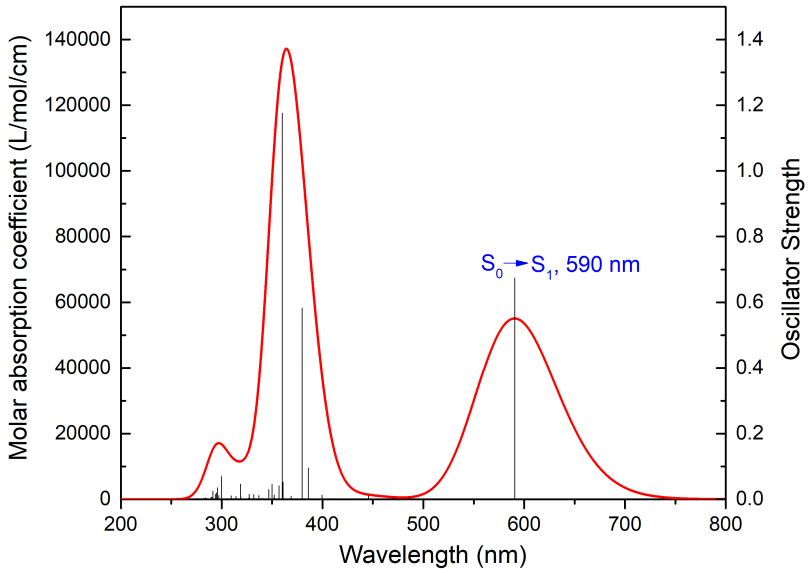

Figure 4.14. Calculated $S_0 \rightarrow S_n$ ($n = 1, ..., 100$) absorption spectrum of TIPS–TAP^{2-}. The spectrum is broadened using Gaussian functions with a full width at half maximum of 0.33 eV. Reproduced from Ref. [4].

In contrast, the $S_1 \rightarrow S_n$ absorption spectrum (Fig. 4.15) features a transition into S_{74} (579 nm, 2.14 eV) with relatively high oscillator strength at nearly the same energy as the $S_0 \rightarrow S_1$ transition. There is also a second optically bright transition at 1157 nm (1.07 eV) which is not of relevance within our experiments because it is not covered by the employed laser spectrum. Hence, we conclude that the 2Q resonance at 4.10 eV in the 3D spectra origins from S_{74} which is only accessible via two consecutive one-photon

transitions $S_0 \rightarrow S_1 \rightarrow S_{74}$. The calculated oscillator strength of the direct $S_0 \rightarrow S_{74}$ one-photon transition is zero which further underlines that S_{74} is a two-photon allowed but a one-photon forbidden electronic state.

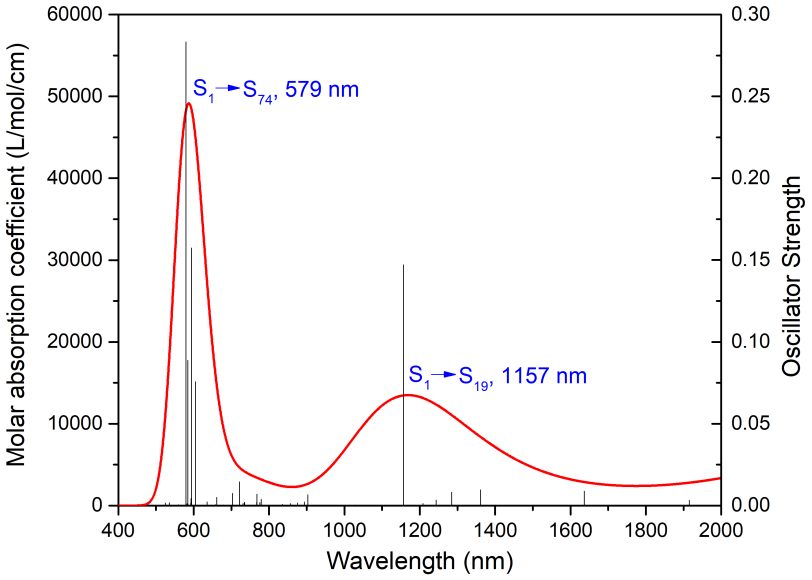

Figure 4.15. Calculated $S_1 \rightarrow S_n$ ($n = 2, ..., 100$) absorption spectrum of TIPS–TAP^{2-}. The spectrum is broadened using Gaussian functions with a full width at half maximum of 0.33 eV. Reproduced from Ref. [4].

4.5.8 Experimental and Simulated Rephasing Fourth- and Sixth-Order 2D Spectra

Figure 4.16 shows a comparison between experimental (top row) and simulated (bottom row) rephasing 1Q–1Q (left column) and rephasing 2Q–1Q (right column) 2D spectra at $T = 18$ fs. While the rephasing 1Q–1Q spectrum has a predominant negative signal, which corresponds to a fourth-order response, the rephasing 2Q–1Q spectrum is opposite in sign because it stems from a sixth-order response. Both lineshapes are phase-twisted and elongated along the diagonal line as typical for rephasing signals. While in the fourth-order process, 1Q coherences are rephased to each other, in the sixth-order process the 2Q coherence is rephased after conversion into a 1Q coherence, thus both the 1Q and 2Q inhomogeneity are convoluted into the response [57]. We observe that the antidiagonal linewidth is similar in both spectra, indicating that the 2Q states do not contribute any substantial inhomogeneity in addition to the pure 1Q inhomogeneity. When further comparing the spectra, the largely different Huang–Rhys factors between different electronic states (see also Sec. 4.5.6) is reflected by means of different peak

amplitudes of the sidepeaks in the 1Q and 2Q domain. These cross peaks correspond to coupling to vibrationally excited states. The cross peak at $(\hbar\omega_\tau, \hbar\omega_t) = (2.06, 2.23)$ eV in the fourth-order signal is much lower in amplitude than the cross peak at $(4.27, 2.23)$ eV. At first glance, this seems contradictory though, however, one must take into account that the laser spectrum has its maximum amplitude at 2.10 eV (see Fig. 4.2a in the main manuscript). Thus, in the two-photon domain, 2Q features in the vicinity of twice that energy will be enhanced compared to 2Q resonances at lower energies. This is further increased because of an overall six-fold multiplication of the laser spectrum into the signal.

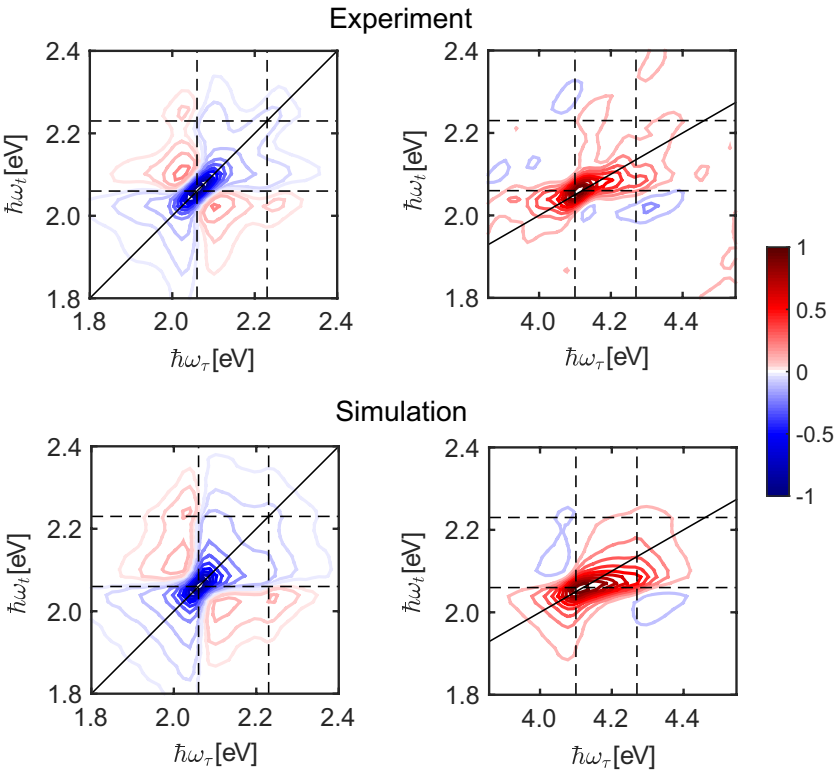

Figure 4.16. Rephasing fourth- and sixth-order 2D spectra of TIPS–TAP^{2-} in THF. Experimental (top) and simulated (bottom) real-valued fourth-order rephasing 1Q–1Q (left column) and sixth-order rephasing 2Q–1Q (right column) 2D spectra, shown at $T = 18$ fs each. All spectra are normalized to their respective maximal absolute value. Contour lines are drawn at identical values in both experimental and simulated spectra. Black dashed lines denote the energies of the $|e_v\rangle$ and $|f_v\rangle$ states that are considered in the model. Reproduced from Ref. [4].

4.5.9 Many-Particle Excitations

In a recent communication, it was shown that to achieve many-particle signal detection of non-interacting particles, phase-sensitive detection such as phase cycling, phase

modulation or photon coincidence detection can be utilized [79]. In this respect, the detection of fluorescence of N non-interacting particles, excited by a pair of pulses with mutual phase $\varphi_{21} = \varphi_1 - \varphi_2$ and separated by delay T, is considered. By extracting, for instance, from the detected fluorescence the part oscillating at $\pm\varphi_{21}$ over T, the discussion can be restricted to the observation of two-particle operators. Starting from a single particle with a ground state $|g\rangle$ and an excited state $|e\rangle$, we can thus formulate a two-particle system in a collective basis with the resulting energy-level scheme depicted in Fig. 4.17a. In the language of Liouville-space pathways, the contributions oscillating at $\pm 2\varphi_{21}$ correspond to the pathways where both particles j and k are in the optical coherence during T, which is expressed as the two-quantum coherence $|e_j e_k\rangle\langle g_j g_k|$ in Fig. 4.17b–e. Within the two-particle basis, the two-particle projection operators can be expressed as:

$$A_{jk}^{ee} = |e_j\rangle\langle e_j| \otimes |e_k\rangle\langle e_k|\,, \tag{4.13}$$

$$A_{jk}^{eg} = |e_j\rangle\langle e_j| \otimes |g_k\rangle\langle g_k|\,, \tag{4.14}$$

$$A_{jk}^{ge} = |g_j\rangle\langle g_j| \otimes |e_k\rangle\langle e_k|\,, \tag{4.15}$$

$$A_{jk}^{gg} = |g_j\rangle\langle g_j| \otimes |g_k\rangle\langle g_k|\,, \tag{4.16}$$

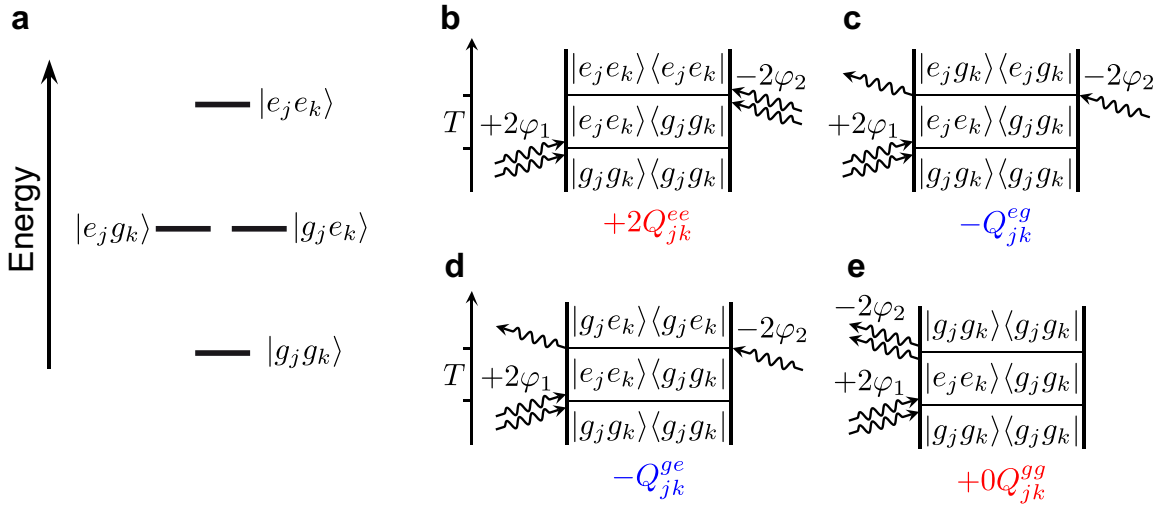

Figure 4.17. Many-particle excitation pathways. (a) Energy-level scheme of two non-interacting two-level systems in a collective basis. (b–e) Double-sided Feynman diagrams that can be accessed by extracting a signal contribution oscillating with $+2\varphi_{21}$ over T by a two-pulse experiment with fluorescence detection. Here, pathways that result from all possible two-particle projection operators are drawn, where the respective fluorescence yield is indicated by a prefactor denoted at the bottom of each diagram. Reproduced from Ref. [4].

where the resulting double-sided Feynman diagrams are shown in Fig. 4.17b–e, respectively. In Ref. [79], it is argued that the only operator observed is A_{jk}^{ee} which corresponds to pathway Q_{jk}^{ee} in Fig. 4.17b. In that case, both particles are in their excited state which results in a weight of two because of the emission of two photons by fluorescence. We believe that it depends on the type of detection which two-particle operators are observed. While in the case of two-photon coincidence detection, contributions from only Q_{jk}^{ee} could indeed be observed. In the case of conventional, non-coincidence, fluorescence detection as in the present work, we also detect one-photon contributions, that is, A_{jk}^{ee}, A_{jk}^{eg}, and A_{jk}^{ge} all contribute. Depicting the respective parts of the response by Liouville-space pathways, we find that while Q_{jk}^{ee} contributes with $+2$, Q_{jk}^{eg} and Q_{jk}^{ge} contribute each by -1 (Q_{jk}^{gg} does not contribute at all because A_{jk}^{gg} projects to the ground state of both particles which does not generate any fluorescence). As a result, the pathways cancel each other, leaving no contribution from the multi-particle states.[4] In Ref. [79], this issue is addressed in the discussion in the last paragraph, arguing that the two-particle contribution does not affect the one-particle fluorescence. Our argumentation is not in contradiction with this statement; we rather argue that one has to consider all observable two-particle operators and not select just one of them.

The assertions made above can directly be transferred to the case of our sixth-order signals where the respective diagrams would display extended versions in terms of additional delays and pulses of those depicted in Fig. 4.17b–d. Formulating, e.g., the sixth-order rephasing 2Q–0Q–1Q pathways by employing a collective basis and the two-particle projector A_{jk}^{ee}, the sign of the resulting pathway would be negative (that is, because of four interactions from the right in the corresponding double-sided Feynman diagrams, giving an initially positive sign which is then multiplied by the prefactor of $\mathrm{i}^6 = -1$ from the perturbative expansion). In our experiment, however, we observe a positive phase in the real part of the sixth-order signals which can only be explained by considering single-particle excitations, as it is displayed by the double-sided Feynman diagram of Fig. 4.6d of the main manuscript. Moreover, for our simulations we explicitly formulate our model in a single-particle basis and use parameters from TD–DFT calculations that confirmed the presence of a single-particle doubly excited state $|f\rangle$. Regarding the excellent agreement with the simulation (see manuscript Fig. 4.5), we

[4] Kühn, Mančal and Pullerits concluded one year later that a similar pathway cancellation effect leads to vanishing cross peaks in the nonrephasing 1Q–0Q–1Q signal. They considered the example of two independent chromophores with different energies of their singly excited states [77]. In the present case, however, we consider 2Q-type signals, such as the 2Q–0Q–1Q signal, which *are* cross-peak signals. Thus, as a general conclusion, *all* cross-peak signals vanish for independent two-level chromophores.

conclude that the single-particle model is fully valid.

In conclusion, many-particle excitations do not contribute to the signals we acquired in our experiment because of complete cancellation of pathways corresponding to the complete manifold of two-particle projection operators. Thus, our signals must stem from microscopic quantum coherence of individual molecules that can be described in a single-particle basis as it is treated in the main manuscript.

4.5.10 Cancelling Sixth-Order Rephasing 2Q–0Q–1Q Pathways

We show double-sided Feynman diagrams of the rephasing 2Q–0Q–1Q process that probe 0Q coherence within the 2Q state over T in Fig. 4.18. It is evident that each positive diagram has an oppositely signed pendant. These two diagrams only differ in their final population state. As noted in the main manuscript, internal conversion from the 2Q-excited states to the 1Q-excited states leads to $\Phi_e = \Phi_f$, meaning that each diagram contributes with equal magnitude to the signal. Thus, both the dynamic evolution of the $|f_1\rangle\langle f_0|$ (highlighted in red) and $|f_0\rangle\langle f_1|$ (highlighted in blue) coherences cannot be probed because the underlying pathways cancel in pairs. This is also valid for diagrams that contain the population density matrix elements $|f_0\rangle\langle f_0|$ and $|f_1\rangle\langle f_1|$ over T (not shown).[5]

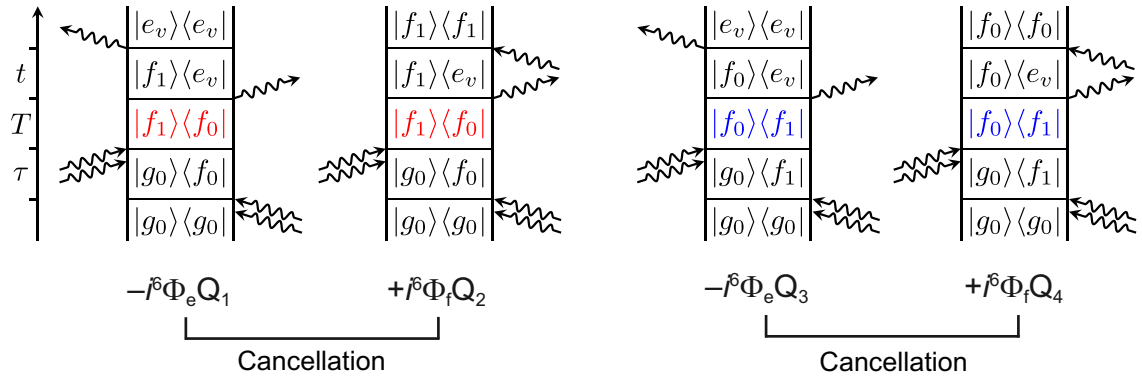

Figure 4.18. Cancelling sixth-order diagrams. Double-sided Feynman diagrams are displayed of the sixth-order rephasing 2Q–0Q–1Q process that include 0Q coherence between vibrational levels of the 2Q state (highlighting in red and blue denotes positive and negative oscillation frequency, respectively). Due to internal conversion, the pathway-specific quantum yields are $\Phi_e = \Phi_f$, so that the diagrams Q_1 and Q_2 as well as Q_3 and Q_4 cancel in pairs. Reproduced from Ref. [4].

[5]The situation is different in case of ultrafast exciton–exciton annihilation in a molecular dimer, which leads to the emergence of an additional pathway including the annihilation dynamics of the biexciton state, as further discussed in Chapter 5.

4.5.11 Simulated Fourth- and Sixth-Order 0Q Transients

In order to evaluate the phase-shifted 0Q coherence dynamics from fourth-order rephasing 1Q–0Q–1Q and sixth-order rephasing 2Q–0Q–1Q contributions in Fig. 4.6 of the main manuscript, we show the respective result from a simulation in Fig. 4.19, where we employed 43 steps along T in order to receive higher-resolved transients. The transients were taken at above-diagonal cross-peak positions in the 1Q–1Q and 2Q–1Q 2D projections of the 3D contributions, which is identical to those positions taken in the experimental ones. The same oscillation period ≈24 fs and the π phase shift between the transients of different orders are in excellent agreement with experimental observations.

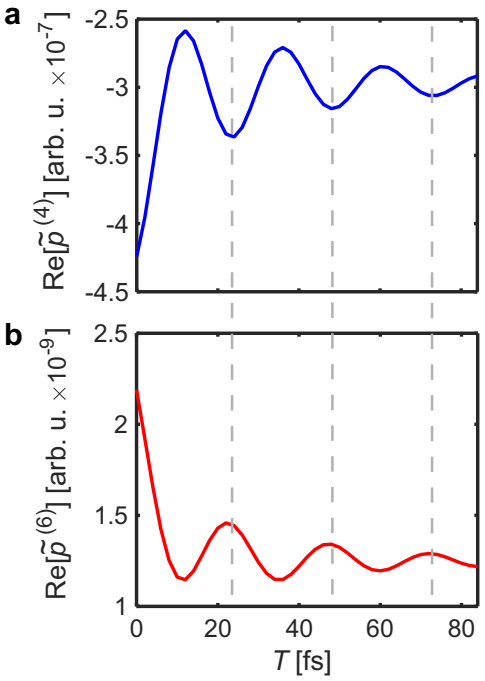

Figure 4.19. Simulated fourth- and sixth-order 0Q coherence dynamics of TIPS–TAP^{2-}. The real-valued 0Q coherence signatures over T which are received from (a) the simulated fourth-order rephasing 1Q–0Q–1Q $\left(\tilde{p}^{(4)}\right)$ and (b) sixth-order rephasing 2Q–0Q–1Q contributions $\left(\tilde{p}^{(6)}\right)$ show a π phase shift. Reproduced from Ref. [4].

Chapter 5

Fluorescence-Detected Exciton–Exciton-Interaction Two-Dimensional Spectroscopy

---

Interactions between photoexcited charge carriers influence the conversion efficiency of light into electrical energy. Under high irradiance, multiple excitons form within a complex, they diffuse through the system and when they meet, they may annihilate, leading to less excitons in the system. This process, also known as exciton–exciton annihilation, poses a loss mechanism that reduces efficient light harvesting. Spectroscopic characterization of these multiexciton-related dynamics is challenging, since signals from single-exciton dynamics strongly contribute to the nonlinear response. In this respect, coherently detected exciton–exciton interaction two-dimensional (EEI2D) spectroscopy has proven to be suitable to isolate signals stemming from the dynamics of exciton–exciton annihilation. Nonetheless, this technique has the drawback that ultrafast annhilation events may be obscured by early-time coherent artifacts and nonresonant response. In this chapter, a novel approach to EEI2D spectroscopy is introduced that employs fluorescence detection. This fluorescence-detected EEI2D (FDEEI2D) spectroscopy is suitable to directly temporally resolve sub-100 fs annihilation dynamics due to the exclusion of nonresonant signals. The developed approach is based on a specific post-processing routine of two different sixth-order nonlinear signals that are acquired by four-pulse sequences with 125-fold phase cycling. It is investigated how annihilation dynamics manifest in sixth-order nonlinear signals. After introducing the theoretical concept, FDEEI2D spectroscopy is experimentally demonstrated by measuring ultrafast exciton–exciton annihilation in a squaraine heterodimer. It is shown that the obtained results agree well with that of a coherently detected EEI2D experiment.

5.1 Introduction

5.1.1 Exciton–Exciton Annihilation

Under high light irradiance, the interaction between multiple excitons poses an important aspect for light-harvesting systems, both for natural complexes and for their artifical imitator devices. This is because these interactions strongly affect the energy transfer dynamics and, in turn, how efficiently photon energy is converted into electrical energy [102, 235]. Once multiple excitons are generated due to high light irradiance, the interaction between these excitons depends, among other factors, strongly on the coupling between the individual system subunits, the degree of exciton mobility as well as the spatial dimensions of the system [66, 102]. We have seen in Chapter 3 on the example of confined nanosystems, that this interaction can be quasi-static, that is, the excitons (which are generated within the same spatial volume) form a long-living, stable particle complex immediately after photoexcitation, which can be characterized by an interaction energy. However, in more extended systems in which multiple absorbing units are in close proximity to each other, like molecular aggregates, there is a probability that multiple excitons may be photogenerated in a large distance to each other. These excitons may then diffuse through the system and when they meet, they interact and may ultimately annihilate, leading to less excitons in the system. This interaction process, also known as exciton–exciton annihilation (EEA), predominantly poses a mechanism that reduces efficient conversion of excitation quanta into electrical energy. In contrast to Chapter 3, this chapter thus focuses on the *dynamics* of the interaction between multiple excitons, rather than the interaction strength.

Microscopically, the process of EEA is described as the fusion of at least two excitons with the direct consequence of resonant energy transfer to a single site, followed by nonradiative relaxation within this site [236]. This process can be illustrated by a dimer consisting of two molecules "A" and "B" in the basis of localized states, which describe excitations residing on specific molecular sites (site basis), as shown in Fig. 5.1, left [7, 235]. Each molecule has a ground state $|g_N\rangle$, a singly excited state $|e_N\rangle$ and a higher excited state $|f_N\rangle$, where $N \in \{\mathrm{A}, \mathrm{B}\}$. As we will focus on heterodimers in this chapter, let us consider that A and B correspond to different molecules, such as the squaraines "SQA" and "SQB," respectively, and thus have distinct transition frequencies. Now we consider that both sites are simultaneously excited to their $|e_N\rangle$ states (e.g., by absorption of two photons). As there is an interaction between the molecules, the presence of one exciton has a direct effect on the other one [102]. Depending on the size of the interaction radius and the spatial extent of the system, there might be a diffusion

process before the actual exciton fusion process (not shown). However, in case of our small heterodimer, the diffusion process is not existent and the fusion process can be considered as an instantaneous event [237]. Once the excitons fuse, the total excitation energy is resonantly transferred to an $|f\rangle$ state of one of the molecules, depending on which site the fusion took place, whereas the other molecule is de-excited to the ground state. In Fig. 5.1, we exemplarily consider that energy is transferred to molecule A. The annihilation process is then completed by nonradiative relaxation within the single site, arriving at just one singly excited molecule (Fig. 5.1, middle). Note that, in an exciton–exciton annihilation process, an excitation quantum is not annihilated in the literal sense of the wording, but rather dissipated into heat.

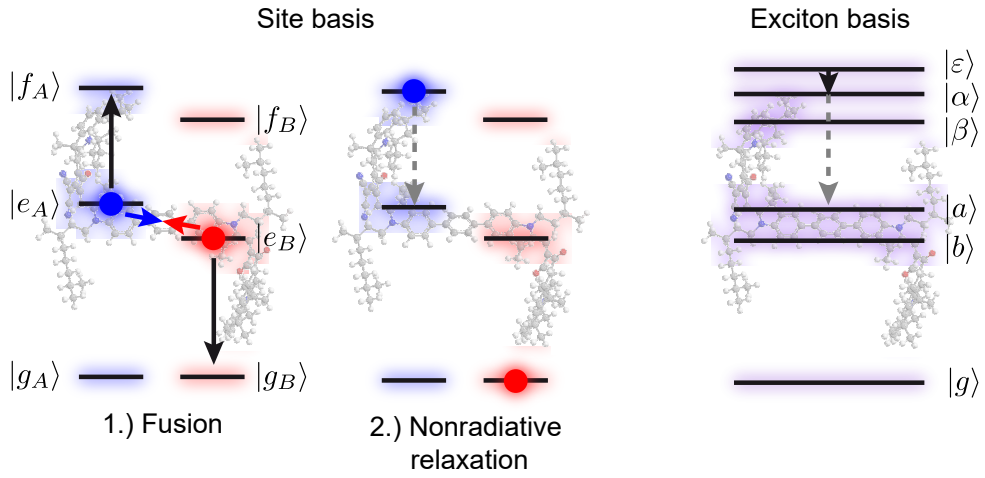

Figure 5.1. Exciton–exciton annihilation in a heterodimer. Two covalently coupled molecules A (blue) and B (red) can be described by using the localized site basis with electronic states $|g_N\rangle$, $|e_N\rangle$, and $|f_N\rangle$ (left). Exciton–exciton annihilation can then be depicted as a two step process – first, two excitations, which reside on different molecules, instantaneously fuse. Resonant energy transfer leaves one molecule in a high excited state, while the other one is transferred to its ground state (black arrows). Second, nonradiative relaxation (gray dashed arrow) leads to one remaining exciton. The same process can be depicted in the delocalized exciton basis (right), where $|a\rangle$ and $|b\rangle$ denote single-exciton states and greek letters signify doubly excited states. In the exciton basis, the biexciton state $|\varepsilon\rangle$ transfers energy to the high excited state $|\alpha\rangle$, followed by internal conversion into $|a\rangle$.

For purposes of spectroscopy and theoretical modeling, it is adequate to use the basis of delocalized exciton states (exciton basis), as we will do in the following. Let us again consider the same heterodimer as above, but we now distinguish between a single ground state $|g\rangle$, the singly excited manifold consisting of $|a\rangle$ and $|b\rangle$ as well as the doubly excited manifold which comprises $|\alpha\rangle$, $|\beta\rangle$, and $|\varepsilon\rangle$ (Fig. 5.1, right). In the exciton basis, the states $|a\rangle$ and $|b\rangle$ are single-exciton states with predominant localization on a specific site, the extent of which is determined by the coupling strength between the

molecules and the energy difference between the singly excited states of the monomers [238]. Analogously, higher excited states with predominant localization on one of the monomers are denoted by $|\alpha\rangle$ and $|\beta\rangle$. In addition, the simultaneous excitation of both sites gives rise to a delocalized biexciton state $|\varepsilon\rangle$. The exciton fusion and resonant energy transfer step is then rather indicated by a single arrow that denotes an energy transfer from the biexciton state to one of the states within the doubly excited manifold [218]. Consecutive nonradiative relaxation (internal conversion) from the doubly to the singly excited manifold then embodies exciton "loss" through dissipation.

On the one hand, such an effective loss of an excitation quantum can be viewed as an undesired mechanism which reduces the conversion efficiency of light into electrical energy, on the other hand, this mechanism can be considered as deliberately efficient dissipation that down-regulates excitation caused by an undesirable excess of photons. Nonetheless, one has to take into account that in natural light-harvesting complexes, the annihilation of excitons takes place under rather "unnatural" conditions [239, 240]. Especially in such extended systems, however, it takes some time until some excitons fuse, which is significantly determined by the exciton diffusion constant. Consequently, by studying exciton annihilation dynamics, one can also ascertain quantitative information about exciton migration [102, 239, 241]. From a general point of view, measuring annihilation dynamics therefore allows us to derive structure–property relationships, knowledge of which enables us to ultimately realize artificial, loss-free energy transfer on a molecular scale. Essentially, characterizing the interactions between excitons is a key competence that helps to understand how to get the most out of sunlight, something nature has been doing with unprecedented efficiency for millions of years.

5.1.2 Measuring Annihilation Dynamics

As indicated in Fig. 5.1 (right), the key to measure exciton–exciton annihilation is to probe the dynamical evolution of the biexciton state $|\varepsilon\rangle$. For that purpose, one needs to interrogate a biexciton population. To accomplish this experimentally, the first step is to create the biexciton population by four interactions with a light field (that is, by two interactions from both the right and the left side on the ground-state population density matrix element $|g\rangle\langle g|$). Second, in order to induce a detectable coherent signal field, an additional interaction after some delay T is required. Thus, the lowest order of nonlinearity needed for the direct observation of EEA is five.

Earlier spectroscopic studies about EEA usually involved pump–probe spectroscopy [242–245]. In these experiments, the fifth-order biexciton-associated EEA dynamics are measured indirectly, that is, as a signal contamination of the dominant third-order

single-exciton-associated signal. This means, in the transient absorption spectra, EEA manifests as an intensity-dependent component, which has a faster time constant than the single-exciton lifetime [242, 245, 246].

An approach with enhanced selectivity is population-period transient spectroscopy (MUPPETS) [247]. A MUPPETS experiment can be viewed as a fifth-order "pump–pump/dump–probe" experiment, where the use of the additional "pump/dump" pulse pair gives rise to two population times. In addition to the possibility to separate homogeneous and heterogeneous rate dispersion [248, 249], the use of two population times allows one to separate single-exciton and biexciton dynamics [247]. However, since MUPPETS does not scan coherence times, it is not sensitive to the frequencies and spectral correlations of the biexciton manifold. Moreover, the emergence of a MUPPETS signal is not unique to EEA because pump–dump processes can not be excluded, and even systems without biexciton states already give rise to a signal [102, 250].

As the most selective approach, one can employ fifth-order 2D spectroscopy to "spectrally" separate the EEA dynamics from the undesired single-exciton dynamics *and* to access spectral correlations within the biexciton manifold. [7, 66, 102, 103, 241, 251]. The "spectral" discrimination is achieved by scanning a coherence time between the first two pairs of light-field interactions, with which one can distinguish between 1Q and 2Q excitation, whereas the latter is exclusive to the fifth-order signal.

The fifth-order excitation sequence is schematically shown in Fig. 5.2a. The first pulse pair is separated by delay τ, followed by a third pulse delayed with T. The first pulse interacts twice and prepares 2Q coherences of the doubly excited manifold with the ground state, which oscillate at roughly two times the single-exciton energies (Fig. 5.2b). Then, a biexciton (and/or doubly excited state) population is induced by a second double-interacting pulse, and this population evolves over T (Fig. 5.2a, yellow). In principle, it is also possible to create single-exciton populations (Fig. 5.2a, light blue), however, it can be shown that the underlying pathways cancel each other out [102, 103]. A subsequent single light-field interaction by $\mathbf{k}_3$ converts the population into a 1Q coherence, that itself is radiative and thus emits the nonlinear signal during t, which can finally be interferometrically measured by a local oscillator on a spectrometer. According to the species of quantum coherences evolving over τ, T, and t, this fifth-order signal can be classified as a 2Q–0Q–1Q-type signal. In particular, two fifth-order 2Q–0Q–1Q signal contributions can be distinguished according to their wave vectors – the rephasing 2Q–0Q–1Q contribution with $-2\mathbf{k}_1 + 2\mathbf{k}_2 + \mathbf{k}_3$, and the nonrephasing 2Q–0Q–1Q contribution with $+2\mathbf{k}_1 - 2\mathbf{k}_2 + \mathbf{k}_3$. In both contributions, the desired information about EEA is contained within the evolution of the biexciton manifold over T.

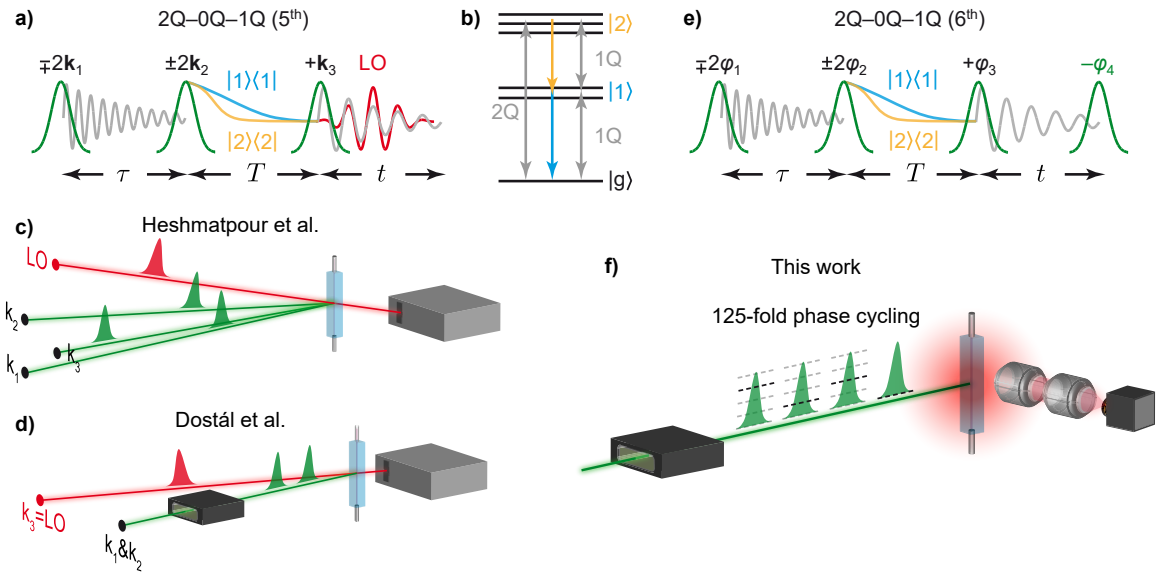

Figure 5.2. Accessing biexciton dynamics by higher-order 2D spectroscopy. (a) Scheme of the coherently detected fifth-order 2Q–0Q–1Q signal. Each pulse interacts with a wave vector $\mathbf{k}$. (b) Energy level scheme of a system consisting of a ground state $|g\rangle$, a single-exciton manifold $|1\rangle$, and a biexciton manifold $|2\rangle$. Gray double arrows denote coherences whereas yellow and blue arrows signify single-exciton and biexciton population transfer, respectively. Biexciton dynamics can experimentally be measured by using (c) a pulse-shaper-assisted pump–probe geometry [102], where the fifth-order signal is self-heterodyned with the third pulse, or (d) in a fully noncollinear geometry [251], where the local oscillator (LO) is a separate pulse. (e) Scheme of the fluorescence-detected sixth-order 2Q–0Q–1Q signal, which is the fluorescence-detected analog of the fifth-order 2Q–0Q–1Q signal. Here, each pulse interacts with a phase φ_k. (f) The experimental approach developed in this work utilizes 125-fold phase cycling of fully collinear four-pulse sequences and fluorescence detection to access the biexciton dynamics. Adapted in part and modified from Ref. [2].

Experimentally, such fifth-order signals can be measured in a fully non-collinear geometry with heterodyne detection, as proposed by Brüggemann and Pullerits [252] and implemented by Heshmatpour et al. [251] (Fig. 5.2c), or in a pump–probe geometry with self-heterodyned detection, as experimentally realized by Dostál et al. [102] (Fig. 5.2d). The pump–probe 2D approach offers the advantage of inherent phasing together with the simultaneous acquisition of purely absorptive third- and fifth-order 2D signals. In contrast, using a fully noncollinear setup, rephasing and nonrephasing signals must be measured separately by altering the time ordering of the excitation pulses [61]. Further, a phasing procedure is required to obtain the phase information of the signals. While third-order signals are usually phased with aid of a separate pump–probe measurement, it is more challenging to phase 2Q-associated signals [39] and in particular fifth-order signals. Concerning the latter, one possible approach is to phase the coherently detected 2Q–0Q–1Q signal to a pump–dump–probe experiment [251]. Both the fully noncollinear

and the pump–probe approach have the advantage that the fifth-order signal is highly selective to EEA, that is, they feature background-free signatures [102, 103, 251]. As a disadvantage, however, the detection of a coherent signal makes the methods prone to contamination with nonresonant signals, which especially occur at early population times.

In a similar fashion, one can seek to access biexciton dynamics using fluorescence-detected 2D spectroscopy. It was previously suggested to utilize time-gating of the fluorescence stemming from fourth-order 1Q–0Q–1Q signal contributions to isolate the annihilation dynamics [76, 218]. However, since 2Q coherences can not be probed, such a signal does not facilitate one to directly spectrally resolve the manifold of doubly excited states, but especially couplings within this manifold pose an important aspect for EEA. Moreover, in view of the moderate fluences needed to induce EEA, fourth-order signals can be contaminated by sixth-order signals which generally complicates the interpretation.

Analogous as in the case with coherent detection, it can be expected that selective information about EEA can be accessed by isolating the higher-order response using fluorescence detection. Thus, the sixth-order 2Q–0Q–1Q signal (Fig. 5.2e) is expected to contain analogous information like the fifth-order 2Q–0Q–1Q signal [4]. The close analogy of these signals becomes clear when comparing Figs. 5.2a und 5.2e. Both experiments probe the same coherences and populations and merely differ in the final signal generation and detection. We can also distinguish between the rephasing and nonrephasing signals via their phase signatures $-2\varphi_1 + 2\varphi_2 + \varphi_3 - \varphi_4$ and $+2\varphi_1 - 2\varphi_2 + \varphi_3 - \varphi_4$, respectively. Indeed, because the sixth-order 2Q–0Q–1Q signal also probes doubly excited populations, the prerequisites for the measurement of EEA are in principle given. However, as it will be analyzed in the next section, it turns out that the sixth-order 2Q–0Q–1Q signal has insufficient selectivity towards EEA, as this signal contains a "background" which contains single-exciton dynamics as well. Nonetheless, by using the approach developed in the previous chapter, we take advantage of the fact that with 125-fold phase cycling, we can measure different 2Q-associated sixth-order signals under identical experimental conditions (Fig. 5.2f). This provides the foundation to develop an approach which will be introduced as "fluorescence-detected exciton–exciton interaction 2D" (FDEEI2D) spectroscopy in the following. It will be shown that FDEEI2D spectroscopy eliminates unwanted contributions – including nonresonant signals – by subtracting specific sixth-order signals to ultimately yield EEA-exclusive information. Noteworthily, FDEEI2D spectroscopy only operates with a single excitation beam, which poses a significant technical advantage.

In the next section, the theoretical concept of FDEEI2D spectroscopy is discussed. The approach is introduced as a means to study ultrafast EEA in molecular dimers. FDEEI2D spectroscopy is then experimentally demonstrated in Sec. 5.3 on a squaraine heterodimer. The signal obtained is verified with aid of the previously established approach of coherently detected EEI2D spectroscopy. In fact, coherently detected EEI2D and FDEEI2D spectroscopy are experimentally closely related to each other, as both techniques require pulse shaping (compare Figs. 5.2d and 5.2f). Hence, both experiments are performed within a single setup using common beam paths and optics.

5.2 Theoretical Concept

In this section, we shall analyze the sixth-order 2Q–0Q–1Q signal in more detail and, in this respect, to what extent EEA contributes to this signal. Then, we discuss how we can isolate the EEA dynamics by the construction of the FDEEI2D signal. To this end, a mathematical expression for the FDEEI2D signal is derived.

As we have seen in Chapter 1, the use of response functions allows us to dissect a nonlinear signal contribution into the individual excitation pathways. This in turn enables one to trace the dynamical evolution of concatenated density matrix elements resulting from a multipulse excitation field. Let us now dissect the rephasing sixth-order 2Q–0Q–1Q signal (Fig. 5.2e). Let us further consider a heterodimer in the exciton basis, which was introduced in Fig. 5.1. For the sake of simplicity, we use the manifold notation "$|2\rangle$" as a generalization of the doubly excited states, i.e., $|2\rangle \in \{|\alpha\rangle, |\beta\rangle, |\varepsilon\rangle\}$, while retaining the individual states $|a\rangle$ and $|b\rangle$ of the single-exciton manifold (Fig. 5.3a). We assume weak electronic coupling between the monomers, which leads to $\mu_{2b} = \mu_{ag}$ (solid black arrow) and $\mu_{2a} = \mu_{bg}$ (dotted black arrow), where μ denotes the transition dipole moment. EEA (yellow arrows) occurs via the two channels $|2\rangle \rightarrow |a\rangle$ and $|2\rangle \rightarrow |b\rangle$, both having the rate k_A, whereas transfer between the single exciton states, $|a\rangle \rightarrow |b\rangle$ (light blue arrow), is described by the rate k_T.

Based on this model system, we consider only those pathways that feature population dynamics. This helps us to significantly reduce the number of pathways without neglecting essential pathway types. Let us further assume that the fluorescence quantum yield Φ_N ($N \in \{a, b, 2\}$) of each pathway is unity. This assumption is also justified for those pathways that end in the $|2\rangle$ manifold due to fast annihilation of the biexciton state (and internal conversion of the higher excited states), which is expected in a dimer [7, 218]. The resulting seven pathways are shown in Fig. 5.3b–d. Note that, in addition those shown in Fig. 5.3c–d, there are in principle pathways in which $+\varphi_3$ could

interact from the left side, i.e., $|a\rangle\langle a| \xrightarrow{+\varphi_3} |2\rangle\langle a|$ and $|b\rangle\langle b| \xrightarrow{+\varphi_3} |2\rangle\langle b|$. However, as discussed in Sec. 4.5.10, pathways that contain biexciton–single-exciton coherences, such as $|2\rangle\langle a|$ and $|2\rangle\langle b|$, always occur in oppositely signed pairs and, since the weights of these pathways are identical due to fast annihilation, these pathways cancel.

The pathways shown in Fig. 5.3 can be grouped into three categories according to type of dynamics which evolves over the population time T. Pathways that feature the

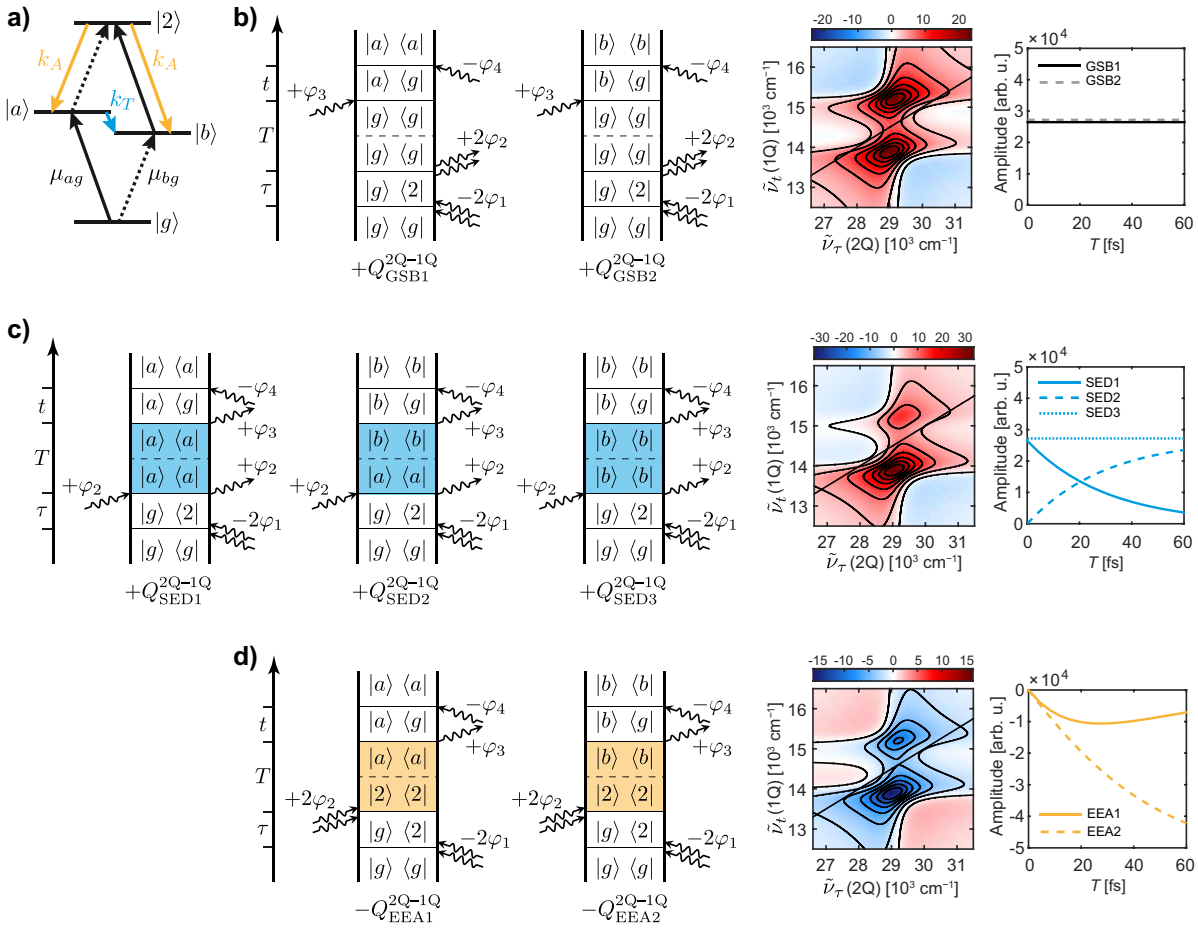

Figure 5.3. Dissecting the rephasing sixth-order 2Q–1Q signal. (a) Effective energy level scheme of a weakly coupled heterodimer with ground state $|g\rangle$, single-exciton states $|b\rangle$ and $|a\rangle$, and a doubly excited (biexciton) state $|2\rangle$. Transitions between the states with dipole moments μ_{ag} (μ_{bg}) are indicated by solid (dotted) black arrows. Exciton–exciton annihilation (yellow arrows) occurs with rate k_A whereas energy transfer between the single-exciton states (light blue arrow) has the rate k_T. The contributing pathways can be grouped into (b) ground-state bleach (GSB) pathways, (c) pathways that contain single-exciton dynamics (SED), and pathways which probe exciton–exciton annihilation (EEA). The sum over each pathway group is illustrated in 2D frequency space at $T = 20$ fs (real part). On the right, the waiting time dynamics of the individual pathways are plotted. Adapted in part and modified from Ref. [2].

dynamics of the ground-state population over T are ground-state bleach (GSB) pathways (Fig. 5.3b). Pathways that feature single-exciton dynamics (SED) are shown in Fig. 5.3c (highlighted in light blue). Finally, we have the EEA pathways (Fig. 5.3d). There are two EEA pathways because of the two annihilation channels (Fig. 5.3a, yellow arrows).

Let us now formulate these pathways mathematically. As a starting point, we can utilize the 2Q–1Q response function in the impulsive limit, which was introduced in Eqs. (1.24)–(1.26) in Sec. 1.2.3, and incorporate the population time dynamics. Under the assumption that the surrounding bath has no memory between successive time intervals, i.e., the dynamics occurring over T do not influence the line shapes,[1] we can factorize the response function. Accordingly, we can formulate each rephasing 2Q–0Q–1Q pathway, for which we shall use the shorter notation "2Q–1Q" in the following, as a product of a rephasing sixth-order 2Q–1Q response function, which describes the dynamics of the coherences over τ and t, and a propagator $\mathcal{U}_{jjkk}(T)$, which describes the dynamics between states k and j over T. If we neglect inhomogeneous broadening, which means that the line shape is only governed by one- and two-exciton pure dephasing rates γ_{2g} and γ_{1g}, respectively, we obtain the general expression

$$Q^{\text{2Q–1Q}}(t,T,\tau) = \mathcal{U}_{jjkk}(T) \times \pm\Phi_N\Theta(t)\Theta(\tau)\left(\frac{i}{\hbar}\right)^6 \mu_{ag}^n\mu_{bg}^m \times \mathrm{e}^{-\mathrm{i}(2\omega_0-\omega_{2g})\tau}\mathrm{e}^{\mathrm{i}(\omega_0-\omega_{1g})t}\mathrm{e}^{-\gamma_{2g}\tau}\mathrm{e}^{-\gamma_{1g}t}, \tag{5.1}$$

where ω_{2g} and ω_{1g} are the one- and two-exciton transition frequencies, respectively. In our example, we shall employ the individual one-exciton frequencies $\omega_{ag}/2\pi c = 15.2 \times 10^3$ cm^{-1} and $\omega_{bg}/2\pi c = 13.9 \times 10^3$ cm^{-1}, whereas the dephasing rates are set to $\gamma_{ag}/2\pi c = \gamma_{bg}/2\pi c = 0.3 \times 10^3$ cm^{-1} $= 0.5\gamma_{2g}/2\pi c$. Then, we can recast Eq. (5.1) into 2D frequency space by using a 2D Fourier transformation,

$$S^{\text{2Q–1Q}}(\omega_\tau,T,\omega_t) = \iint \mathrm{d}\tau\mathrm{d}t\; Q^{\text{2Q–1Q}}(t,T,\tau)\mathrm{e}^{\mathrm{i}\omega_\tau\tau}\mathrm{e}^{\mathrm{i}\omega_t t}. \tag{5.2}$$

An analytical solution to the integral of Eq. (5.2) is a 2D Lorentzian function [17, 27, 43],

$$S^{\text{2Q–1Q}}(\omega_\tau,T,\omega_t) = \mathcal{U}_{jjkk}(T)\frac{\mu_{ag}^n\mu_{bg}^m}{\hbar^6}\frac{1}{\mathrm{i}(-\omega_\tau+\omega_{2g})-\gamma_{2g}} \times \frac{1}{\mathrm{i}(\omega_t-\omega_{1g})-\gamma_{1g}}. \tag{5.3}$$

Henceforth, we consider rephasing 2Q–1Q 2D spectra which propagate with $\mathcal{U}_{jjkk}(T)$. By formulating Eq. (5.3) for each pathway of Fig. 5.3b–d explicitly, we obtain

$$S_{\text{GSB1}}^{\text{2Q–1Q}}(\omega_\tau,T,\omega_t) = 4\Theta(T)\frac{\mu_{ag}^4\mu_{bg}^2}{\hbar^6}\frac{1}{\mathrm{i}(-\omega_\tau+\omega_{2g})-\gamma_{2g}} \times \frac{1}{\mathrm{i}(\omega_t-\omega_{ag})-\gamma_{ag}}, \tag{5.4}$$

[1] A consequence of this assumption is that spectral diffusion can not be described [17]. Such an assumption, however, is justified if the bath reorganization occurs on a time scale much longer than k_A and k_T.

$$S^{\text{2Q–1Q}}_{\text{GSB2}}(\omega_\tau, T, \omega_t) = 4\Theta(T)\frac{\mu_{bg}^4\mu_{ag}^2}{\hbar^6}\frac{1}{\mathrm{i}(-\omega_\tau+\omega_{2g})-\gamma_{2g}}\times\frac{1}{\mathrm{i}(\omega_t-\omega_{bg})-\gamma_{bg}}, \tag{5.5}$$

$$S^{\text{2Q–1Q}}_{\text{SED1}}(\omega_\tau, T, \omega_t) = 4\Theta(T)\mathrm{e}^{-k_T T}\frac{\mu_{ag}^4\mu_{bg}^2}{\hbar^6}\frac{1}{\mathrm{i}(-\omega_\tau+\omega_{2g})-\gamma_{2g}}\times\frac{1}{\mathrm{i}(\omega_t-\omega_{ag})-\gamma_{ag}}, \tag{5.6}$$

$$\begin{aligned} S^{\text{2Q–1Q}}_{\text{SED2}}(\omega_\tau, T, \omega_t) &= 4\Theta(T)\left(1-\mathrm{e}^{-k_T T}\right) \\ &\quad\times\frac{\mu_{bg}^4\mu_{ag}^2}{\hbar^6}\frac{1}{\mathrm{i}(-\omega_\tau+\omega_{2g})-\gamma_{2g}}\times\frac{1}{\mathrm{i}(\omega_t-\omega_{bg})-\gamma_{bg}}, \end{aligned} \tag{5.7}$$

$$S^{\text{2Q–1Q}}_{\text{SED3}}(\omega_\tau, T, \omega_t) = 4\Theta(T)\frac{\mu_{bg}^4\mu_{ag}^2}{\hbar^6}\frac{1}{\mathrm{i}(-\omega_\tau+\omega_{2g})-\gamma_{2g}}\times\frac{1}{\mathrm{i}(\omega_t-\omega_{bg})-\gamma_{bg}}, \tag{5.8}$$

$$\begin{aligned} S^{\text{2Q–1Q}}_{\text{EEA1}}(\omega_\tau, T, \omega_t) &= -4\Theta(T)\left[\frac{k_A}{-k_A+k_T}\left(\mathrm{e}^{-k_A T}-\mathrm{e}^{-k_T T}\right)\right] \\ &\quad\times\frac{\mu_{ag}^4\mu_{bg}^2}{\hbar^6}\frac{1}{\mathrm{i}(-\omega_\tau+\omega_{2g})-\gamma_{2g}}\times\frac{1}{\mathrm{i}(\omega_t-\omega_{ag})-\gamma_{ag}}, \end{aligned} \tag{5.9}$$

$$\begin{aligned} S^{\text{2Q–1Q}}_{\text{EEA2}}(\omega_\tau, T, \omega_t) &= -4\Theta(T)\left[1-\mathrm{e}^{-k_A T}+\frac{k_T}{-k_A+k_T}\left(1-\mathrm{e}^{-k_A T}\right)\right. \\ &\quad\left.-\frac{k_A}{-k_A+k_T}\left(1-\mathrm{e}^{-k_T T}\right)\right] \\ &\quad\times\frac{\mu_{bg}^4\mu_{ag}^2}{\hbar^6}\frac{1}{\mathrm{i}(-\omega_\tau+\omega_{2g})-\gamma_{2g}}\times\frac{1}{\mathrm{i}(\omega_t-\omega_{bg})-\gamma_{bg}}, \end{aligned} \tag{5.10}$$

where the prefactors of four are a result of time ordering. Note that $S^{\text{2Q–1Q}}_{\text{GSB1}}$, $S^{\text{2Q–1Q}}_{\text{GSB2}}$, and $S^{\text{2Q–1Q}}_{\text{SED3}}$ propagate stationary with unity throughout positive T delays, that is, $\mathcal{U}_{bbbb}(T) = \mathcal{U}_{gggg}(T) = \Theta(T)$, which is due to the life time of the lowest excited state $|b\rangle$ (and in turn the repopulation time of the ground state) being usually a few nanoseconds [253]. The propagators of $S^{\text{2Q–1Q}}_{\text{EEA1}}$ and $S^{\text{2Q–1Q}}_{\text{EEA2}}$ result from the solution of coupled rate equations, since the populations $|a\rangle\langle a|$ and $|b\rangle\langle b|$ depend both on the rates k_T and k_A.

The sum over each pathway group is illustrated in 2D frequency space at $T = 20$ fs on the right side in Fig. 5.3b–d, accompanied with plots of the waiting time propagators of each individual pathway. It is evident that the 2Q–1Q signal in principle holds the information about the EEA dynamics (Fig. 5.3d), however, this information is on top of an oppositely signed background of other pathways which contain single-exciton dynamics as well (5.3b and c). Note that oscillatory SED pathways, i.e., those that oscillate due to coherence between $|a\rangle$ and $|b\rangle$ are neglected here, however, these would also superimpose with the EEA dynamics. Altogether, these circumstances make it difficult to infer the annihilation time from the 2Q–1Q signal kinetics. In other words, the 2Q–1Q signal is annihilation sensitive but *not* annihilation selective. Hence, one has to seek for a strategy to eliminate the GSB and SED pathways from the 2Q–1Q signal.

As shown in Chapter 4, the 125-fold phase-cycling protocol gives access to many other

sixth-order signals. Are there any other signals that feature a higher degree of selectivity towards EEA? The answer is no, since the sixth-order 2Q–1Q signal is the only one that probes biexciton populations over T. Nonetheless, let us focus on the "inverted" 2Q–1Q signal – the 1Q–2Q signal. It is "inverted" in a sense that the phase-specific interaction pattern, $-\varphi_1 + \varphi_2 + 2\varphi_3 - 2\varphi_4$, is exactly the reverse of that of the 2Q–1Q signal.

In the sixth-order 1Q–2Q process, the first two pulses contribute both by a single interaction, which only gives rise to ground- or single-exciton state populations evolving over T. The 1Q–2Q signal can thus be described by only the five pathways shown in Fig. 5.4. Here, we have only GSB (Fig. 5.4a) and SED pathway types (Fig. 5.4b). Similar to above, we can formulate each pathway in 2D frequency space:

$$S^{\text{1Q–2Q}}_{\text{GSB1}}(\omega_\tau, T, \omega_t) = 4\Theta(T)\frac{\mu_{ag}^4\mu_{bg}^2}{\hbar^6}\frac{1}{\mathrm{i}(-\omega_\tau + \omega_{ag}) - \gamma_{ag}} \times \frac{1}{\mathrm{i}(\omega_t - \omega_{2g}) - \gamma_{2g}}, \tag{5.11}$$

$$S^{\text{1Q–2Q}}_{\text{GSB2}}(\omega_\tau, T, \omega_t) = 4\Theta(T)\frac{\mu_{bg}^4\mu_{ag}^2}{\hbar^6}\frac{1}{\mathrm{i}(-\omega_\tau + \omega_{bg}) - \gamma_{bg}} \times \frac{1}{\mathrm{i}(\omega_t - \omega_{2g}) - \gamma_{2g}}, \tag{5.12}$$

$$S^{\text{1Q–2Q}}_{\text{SED1}}(\omega_\tau, T, \omega_t) = 4\Theta(T)\mathrm{e}^{-k_T T}\frac{\mu_{ag}^4\mu_{bg}^2}{\hbar^6}\frac{1}{\mathrm{i}(-\omega_\tau + \omega_{ag}) - \gamma_{ag}} \times \frac{1}{\mathrm{i}(\omega_t - \omega_{2g}) - \gamma_{2g}}, \tag{5.13}$$

$$\begin{aligned} S^{\text{1Q–2Q}}_{\text{SED2}}(\omega_\tau, T, \omega_t) &= 4\Theta(T)\left(1 - \mathrm{e}^{-k_T T}\right) \\ &\quad \times \frac{\mu_{ag}^4\mu_{bg}^2}{\hbar^6}\frac{1}{\mathrm{i}(-\omega_\tau + \omega_{ag}) - \gamma_{ag}} \times \frac{1}{\mathrm{i}(\omega_t - \omega_{2g}) - \gamma_{2g}}, \end{aligned} \tag{5.14}$$

$$S^{\text{1Q–2Q}}_{\text{SED3}}(\omega_\tau, T, \omega_t) = 4\Theta(T)\frac{\mu_{bg}^4\mu_{ag}^2}{\hbar^6}\frac{1}{\mathrm{i}(-\omega_\tau + \omega_{bg}) - \gamma_{bg}} \times \frac{1}{\mathrm{i}(\omega_t - \omega_{2g}) - \gamma_{2g}}. \tag{5.15}$$

The sum over the individual pathway groups is illustrated at $T = 20$ fs on the right side of Fig. 5.4. It is evident from the propagators of the individual pathways, which are also plotted in Fig. 5.4 (right), that the 1Q–2Q signal is completely insensitive to EEA.

Nonetheless, note the close relation between the 2Q–1Q and 1Q–2Q pathways. At first glance, only the roles of τ (ω_τ) and t (ω_t) seem to be interchanged. Most importantly, the propagators of the GSB and the SED pathways of both signals are identical [compare Eqs. (5.4)–(5.8) with Eqs. (5.11)–(5.15), and the right sides of Figs. 5.3 and 5.4]. It is precisely the latter which shall be exploited to eliminate the GSB and SED pathways by subtracting the 1Q–2Q signal from the 2Q–1Q signal. Before we do so, however, we have to perform an appropriate procedure to "visually transform" the 1Q–2Q 2D spectrum to match the 2Q–1Q representation, which is described in the following.

The concept is essentially based on the fact that the inversion of an inverted process again corresponds to the process itself. To illustrate this, let us consider the sixth-order 2Q–1Q process, which is schematically shown in Fig. 5.5a, top. The sixth-order 1Q–2Q process (Fig. 5.5b, top left), which is formally the inversion of the 2Q–1Q process, can

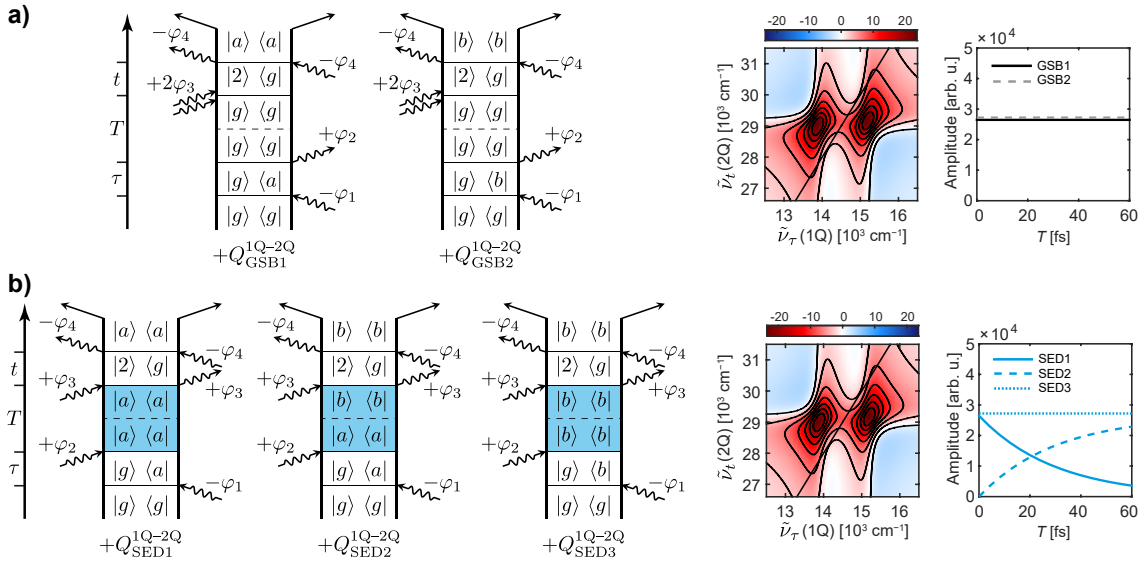

Figure 5.4. Dissecting the rephasing sixth-order 1Q–2Q signal. The contributing pathways can be grouped into (b) ground-state bleach (GSB) pathways and (b) pathways that contain single-exciton dynamics (SED). The sum over each pathway group is illustrated in 2D frequency space at $T = 20$ fs (real part). On the right, the waiting time dynamics of the individual pathways are plotted. Adapted in part and modified from Ref. [2].

effectively be transformed into the 2Q–1Q process (Fig. 5.5b, top right) by inverting the order of the phase-specific interactions (red double arrows). To achieve the same effect in frequency domain (bottom panels of Fig. 5.5a and b), we can employ a mathematical operation $\hat{\mathcal{O}}$ that flips the 1Q–2Q spectrum along the diagonal (that is, exchanging ω_τ and ω_t) and performs a complex conjugation. The complex conjugation is necessary to resolve the mismatch of the coherence phases between the two sixth-order signals. In general terms, the operation $\hat{\mathcal{O}}$ acting on $S^{\text{1Q–2Q}}$ can be formulated as

$$\begin{aligned}\hat{\mathcal{O}}\left(S^{\text{1Q–2Q}}(\omega_\tau, T, \omega_t)\right) &= \hat{\mathcal{O}}\left(\mathcal{U}_{jjkk}(T)\frac{\mu_{ag}^n \mu_{bg}^m}{\hbar^6}\frac{1}{\mathrm{i}(-\omega_\tau + \omega_{1g}) - \gamma_{1g}} \times \frac{1}{\mathrm{i}(\omega_t - \omega_{2g}) - \gamma_{2g}}\right), \\ &= \mathcal{U}_{jjkk}(T)\frac{\mu_{ag}^n \mu_{bg}^m}{\hbar^6}\frac{1}{\mathrm{i}(\omega_t - \omega_{1g}) - \gamma_{1g}} \times \frac{1}{\mathrm{i}(-\omega_\tau + \omega_{2g}) - \gamma_{2g}}, \quad (5.16)\end{aligned}$$

which apparently yields an expression corresponding to that of the 2Q–1Q representation of Eq. (5.3). Note that the propagators are real valued, i.e., $\mathcal{U}_{jjkk}(T) = \mathcal{U}^*_{jjkk}(T)$.

Finally, we can subtract the thus-transformed 1Q–2Q signal from the 2Q–1Q signal to yield the FDEEI signal,

$$S^{\text{FDEEI}}(\omega_\tau, T, \omega_t) = S^{\text{2Q–1Q}}(\omega_\tau, T, \omega_t) - \hat{\mathcal{O}}\left(S^{\text{1Q–2Q}}(\omega_\tau, T, \omega_t)\right). \quad (5.17)$$

By formulating $S^{\text{2Q–1Q}}$ and $S^{\text{1Q–2Q}}$ as the sums over Eqs. (5.4)–(5.10) and Eqs. (5.11)–(5.15), respectively, the following expression for the integrated FDEEI signal amplitude

can be constructed:

$$\begin{aligned} S^{\mathrm{FDEEI}}(T) \propto & -4\left(\mu_{ag}^4\mu_{bg}^2+\mu_{ag}^2\mu_{bg}^4\right) \\ & +4\left(\mu_{ag}^4\mu_{bg}^2-\mu_{bg}^4\mu_{ag}^2\right)\left(1+\frac{k_A}{-k_A+k_T}\right)\mathrm{e}^{-k_T T} \\ & +4\mu_{bg}^2\mu_{ag}^2\left[\mu_{bg}^2\left(1+\frac{k_T}{-k_A+k_T}\right)-\mu_{ag}^2\frac{k_A}{-k_A+k_T}\right]\mathrm{e}^{-k_A T}. \end{aligned} \tag{5.18}$$

From Eq. (5.18), we can derive important properties of the FDEEI signal. Most importantly, the contribution of the actual annihilation kinetics to the FDEEI signal

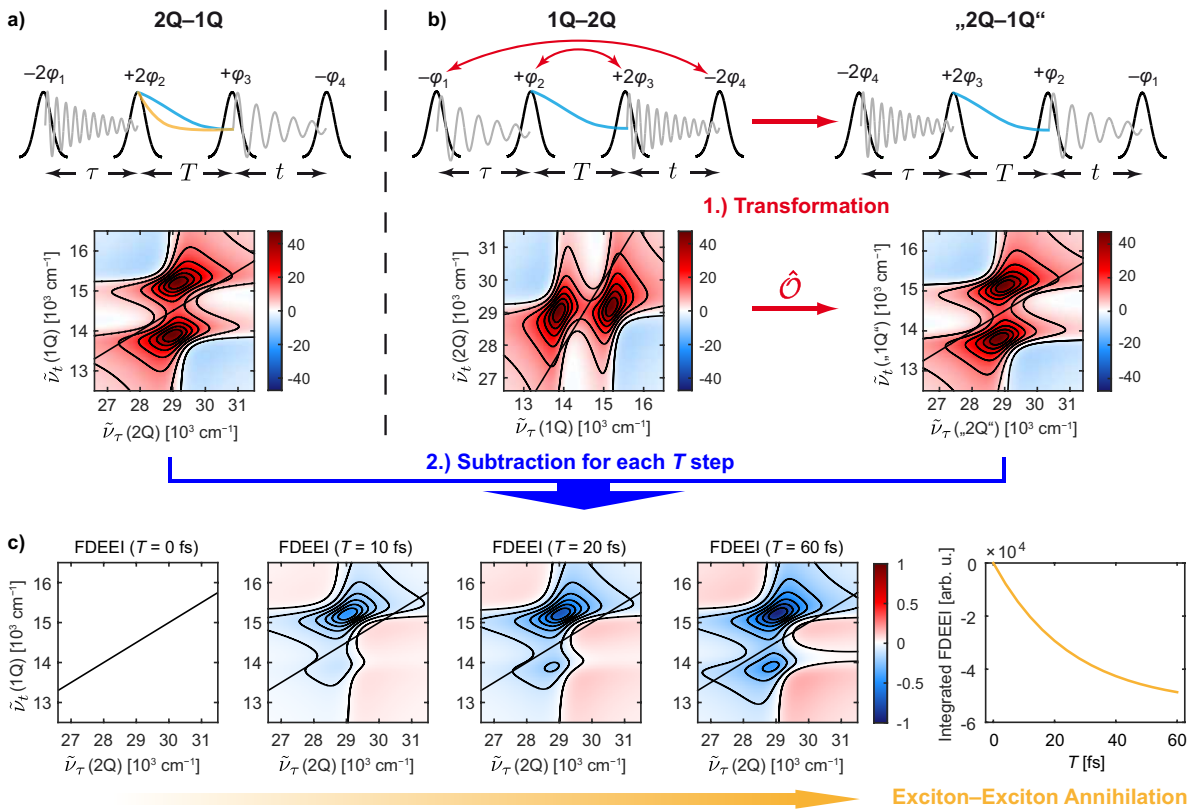

Figure 5.5. Construction of the fluorescence-detected exciton–exciton interaction (FDEEI) signal. (a) Top: pulse sequence of the sixth-order 2Q–1Q process, which probes both single-exciton dynamics (light blue) and biexciton dynamics (yellow) over T. Bottom: real part of the calculated 2Q–1Q 2D spectrum at $T = 0$ of the dimer system of Fig. 5.3a with $\mu_{ag} = \mu_{bg}$. (b) Top: pulse sequence of the sixth-order 1Q–2Q process, which only probes single exciton dynamics over T. The 1Q–2Q signal can be visually transformed into the "2Q–1Q" fashion by inverting the phase-specific interaction sequence (red arrows). In the spectral domain (bottom, 2D spectra are shown at $T = 0$), this procedure is effectively carried out using a transformation operator $\hat{\mathcal{O}}$ (see text). The subtraction of the sixth-order 2Q–1Q and the transformed 1Q–2Q signal yields (c) the FDEEI signal. The real parts of the FDEEI2D spectra are shown at four different T steps (normalized to the highest absolute value of the 2D spectrum at $T = 60$ fs). The integrated FDEEI2D spectrum (rightmost panel) exclusively decays with the rate k_A of exciton–exciton annihilation from zero. The annihilation time $\tau_A = k_A^{-1}$ is here set to 25 fs.

depends on the magnitudes of the transition dipole moments μ_{ag} and μ_{bg}. If they are the same, i.e., $\mu_{ag} = \mu_{bg} = \mu$, then the integrated FDEEI signal reduces to

$$S^{\mathrm{FDEEI}}(T) \propto 8\mu^6 \left[-1 + \mathrm{e}^{-k_A T}\right], \tag{5.19}$$

which means that the FDEEI signal *exclusively* decays with the annihilation rate from zero. This scenario is illustrated in Fig. 5.5c. Note that the FDEEI vanishes at $T = 0$, since the 2Q–1Q and 1Q–2Q 2D spectra have identical amplitude, as shown in the bottom panels of Fig. 5.5a and b.

The situation is different if $\mu_{ag} \approx \mu_{bg}$. The reason lies in the second term of Eq. (5.18), which contains transfer dynamics between the single-exciton states and somewhat scales with the difference of the transition dipole moments. Thus, the weight of this term increases with increasing difference between the transition dipole moments μ_{ag} and μ_{bg}. This poses a limiting factor with regard to the meaningfulness of the FDEEI signal, as the signal is contaminated with single-exciton dynamics in case of systems with largely differing transition dipole moments. In fact, the ratio of the rates k_T and k_A quantitatively influences the degree of this contamination as well. Using the second and the third term of Eq. (5.18) while assuming that $k_A > k_T$, a landscape can be calculated that quantifies to which extent the FDEEI signal describes EEA kinetics (Fig. 5.6).

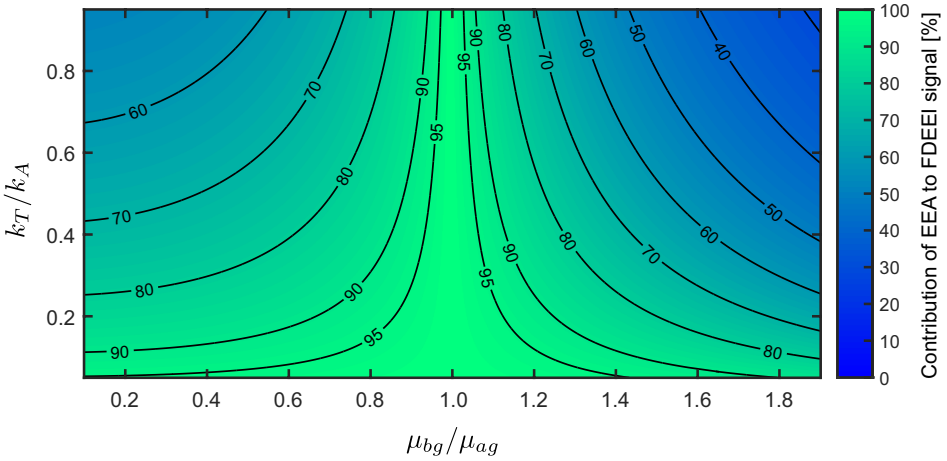

Figure 5.6. Quantifying the contamination of the FDEEI signal by single-exciton dynamics. Contributions of EEA kinetics are expressed as percentages of the total FDEEI signal while the contour lines are drawn at the percentages indicated. The FDEEI signal fully describes annihilation dynamics in case of equal transition dipole moments $\mu_{ag} = \mu_{bg}$ for all ratios between the single-exciton population transfer rate k_T and the exciton–exciton annihilation rate k_A.

Accordingly, the FDEEI signal is most contaminated by single-exciton dynamics in systems in which k_A is close to k_T and where the transition dipole moments differ by more than one order of magnitude at the same time. Note, however, that the FDEEI

signal almost completely describes EEA kinetics for the total range of k_T/k_A in case of $\mu_{ag} \approx \mu_{bg}$. Even for many heterodimers, $\mu_{ag} \approx \mu_{bg}$ often holds, such that the subtraction procedure of Eq. (5.17) will yield an FDEEI signal which is practically entirely governed by EEA. Nevertheless, in cases where single-exciton dynamics still substantially contribute to the integrated FDEEI signal, the contamination landscape of Fig. 5.6 can be used to determine fixed parameters or at least reasonable fitting constraints for a biexponential fitting model.

Summarizing, in this section, the FDEEI signal, a sixth-order nonlinear signal which selectively propagates with the biexciton dynamics, was constructed. The applicability of the approach was quantitatively assessed in terms of residual contributions from single-exciton dynamics, whereas the latter is found to pose a considerably low contribution in a wide range of small aggregates. In case of equal excitonic transition dipole moments, the FDEEI signal can be utilized as a background-free probe for ultrafast exciton–exciton annihilation kinetics using fluorescence detection. The approach proposed herein thus features analogous selectivity as coherently detected EEI2D spectroscopy [102] towards annihilation kinetics. In the next section, the approach proposed herein is demonstrated on the example of squaraine heterodimers.

5.3 Experimental Demonstration

5.3.1 Setup

In order to validate the FDEEI 2D experiment, we additionally carry out a coherently detected EEI2D experiment. From a technical point of view, FDEEI2D spectroscopy is most closely related to coherently detected EEI2D spectroscopy in the pump–probe geometry (see Fig. 5.2d and f), whereas we refer to the latter approach as "CDEEI2D" spectroscopy in the following. Both experiments can thus be realized in a single setup, as shown in Fig. 5.7. The setup is essentially based on the fluorescence-based setup shown in Fig. 4.7 (for further details see Sec. 4.5.1), with the difference of an additional probe beam and a second detection path for the coherently emitted signal of the CDEEI2D experiment, as indicated by the dashed lines.

In brief, the spatially stabilized laser beam of a Ti:Sa chirped-pulse amplifier system is focused into a hollow-core fiber (HCF), which is filled with a mixture of argon and neon, to generate a coherent supercontinuum. The supercontinuum pulses are subsequently compressed by chirped mirrors (CMC, Ultrafast Innovations). The near-IR part of the supercontinuum spectrum is removed by a 750 nm shortpass filter (SP, FESH750, Thorlabs). A part of the resulting beam is then split off by a pair of thin wedges (WP)

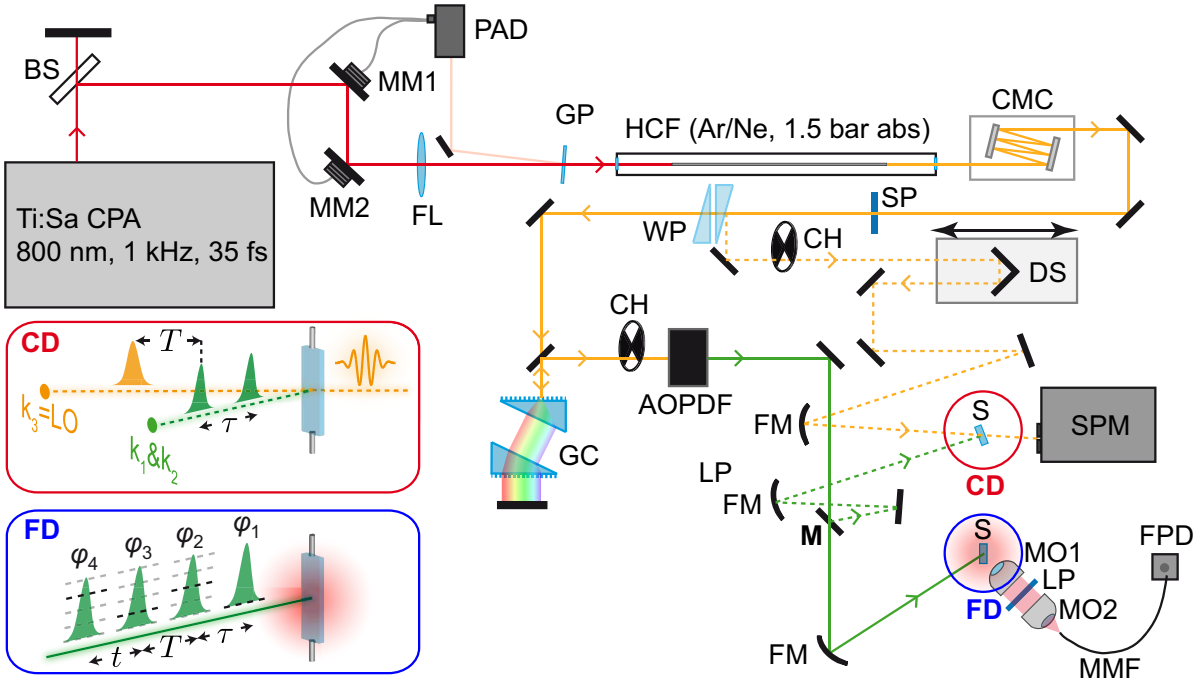

Figure 5.7. Setup of coherently (CD) and fluorescence-detected (FD) EEI2D spectroscopy. CPA: chirped-pulse amplifier; BS: beam splitter; MM1, MM2: motorized mirrors; FL: fused-silica focusing lens ($f = 120$ cm); PAD: position and angle detector; GP: fused-silica glass plate; HCF: hollow-core fiber (filled with a mixture of argon and neon); CMC: chirped mirror compressor; SP: short-pass filter; WP: pair of wedges; CH: chopper; DS: delay stage; GC: dual grism compressor; AOPDF: acousto-optic programmable dispersive filter; FM: focusing mirror; M: flippable mirror; S: sample, being pumped through a flow cell; SPM: spectrometer; MO1, MO2: microscope objectives, LP: long-pass filter; MMF: multimode fiber; FPD: fast photodiode. The supercontinuum beam generated by the HCF is drawn in yellow, whereas the pump beam paths are drawn in green (solid: FDEEI2D; dashed: CDEEI2D). The excitation sequences for CDEEI2D and FDEEI2D spectroscopy are shown the red and blue panels, respectively, at the bottom left. In CDEEI2D spectroscopy, the coherently emitted signal is self-heterodyned with the probe beam (dashed yellow line) whereas in FDEEI2D spectroscopy, fluorescence is measured instead.

to serve as the probe beam for the CDEEI2D experiment, where a motorized delay stage (DS, Newport) is employed to scan the population time T. The majority of the HCF output is guided through a grism compressor (GC) to pre-compensate the dispersion of the acousto-optic disersive filter (AOPDF). The AOPDF generates two-pulse sequences with delay τ in case of the CDEEI2D experiment or phase-cycled four-pulse sequences with delays τ, T, and t for the FDEEI2D experiment (Fig. 5.7, bottom left panels). The duration of each excitation pulse is 12 fs, as determined by collinear SHG-FROG. For both FDEEI2D and CDEEI2D spectroscopy, the sample solution of squaraine heterodimers SQA–SQB in toluene with an optical density of 0.1 (at 200 µm path length) is

continuously pumped through a 200 µm thin flow cell at a rate of approximately 2 µL/s.

In the FDEEI2D experiment, the single excitation beam (solid green line in Fig. 5.7) is focused on the flow cell, which is oriented at an angle of ≈45° relative to the incident beam. The excitation energy is 150 nJ at maximum pulse overlap. The fluorescence is collected at a right angle by a pair of microscope objectives (MO), filtered by a 750 nm long-pass filter (LP, FELH750, Thorlabs), and then guided by an optical fiber to a fast photodiode (FPD, model FPD610-FC-VIS, Menlo systems) for detection. In the FDEEI2D excitation sequence, a 1×5×5×5 phase-cycling scheme is employed [4], while the coherence times τ and t are scanned from 0 to 84 fs in 6 fs steps in a fully rotating frame of 438 THz (685 nm). The population time T is scanned from 0 to 60 fs in 4 fs steps. After the experiment, the rephasing and nonrephasing 2Q–0Q–1Q as well as the rephasing 1Q–0Q–2Q contributions are extracted by using Eq. (4.1) together with the weighting factors listed in Table 4.1 (see Chapter 4). The obtained data is corrected for a slight detector nonlinearity according to a previously reported procedure [254]. To yield the 2D spectra $S(\omega_\tau, T, \omega_t)$ of the individual signal contributions, a 2D Fourier transformation with respect to τ and t of each contribution is performed.

In the CDEEI2D experiment, the pump beam (green dashed line in Fig. 5.7) is instead reflected by the flippable mirror (M). The pump beam has an energy of 110 nJ (at maximum pulse overlap) and is focused on the flow cell, which is perpendicularly oriented relative to the pump beam. The probe beam (yellow dashed line) is focused on the sample in a small angle relative to the pump beam. Residual chirp results in a probe pulse duration of 22 fs, as determined by cross-correlation SFG-FROG, where the prior characterized pump pulse served as a reference. Pump and probe pulses are chopped at 100 Hz and 200 Hz, respectively, in order to separate the differential signal and to suppress pump scattering, according to a previously reported procedure [102]. The coherently emitted signal field is self-heterodyned with the probe pulse, i.e., the probe pulse acts both as the third excitation pulse and a local oscillator (LO) which measures the signal emitted in $\mathbf{k}_3$ direction by interference. The resulting interference spectra in the ω_t domain are measured on a spectrometer (SPM), which is composed of a spectrograph (Acton SP2500, Princeton Instruments) and a CCD camera (Pixis 2K, Princeton Instruments). The delay τ between the pump pulses is scanned via the AOPDF from 0 to 88 fs in 0.44 fs steps in the laboratory frame. The population time T is varied from −42 to 120 fs in 6 fs steps using the delay stage. To obtain the 2D spectra $S(\omega_\tau, T, \omega_t)$, the obtained interferograms $S(\tau, T, \omega_t)$ are Fourier transformed with respect to delay τ.

5.3.2 Results and Discussion

The chemical structure of the SQA–SQB heterodimers investigated in this work is shown in Fig. 5.8a. The SQA (blue) and SQB (red) monomers are connected by a phenyl spacer. According to a previous finding on directly covalently linked SQA–SQB dimers, the dimer structure can be considered as linear [253]. The monomeric dipole moments of the $S_0 \rightarrow S_1$ transitions are approximately oriented along the length of each monomer [255], giving rise to J-type electronic coupling [256] with a coupling constant of $J = -240$ cm^{-1} in toluene [257].[2] In comparison to similar squaraine heterodimers, which feature spacers resulting in smaller distances between the chromophores and thus stronger coupling, the coupling strength in the dimers considered here can be regarded as relatively weak, resulting in exciton states with partially localized character [7, 257].

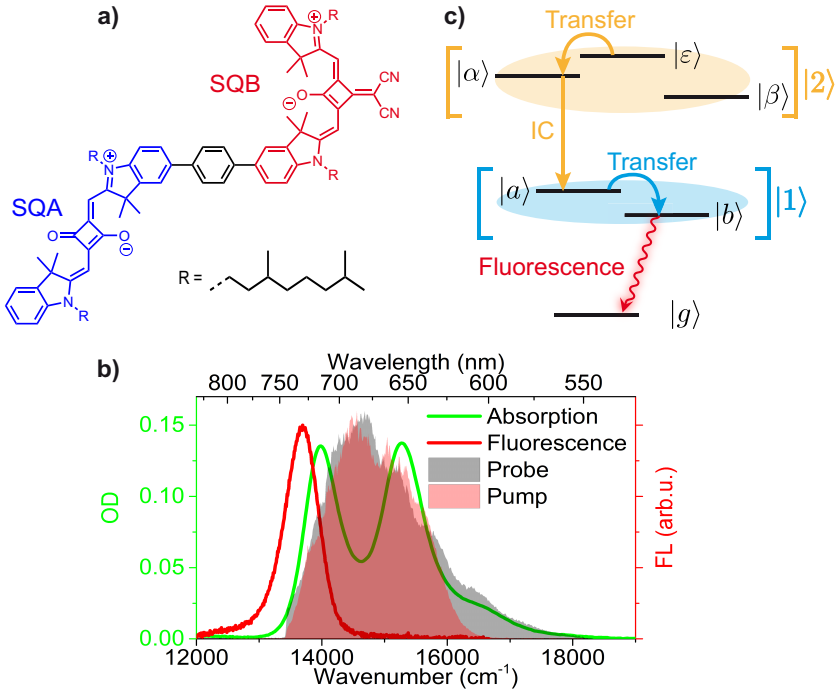

Figure 5.8. Properties of the investigated sample. (a) Chemical structure of the SQA–SQB squaraine heterodimer. The heterodimer is composed of a SQA (blue) and a SQB (red) monomer, which are linked with a phenyl group. (b) Linear absorption (green) and fluorescence (red) spectra of the SQA–SQB dimer in toluene. The pump spectrum in the CDEEI2D experiment, which is also employed in the FDEEI2D experiment for excitation, is shown as a red shaded area. The spectrum drawn as a gray shaded area is used as the probe spectrum in the CDEEI2D experiment. Reprinted in part from Ref. [2], with the permission of AIP Publishing.

[2]The electronic coupling strength is given by $J = \frac{\vec{\mu}_{ag}\vec{\mu}_{bg}}{r^3} - \frac{3(\vec{\mu}_{ag}\vec{r})(\vec{\mu}_{bg}\vec{r})}{r^5}$, where r is the distance between the monomers. In addition to r, the coupling strength thus crucially depends on the relative orientation of the monomeric transition dipole moments [256].

The splitting between the single-exciton states is 1290 cm^{-1} [257], as assessable from the linear absorption spectrum in Fig. 5.8b. The absorption maximum of the single-exciton state $|b\rangle$ is at 13950 cm^{-1} whereas the maximum at 15240 cm^{-1} is assigned to $|a\rangle$. Both absorption bands have nearly identical intensity, which indicates that the transition dipole moments μ_{bg} and μ_{ag} have approximately the same magnitude. The linear absorption spectrum in the region between 25000 cm^{-1} and 30000 cm^{-1} features additional absorption bands which can be attributed to those of the doubly excited exciton states $|\alpha\rangle$, $|\beta\rangle$ and $|\varepsilon\rangle$ (see Appendix C).

The energy level scheme of the dimer in the exciton basis is shown in Fig. 5.8c and essentially corresponds to the one introduced in Fig. 5.1. The exciton states can be grouped into the singly excited manifold $|1\rangle$ (light blue) and the doubly excited manifold $|2\rangle$ (yellow). Due to delocalization, the states of the respective manifolds mix, as indicated by the light blue and yellow ellipses in Fig. 5.8c. According to Kasha's rule [31], fluorescence is emitted from the single-exciton state $|b\rangle$. The fluorescence quantum yield is $\Phi = 0.81$ and the emission spectrum is shown in Fig. 5.8b. The lifetime of state $|b\rangle$ is 2.83 ns [257], which can be considered as constant in relation to the scanned time scale of the population time T. Energy transfer within the single-exciton manifold proceeds fast with a time constant of about 30 fs, as confirmed by third- and fourth-order 2D spectroscopy [2, 7]. Apart from the excitonic states depicted in Fig. 5.8c, there are additional vibronically excited states resulting from a dominant intramolecular vibrational mode with $\tilde{\nu}_{\mathrm{vib}} = 1220\ \mathrm{cm}^{-1}$, as evident by the vibronic progression band in the absorption spectrum (Fig. 5.8b). Due to $\tilde{\nu}_{\mathrm{vib}}$ being near-resonant with the excitonic splitting, this mode plays an important role in the energy transfer between the single-exciton states [253]. However, as we focus on EEA dynamics in the following, the effective excitonic model of Fig. 5.8c is sufficient to describe the EEA kinetics and the essential features observed in the 2D spectra. Because of the mixing of the higher excited states $|\alpha\rangle$ and $|\beta\rangle$ with the biexciton state $|\varepsilon\rangle$, EEA proceeds via ultrafast energy transfer within the $|2\rangle$ manifold with consecutive internal conversion into the $|1\rangle$ manifold (yellow arrows in Fig. 5.8c). In the manifold picture, both processes can be combined to a single step, i.e., $|2\rangle \rightarrow |1\rangle$, which is associated with the annihilation rate k_A.

Let us now compare the obtained experimental fifth- and sixth-order 2Q–1Q 2D spectra in order to illustrate the difference between these two signals, before we proceed to extract the annihilation dynamics from both. In the pump–probe geometry, both rephasing and nonrephasing fifth-order 2Q–1Q contributions are inherently acquired as a sum [211], resulting in the purely absorptive 2Q–1Q spectrum, i.e., the CDEEI2D spectrum, the real part of which is shown at $T = 30$ fs in Fig. 5.9a (top left). In the

fluorescence-detected case, the real parts of the separately isolated rephasing and non-rephasing sixth-order 2Q–1Q 2D spectra are added to produce the purely absorptive 2Q–1Q spectrum (Fig. 5.9a, top right).

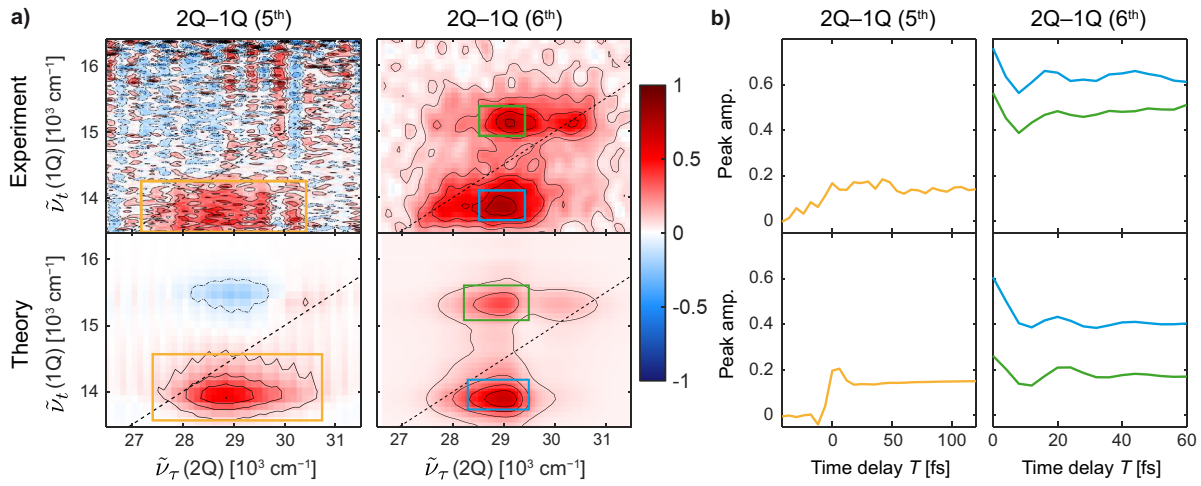

Figure 5.9. Fifth-order coherently detected and sixth-order fluorescence-detected 2Q–1Q 2D spectra of the squaraine heterodimer SQA–SQB in toluene. (a) Top left: real part of the experimental purely absorptive fifth-order 2Q–1Q 2D spectrum (i.e., the CDEEI2D spectrum). Top right: real part of the purely absorptive sixth-order 2Q–1Q 2D spectrum. Bottom: simulated 2D spectra. The dashed diagonal line is drawn at $\tilde{\nu}_\tau = 2\tilde{\nu}_t$. The 2D spectra are shown at $T = 30$ fs and normalized over all population times. (b) Spectral dynamics over T (top: experiment, bottom: simulation), obtained from integrating over certain respective regions of interest which are indicated as colored boxes in (a). Adapted and modified from Ref. [2].

Both fifth- and sixth-order 2D spectra map spectral correlations between the doubly excited manifold and the singly excited manifold. The CDEEI2D spectrum features a strong peak at around $\tilde{\nu}_\tau = 29000$ cm^{-1} and $\tilde{\nu}_t = 13500$ cm^{-1}, whereas $\tilde{\nu}_\tau$ is close to the sum of the single-exciton frequencies and can thus be assigned to the biexciton state $|\varepsilon\rangle$. The line shape of the peak is substantially broadened along the $\tilde{\nu}_\tau$-axis, which is due to the fast dephasing of the $|g\rangle\langle 2|$ coherences. The mixing of the higher excited states $|\alpha\rangle$ and $|\beta\rangle$ with the biexciton state poses an additional source of line-shape elongation along the $\tilde{\nu}_\tau$-axis. The minor vertical ripples in the CDEEI2D spectrum can be attributed to truncation artifact, which is a result of the detected signal not completely decaying until zero within the coherence time τ.

The sixth-order 2Q–1Q 2D spectrum exhibits more distinct features, being aligned at the frequencies of the single-exciton states along the $\tilde{\nu}_t$-axis. Both peaks appear at the frequency of the biexciton state along $\tilde{\nu}_\tau$ whereas the lower peak is "pulled" to lower $\tilde{\nu}_\tau$ frequencies and the upper peak features a tail towards higher $\tilde{\nu}_\tau$ frequencies. This

distortion along the $\tilde{\nu}_\tau$-axis can also be attributed to mixing within the $|2\rangle$ manifold.

The population time dynamics of the fifth- and sixth-order 2D spectra (Fig. 5.9b) are remarkably different. The CDEEI2D spectrum shows an instantaneous signal rise up to a constant signal level. This rise is entirely attributed to EEA, as further discussed below. In stark contrast to that, both peaks of the sixth-order 2Q–1Q 2D spectrum are strongly modulated by coherent oscillations which occur with an oscillation period of about 25 fs. The oscillation frequency of $\approx$1300 cm^{-1} is close to $\tilde{\nu}_{\mathrm{vib}}$, such that the origin of these oscillations can be attributed to vibronic coherence. Evidently, the evolution of the sixth-order 2Q–1Q signal during T is dominated by single-exciton dynamics, which is in line with the theoretical expectation (see Sec. 5.2).

Both signals can be simulated within the framework of time-dependent Redfield theory in the secular approximation (Fig. 5.9a, bottom) using the Frenkel-exciton model of Fig. 5.8c (for further details see Appendix C). The simulation reproduces the line shape and peak positions of the positive and negative signal features in the fifth-order 2Q–1Q 2D spectrum very well. Moreover, the simulated spectral population time dynamics (Fig. 5.9b, bottom) are in good agreement with the experimental data. The simulated CDEEI2D signal also shows an almost instantaneous rise around $T = 0$ fs. Deviations between experimental and simulated 2D spectra may arise due to the neglection of structural disorder in the simulations, which is a source of inhomogeneous broadening in such dimers [253]. Furthermore, additional vibronically excited states not accounted in the model may have an effect of the precise line shape observed in the experiment. Another source of line shape deviations between experiment and simulation could be an overestimated coupling strength to the vibrational bath. Discrepancies between the behavior of the experimental and simulated CDEEI2D transients can be ascribed to the use of unchirped probe pulses in the simulation. In particular, the residual probe chirp in the experiment may affect the structure of the coherent artifact near time zero and at which time the signal begins to rise. Noteworthily, toluene was employed as a solvent, which has a large nonresonant response that substantially contributes to early-time coherent artifacts [186, 258]. In contrast, coherent artifacts are completely absent in the transients of the sixth-order spectra, since the signal is measured by incoherent fluorescence. The simulated sixth-order 2Q–1Q 2D spectrum excellently reproduces the oscillatory behavior of the experimental signal. Overall, in view of the reproduction of essential spectral features, peak distortions and the behavior of the population time dynamics, the experimental data can be well described using the excitonic model of Fig. 5.8c.

Let us now focus on the EEA dynamics. The experimental integrated CDEEI transient

of Fig. 5.9b is replotted in Fig. 5.10a, shown along with the two double-sided Feynman diagrams in the manifold basis which describe the signal behavior, and which result after cancellation of other pathways [102]. The signs of these pathways take into account the nature of the differential pump–probe 2D signal. The propagation of R_{GSB} can be considered as constant during T whereas R_{EEA} evolves with the biexciton population dynamics. At $T = 0$, both pathways have identical weight and cancel each other. However, as T progresses, population is continuously removed from $|2\rangle\langle 2|$ due to EEA. Accordingly, the interference between these two pathways is responsible for the signal rise on a constant background over T. In the case of $\mu_{bg} = \mu_{ag} = \mu$, the dynamics of the integrated CDEEI signal can thus be expressed in the impulsive limit as

$$S^{\mathrm{CDEEI}}(T) \propto -8\mu^6 \left[-1 + \mathrm{e}^{-k_A T}\right], \tag{5.20}$$

which is, in magnitude, identical to the signal dynamics of the integrated FDEEI signal [Eq. (5.19)]. Note that Eq. (5.20) only holds in the impulsive limit. In real experiments, however, one has to consider the finite duration of the laser pulses, which is described by the instrumental response function (IRF). To extract the annihilation time τ_A from the CDEEI transient, the data must thus be fitted by means of a convolution of the IRF with the EEA propagator $\mathcal{U}_{1122}(T) = a\Theta(T)\left(b - \exp(-\frac{T-T_0}{\tau_A})\right)$. In order to construct an analytical fit expression, the IRF is assumed to be Gaussian with width σ, leading to

$$\begin{aligned} f(T) = a\Bigg[& -\frac{1}{2}\exp\left(-\frac{T-T_0}{\tau_A} + \frac{\sigma^2}{2\tau_A^2}\right)\left(1 + \mathrm{erf}\left\{\frac{1}{\sqrt{2}}\left(\frac{T-T_0-\frac{\sigma^2}{\tau_A}}{\sigma}\right)\right\}\right) \\ & + \frac{1}{2}b\left(1 + \mathrm{erf}\left\{\frac{1}{\sqrt{2}}\left(\frac{T-T_0}{\sigma}\right)\right\}\right)\Bigg]. \end{aligned} \tag{5.21}$$

Taking into account the fourfold convolution of the pump electric field with the twofold convolution of the probe electric field, the fit shown in Fig. 5.10a (middle), yields an annihilation time of $\tau_A = 28$ fs.

As mentioned above, in case of the fluorescence-detected sixth-order 2Q–1Q signal, the single-exciton dynamics considerably obscure the underlying annihilation dynamics which hampers the extraction of the annihilation time from this signal alone. However, as shown in Sec. 5.2, the single-exciton contributions can be eliminated by the construction of the FDEEI signal. For that purpose, we take the real parts of the rephasing sixth-order 2Q–1Q and 1Q–2Q 2D spectra and perform the transformation and subtraction procedure of Eq. (5.17), as illustrated in Fig. 5.10b (top). In view of the nearly identical magnitude of the transition dipole moments μ_{ag} and μ_{bg}, it can be expected that the FDEEI signal reflects EEA dynamics in the order of 95% (see Fig. 5.6).

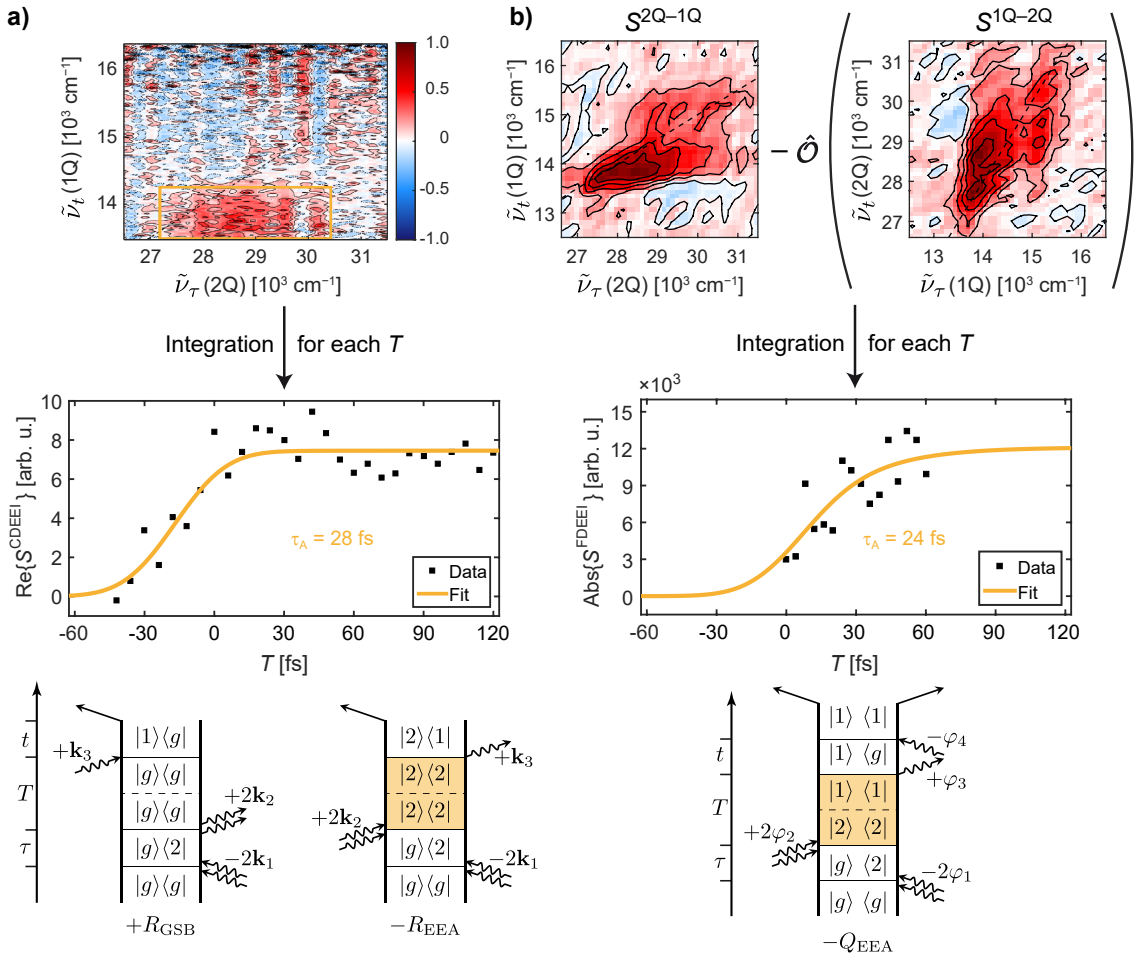

Figure 5.10. Extracting the annihilation time from the CDEEI and the FDEEI signals. (a) Top: real part of the CDEEI spectrum at $T = 30$ fs, normalized to the maximal value, with the region of interest considered for signal integration denoted by the yellow rectangle. The annihilation time τ_A is determined by fitting the obtained data using Eq. (5.21), as shown in the middle panel. The CDEEI signal can be described by the double-sided Feynman diagrams shown at the bottom, with diagram signs according to the pump–probe convention. (b) Top: real parts of the rephasing sixth-order 2Q–1Q and 1Q–2Q 2D spectra at $T = 20$ fs (normalized to their maximal absolute values). The subtraction according to Eq. (5.17) yields the FDEEI signal, which is shown in absolute values in the middle panel, and can be fitted using the same fit expression of Eq. (5.21). Bottom: double-sided Feynman diagram describing the FDEEEI signal. Adapted and modified from Ref. [2].

Analogously to the CDEEI signal, the FDEEI rises in magnitude from zero with the annihilation time. Note that the magnitude representation of the FDEEI signal further allows us to use the same fit function as the one used for fitting the CDEEI signal. In contrast to the CDEEI signal, where probe chirp may shift the rising signal relative to $T = 0$ fs [259], the FDEEI signal begins to rise closer to $T = 0$ fs because all excitation pulses are compressed. Hence, taking into account that the FDEEI signal results

from a six-fold convolution with the excitation field, fitting the FDEEI transient with Eq. (5.21) yields an annihilation time of $\tau_A = 24$ fs, which is in fair agreement with the time determined from the CDEEI signal. The annihilation times determined from both experiments are further in accordance with previous findings [7, 241] and, moreover, with the recently reported annihilation time of 30 fs in squaraine trimers, which was determined by noncollinear coherently detected fifth-order 2D spectroscopy [251]. Generally, both time constants determined here provide experimental evidence that exciton–exciton annihilation occurs almost instantaneously in the SQA–SQB heterodimer, which is most reasonably due to the creation of these excitons in close proximity to one another.

5.4 Conclusion

Summarizing, a novel nonlinear signal that selectively probes the dynamics arising from exciton–exciton annihilation, the fluorescence-detected exciton–exciton interaction (FDEEI) signal, was introduced. The proposed FDEEI2D spectroscopy is based on a four-pulse sequence with 125-fold phase cycling and can be performed by only using a single excitation beam. A post-processing strategy to isolate the exciton–exciton annihilation contribution from two sixth-order nonlinear signals was developed. This strategy relies on the subtraction of a suitably transformed sixth-order 1Q–2Q 2D spectrum from the sixth-order 2Q–1Q 2D spectrum for each population time step. To explore the limits of the approach, a mathematical expression for the FDEEI signal amplitude was derived and it was quantified, to which extent annihilation kinetics contribute to the FDEEI signal. As long as the single-exciton transition dipole moments have approximately the same magnitude, the FDEEI signal practically entirely describes the annihilation kinetics.

The applicability of the approach was verified on an exemplary squaraine heterodimer with aid of coherently detected EEI2D spectroscopy, acquired in a setup with as much common beam paths and optics as possible. The annihilation times determined from these two experiments are in mutual agreement and in accordance with recent observations on related squaraine trimers in the literature.

Altogether, FDEEI2D spectroscopy enables one, under certain approximations, to directly temporally resolve nearly instantaneous annihilation dynamics, analogously to coherently detected EEI2D spectroscopy, but here using an incoherent observable. As an advantage, FDEEI2D spectroscopy is free of undesired solvent signals and coherent artifacts which perturb the analysis of early population time dynamics.

Chapter 6

General Discussion and Outlook

6.1 Discussion

In the past, optical coherent multidimensional spectroscopy has undoubtedly proven useful for studying details about the electronic structure of quantum systems. Many variants of coherently detected multidimensional spectroscopy have been developed to investigate the spectral and dynamical properties of the landscape of electronically excited states. This work adds several new approaches to the toolkit of coherent multidimensional spectroscopy, which, in fact, can all be performed with a unified, systematic experimental procedure.

In this work, the concept of coherent multiple-quantum multidimensional fluorescence spectroscopy was established. The measurement of several novel sixth-order nonlinear signals has been demonstrated in order to characterize high-excited electronic states in molecules [3, 4], molecular aggregates [2], and semiconductor nanocrystals [1] in the liquid phase. The experiments reported herein demonstrate that one can acquire a high density of information about the nonlinear response of a quantum system – enclosing multiple nonlinear orders – in just a single experiment, and with just a single excitation beam. Thus, the approaches of this work mark a significant step towards fulfilling the vision of a complete characterization of the nonlinear response of a system. The developed approaches pose complementary or even exclusive additions to the family of coherent multidimensional spectroscopies. From a technical viewpoint, fluorescence detection provides significant advantages such as interpulse phase stability due to the single-beam fashion, the absence of nonresonant response and scattering, and the simultaneous acquisition of multiple nonlinear signals under identical experimental conditions.

As shown in this work, the essential requirement to resolve a multitude of nonlinear

signals at once is to systematically extend the sampling space of interpulse phases, that is, the use of special phase-cycling procedures. Two new phase-cycling schemes have been developed, which have been shown to isolate selectively information about high-excited electronic states such as their energies, correlations and ultrafast dynamics [1–4]. In Sec. 1.2.5 of Chapter 1, a diagrammatic approach to phase-cycling schemes was introduced on the basis of the mathematical theory developed by Tan [29]. With such an approach, one can conveniently determine which nonlinear signal contributions are aliased in case of insufficient phase cycling. In turn, it is envisioned that these diagrams may be of practical use to determine suitable phase-cycling schemes, which resolve nonlinear signals up to an arbitrary order of nonlinearity without aliasing.

In Chapter 2, multiple-quantum 2D fluorescence spectroscopy was developed as a means to investigate the excited-state landscape of molecular systems in the liquid phase [3]. For that purpose, a 36-fold phase-cycling scheme was implemented to discriminate against three fourth- and six sixth-order signals. A particular goal was to prove that the obtained nonlinear signals are free of unwanted wave-mixing cascades or other signals that would potentially emulate multiple-quantum coherence such as previously debated collective excitations [79]. The absence of these unwanted signals was verified by measuring the concentration dependence of all nine fourth- and sixth-order nonlinear signals, which was found to be linear for all signals. Besides that, a general simulation strategy for multiple-quantum 2D spectra was developed. When simulating the data, one can take advantage of the fact that nine different signals are simultaneously acquired. Simulating with respect to a mutual agreement with the experimental data poses a reliable approach to minimize ambiguity in the system description. This is especially important for multiple-quantum 2D spectroscopy, as the experiment actually probes 2D projections of a fourth- and sixth-order response function, which have in fact a higher dimensionality than two. This projective ambiguity was overcome by approximating a best possible description of all projections at the same time. Although the simulation of the experimental data was achieved by varying one simulation parameter of another, however, the underlying problem has actually to be treated on a multidimensional parameter space, which is a challenging task. A multidimensional parameter optimization with aid of neural networks may help to address these concerns [260].

In Chapter 3, the concept of multiple-quantum 2D fluorescence spectroscopy was generalized as multiexciton 2D fluorescence spectroscopy. On the example of colloidal semiconductor quantum dots, it was shown that multiexciton 2D spectroscopy systematically dissects the manifold of multiexciton states [1]. In this respect, the 1Q–2Q and 1Q–3Q signals were utilized as selective probes for biexciton and triexciton states. These

signals facilitate one to directly spectrally resolve the electronic structure of biexcitons, and, in general, to understand the highly correlated nature of excitons in such confined nanosystems. Distinct spectral signatures witnessed the existence of strong anticorrelations between energy fluctuations of the transitions into excitons and biexcitons. On the other hand, transition energy fluctuations between biexcitons and triexcitons were found to be strongly correlated. These findings may have important implications for the design of novel quantum dot materials, since the obtained results indicate that changes in the single-exciton structure has a significant effect on the multiexciton structure. An extension of the approach described therein to quadexcitons, that is, particle complexes consisting of four electron–hole pairs, is in principle realizable with the currently existing setup. To isolate such eight-order quadexciton 2D spectra, a 64-fold phase-cycling scheme (1×8×8) would be necessary.

While the approach of Chapters 2 and 3 yielded 2D projections of both the fourth-order and the sixth-order nonlinear responses, which both actually have higher dimensionality, the extension into a third spectral dimension via addition of a fourth laser pulse achieves spectral decongestion. With that, one can visualize the full dimensionality of at least the fourth-order nonlinear response. Moreover, by introducing an additional time delay into the pulse sequence, the sixth-order signals now become susceptible to the population dynamics of doubly excited states. This three-dimensional coherent fluorescence spectroscopy was developed by using a 125-fold phase-cycling scheme and demonstrated as a means to obtain a maximum density of nonlinear signals of multiple orders in a short period of acquisition time [4]. In this respect, the short acquisition time facilitated to study the nonlinear response of a molecular system with limited stability, such as the dianion of TIPS-tetraazapentacene. Sample degradation was found to have a minor effect on the obtained data, since the sampling of experimental delays and phases occurs on a much faster time scale due to 1 kHz shot-to-shot acquisition. 3D fluorescence spectroscopy was shown to resolve signal ambiguity by an increased overall frequency resolution through the third spectral dimension. This is especially advantageous for liquid phase systems as their spectra are often congested with overlapping features due to relatively broad linewidths caused by the solvent environment. By unfolding the fourth-order response into three frequency dimensions, all possible permutations of 0Q, 1Q, and 2Q coherence correlations could be constructed. Moreover, any possible fourth-order 2D spectra with parametric dependence on any of the three time-delays can be obtained via projecting the 3D dataset onto certain frequency axes. Notably, also those projections that evolve with the "detection time" t can be obtained in 3D fluorescence spectroscopy as well. Such projections are not accessible in coherently detected spectroscopy, since the "de-

tection axis" is directly acquired in frequency space due to heterodyne detection. The experimental 3D spectra were evaluated with aid of quantum chemical calculations and quantum dynamical simulations of the 3D spectra close to the experiment. The spectra analysis revealed properties of a two-photon excited singlet state of a dianionic molecule. A π phase-shift of excited-state wave-packet oscillations was observed between fourth- and sixth-order signals, further validating the isolation of cascade-free sixth-order signals. Additional theoretical analysis led to the conclusion that many-particle signals do not contribute to the signal as long as no coincidence detection is employed. Thus, Chapters 2 to 4 together provide strong evidence that fluorescence-detected multidimensional spectroscopy is able to probe multiple-quantum coherences.

In Chapter 5, the four-pulse sequence with 125-fold phase cycling was utilized to construct a novel nonlinear signal, which exclusively probes exciton–exciton annihilation in molecular aggregates. As shown in Chapters 2 and 3, population-based detection grants access to 1Q–NQ type signals, which represent the inverted signals of NQ–1Q contributions. However, 1Q–NQ signals generally feature fewer pathways. This circumstance was particularly exploited in Chapter 5, where the use of the 125-fold phase-cycled four-pulse sequence led to the isolation of both 2Q–0Q–1Q and 1Q–0Q–2Q signals, where the former is annihilation sensitive, and the latter is annihilation insensitive, however, both signals probe single-exciton dynamics. In order to remove single-exciton contributions, a post-processing strategy was developed, which effectively produced an annihilation-selective sixth-order signal. This was made possible by the simultaneous acquisition of multiple sixth-order signals under *identical* experimental conditions. Due to the rapid acquisition, experimental drifts in spatial and energetic laser properties do not diverge among the various nonlinear contributions, which would otherwise have a detrimental effect on the subtraction procedure. An analytic expression of the thus-constructed fluorescence-detected exciton–exciton annihilation 2D (FDEEI2D) signal was derived, and the limits of the approach were discussed. The approach was demonstrated on a squaraine heterodimer and verified by a control experiment with previously established coherently detected EEI2D spectroscopy. The obtained annihilation time of 24 fs was in line with previous observations in the literature [241, 251]. It was concluded that FDEEI2D spectroscopy can be best applied to molecular aggregates, in which the excitonic transition dipole moments are nearly the same. Nonetheless, many systems such as homo-oligomers and homo-polymers are included in this category and could thus be investigated in future experiments. Importantly, FDEEI2D spectroscopy is suitable to directly temporally resolve nearly-instantaneous exciton–exciton annihilation dynamics due to the absence of coherent artifacts.

In this work, a central aspect for signal evaluation and interpretation was the use of nonperturbative simulations. The simulation strategies presented in this work may provide guidance for the interpretation of high-order multidimensional spectra of similar systems. Apart from that, the framework for the simulation of multidimensional spectra based on the numerical solution of the Lindblad equation was prepared in a form that could be used by the general public [5]. This "quantum dynamics toolbox" (QDT) has been further developed as a modular MATLAB program which performs mathematical procedures like operator constructions and Hilbert space expansions automatically and further features a minimized user input [5]. Tutorials and code examples can be found at qd-toolbox.org, which sets the stage to utilize QDT for teaching purposes. In particular, QDT was modified to be executed on large CPU clusters by parallelization of computation tasks in MATLAB. Beyond that, in future, further runtime optimization could be achieved by implementing the central routine which solves the differential equations, i.e., the fourth-order Runge–Kutta solver, into a computationally more efficient external C++ interface in order to further significantly increase computation speed [261].

In general terms, all experimental approaches discussed in this work can be directly transferred to the detection of other incoherent signals, facilitating multiple-quantum 2D and 3D spectroscopy in all states of matter, just by modifying the detecting part of the setup. In particular, solid-state samples could also be measured in combination with fluorescence microscopy in order to characterize correlations, binding energies and dynamics of multiexcitonic states. Especially the method of FDEEI2D spectroscopy developed in this thesis (Chapter 5) offers new perspectives for the characterization of ultrafast exciton–exciton annihilation in solid-state samples. Importantly, FDEEI2D spectroscopy is a single-beam technique. This aspect makes the approach particularly suitable for combination with ultrafast 2D microscopy, as demonstrated earlier for fourth-order signals [158, 217]. Future experiments could address the measurement of ultrafast exciton–exciton annihilation processes in solid-state materials with combined spatial resolution, which enables one to investigate the impact of structural factors on the annihilation dynamics. Moreover, instead of fluorescence detection, internal photocurrents [87, 89, 262, 263], photoelectron emission of solid-state samples [228], or mass-resolved photoions of gas-phase systems [86, 229] are further suitable population-based signals being analogous to fluorescence, since all these observables have in common that they originate from an excited-state population. The concepts presented in this thesis can thus be utilized to develop related methods like "multiple-quantum multidimensional nanoscopy" or "multiple-quantum multidimensional mass spectrometry."

6.2 Outlook

The seeds of scientific progress are elaborated concepts for novel approaches. The development of new spectroscopic methods, as discussed in this work, benefits enormously from theoretical predictions, with the help of which potential experimental challenges can be addressed in a more targeted manner. The following sections briefly outline the concepts of two novel approaches that shall add to the toolkit of coherent fluorescence-detected multidimensional spectroscopy. These proposed techniques are multiexciton-generation three-dimensional fluorescence spectroscopy (MEG3DFS) and five-dimensional fluorescence-detected all-resonant electronic spectroscopy (5D FLARES).

6.2.1 Multiexciton-Generation Three-Dimensional Fluorescence Spectroscopy (MEG3DFS)

Semiconductor nanocrystals feature bound particle complexes that consist of multiple electron–hole pairs, i.e., multiexcitonic states, which can be generated via multiphoton excitation, as discussed in Chapter 3. Under certain conditions, however, these multiexcitonic states can be generated even though only a single photon is used for excitation. This process, also known as multiexciton generation (MEG), which has been first observed in PbSe nanocrystals [264], brought nanocrystals into the focus of artificial solar energy conversion [265–267]. Since then, the mechanism behind MEG has been discussed controversially in the literature. In particular, several mechanisms have been suggested [267, 268]: incoherent models, such as impact ionization (i.e., an inverse Auger process) [264, 269] and Coulomb coupling of virtual single-exciton states to multiexciton states [121], and a coherent model, which considers that coherent superpositions of multiexciton and single-exciton states are involved [270, 271]. To date, the detailed mechanism behind MEG has not yet been fully deciphered – both coherent and incoherent models are still the subject of discussion in recent literature [272–276].

The potential existence of coherent superpositions between single-exciton and biexciton states should in principle give rise to oscillatory signatures, which may be measurable by femtosecond spectroscopy [270]. However, specific spectroscopic tools that provide unambiguous proof for coherences between single-exciton and biexciton states are scarce, possibly due to the lack of experimental selectivity and the high time resolution needed to resolve such coherences, which decay within 100 fs [272]. Here, a concept for a novel sixth-order 3D experiment is proposed, which is expected to shed light on the role of quantum coherence in MEG, since this experiment has extraordinary selectivity to only those pathways, that result from coherences between single-exciton and biexciton states.

The core idea of multiexciton 3D fluorescence spectroscopy (MEG3DFS) is based on two-color 2D spectroscopy [207, 212, 277]. However, the novel aspect of MEG3DFS is the combination of two-color excitation with one-photon and two-photon selection rules in quantum dots. In this respect, considering that one-photon processes only excite single-exciton states and two-photon processes only excite biexciton states, the use of both UV ("one-photon") and VIS ("two-photon") pulses within the excitation sequence (Fig. 6.1a) enables one to construct and probe correlations between high-excited single-exciton and biexciton states. This shall be shown on the example in Fig. 6.1b, which resembles a generic energy level scheme of a quantum dot in the exciton basis.

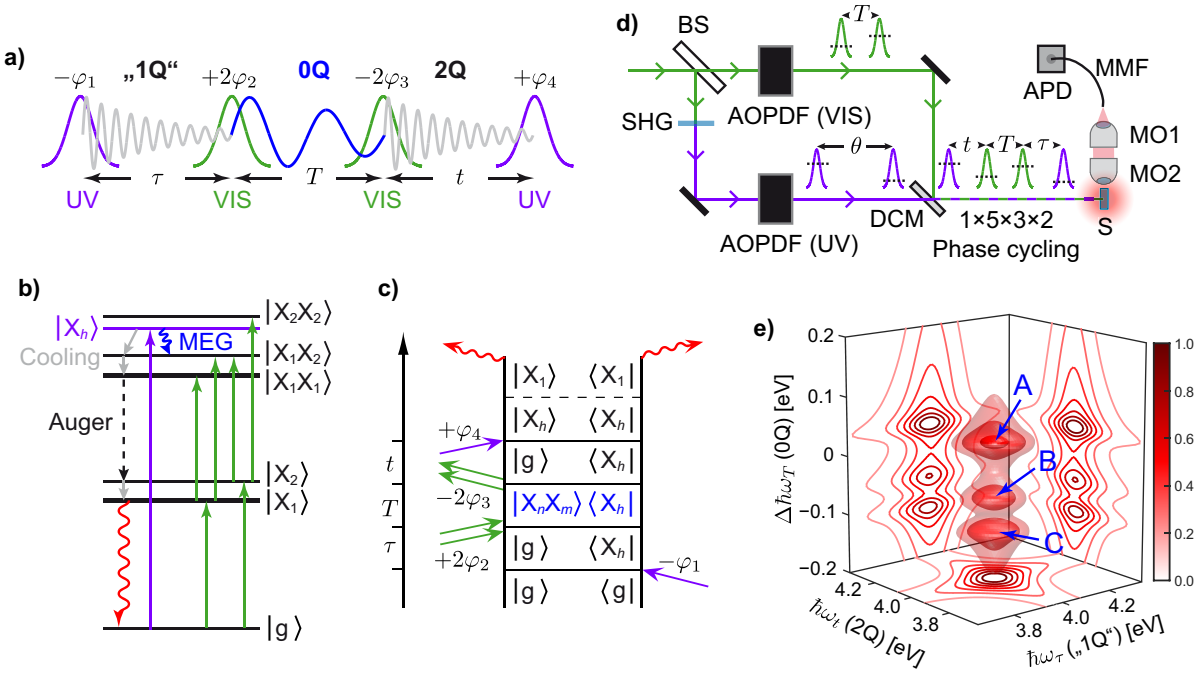

Figure 6.1. Concept of multiexciton generation (MEG) 3D fluorescence spectroscopy (MEG3DFS). (a) Pulse sequence of MEG3DFS. The combined use of ultraviolet (UV, violet) and visible (VIS, green) pulses gives rise to a "1Q"–0Q–2Q-type contribution with phase signature as indicated on top of the pulses. (b) Energy level scheme of an exemplary semiconductor quantum dot in the exciton basis with ground state $|\mathrm{g}\rangle$, low-energy single-exciton states $|\mathrm{X}_1\rangle$ and $|\mathrm{X}_2\rangle$, a high-energy single-exciton state $|\mathrm{X}_h\rangle$, and the biexciton states $|\mathrm{X}_1\mathrm{X}_1\rangle$, $|\mathrm{X}_1\mathrm{X}_2\rangle$ and $|\mathrm{X}_2\mathrm{X}_2\rangle$. Hot exciton cooling is indicated by gray solid arrows, whereas Auger relaxation is drawn as a black dashed arrow. Fluorescence emission is denoted by a red wavy arrow. An exemplary MEG channel is shown in blue. (c) Double-sided Feynman diagram which corresponds to the only pathway contributing to the MEG3D signal. The biexciton–single-exciton coherence is highlighted in blue. (d) Experimental schematic of MEG3DFS. BS: beam splitter; SHG: second-harmonic generation crystal; AOPDF: acoust-optic programmable dispersive filter; DCM: dichroic mirror; S: sample; MO: microscope objective; MMF: multimode fiber; APD: avalanche photodiode. (e) Simulated MEG3D spectrum in absolute values. Peaks A, B, and C correspond to biexciton–single-exciton coherences $|\mathrm{X}_2\mathrm{X}_2\rangle\langle\mathrm{X}_h|$, $|\mathrm{X}_1\mathrm{X}_2\rangle\langle\mathrm{X}_h|$, and $|\mathrm{X}_1\mathrm{X}_1\rangle\langle\mathrm{X}_h|$, respectively.

The transitions between the ground state $|\mathrm{g}\rangle$ and the single exciton states $|\mathrm{X}_1\rangle$ and $|\mathrm{X}_2\rangle$ as well as the transitions between the single-exciton states and the biexciton states $|\mathrm{X}_n\mathrm{X}_m\rangle$ $(n, m = 1, 2)$ are caused by the visible pulses (green in Fig. 6.1). On the other hand, the excitation from the ground state to the high-excited single-exciton state $|\mathrm{X}_h\rangle$ is accomplished by the UV pulses (violet). The detailed action of the MEG3D pulse sequence is visualized by the double-sided Feynman diagram given in Fig. 6.1c. The first UV pulse creates a coherence between $|\mathrm{g}\rangle$ and $|\mathrm{X}_h\rangle$, which evolves over τ. The second pulse is a VIS pulse and thus converts this coherence into a biexciton–single-exciton coherence $|\mathrm{X}_n\mathrm{X}_m\rangle\langle\mathrm{X}_h|$ by a resonant two-photon transition from $|\mathrm{g}\rangle$ via the single-exciton states. The resulting $|\mathrm{X}_n\mathrm{X}_m\rangle\langle\mathrm{X}_h|$ coherence evolves over T. The third pulse, also a VIS pulse, converts this coherence back into the coherence between the $|\mathrm{g}\rangle$ and $|\mathrm{X}_h\rangle$, evolving during t, before the last UV pulse creates an excited-state population, which nonradiatively decays into $|\mathrm{X}_1\rangle$ with subsequent fluorescence emission.

Due to the first UV and the second double-VIS interaction, it is not possible to generate a single-exciton population or a biexciton population that would evolve over T. In other words, given by the one- and two-photon selection rules, the MEG3DFS sequence features a high selectivity towards the single class of Liouville pathways shown in Fig. 6.1c, and thus, MEG3DFS is quantum-coherence selective. As a consequence, there is *only* a signal if a coherent superposition between single-exciton and biexciton states is present.

Experimentally, MEG3DFS can be realized using a setup with two acousto-optic programmable dispersive filters (AOPDFs), which create time-delayed VIS and UV pulse pairs, as schematically shown in Fig. 6.1d. The first AOPDF creates visible two-pulse sequences, separated by delay T. The second AOPDF creates an UV pulse pair separated by delay $\theta = t + T + \tau$. The input UV beam can be created, for example, by second-harmonic generation (SHG) of the visible pulses. Both AOPDF's are synchronized with respect to the repetition rate of the laser. To isolate the MEG3D contribution with phase $-\varphi_1 + 2\varphi_2 - 2\varphi_3 + \varphi_4$, a 1×5×3×2 phase-cycling scheme is sufficient according to the phase-cycling scheme selection procedure [29]. By using a dichroic mirror (DCM), the UV and VIS beams are collinearly recombined and focused on a sample (S). Fluorescence detection can be carried out analogously as previously described [1].

The MEG3D spectrum of the model system of Fig. 6.1b is displayed in Fig. 6.1e. This spectrum was simulated using the Lindblad master equation (see Sec. 2.5.3) by employing an external electric field with $\omega_0 = 2.0$ eV$/\hbar$, but in which the first and the last pulse are frequency doubled with respect to the two middle pulses (Fig. 6.1a). Deviating from Fig. 6.1b, coherences of $|\mathrm{X}_h\rangle$ with all biexciton states are imposed in the model

to illustrate the general selectivity towards all biexciton–single-exciton coherences. The MEG3D spectrum only features three peaks, which are precisely aligned at the energies of the biexciton–single-exciton 0Q coherences $|X_2X_2\rangle\langle X_h|$ (A), $|X_1X_2\rangle\langle X_h|$ (B), and $|X_1X_1\rangle\langle X_h|$ (C) along the $\Delta\hbar\omega_T$ axis. The arrangement of the MEG3D peaks further gives insight into the electronic structure of the biexciton states relative to the high single-exciton state accessed by the UV pulse. On the one hand, the 3D peak A is shifted to a positive 0Q energy, which indicates that $|X_2X_2\rangle$ is energetically above $|X_h\rangle$. On the other hand, the peaks B and C are shifted to negative 0Q energies, signifying that $|X_1X_2\rangle$ and $|X_1X_1\rangle$ have a lower energy than $|X_h\rangle$. The bottom projection of the MEG3D solid is rather featureless due to the fast dephasing of $|X_h\rangle$, which gives rise to a broad line shape. It can be expected that the line shape of a MEG3D peak along $\Delta\hbar\omega_T$ is further a sensitive probe for the MEG efficiency, since MEG is connected to the dephasing of the biexciton–single-exciton coherence [278].

Concluding, MEG3DFS spectroscopy is proposed as a means to investigate selectively coherent superpositions between high-excited single-exciton states and biexciton states and thus may contribute to unravel the microscopic origin behind MEG in semiconductor nanocrystals.

6.2.2 Five-Dimensional Fluorescence-Detected All-Resonant Electronic Spectroscopy (5D FLARES)

In this thesis, it was shown that the sixth-order nonlinear response bears exclusive information about the electronic structure and dynamics of high-excited electronic states. However, a general problem of higher-order spectroscopies is the exponential increase of the number of pathways with the number of interactions [279], leading to many overlapping pathways and in turn signal ambiguities. These ambiguities, for example, may complicate the identification of the origin of 0Q coherences [208, 280, 281]. Apart from signal subtraction strategies such as the one presented in Chapter 5, the problem of spectral congestion can be solved by matching the dimensionality of a multidimensional spectrum to the dimensionality of the response.[1]

In Chapter 4 of this thesis, it was shown that 3D fluorescence spectroscopy provides the maximum pathway separation of the fourth-order nonlinear response by unfolding the complete dimensionality of the response. In the limit of strict time ordering, *complete* in this case means that all dynamic events which occur between four successive light-field

[1] In NMR spectroscopy, an increased spectroscopic dimensionality provides sufficient resolution and selectivity to facilitate the determination of the geometrical structure of complex proteins [282–284]. In Ref. [282], a single 4D NMR experiment "only" took 6 days.

interactions can be separately resolved over three distinct time intervals. In other words, the general requirement is one excitation per pulse. In an analogous way, the complete measurement of the sixth-order response function can be achieved by using a six-pulse sequence which unfolds the dynamics evolving between the pulses over five temporal dimensions. In virtue of the fact that the experimental setup used in this work offers an inherent phase stability, it makes sense to logically extend the approaches described in this thesis to higher spectral dimensions.

Recent work by Harel et al. has shown that it is indeed possible to conduct 4D spectroscopy using optical pulses [101, 285]. Their approach is based on nonresonant pre-pumping using two near-IR pulses, followed by a visible three-pulse sequence, which yields a fifth-order nonlinear signal that encodes electronic and Raman coherences over two dimensions each [101]. Exorbitant acquisition times are avoided by using a single-shot acquisition scheme, where tilted pulse fronts are employed to spatially encode a continuous range of interpulse delays into the sample [286].

Here, a fluorescence-detected approach is proposed which employs an all-resonant excitation sequence, and completely unfolds the sixth-order response over five temporal dimensions. This method shall be called five-dimensional fluorescence-detected all-resonant electronic spectroscopy (5D FLARES). The FLARES sequence is shown in Fig. 6.2a. To acquire a 5D dataset, six collinear phase-coherent pulses with delays τ, T, t, Θ, and ϑ are employed. By using a $1{\times}3{\times}3{\times}3{\times}3{\times}3 = 243$-fold phase-cycling scheme, a multitude of different sixth-order signal contributions can be distinguished. To illustrate the concept of FLARES, we shall only consider the "1Q–0Q–1Q–0Q–1Q"-type contribution with phase signature $-\varphi_1 + \varphi_2 + \varphi_3 - \varphi_4 + \varphi_5 - \varphi_6$ in the following. Apart from this signal, the 243-fold phase cycling resolves three additional 1Q–0Q–1Q–0Q–1Q-type contributions which can be added to obtain a purely absorptive 5D dataset, as demonstrated for fifth-order spectroscopy [113, 214]. Moreover, if time delays are sampled appropriately with regard to the Nyquist limit [287], multiple-quantum contributions such as "1Q–2Q–3Q–2Q–1Q" can be resolved as well. A challenge for the feasibility of a FLARES experiment lies in the vast amount of sampling steps. However, the reduction of acquisition times can be accomplished by utilizing high-repetition-rate shot-to-shot pulse shaping with rotating frame acquisition [288], possibly in combination with cogwheel phase cycling [57, 289], whereas the latter would lead to less necessary phase-cycling steps, ultimately yielding acquisition times in the order of minutes.

We shall not discuss all features of the method in detail but rather focus on a few new aspects that 5D FLARES offers us. For that purpose, the sensitivity of a 5D FLARES spectrum towards (i) changes in the curvature of the electronically excited state potential

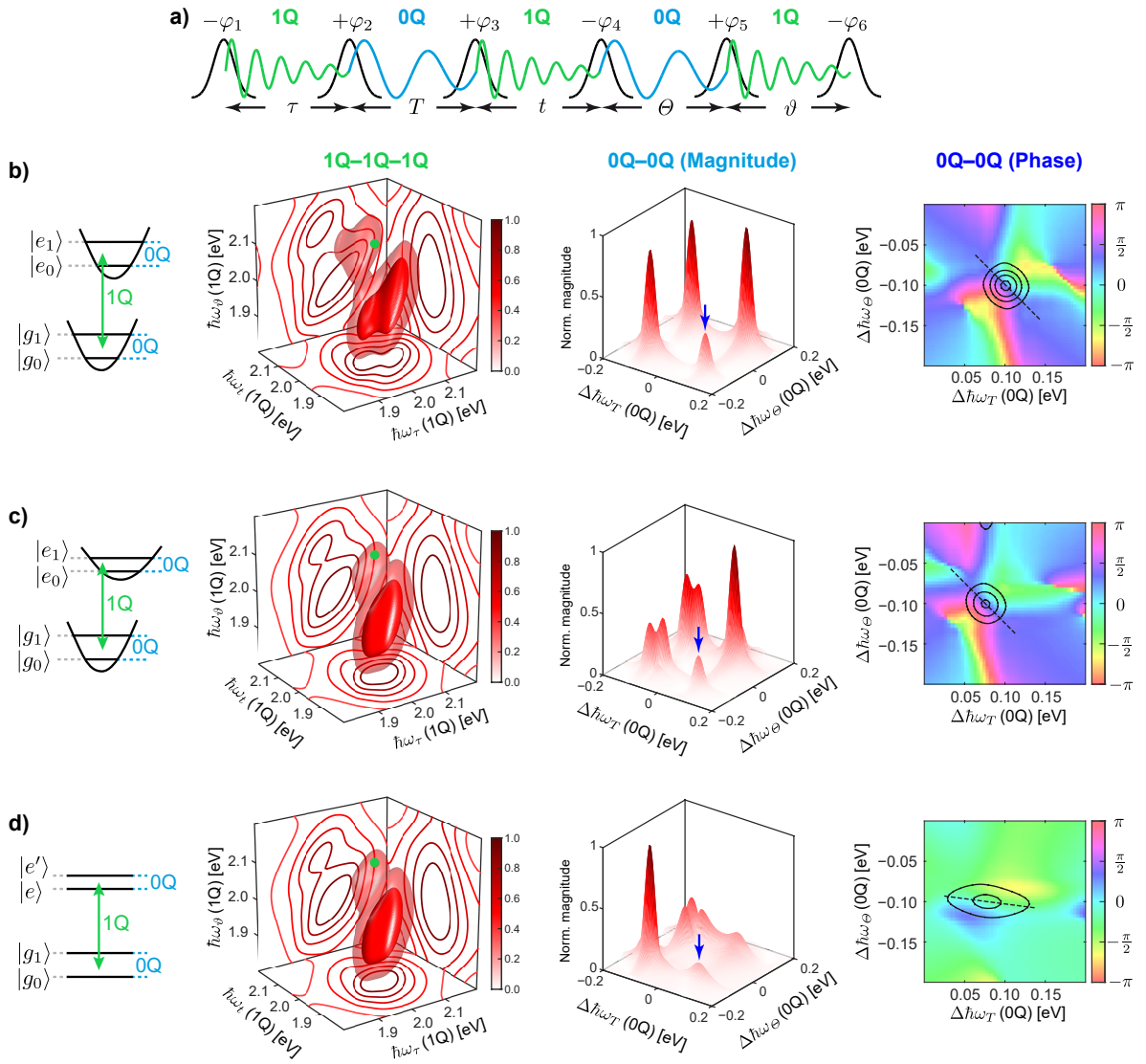

Figure 6.2. Five-dimensional fluorescence-detected all-resonant electronic spectroscopy (5D FLARES). (a) FLARES pulse sequence with coherence times τ, t, and ϑ, and population times T and Θ. The phase signature of one possible FLARES contribution is indicated on top of the pulses. (b–d) Calculated FLARES spectra of three different model systems (far left column), separated into the absolute-valued 1Q–1Q–1Q electronic 3D spectrum at ($T = 0$ fs, $\Theta = 0$ fs) (middle left column), and a 0Q–0Q 2D spectrum (absolute values, middle right column), taken at the voxel marked by the green dot in the 3D spectrum. The phase of the peak highlighted by a blue arrow is shown in the far right column where the dashed line indicates the tilt of the phase twist. The model systems are (b) two displaced electronic states, consisting of ground $|g_v\rangle$ and excited state $|e_v\rangle$ ($v = 0, 1$), both with a single vibrational mode with the same frequencies, (c) two displaced electronic states in which the excited electronic state has a vibrational mode with a frequency lower than that of the electronic ground state, and (d) an excitonic model system with a vibration in the ground-state and two different excitonic states $|e\rangle$ and $|e'\rangle$.

and (ii) the manifestation of interexcitonic coherence is illustrated by means of the three model systems shown in the far left column of Fig. 6.2b–d. Similar analysis was discussed in detail with regard to coherently detected 4D spectroscopy by Harel [279]. Figure 6.2b features a displaced electronic model consisting of a ground state $|g_v\rangle$ and an electronic state $|e_v\rangle$ ($v = 0, 1$) with a single vibrational sublevel having identical frequencies in the ground and electronic state. Figure 6.2c corresponds to same displaced electronic model but where the excited state vibration is softened relative to the ground-state vibration. In Fig. 6.2d, an excitonic model with a vibrationally excited electronic ground state and two single-exciton states $|e\rangle$ and $|e'\rangle$ is considered.

The 5D sixth-order response function for all systems can be calculated by constructing all pathways for a generic four-level system, which can be performed similar to Eqs. (1.20)–(1.23) in Sec. 1.2.3, and by summing over all these pathways. In the response function calculation, inhomogeneous broadening with $\sigma = 50$ meV is incorporated and the dephasing time of 1Q coherences is 20 fs. In the three model systems, the $|g_0\rangle \rightarrow |e_0\rangle$ and $|g_0\rangle \rightarrow |e\rangle$ transition has an energy of 2.0 eV. The Huang–Rhys factor for Fig. 6.2b and c is chosen to be 0.8, and the transition dipole moment scalings for all other electronic transitions is calculated according to Eqs. (4.9)–(4.11). In the excitonic model (Fig. 6.2d), the transition dipole moments into the excitonic states $|e\rangle$ and $|e'\rangle$ are chosen so that they correspond to those of the other two model systems. For all model systems, the energy of the ground-state vibration is 100 meV. The excited state vibration is set to 100 meV in Fig. 6.2b and to 75 meV in Fig. 6.2c, whereas the latter is identical to the excitonic splitting of $|e\rangle$ and $|e'\rangle$ in Fig. 6.2d. Vibrational dephasing is modeled to be 2 ps in the ground state and 1 ps in the excited state, while excitonic dephasing proceeds with 25 fs.

Let us now discuss the 5D FLARES spectra of these model systems. How can we visualize a 5D dataset? At least for humans, the visualization of multidimensional spectra beyond three frequency dimensions can only be accomplished by means of suitable lower-dimensional projections, which virtually calls the sense of 5D spectroscopy into question. Nonetheless, as demonstrated by Spencer et al. on 4D data [101], we can preserve a high informative content of the dataset by "slicing" it with regard to the individual coherence types, which effectively yields a "spectrum within a spectrum." Thus, one possible way to visualize 5D FLARES data $S^{(6)}(\tau, T, t, \Theta, \vartheta)$ is to perform a 3D Fourier transformation with respect to the coherence times τ, t, and ϑ to yield the sixth-order 1Q–1Q–1Q 3D electronic spectrum $S^{(6)}(\omega_\tau, T, \omega_t, \Theta, \omega_\vartheta)$, which is shown in the middle left column of Fig. 6.2 at ($T = 0$ fs, $\Theta = 0$ fs). Then, for each voxel, i.e., each triple of electronic transition frequencies, a 0Q–0Q 2D spectrum can be con-

structed by 2D Fourier transformation of $S^{(6)}(\omega_\tau, T, \omega_t, \Theta, \omega_\vartheta)$ with respect to T and Θ. Hence, a 5D FLARES spectrum can be visualized as a "2D spectrum within a 3D spectrum." In the middle right column of Fig. 6.2b–d, an exemplary 0Q–0Q 2D spectrum is shown, which is taken at the high-energy region of the 3D electronic spectrum ($\hbar\omega_\tau = \hbar\omega_t = \hbar\omega_\vartheta = 2.08$ eV), as indicated by the green dot on the spectral solid. Population dynamics were removed by subtracting the pathways which are non-oscillatory during T and Θ from the total response function. Such 0Q–0Q 2D spectra are exclusive to spectroscopy beyond three frequency dimensions [101, 290]. In molecular systems, the 0Q–0Q 2D spectra display coupling among different vibrations, vibrational combination bands as well as vibrational anharmonicity [279].[2]

The electronic 3D spectra of the three model systems (Fig. 6.2b–d, middle left column) are very similar, however, their 0Q–0Q 2D spectra (Fig. 6.2b–d, middle right column) are significantly different. Let us put particular emphasis on these 0Q–0Q 2D spectra. In case all 0Q frequencies are the same, the 0Q–0Q 2D spectrum features a single narrow diagonal peak in each quadrant (Fig. 6.2b). In case the vibrational frequency of the excited electronic state differs, such as in Fig. 6.2c, the 0Q–0Q peaks split, which is a consequence of the fact that the transitions between the electronic states mediate coupling between the higher-frequency ground-state vibration and the lower-frequency excited-state vibration. Similarly, such peak splitting is also observable in the 0Q–0Q 2D spectrum of the excitonic system (Fig. 6.2d).

Now, let us focus on the phase of the peak in the lower right $(\Delta\hbar\omega_T, \Delta\hbar\omega_\Theta)$-quadrant (far right column in Fig. 6.2b–d), which is marked by a blue arrow in the 0Q–0Q 2D spectrum. The "purely vibrational" systems (Fig. 6.2b and c) exhibit a very similar phase profile, both with a phase twist oriented parallel to the spectral diagonal. However, in the excitonic system (Fig. 6.2d), the coupling of the long-living ground-state vibrational coherence with the short-lived interexcitonic coherence results in a different characteristic phase profile which has a significantly tilted phase twist. Hence, the phase of the 0Q–0Q 2D spectrum provides a unique signature to identify excitonic coherences. In turn, with 5D FLARES, one can distinguish excitonic coherence from vibrational coherence, a problem which has been subject to numerous examples in literature [80, 197, 223, 291–293].

[2] Alternatively, a 5D FLARES spectrum can be visualized as a "3D beating surface" after direct 5D Fourier transformation of $S^{(6)}(\tau, T, t, \Theta, \vartheta)$, displaying which triples of electronic transition frequencies mediate coupling between a pair of given 0Q coherence frequencies ω_T and ω_Θ within or between the ground and excited electronic state. Another possibility to analyze FLARES data is to trace the temporal evolution of $S^{(6)}(\omega_\tau, T, \omega_t, \Theta, \omega_\vartheta)$ with respect to T and Θ, with which cascaded energy transfer can be followed [210].

Coherently detected 4D spectroscopy provides quantum-coherence selectivity with respect to the first population time interval due to the first two nonresonant interactions [101]. However, exactly this poses a limitation of coherently detected 4D spectroscopy, as correlations between vibrations in the excited electronic state cannot be constructed. In contrast, as a fully resonant technique, 5D FLARES is capable of measuring correlations between vibrational states within both the electronic ground *and* excited electronic states. In this respect, an advantage of the high spectral resolution for electronic transitions is the ability to select electronic transition frequency coordinates, which are selectively associated with either vibrations in the ground or the excited electronic state. Essentially, FLARES features extraordinary decongestion of the electronic and vibrational substructure of molecular systems and provides a sensitive probe for interexcitonic coherence. Moreover, 5D FLARES may generally be useful to investigate systems which exhibit a multipoint correlation function.

Summary

This thesis describes novel concepts for the measurement of the static and dynamic properties of the electronic structure of molecules and nanocrystals in the liquid phase by means of coherent fluorescence-detected spectroscopy in two and three frequency dimensions. These concepts are based on the systematic variation ("phase cycling") of a sequence of multiple time-delayed femtosecond excitation pulses in order to decode a multitude of novel nonlinear signals from the resulting phase-dependent fluorescence signal. These signals represent any permutation of correlations between zero-, one-, two-, and three-quantum coherences. To this end, two new phase-cycling schemes have been developed which can simultaneously resolve and discriminate several nonlinear signals of sixth order, including those of the fourth order of nonlinearity.

By means of the sixth-order signals recorded in this work, static properties of highly excited electronic states in molecules such as their energies, transition dipole moments, and relative displacement of electronic potential surfaces, as well as dynamic properties in terms of their relaxation kinetics, can be ascertained. Furthermore, it was shown that these signals are suitable for the characterization of exciton–exciton correlations in colloidal quantum dots and for the measurement of ultrafast exciton–exciton annihilation in molecular aggregates.

The experiments performed in this thesis mark an important step towards the complete characterization of the nonlinear response of quantum systems. In view of this, the concept of fluorescence-detected multiple-quantum coherence multidimensional spectroscopy introduced here offers a unified, systematic approach.

In virtue of the technical advantages such as the use of a single excitation beam and the absence of nonresonant contributions, the measurement protocols developed here can be directly transferred to other incoherent observables and to sample systems in other states of matter. Furthermore, the approaches presented here can be systematically extended to higher frequency dimensions and higher orders of nonlinearity.

Zusammenfassung

Diese Arbeit beschreibt neuartige Konzepte zur Messung der statischen und dynamischen Eigenschaften der elektronischen Stuktur von Molekülen und Nanokristallen in der flüssigen Phase mittels kohärenter Fluoreszenz-detektierter Spektroskopie in zwei und drei Frequenzdimensionen. Diese Konzepte beruhen auf der systematischen Phasenvariation ("Phase Cycling") einer Sequenz mehrerer zeitverzögerter Femtosekunden-Anregepulse, um aus dem resultierenden phasenabhängigen Fluoreszenzsignal eine Vielzahl von neuartigen nichtlinearen Signalen zu dekodieren. Diese Signale stellen jegliche Permutationen von Korrelationen zwischen Null-, Ein-, Zwei- und Drei-Quantenkohärenzen dar. Hierzu wurden zwei neue Phase-Cycling Schemata entwickelt, welche gleichzeitig mehrere nichtlineare Signale der sechsten Ordnung auflösen und voneinander unterscheiden können, inklusive der Signale der vierten nichtlinearen Ordnung.

Mit den in dieser Arbeit aufgenommenen Signalen der sechsten Ordnung können statische Eigenschaften hoch-angeregter elektronischer Zustände in Molekülen wie deren Energien, Übergangsdipolmomente, relative Verschiebung elektronischer Potentialflächen zueinander, sowie dynamische Eigenschaften in Bezug auf deren Relaxationskinetik ermittelt werden. Ferner wurde gezeigt, dass diese Signale zur Charakterisierung von Exziton–Exziton-Korrelationen in kolloidalen Quantenpunkten sowie zur Messung ultraschneller Exziton–Exziton-Annihilierung in molekularen Aggregaten geeignet sind.

Die Experimente dieser Arbeit markieren einen wichtigen Schritt in Richtung der vollständigen Charakterisierung der nichtlinearen Antwort von Quantensystemen. Das hier eingeführte Konzept der Fluoreszenz-detektierten multidimensionalen Multiquantenkohärenz-Spektroskopie bietet hierfür einen vereinheitlichten, systematischen Ansatz.

In Hinblick auf technische Vorteile wie der Verwendung eines einzigen Anregestrahls und der Abwesenheit von nichtresonanten Beiträgen lassen sich die hier entwickelten Messprotokolle direkt auf andere inkohärente Observablen und auf Probesysteme in anderen Aggregatszuständen übertragen. Ferner lassen sich die vorgestellten Ansätze systematisch auf höhere Frequenzdimensionen und nichtlineare Ordnungen erweitern.

Appendices

A Nonlinear Signals Accessible by Three Pulses

The following table summarizes all second-, fourth- and sixth-order nonlinear signals accessible by a three-pulse sequence. All these signals can be discriminated against each other without aliasing by using a 1×6×6 phase-cycling scheme.

Table A1. Complete list of second-, fourth- and sixth-order signals $\tilde{p}^{(n)}$ with their specific signal-phase coefficients α, β, and γ. Two-pulse contributions are indicated as "TP" whereas three-pulse contributions are denoted as correlations between quantum coherences (1Q: one-quantum, 2Q: two-quantum, 3Q: three-quantum). For the three-pulse contributions, the asterisk signifies the complex conjugate, whereas the additional label "R" denotes a rephasing signal contribution.

n	$\tilde{p}^{(n)}$	α	β	γ
2	TP	−1	+1	0
2	TP	−1	0	+1
2	TP	0	−1	+1
2	TP	0	+1	−1
2	TP	+1	−1	0
2	TP	+1	0	−1
4	TP	−2	+2	0
4	TP	−2	0	+2
4	TP	0	−2	+2
4	TP	0	+2	−2

continues on next page

4	TP	+2	−2	0
4	TP	+2	0	−2
4	1Q–1Q (R)	−1	+2	−1
4	2Q–1Q	+2	−1	−1
4	1Q–2Q	+1	+1	−2
4	1Q–1Q*	+1	−2	+1
4	2Q–1Q*	−2	+1	+1
4	1Q–2Q*	−1	−1	+2
6	TP	−3	+3	0
6	TP	−3	0	+3
6	TP	0	−3	+3
6	TP	0	+3	−3
6	TP	+3	−3	0
6	TP	+3	0	−3
6	2Q–1Q (R)	−2	+3	−1
6	1Q–2Q (R)	−1	+3	−2
6	3Q–1Q	+3	−2	−1
6	3Q–2Q	+3	−1	−2
6	1Q–3Q	+1	+2	−3
6	2Q–3Q	+2	+1	−3
6	2Q–1Q* (R)	+2	−3	+1
6	1Q–2Q* (R)	+1	−3	+2
6	3Q–1Q*	−3	+2	+1
6	3Q–2Q*	−3	+1	+2
6	1Q–3Q*	−1	−2	+3
6	2Q–3Q*	−2	−1	+3

B Phase-Cycling Diagrams of a Four-Pulse Sequence

Similar to Eq. (1.34) in Sec. 1.2.5, we can formulate a general expression for a nonlinear signal contribution $\tilde{p}_{(4)}$, which is acquired by four pulses (Fig. 1.7c),

$$\tilde{p}_{(4)}(\tau,T,t,\beta,\gamma,\delta) = \frac{1}{LMN}\sum_{n=0}^{N-1}\sum_{m=0}^{M-1}\sum_{l=0}^{L-1} p\left(\tau,T,t,l\Delta\varphi_{21},m\Delta\varphi_{31},n\Delta\varphi_{41}\right) \times \mathrm{e}^{-\mathrm{i}l\beta\Delta\varphi_{21}}\mathrm{e}^{-\mathrm{i}m\gamma\Delta\varphi_{31}}\mathrm{e}^{-\mathrm{i}n\delta\Delta\varphi_{41}}, \tag{B.1}$$

where the experimental phase increments are defined as $\Delta\varphi_{21} = 2\pi/L$, $\Delta\varphi_{31} = 2\pi/M$ and $\Delta\varphi_{41} = 2\pi/N$, and where $L\times M\times N$ corresponds to the phase-cycling scheme [29]. For four pulses, the rules for the signal-specific coefficients α,β, γ, and δ are

$$\alpha + \beta + \gamma + \delta = 0, \tag{B.2}$$

$$|\alpha| + |\beta| + |\gamma| + |\delta| \leq 6, \tag{B.3}$$

whereas for the latter we imposed to consider signals up to the sixth order of nonlinearity.

For a four-pulse sequence, we can now depict three different φ-spaces, φ_{21}, φ_{31} and φ_{41} (see Fig. B.1), analogous to the diagrams shown in Figs. 1.8 and 1.9. For that purpose, let us exemplarily consider the fourth-order rephasing 1Q–0Q–1Q signal (blue), and the sixth-order nonrephasing 1Q–0Q–2Q signal (red), the signal-specific coefficients of which are taken from Table 4.1 [4].

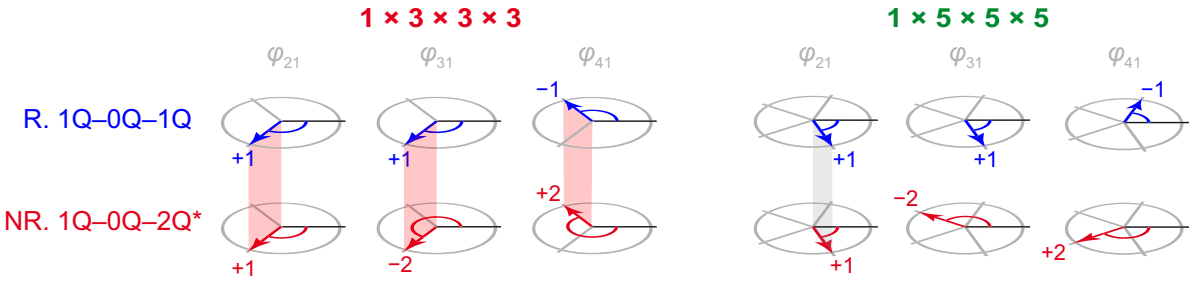

Figure B.1. Distinguishing fourth- and sixth-order signals in a four-pulse sequence by phase cycling. The fourth-order rephasing (R) 1Q–0Q–1Q signal (blue) and the complex conjugate of the nonrephasing (NR) 1Q–0Q–2Q signal are exemplarily illustrated using the diagrammatic representation of phase-cycling schemes (see also Sec. 1.2.5). The 1×3×3×3 phase-cycling scheme (left) leads to aliasing between the fourth- and sixth-order signals because of simultaneous coefficient ambiguity in all φ-spaces, as indicated by the red shaded planes. The 1×5×5×5 scheme (right) is sufficient in order to discriminate them, since each signal now has a unique configuration of signal vectors.

A 1×3×3×3-fold phase-cycling scheme was previously demonstrated to be appropriate to distinguish between various fourth-order signals [29, 71]. However, as exemplarily shown by the phase-cycling diagram of Fig. B.1, left, there is aliasing between the fourth- and sixth-order signals. This is because of coefficient ambiguity of +1 (−1) and −2 (+2). By increasing the phase-cycling scheme to 1×5×5×5, the five-step phase cycling in each φ-space effectively resolves these coefficient ambiguities, and the signals can be distinguished from one another. This is because each signal contribution can now be represented by a unique set of signal vectors (Fig. B.1, right).

C Simulation Parameters of the Squaraine Dimer

The 2D spectra of the squaraine heterodimer SQA–SQB investigated in Chapter 5 (Fig. 5.9) were calculated by numerical solution of the Redfield master equation,

$$\frac{\partial}{\partial t'}\rho(t') = -\frac{i}{\hbar}[H_0, \rho(t')] - \mathcal{R}\rho(t') + \frac{\mathrm{i}}{\hbar}[\mu, \rho(t')]E(t'), \tag{C.1}$$

where H_0 is the stationary Hamiltonian in the exciton basis (see Fig. 5.8c for an energy-level scheme), and $\mathcal{R}$ is the Redfield relaxation superoperator (a tensor) that takes into account the system-bath interaction. The external electric field $E(t')$ is explicitly incorporated as a multipulse sequence with parallelly polarized pulses, and the transition dipole moments of the dimer are approximated to be parallel. The dynamics are calculated in the secular approximation, and the system–bath interaction is treated within second-order perturbation theory. The bath is described as an ensemble of overdamped harmonic oscillators. The relaxation of the higher excited states $|\alpha\rangle$ and $|\beta\rangle$ to the single-exciton states $|a\rangle$ and $|b\rangle$ is modelled using the Lindblad formalism [2].

For the simulation of the fifth-order CDEEI2D experiment, the nonlinear polarization P is calculated via

$$P(t', T, \tau) = \mathrm{Tr}\,\{\mu\rho(t', T, \tau)\}, \tag{C.2}$$

where τ corresponds to the delay between the two pump pulses, and T is the delay between the last pump pulse and the probe pulse (see also Fig. 5.7). The CDEEI2D signal is obtained via the differential calculation of the pumped/un-pumped polarization. In order to isolate the signal in the probe direction, a two-step phase cycling of the probe pulse is carried out [2].

In case of the simulation of the fluorescence-detected sixth-order 2D experiment, the fluorescence intensity I_{FL} is given by

$$I_{\mathrm{FL}}(t, T, \tau, \boldsymbol{\varphi}) \propto \sum_{i>0} \rho_{ii}(t, T, \tau, \boldsymbol{\varphi}), \tag{C.3}$$

where ρ_{ii} is an excited-state population density matrix element, τ is the delay between the first two pulses, T the delay between the second and third pulse, and t the delay between the last two pulses (see also Fig. 5.7). The vector $\boldsymbol{\varphi}$ contains the individual pulse phases. The fluorescence quantum yield is assumed to be the same in the excited states, which is justified through efficient exciton–exciton annihilation. The excited-state population density matrix elements are obtained by Eq. (C.1) after the action of the external field.

The simulation parameters are summarized in Table C.1 and correspond to those of previous work [2, 7].

Table C.1. Simulation parameters for the simulations of the fifth- and sixth-order 2D spectra. Reprinted from Ref. [2], with the permission of AIP Publishing.

Quantity	**Variable**	**Value**
SQA, SQB transition energy	e_B, e_A	13950 cm^{-1}, 15240 cm^{-1}
Transition energy between first and higher excited monomer state	E_f	12500 cm^{-1}
Electronic coupling between one-exciton transitions	J_AB	-350 cm^{-1}
Scaling of transition coupling into higher excited states	$\zeta = J_\mathrm{fe}/J_\mathrm{eg}$	0.8
One-exciton transition dipole moment scaling	μ_A, μ_B	$1.15, 1.0$
Scaling of transition dipole moments to higher excited states	$\mu^\mathrm{f}_\mathrm{A,B}/\mu_\mathrm{A,B}$	0.66
Scaling of coupling to the bath	ν_A, ν_B	$1.0, 1.46$
Scaling of coupling to the bath for higher excited states	$\nu^\mathrm{f}_\mathrm{A,B}/\nu_\mathrm{A,B}$	1.8
Bath reorganization energy	λ	240 cm^{-1}
Bath inverse correlation time	Λ	666 cm^{-1}
Strong vibrational mode parameters: frequency, damping, Huang–Rhys factor	Ω, γ, S	1220 cm^{-1}, 50 cm^{-1}, 0.15
Internal conversion time	τ_IC	30 fs
Pulse duration (intensity FWHM), central frequency	t_pulse, ω_0	12 fs, 14700 cm^{-1}

The extended absorption spectrum of the SQA–SQB dimer in toluene is shown in Fig. C.1. As a reference, the spectrum obtained by probing the transitions from the single-exciton states pumped by the pump pulse is shown as a yellow shaded area, demonstrating that the higher excited states $|\beta\rangle$ and $|\alpha\rangle$ are not directly probed.

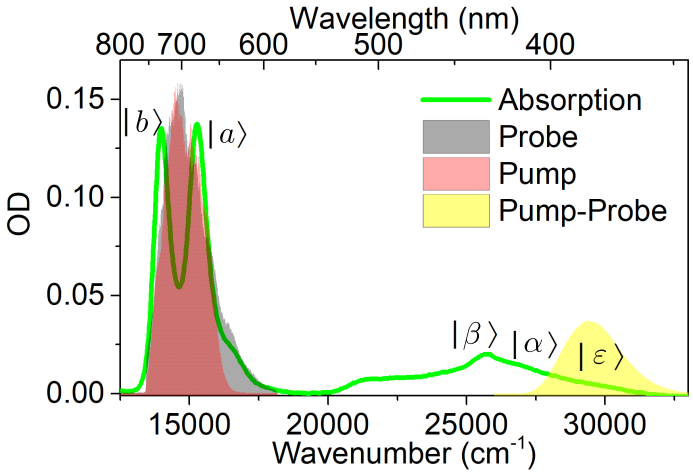

Figure C.1. Absorption spectrum of the SQA–SQB dimer in toluene (recorded using a 200 µm cuvette), covering high optical frequencies. The absorption peaks are denoted by single-exciton states $|b\rangle$ and $|a\rangle$, higher-excited states $|\beta\rangle$ and $|\alpha\rangle$, and a biexciton state $|\varepsilon\rangle$. The red shaded area denotes the pump spectrum used in the fifth-order experiment as well as the excitation spectrum used in the sixth-order experiment, whereas the gray shaded area corresponds to the probe spectrum used in the fifth-order experiment. The effective spectral region obtained by first pumping into the single-exciton states and subsequent probing ("pump–probe") is indicated by a yellow shaded area. Adapted and modified from Ref. [2].

List of Abbreviations

1D	one-dimensional
2D	two-dimensional
3D	three-dimensional
5D	five-dimensional
0Q	zero-quantum
1Q	one-quantum
2Q	two-quantum
3Q	three-quantum
AOPDF	acousto-optic programmable dispersive filter
APD	avalanche photodiode
CDEEI	coherently detected exciton–exciton interaction
COSY	correlated spectroscopy
EEA	exciton–exciton annihilation
EEI	exciton–exciton interaction
ESA	excited-state absorption
FDEEI	fluorescence-detected exciton–exciton interaction
FLARES	fluorescence-detected all-resonant electronic spectroscopy
GSB	ground-state bleach
IC	internal conversion
IRF	instrumental response function
LO	longitudinal optical
MEG	multiexciton generation
NMR	nuclear magnetic resonance
NR	nonrephasing
QDT	quantum dynamics toolbox
R	rephasing
RMSD	root–mean–squared difference

ROI	region of interest
SED	single-exciton dynamics
SHG	second-harmonic generation
SQD	squared difference
TAP	tetraazapentacene
TIPS	triisopropylsilyl
UV	ultraviolet
VIS	visible

References

[1] S. Mueller, J. Lüttig, L. Brenneis, D. Oron, and T. Brixner.
Observing multiexciton correlations in colloidal semiconductor quantum dots via multiple-quantum two-dimensional fluorescence spectroscopy.
ACS Nano **15**, 4647–4657 (2021).

[2] P. Malý, S. Mueller, J. Lüttig, C. Lambert, and T. Brixner.
Signatures of exciton dynamics and interaction in coherently and fluorescence-detected four- and six-wave-mixing two-dimensional electronic spectroscopy.
J. Chem. Phys. **153**, 144204 (2020).

[3] S. Mueller and T. Brixner.
Molecular coherent three-quantum two-dimensional fluorescence spectroscopy.
J. Phys. Chem. Lett. **11**, 5139–5147 (2020).

[4] S. Mueller, J. Lüttig, P. Malý, L. Ji, J. Han, M. Moos, T. B. Marder, U. H. F. Bunz, A. Dreuw, C. Lambert, and T. Brixner.
Rapid multiple-quantum three-dimensional fluorescence spectroscopy disentangles quantum pathways.
Nat. Commun. **10**, 4735 (2019).

[5] T. Kenneweg, S. Mueller, T. Brixner, and W. Pfeiffer.
QDT — a Matlab toolbox for the simulation of coupled quantum systems and multidimensional spectroscopy.
in preparation (2021).

[6] P. Malý, S. Müller, J. Lüttig, M. Schreck, C. Lambert, and T. Brixner.
Coherently and fluorescence-detected four- and six-wave-mixing two-dimensional electronic spectroscopy: Measuring multi-exciton dynamics and delocalization.
The 22nd International Conference on Ultrafast Phenomena 2020, F. Kärtner, M. Khalil, R. Li, F. Légaré, and T. Tahara, eds., OSA Technical Digest (Optical Society of America, 2020), paper Tu4A.4 (2020).

[7] P. Malý, J. Lüttig, S. Mueller, M. Schreck, C. Lambert, and T. Brixner.
Coherently and fluorescence-detected two-dimensional electronic spectroscopy: Direct comparison on squaraine dimers.
Phys. Chem. Chem. Phys. **22**, 21222–21237 (2020).

[8] S. Müller, S. Draeger, N. Klosterhalfen, and T. Brixner.
Fluorescence-detected two-quantum and one-quantum–two-quantum 2D electronic spectroscopy of Rhodamine 700.
EPJ Web Conf. **205**, 03012 (2019).

[9] S. Mueller, S. Draeger, X. Ma, M. Hensen, T. Kenneweg, W. Pfeiffer, and T. Brixner.
Fluorescence-detected two-quantum and one-quantum–two-quantum 2D electronic spectroscopy.
J. Phys. Chem. Lett. **9**, 1964–1969 (2018).

[10] R. König, S. Müller, R. E. Dinnebier, B. Hinrichsen, P. Müller, A. Ribbens, J. Hwang, R. Liebscher, M. Etter, and C. Pistidda.
The crystal structures of carbonyl iron powder – revised using in situ synchrotron XRPD.
Z. Kristallogr. Cryst. Mater. **232**, 835–842 (2017).

[11] E. L. Hahn.
Nuclear induction due to free Larmor precession.
Phy. Rev. **77**, 297 (1950).

[12] D. Keusters, H.-S. Tan, and W. S. Warren.
Role of pulse phase and direction in two-dimensional optical spectroscopy.
J. Phys. Chem. A **103**, 10369–10380 (1999).

[13] N. A. Kurnit, I. D. Abella, and S. R. Hartmann.
Observation of a Photon Echo.
Phys. Rev. Lett. **13**, 567–568 (1964).

[14] The Nobel Foundation.
Press release: The Nobel Prize in Physics 2018.
`https://www.nobelprize.org/prizes/physics/2018/press-release/`, accessed: March 29, 2021.

[15] L. de Broglie.
XXXV. A tentative theory of light quanta.
Phil. Mag. **47**, 446–458 (1924).

[16] R. P. Feynman.
QED: Die seltsame Theorie des Lichts und der Materie.
20th edition. Piper Verlag, München (2016).

[17] P. Hamm and M. Zanni.
Concepts and methods of 2D infrared spectroscopy.
First edition. Cambridge University Press, New York (2011).

[18] L. Valkunas, D. Abramavicius, and T. Mančal.
Molecular excitation dynamics and relaxation: quantum theory and spectroscopy.
First edition. Wiley-VCH, Weinheim (2013).

[19] S. Mukamel.
Principles of nonlinear optical spectroscopy.
First edition. Oxford University Press, New York (1995).

[20] P. A. Rose and J. J. Krich.
Efficient numerical method for predicting nonlinear optical spectroscopies of open systems.
J. Chem. Phys. **154**, 034108 (2021).

[21] G. Lindblad.
On the generators of quantum dynamical semigroups.
Commun. Math. Phys. **48**, 119–130 (1976).

[22] D. Manzano.
A short introduction to the Lindblad master equation.
AIP Adv. **10**, 025106 (2020).

[23] M. Munowitz and A. Pines.
Multiple-quantum nuclear magnetic resonance spectroscopy.
Science **233**, 525–531 (1986).

[24] T. J. Norwood.
Multiple-quantum NMR methods.
Prog. Nucl. Magn. Reson. Spectrosc. **24**, 295–375 (1992).

[25] Y. Tanimura and S. Mukamel.
Two-dimensional femtosecond vibrational spectroscopy of liquids.
J. Chem. Phys. **99**, 9496–9511 (1993).

[26] A. Perdomo-Ortiz, J. R. Widom, G. A. Lott, A. Aspuru-Guzik, and A. H. Marcus.
Conformation and electronic population transfer in membrane-supported self-assembled porphyrin dimers by 2D fluorescence spectroscopy.
J. Phys. Chem. B **116**, 10757–10770 (2012).

[27] M. Schröter, T. Pullerits, and O. Kühn.
Using fluorescence detected two-dimensional spectroscopy to investigate initial exciton delocalization between coupled chromophores.
J. Chem. Phys. **149**, 114107 (2018).

[28] S. Mukamel and R. F. Loring.
Nonlinear response function for time-domain and frequency-domain four-wave mixing.
J. Opt. Soc. Am. B **3**, 595–606 (1986).

[29] H.-S. Tan.
Theory and phase-cycling scheme selection principles of collinear phase coherent multidimensional optical spectroscopy.
J. Chem. Phys. **129**, 124501 (2008).

[30] S. Mukamel and M. Richter.
Multidimensional phase-sensitive single-molecule spectroscopy with time-and-frequency-gated fluorescence detection.
Phys. Rev. A **83**, 013815 (2011).

[31] M. Kasha.
Characterization of electronic transitions in complex molecules.
Discuss. Faraday Soc. **9**, 14 (1950).

[32] J. D. Hybl, A. W. Albrecht, S. M. Gallagher Faeder, and D. M. Jonas.
Two-dimensional electronic spectroscopy.
Chem. Phys. Lett. **297**, 307–313 (1998).

[33] A. D. Bain.
Coherence levels and coherence pathways in NMR. A simple way to design phase cycling procedures.
J. Magn. Res. (1969) **56**, 418–427 (1984).

[34] M. Cho, N. F. Scherer, G. R. Fleming, and S. Mukamel.
Photon echoes and related four-wave-mixing spectroscopies using phase-locked pulses.
J. Chem. Phys. **96**, 5618–5629 (1992).

[35] M. E. Siemens, G. Moody, H. Li, A. D. Bristow, and S. T. Cundiff.
Resonance lineshapes in two-dimensional Fourier transform spectroscopy.
Opt. Express **18**, 17699–17708 (2010).

[36] S. Mukamel, R. Oszwałdowski, and L. Yang.
A coherent nonlinear optical signal induced by electron correlations.
J. Chem. Phys. **127**, 221105 (2007).

[37] Z. Li, D. Abramavicius, and S. Mukamel.
Probing electron correlations in molecules by two-dimensional coherent optical spectroscopy.
J. Am. Chem. Soc. **130**, 3509–3515 (2008).

[38] J. Kim, V. M. Huxter, C. Curutchet, and G. D. Scholes.
Measurement of electron–electron interactions and correlations using two-dimensional electronic double-quantum coherence spectroscopy.
J. Phys. Chem. A **113**, 12122–12133 (2009).

[39] A. Nemeth, F. Milota, T. Mančal, T. Pullerits, J. Sperling, J. Hauer, H. F. Kauffmann, and N. Christensson.
Double-quantum two-dimensional electronic spectroscopy of a three-level system: Experiments and simulations.
J. Chem. Phys. **133**, 094505 (2010).

[40] K. W. Stone, D. B. Turner, K. Gundogdu, S. T. Cundiff, and K. A. Nelson.

Exciton–exciton correlations revealed by two-quantum, two-dimensional Fourier transform optical spectroscopy.
Acc. Chem. Res. **42**, 1452–1461 (2009).

[41] H. Li, A. D. Bristow, M. E. Siemens, G. Moody, and S. T. Cundiff.
Unraveling quantum pathways using optical 3D Fourier-transform spectroscopy.
Nat. Commun. **4**, 1390 (2013).

[42] S. T. Cundiff.
Optical three dimensional coherent spectroscopy.
Phys. Chem. Chem. Phys. **16**, 8193–8200 (2014).

[43] M. Titze and H. Li.
Interpretation of optical three-dimensional coherent spectroscopy.
Phys. Rev. A **96**, 032508 (2017).

[44] V. Perlík, J. Hauer, and F. Šanda.
Finite pulse effects in single and double quantum spectroscopies.
J. Opt. Soc. Am. B **34**, 430–439 (2017).

[45] C. L. Smallwood, T. M. Autry, and S. T. Cundiff.
Analytical solutions to the finite-pulse Bloch model for multidimensional coherent spectroscopy.
J. Opt. Soc. Am. B **34**, 419–429 (2017).

[46] T. N. Do, M. F. Gelin, and H.-S. Tan.
Simplified expressions that incorporate finite pulse effects into coherent two-dimensional optical spectra.
J. Chem. Phys. **147**, 144103 (2017).

[47] R. Tempelaar, A. Halpin, P. J. M. Johnson, J. Cai, R. S. Murphy, J. Knoester, R. J. D. Miller, and T. L. C. Jansen.
Laser-Limited Signatures of Quantum Coherence.
J. Phys. Chem. A **120**, 3042–3048 (2016).

[48] P. Tian, D. Keusters, Y. Suzaki, and W. S. Warren.
Femtosecond phase-coherent two-dimensional spectroscopy.
Science **300**, 1553–1555 (2003).

[49] S. Yan and H.-S. Tan.
Phase cycling schemes for two-dimensional optical spectroscopy with a pump–probe beam geometry.
Chem. Phys. **360**, 110–115 (2009).

[50] Z. Zhang, K. L. Wells, E. W. J. Hyland, and H.-S. Tan.
Phase-cycling schemes for pump–probe beam geometry two-dimensional electronic spectroscopy.
Chem. Phys. Lett. **550**, 156–161 (2012).

[51] H. Seiler, S. Palato, and P. Kambhampati.
Coherent multi-dimensional spectroscopy at optical frequencies in a single beam with optical read-out.
J. Chem. Phys. **147**, 094203 (2017).

[52] P. Brosseau, S. Palato, H. Seiler, H. Baker, and P. Kambhampati.
Fifth-order two-quantum absorptive two-dimensional electronic spectroscopy of CdSe quantum dots.
J. Chem. Phys. **153**, 234703 (2020).

[53] D. B. Turner and K. A. Nelson.
Coherent measurements of high-order electronic correlations in quantum wells.
Nature **466**, 1089–1092 (2010).

[54] P. Wen, G. Christmann, J. J. Baumberg, and K. A. Nelson.
Influence of multi-exciton correlations on nonlinear polariton dynamics in semiconductor microcavities.
New J. Phys. **15**, 025005 (2013).

[55] F. D. Fuller and J. P. Ogilvie.
Experimental implementations of two-dimensional Fourier transform electronic spectroscopy.
Annu. Rev. Phys. Chem. **66**, 667–690 (2015).

[56] T. A. Gellen, L. A. Bizimana, W. P. Carbery, I. Breen, and D. B. Turner.
Ultrabroadband two-quantum two-dimensional electronic spectroscopy.
J. Chem. Phys. **145**, 064201 (2016).

[57] D. B. Turner, K. W. Stone, K. Gundogdu, and K. A. Nelson.
The coherent optical laser beam recombination technique (COLBERT) spectrometer: Coherent multidimensional spectroscopy made easier.
Rev. Sci. Instrum. **82**, 081301 (2011).

[58] S. Garrett-Roe and P. Hamm.
Purely absorptive three-dimensional infrared spectroscopy.
J. Chem. Phys. **130**, 164510 (2009).

[59] W. O. Hutson, A. P. Spencer, and E. Harel.
Isolated ground-state vibrational coherence measured by fifth-order single-shot two-dimensional electronic spectroscopy.
J. Phys. Chem. Lett. **7**, 3636–3640 (2016).

[60] D. M. Jonas.
Two-dimensional femtosecond spectroscopy.
Annu. Rev. Phys. Chem. **54**, 425–463 (2003).

[61] F. Milota, C. N. Lincoln, and J. Hauer.
Precise phasing of 2D-electronic spectra in a fully non-collinear phase-matching geometry.
Opt. Express **21**, 15904–15911 (2013).

[62] V. Singh, A. Fidler, B. Rolczynski, and G. Engel.
Independent phasing of rephasing and non-rephasing 2D electronic spectra.
J. Chem. Phys. **139**, 084201 (2013).

[63] A. F. Fidler, E. Harel, and G. S. Engel.
Dissecting hidden couplings using fifth-order three-dimensional electronic spectroscopy.
J. Phys. Chem. Lett. **1**, 2876–2880 (2010).

[64] F. Ding and M. T. Zanni.
Heterodyned 3D IR spectroscopy.
Chem. Phys. **341**, 95–105 (2007).

[65] S. Ruetzel, M. Kullmann, J. Buback, P. Nuernberger, and T. Brixner.
Tracing the Steps of Photoinduced Chemical Reactions in Organic Molecules by Coherent Two-Dimensional Electronic Spectroscopy Using Triggered Exchange.
Phys. Rev. Lett. **110**, 148305 (2013).

[66] B. Kriete, J. Lüttig, T. Kunsel, P. Malý, T. L. C. Jansen, J. Knoester, T. Brixner, and M. S. Pshenichnikov.
Interplay between structural hierarchy and exciton diffusion in artificial light harvesting.
Nat. Commun. **10**, 4615 (2019).

[67] J. Kim, S. Mukamel, and G. D. Scholes.
Two-dimensional electronic double-quantum coherence spectroscopy.
Acc. Chem. Res. **42**, 1375–1384 (2009).

[68] K. Raghavachari and J. B. Anderson.
Electron correlation effects in molecules.
J. Phys. Chem. **100**, 12960–12973 (1996).

[69] P. F. Tekavec, G. A. Lott, and A. H. Marcus.
Fluorescence-detected two-dimensional electronic coherence spectroscopy by acousto-optic phase modulation.
J. Chem. Phys. **127**, 214307 (2007).

[70] W. Wagner, C. Li, J. Semmlow, and W. Warren.
Rapid phase-cycled two-dimensional optical spectroscopy in fluorescence and transmission mode.
Opt. Express **13**, 3697–3706 (2005).

[71] A. K. De, D. Monahan, J. M. Dawlaty, and G. R. Fleming.
Two-dimensional fluorescence-detected coherent spectroscopy with absolute phasing by confocal imaging of a dynamic grating and 27-step phase-cycling.
J. Chem. Phys. **140**, 194201 (2014).

[72] S. Draeger, S. Roeding, and T. Brixner.
Rapid-scan coherent 2D fluorescence spectroscopy.
Opt. Express **25**, 3259–3267 (2017).

[73] A. A. S. Kalaee, F. Damtie, and K. J. Karki.
Differentiation of true nonlinear and incoherent mixing of linear signals in action-detected 2D spectroscopy.
J. Phys. Chem. A **123**, 4119–4124 (2019).

[74] P. Grégoire, A. R. Srimath Kandada, E. Vella, C. Tao, R. Leonelli, and C. Silva.
Incoherent population mixing contributions to phase-modulation two-dimensional coherent excitation spectra.
J. Chem. Phys. **147**, 114201 (2017).

[75] K. J. Karki, J. Chen, A. Sakurai, Q. Shi, A. T. Gardiner, O. Kühn, R. J. Cogdell, and T. Pullerits.
Before Förster. Initial excitation in photosynthetic light harvesting.
Chem. Sci. **10**, 7923–7928 (2019).

[76] T. Kunsel, V. Tiwari, Y. A. Matutes, A. T. Gardiner, R. J. Cogdell, J. P. Ogilvie, and T. L. C. Jansen.
Simulating fluorescence-detected two-dimensional electronic spectroscopy of multichromophoric systems.
J. Phys. Chem. B **123**, 394–406 (2019).

[77] O. Kühn, T. Mančal, and T. Pullerits.
Interpreting fluorescence detected two-dimensional electronic spectroscopy.
J. Phys. Chem. Lett. **11**, 838–842 (2020).

[78] L. Bruder, M. Binz, and F. Stienkemeier.
Efficient isolation of multiphoton processes and detection of collective resonances in dilute samples.
Phys. Rev. A: At., Mol., Opt. Phys. **92**, 053412 (2015).

[79] S. Mukamel.
Communication: The origin of many-particle signals in nonlinear optical spectroscopy of noninteracting particles.
J. Chem. Phys. **145**, 041102 (2016).

[80] G. S. Engel, T. R. Calhoun, E. L. Read, T.-K. Ahn, T. Mančal, Y.-C. Cheng, R. E. Blankenship, and G. R. Fleming.
Evidence for wavelike energy transfer through quantum coherence in photosynthetic systems.
Nature **446**, 782–786 (2007).

[81] K. W. Stone, K. Gundogdu, D. B. Turner, X. Li, S. T. Cundiff, and K. A. Nelson.
Two-quantum 2D FT electronic spectroscopy of biexcitons in GaAs quantum wells.
Science **324**, 1169–1173 (2009).

[82] O. Bixner, V. Lukeš, T. Mančal, J. Hauer, F. Milota, M. Fischer, I. Pugliesi, M. Bradler, W. Schmid, E. Riedle, H. F. Kauffmann, and N. Christensson.
Ultrafast photo-induced charge transfer unveiled by two-dimensional electronic spectroscopy.
J. Chem. Phys. **136**, 204503 (2012).

[83] K. L. Wells, P. H. Lambrev, Z. Zhang, G. Garab, and H.-S. Tan.
Pathways of energy transfer in LHCII revealed by room-temperature 2D electronic spectroscopy.
Phys. Chem. Chem. Phys. **16**, 11640–11646 (2014).

[84] J. Dostál, J. Pšenčík, and D. Zigmantas.
In situ mapping of the energy flow through the entire photosynthetic apparatus.
Nat. Chem. **8**, 705–710 (2016).

[85] P. Akhtar, C. Zhang, T. N. Do, G. Garab, P. H. Lambrev, and H.-S. Tan.
Two-dimensional spectroscopy of chlorophyll a excited-state equilibration in light-harvesting complex II.
J. Phys. Chem. Lett. **8**, 257–263 (2017).

[86] L. Bruder, U. Bangert, M. Binz, D. Uhl, R. Vexiau, N. Bouloufa-Maafa, O. Dulieu, and F. Stienkemeier.
Coherent multidimensional spectroscopy of dilute gas-phase nanosystems.
Nat. Commun. **9**, 4823 (2018).

[87] K. J. Karki, J. R. Widom, J. Seibt, I. Moody, M. C. Lonergan, T. Pullerits, and A. H. Marcus.
Coherent two-dimensional photocurrent spectroscopy in a PbS quantum dot photocell.
Nat. Commun. **5**, 5869 (2014).

[88] A. De Sio, F. Troiani, M. Maiuri, J. Réhault, E. Sommer, J. Lim, S. F. Huelga, M. B. Plenio, C. A. Rozzi, G. Cerullo, E. Molinari, and C. Lienau.
Tracking the coherent generation of polaron pairs in conjugated polymers.
Nat. Commun. **7**, 13742 (2016).

[89] E. Vella, H. Li, P. Grégoire, S. M. Tuladhar, M. S. Vezie, S. Few, C. M. Bazán, J. Nelson, C. Silva-Acuña, and E. R. Bittner.
Ultrafast decoherence dynamics govern photocarrier generation efficiencies in polymer solar cells.
Sci. Rep. **6**, 29437 (2016).

[90] P. Grégoire, E. Vella, M. Dyson, C. M. Bazán, R. Leonelli, N. Stingelin, P. N. Stavrinou, E. R. Bittner, and C. Silva.
Excitonic coupling dominates the homogeneous photoluminescence excitation linewidth in semicrystalline polymeric semiconductors.
Phys. Rev. B: Condens. Matter Matter. Phys. **95**, 180201(R) (2017).

[91] A. D. Bristow, D. Karaiskaj, X. Dai, T. Zhang, C. Carlsson, K. R. Hagen, R. Jimenez, and S. T. Cundiff.
A versatile ultrastable platform for optical multidimensional Fourier-transform spectroscopy.
Rev. Sci. Instrum. **80**, 073108 (2009).

[92] L. Bolzonello, A. Volpato, E. Meneghin, and E. Collini.
Versatile setup for high-quality rephasing, non-rephasing, and double quantum 2D electronic spectroscopy.
J. Opt. Soc. Am. B **34**, 1223 (2017).

[93] E. C. Fulmer, P. Mukherjee, A. T. Krummel, and M. T. Zanni.
A pulse sequence for directly measuring the anharmonicities of coupled vibrations: Two-quantum two-dimensional infrared spectroscopy.
J. Chem. Phys. **120**, 8067–8078 (2004).

[94] E. C. Fulmer, F. Ding, and M. T. Zanni.
Heterodyned fifth-order 2D-IR spectroscopy of the azide ion in an ionic glass.
J. Chem. Phys. **122**, 034302 (2005).

[95] E. C. Fulmer, F. Ding, P. Mukherjee, and M. T. Zanni.
Vibrational dynamics of ions in glass from fifth-order two-dimensional infrared spectroscopy.
Phys. Rev. Lett. **94**, 067402 (2005).

[96] S. Sul, D. Karaiskaj, Y. Jiang, and N.-H. Ge.
*Conformations of N-Acetyl-*L*-prolinamide by two-dimensional infrared spectroscopy.*
J. Phys. Chem. B **110**, 19891–19905 (2006).

[97] N. Christensson, F. Milota, A. Nemeth, I. Pugliesi, E. Riedle, J. Sperling, T. Pullerits, H. F. Kauffmann, and J. Hauer.
Electronic double-quantum coherences and their impact on ultrafast spectroscopy: The example of beta-Carotene.
J. Phys. Chem. Lett. **1**, 3366–3370 (2010).

[98] D. Karaiskaj, A. D. Bristow, L. Yang, X. Dai, R. P. Mirin, S. Mukamel, and S. T. Cundiff.
Two-quantum many-body coherences in two-dimensional Fourier-transform spectra of exciton resonances in semiconductor quantum wells.
Phys. Rev. Lett. **104**, 117401 (2010).

[99] J. Tollerud and J. A. Davis.
Two-dimensional double-quantum spectroscopy: Peak shapes as a sensitive probe of carrier interactions in quantum wells.
J. Opt. Soc. Am. B **33**, C108–C114 (2016).

[100] F. Thouin, S. Neutzner, D. Cortecchia, V. A. Dragomir, C. Soci, T. Salim, Y. M. Lam, R. Leonelli, A. Petrozza, A. R. S. Kandada, and C. Silva.
Stable biexcitons in two-dimensional metal-halide perovskites with strong dynamic lattice disorder.
Phys. Rev. Mater. **2**, 034001 (2018).

[101] A. P. Spencer, W. O. Hutson, and E. Harel.
Quantum coherence selective 2D Raman–2D electronic spectroscopy.
Nat. Commun. **8**, 14732 (2017).

[102] J. Dostál, F. Fennel, F. Koch, S. Herbst, F. Würthner, and T. Brixner.
Direct observation of exciton–exciton interactions.
Nat. Commun. **9**, 2466 (2018).

[103] C. Heshmatpour, J. Hauer, and F. Šanda.
Interplay of exciton annihilation and transport in fifth order electronic spectroscopy.
Chem. Phys. **528**, 110433 (2020).

[104] F. Ding, E. C. Fulmer, and M. T. Zanni.
Heterodyned fifth-order two-dimensional IR spectroscopy: Third-quantum states and polarization selectivity.
J. Chem. Phys. **123**, 094502 (2005).

[105] M. Gessner, F. Schlawin, H. Häffner, S. Mukamel, and A. Buchleitner.
Nonlinear spectroscopy of controllable many-body quantum systems.
New J. Phys. **16**, 092001 (2014).

[106] L. Bruder, A. Eisfeld, U. Bangert, M. Binz, M. Jakob, D. Uhl, M. Schulz-Weiling, E. R. Grant, and F. Stienkemeier.
Delocalized excitons and interaction effects in extremely dilute thermal ensembles.
Phys. Chem. Chem. Phys. **21**, 2276–2282 (2019).

[107] S. Yu, M. Titze, Y. Zhu, X. Liu, and H. Li.
Observation of scalable and deterministic multi-atom Dicke states in an atomic vapor.
Opt. Lett. **44**, 2795–2798 (2019).

[108] T. M. Autry, G. Moody, J. Fraser, C. McDonald, R. P. Mirin, and K. Silverman.
Single-scan acquisition of multiple multidimensional spectra.
Optica **6**, 735 (2019).

[109] L. Kringle, N. P. D. Sawaya, J. Widom, C. Adams, M. G. Raymer, A. Aspuru-Guzik, and A. H. Marcus.
Temperature-dependent conformations of exciton-coupled Cy3 dimers in double-stranded DNA.
J. Chem. Phys. **148**, 085101 (2018).

[110] M. Sauer, K.-T. Han, R. Müller, S. Nord, A. Schulz, S. Seeger, J. Wolfrum, J. Arden-Jacob, G. Deltau, N. J. Marx, C. Zander, and K. H. Drexhage.
New fluorescent dyes in the red region for biodiagnostics.
J. Fluoresc. **5**, 247–261 (1995).

[111] A. Dvornikov, H. Zhang, and P. Rentzepis.
Transient spectra, kinetics and mechanism of Rhodamine 700 dye precursor photoreaction.
J. Photochem. Photobiol. A **201**, 57–61 (2009).

[112] D. A. Blank, L. J. Kaufman, and G. R. Fleming.
Fifth-order two-dimensional Raman spectra of CS_2 are dominated by third-order cascades.
J. Chem. Phys. **111**, 3105–3114 (1999).

[113] Z. Zhang, K. L. Wells, M. T. Seidel, and H.-S. Tan.
Fifth-order three-dimensional electronic spectroscopy using a pump–probe configuration.
J. Phys. Chem. B **117**, 15369–15385 (2013).

[114] M. D. Barnes, W. B. Whitten, S. Arnold, and J. M. Ramsey.
Homogeneous linewidths of Rhodamine 6G at room temperature from cavity-enhanced spontaneous emission rates.
J. Chem. Phys. **97**, 7842–7845 (1992).

[115] G. Calzaferri and R. Rytz.
Electronic Transition Oscillator Strength by the Extended Hueckel Molecular Orbital Method.
J. Phys. Chem. **99**, 12141–12150 (1995).

[116] U. Woggon.
Optical properties of semiconductor quantum dots, volume 136 of *Springer Tracts in Modern Physics.*
Springer, Berlin, Heidelberg (1997).

[117] X. Li, Y. Wu, D. Steel, D. Gammon, T. H. Stievater, D. S. Katzer, D. Park, C. Piermarocchi, and L. J. Sham.
An all-optical quantum gate in a semiconductor quantum dot.
Science **301**, 809–811 (2003).

[118] V. I. Klimov.
Mechanisms for photogeneration and recombination of multiexcitons in semiconductor nanocrystals: Implications for lasing and solar energy conversion.
J. Phys. Chem. B **110**, 16827–16845 (2006).

[119] V. I. Klimov, S. A. Ivanov, J. Nanda, M. Achermann, I. Bezel, J. A. McGuire, and A. Piryatinski.
Single-exciton optical gain in semiconductor nanocrystals.
Nature **447**, 441–446 (2007).

[120] P. Kambhampati.
Multiexcitons in semiconductor nanocrystals: A platform for optoelectronics at high carrier concentration.
J. Phys. Chem. Lett. **3**, 1182–1190 (2012).

[121] R. D. Schaller, V. M. Agranovich, and V. I. Klimov.
High-efficiency carrier multiplication through direct photogeneration of multi-excitons via virtual single-exciton states.
Nat. Phys. **1**, 189–194 (2005).

[122] E. Moreau, I. Robert, L. Manin, V. Thierry-Mieg, J. M. Gérard, and I. Abram.
Quantum Cascade of Photons in Semiconductor Quantum Dots.
Phys. Rev. Lett. **87**, 183601 (2001).

[123] O. Benson, C. Santori, M. Pelton, and Y. Yamamoto.
Regulated and Entangled Photons from a Single Quantum Dot.
Phys. Rev. Lett. **84**, 2513–2516 (2000).

[124] V. I. Klimov, A. A. Mikhailovsky, D. W. McBranch, C. A. Leatherdale, and M. G. Bawendi.
Quantization of multiparticle Auger rates in semiconductor quantum dots.
Science **287**, 1011–1013 (2000).

[125] J.-M. Caruge, Y. Chan, V. Sundar, H. J. Eisler, and M. G. Bawendi.
Transient photoluminescence and simultaneous amplified spontaneous emission from multiexciton states in CdSe quantum dots.
Phys. Rev. B **70**, 085316 (2004).

[126] S. L. Sewall, R. R. Cooney, K. E. H. Anderson, E. A. Dias, D. M. Sagar, and P. Kambhampati.
State-resolved studies of biexcitons and surface trapping dynamics in semiconductor quantum dots.
J. Chem. Phys. **129**, 084701 (2008).

[127] S. L. Sewall, R. R. Cooney, E. A. Dias, P. Tyagi, and P. Kambhampati.
State-resolved observation in real time of the structural dynamics of multiexcitons in semiconductor nanocrystals.
Phys. Rev. B **84**, 235304 (2011).

[128] P. Kambhampati.
Unraveling the structure and dynamics of excitons in semiconductor quantum dots.
Acc. Chem. Res. **44**, 1–13 (2011).

[129] P. Kambhampati.
Hot exciton relaxation dynamics in semiconductor quantum dots: radiationless transitions on the nanoscale.
J. Phys. Chem. C **115**, 22089–22109 (2011).

[130] P. Geiregat, A. Houtepen, Y. Justo, F. C. Grozema, D. Van Thourhout, and Z. Hens.
Coulomb shifts upon exciton addition to photoexcited PbS colloidal quantum dots.
J. Phys. Chem. C **118**, 22284–22290 (2014).

[131] C. Zhang, T. N. Do, X. Ong, Y. Chan, and H.-S. Tan.
Understanding the features in the ultrafast transient absorption spectra of CdSe quantum dots.
Chem. Phys. **481**, 157–164 (2016).

[132] N. Lenngren, T. Garting, K. Zheng, M. Abdellah, N. Lascoux, F. Ma, A. Yartsev, K. Žídek, and T. Pullerits.
Multiexciton absorption cross sections of CdSe quantum dots determined by ultrafast spectroscopy.
J. Phys. Chem. Lett. **4**, 3330–3336 (2013).

[133] C. Bonati, M. B. Mohamed, D. Tonti, G. Zgrablic, S. Haacke, F. van Mourik, and M. Chergui.
Spectral and dynamical characterization of multiexcitons in colloidal CdSe semiconductor quantum dots.
Phys. Rev. B **71**, 205317 (2005).

[134] J. Huang, Z. Huang, Y. Yang, H. Zhu, and T. Lian.
Multiple exciton dissociation in CdSe quantum dots by ultrafast electron transfer to adsorbed Methylene Blue.
J. Am. Chem. Soc. **132**, 4858–4864 (2010).

[135] H. Zhu, Y. Yang, and T. Lian.
Multiexciton annihilation and dissociation in quantum confined semiconductor nanocrystals.
Acc. Chem. Res. **46**, 1270–1279 (2013).

[136] W. Yang, Y. Yang, A. L. Kaledin, S. He, T. Jin, J. R. McBride, and T. Lian.
Surface passivation extends single and biexciton lifetimes of InP quantum dots.
Chem. Sci. **11**, 5779–5789 (2020).

[137] H. Seiler, S. Palato, C. Sonnichsen, H. Baker, and P. Kambhampati.
Seeing multiexcitons through sample inhomogeneity: Band-edge biexciton structure in CdSe nanocrystals revealed by two-dimensional electronic spectroscopy.
Nano Lett. **18**, 2999–3006 (2018).

[138] S. Palato, H. Seiler, H. Baker, C. Sonnichsen, P. Brosseau, and P. Kambhampati.
Investigating the electronic structure of confined multiexcitons with nonlinear spectroscopies.
J. Chem. Phys. **152**, 104710 (2020).

[139] S. Palato, H. Seiler, P. Nijjar, O. Prezhdo, and P. Kambhampati.
Atomic fluctuations in electronic materials revealed by dephasing.
Proc. Natl. Acad. Sci. U. S. A. **117**, 11940–11946 (2020).

[140] D. B. Turner, Y. Hassan, and G. D. Scholes.
Exciton superposition states in CdSe nanocrystals measured using broadband two-dimensional electronic spectroscopy.
Nano Lett. **12**, 880–886 (2012).

[141] J. R. Caram, H. Zheng, P. D. Dahlberg, B. S. Rolczynski, G. B. Griffin, A. F. Fidler, D. S. Dolzhnikov, D. V. Talapin, and G. S. Engel.
Persistent interexcitonic quantum coherence in CdSe quantum dots.
J. Phys. Chem. Lett. **5**, 196–204 (2014).

[142] E. Cassette, R. D. Pensack, B. Mahler, and G. D. Scholes.
Room-temperature exciton coherence and dephasing in two-dimensional nanostructures.
Nat. Commun. **6**, 6086 (2015).

[143] E. Collini, H. Gattuso, L. Bolzonello, A. Casotto, A. Volpato, C. N. Dibenedetto, E. Fanizza, M. Striccoli, and F. Remacle.
Quantum phenomena in nanomaterials: Coherent superpositions of fine structure states in CdSe nanocrystals at room temperature.
J. Phys. Chem. C **123**, 31286–31293 (2019).

[144] E. Collini, H. Gattuso, Y. Kolodny, L. Bolzonello, A. Volpato, H. T. Fridman, S. Yochelis, M. Mor, J. Dehnel, E. Lifshitz, Y. Paltiel, R. D. Levine, and F. Remacle.
Room-temperature inter-dot coherent dynamics in multilayer quantum dot materials.
J. Phys. Chem. C **124**, 16222–16231 (2020).

[145] F. Novelli, J. O. Tollerud, D. Prabhakaran, and J. A. Davis.
Persistent coherence of quantum superpositions in an optimally doped cuprate revealed by 2D spectroscopy.
Sci. Adv. **6**, eaaw9932 (2020).

[146] C. Y. Wong and G. D. Scholes.
Biexcitonic fine structure of CdSe nanocrystals probed by polarization-dependent two-dimensional photon echo spectroscopy.
J. Phys. Chem. A **115**, 3797–3806 (2011).

[147] E. Harel, S. M. Rupich, R. D. Schaller, D. V. Talapin, and G. S. Engel.
Measurement of electronic splitting in PbS quantum dots by two-dimensional nonlinear spectroscopy.
Phys. Rev. B **86**, 075412 (2012).

[148] J. R. Caram, H. Zheng, P. D. Dahlberg, B. S. Rolczynski, G. B. Griffin, D. S. Dolzhnikov, D. V. Talapin, and G. S. Engel.
Exploring size and state dynamics in CdSe quantum dots using two-dimensional electronic spectroscopy.
J. Chem. Phys. **140**, 084701 (2014).

[149] Y. Kobayashi, C.-H. Chuang, C. Burda, and G. D. Scholes.
Exploring ultrafast electronic processes of quasi-type II nanocrystals by two-dimensional electronic spectroscopy.
J. Phys. Chem. C **118**, 16255–16263 (2014).

[150] E. Cassette, J. C. Dean, and G. D. Scholes.
Two-dimensional visible spectroscopy for studying colloidal semiconductor nanocrystals.
Small **12**, 2234–2244 (2016).

[151] N. Lenngren, M. A. Abdellah, K. Zheng, M. J. Al-Marri, D. Zigmantas, K. Žídek, and T. Pullerits.
Hot electron and hole dynamics in thiol-capped CdSe quantum dots revealed by 2D electronic spectroscopy.
Phys. Chem. Chem. Phys. **18**, 26199–26204 (2016).

[152] T. A. Gellen, J. Lem, and D. B. Turner.
Probing homogeneous line broadening in CdSe nanocrystals using multidimensional electronic spectroscopy.
Nano Lett. **17**, 2809–2815 (2017).

[153] H. Seiler, S. Palato, and P. Kambhampati.

Investigating exciton structure and dynamics in colloidal CdSe quantum dots with two-dimensional electronic spectroscopy.
J. Chem. Phys. **149**, 074702 (2018).

[154] M. Righetto, L. Bolzonello, A. Volpato, G. Amoruso, A. Panniello, E. Fanizza, M. Striccoli, and E. Collini.
Deciphering hot- and multi-exciton dynamics in core–shell QDs by 2D electronic spectroscopies.
Phys. Chem. Chem. Phys. **20**, 18176–18183 (2018).

[155] A. Liu, D. Almeida, W. Bae, L. Padilha, and S. Cundiff.
Non-Markovian exciton-phonon interactions in core-shell colloidal quantum dots at femtosecond timescales.
Phys. Rev. Lett. **123**, 057403 (2019).

[156] V. Delmonte, J. F. Specht, T. Jakubczyk, S. Höfling, M. Kamp, C. Schneider, W. Langbein, G. Nogues, M. Richter, and J. Kasprzak.
Coherent coupling of individual quantum dots measured with phase-referenced two-dimensional spectroscopy: Photon echo versus double quantum coherence.
Phys. Rev. B **96**, 041124 (2017).

[157] E. W. Martin and S. T. Cundiff.
Inducing coherent quantum dot interactions.
Phys. Rev. B **97**, 081301 (2018).

[158] V. Tiwari, Y. A. Matutes, A. T. Gardiner, T. L. C. Jansen, R. J. Cogdell, and J. P. Ogilvie.
Spatially-resolved fluorescence-detected two-dimensional electronic spectroscopy probes varying excitonic structure in photosynthetic bacteria.
Nat. Commun. **9**, 4219 (2018).

[159] P. Maity, T. Debnath, and H. N. Ghosh.
Slow electron cooling dynamics mediated by electron–hole decoupling in highly luminescent CdS_xSe_{1-x} alloy quantum Dots.
J. Phys. Chem. C **119**, 10785–10792 (2015).

[160] H. Duan, Y. Jiang, Y. Zhang, D. Sun, C. Liu, J. Huang, X. Lan, H. Zhou, L. Chen, and H. Zhong.
High quantum-yield $CdSe_xS_{1-x}$/ZnS core/shell quantum dots for warm white light-emitting diodes with good color rendering.
Nanotechnology **24**, 285201 (2013).

[161] L.-W. Yin, Y. Bando, J.-H. Zhan, M.-S. Li, and D. Golberg.
Self-assembled highly faceted wurtzite-type ZnS single-crystalline nanotubes with hexagonal cross-sections.
Adv. Mater. **17**, 1972–1977 (2005).

[162] P. K. Nampoothiri, M. N. Gandhi, and A. R. Kulkarni.
Effect of surface grafting coefficient and chain length of fatty acids on the luminescence of neodymium^{3+}-doped LaF_3 nanoparticles.

J. Mater. Chem. C **3**, 1817–1822 (2015).

[163] D. J. Norris and M. G. Bawendi.
Measurement and assignment of the size-dependent optical spectrum in CdSe quantum dots.
Phys. Rev. B **53**, 16338–16346 (1996).

[164] D. Tonti, F. van Mourik, and M. Chergui.
On the excitation wavelength dependence of the luminescence yield of colloidal CdSe quantum dots.
Nano Lett. **4**, 2483–2487 (2004).

[165] L.-W. Wang and A. Zunger.
High-energy excitonic transitions in CdSe quantum dots.
J. Phys. Chem. B **102**, 6449–6454 (1998).

[166] A. M. Smith, L. A. Lane, and S. Nie.
Mapping the spatial distribution of charge carriers in quantum-confined heterostructures.
Nat. Commun. **5**, 4506 (2014).

[167] A. V. Baranov, Y. P. Rakovich, J. F. Donegan, T. S. Perova, R. A. Moore, D. V. Talapin, A. L. Rogach, Y. Masumoto, and I. Nabiev.
Effect of ZnS shell thickness on the phonon spectra in CdSe quantum dots.
Phys. Rev. B **68**, 165306 (2003).

[168] K. I. Kang, A. D. Kepner, S. V. Gaponenko, S. W. Koch, Y. Z. Hu, and N. Peyghambarian.
Confinement-enhanced biexciton binding energy in semiconductor quantum dots.
Phys. Rev. B **48**, 15449–15452 (1993).

[169] A. Avidan and D. Oron.
Large blue shift of the biexciton state in tellurium doped CdSe colloidal quantum dots.
Nano Letters **8**, 2384–2387 (2008).

[170] S. L. Sewall, A. Franceschetti, R. R. Cooney, A. Zunger, and P. Kambhampati.
Direct observation of the structure of band-edge biexcitons in colloidal semiconductor CdSe quantum dots.
Phys. Rev. B **80**, 081310 (2009).

[171] V. Klimov, S. Hunsche, and H. Kurz.
Biexciton effects in femtosecond nonlinear transmission of semiconductor quantum dots.
Phys. Rev. B **50**, 8110–8113 (1994).

[172] A. Franceschetti and Y. Zhang.
Multiexciton absorption and multiple exciton generation in CdSe quantum dots.
Phys. Rev. Lett. **100**, 136805 (2008).

[173] V. I. Klimov.
Spectral and dynamical properties of multiexcitons in semiconductor nanocrystals.
Annu. Rev. Phys. Chem. **58**, 635–673 (2007).

[174] O. V. Prezhdo.
Photoinduced dynamics in semiconductor quantum dots: Insights from time-domain ab initio studies.
Acc. Chem. Res. **42**, 2005–2016 (2009).

[175] S. V. Kilina, D. S. Kilin, and O. V. Prezhdo.
Breaking the phonon bottleneck in PbSe and CdSe quantum dots: time-domain density functional theory of charge carrier relaxation.
ACS Nano **3**, 93–99 (2009).

[176] S. L. Sewall, R. R. Cooney, and P. Kambhampati.
Experimental tests of effective mass and atomistic approaches to quantum dot electronic structure: Ordering of electronic states.
Appl. Phys. Lett. **94**, 243116 (2009).

[177] A. Franceschetti and M. C. Troparevsky.
Radiative recombination of triexcitons in CdSe colloidal quantum dots.
J. Phys. Chem. C **111**, 6154–6157 (2007).

[178] K. E. Shulenberger, T. S. Bischof, J. R. Caram, H. Utzat, I. Coropceanu, L. Nienhaus, and M. G. Bawendi.
Multiexciton lifetimes reveal triexciton emission pathway in CdSe nanocrystals.
Nano Lett. **18**, 5153–5158 (2018).

[179] B. Lomsadze and S. T. Cundiff.
Line-shape analysis of double-quantum multidimensional coherent spectra.
Phys. Rev. A **102**, 043514 (2020).

[180] M. Khalil, N. Demirdöven, and A. Tokmakoff.
Coherent 2D IR spectroscopy: Molecular structure and dynamics in solution.
J. Phys. Chem. A **107**, 5258–5279 (2003).

[181] F. Šanda, V. Perlík, C. N. Lincoln, and J. Hauer.
Center line slope analysis in two-dimensional electronic spectroscopy.
J. Phys. Chem. A **119**, 10893–10909 (2015).

[182] D. J. Hoffman and M. D. Fayer.
CLS next gen: Accurate frequency–frequency correlation functions from center line slope analysis of 2D correlation spectra using artificial neural networks.
J. Phys. Chem. A **124**, 5979–5992 (2020).

[183] S. A. Empedocles.
Quantum-Confined Stark Effect in Single CdSe Nanocrystallite Quantum Dots.
Science **278**, 2114–2117 (1997).

[184] K. Park, Z. Deutsch, J. J. Li, D. Oron, and S. Weiss.

Single Molecule Quantum-Confined Stark Effect Measurements of Semiconductor Nanoparticles at Room Temperature.
ACS Nano **6**, 10013–10023 (2012).

[185] S. Roeding.
Coherent Multidimensional Spectroscopy in Molecular Beams and Liquids Using Incoherent Observables.
Ph.D. thesis, Würzburg (2017).

[186] J. K. Wilmshurst and H. J. Bernstein.
The infrared and raman spectra of toluene, toluene-α-d_3, m-xylene, and m-xylene-$\alpha\alpha'$-d_6.
Can. J. Chem. **35**, 911–925 (1957).

[187] W. Qin, R. A. Shah, and P. Guyot-Sionnest.
CdSeS/ZnS alloyed nanocrystal lifetime and blinking studies under electrochemical control.
ACS Nano **6**, 912–918 (2012).

[188] M. Binz, L. Bruder, L. Chen, M. F. Gelin, W. Domcke, and F. Stienkemeier.
Effects of high pulse intensity and chirp in two-dimensional electronic spectroscopy of an atomic vapor.
Opt. Express **28**, 25806–25829 (2020).

[189] G. Nair and M. G. Bawendi.
Carrier multiplication yields of CdSe and CdTe nanocrystals by transient photoluminescence spectroscopy.
Phys. Rev. B **76**, 081304 (2007).

[190] T. Brixner, J. Stenger, H. M. Vaswani, M. Cho, R. E. Blankenship, and G. R. Fleming.
Two-dimensional spectroscopy of electronic couplings in photosynthesis.
Nature **434**, 625–628 (2005).

[191] N. S. Ginsberg, Y.-C. Cheng, and G. R. Fleming.
Two-dimensional electronic spectroscopy of molecular aggregates.
Acc. Chem. Res. **42** (2009).

[192] J. A. Myers, K. L. M. Lewis, F. D. Fuller, P. F. Tekavec, C. F. Yocum, and J. P. Ogilvie.
Two-dimensional electronic spectroscopy of the D1-D2-cyt b559 photosystem II reaction center complex.
J. Phys. Chem. Lett. **1**, 2774–2780 (2010).

[193] M. Kullmann, S. Ruetzel, J. Buback, P. Nuernberger, and T. Brixner.
Reaction dynamics of a molecular switch unveiled by coherent two-dimensional electronic spectroscopy.
J. Am. Chem. Soc. **133**, 13074–13080 (2011).

[194] S. Ruetzel, M. Diekmann, P. Nuernberger, C. Walter, B. Engels, and T. Brixner.
Multidimensional spectroscopy of photoreactivity.
Proc. Natl. Acad. Sci. U. S. A. **111**, 4764–4769 (2014).

[195] J. R. Caram, A. F. Fidler, and G. S. Engel.
Excited and ground state vibrational dynamics revealed by two-dimensional electronic spectroscopy.
J. Chem. Phys. **137**, 024507 (2012).

[196] F. Milota, V. I. Prokhorenko, T. Mancal, H. von Berlepsch, O. Bixner, H. F. Kauffmann, and J. Hauer.
Vibronic and vibrational coherences in two-dimensional electronic spectra of supramolecular J-aggregates.
J. Phys. Chem. A **117**, 6007–6014 (2013).

[197] V. Perlík, C. Lincoln, F. Šanda, and J. Hauer.
Distinguishing electronic and vibronic coherence in 2D spectra by their temperature dependence.
J. Phys. Chem. Lett. **5**, 404–407 (2014).

[198] J. Lim, D. Paleček, F. Caycedo-Soler, C. N. Lincoln, J. Prior, H. Von Berlepsch, S. F. Huelga, M. B. Plenio, D. Zigmantas, and J. Hauer.
Vibronic origin of long-lived coherence in an artificial molecular light harvester.
Nat. Commun. **6**, 7755 (2015).

[199] A. A. Bakulin, S. E. Morgan, T. B. Kehoe, M. W. B. Wilson, A. W. Chin, D. Zigmantas, D. Egorova, and A. Rao.
Real-time observation of multiexcitonic states in ultrafast singlet fission using coherent 2D electronic spectroscopy.
Nat. Chem. **8**, 16–23 (2016).

[200] A. Galestian Pour, C. N. Lincoln, V. Perlík, F. Šanda, and J. Hauer.
Anharmonic vibrational effects in linear and two-dimensional electronic spectra.
Phys. Chem. Chem. Phys. **19**, 24752–24760 (2017).

[201] E. Thyrhaug, R. Tempelaar, M. J. P. Alcocer, K. Žídek, D. Bína, J. Knoester, T. L. C. Jansen, and D. Zigmantas.
Identification and characterization of diverse coherences in the Fenna–Matthews–Olson complex.
Nat. Chem. **10**, 780–786 (2018).

[202] E. Thyrhaug, K. Žídek, J. Dostál, D. Bína, and D. Zigmantas.
Exciton structure and energy transfer in the Fenna–Matthews–Olson complex.
J. Phys. Chem. Lett. **7**, 1653–1660 (2016).

[203] T. Brixner, R. Hildner, J. Köhler, C. Lambert, and F. Würthner.
Exciton transport in molecular aggregates – from natural antennas to synthetic chromophore systems.
Adv. Energy Mater. **7**, 1700236 (2017).

[204] A. Niedringhaus, V. R. Policht, R. Sechrist, A. Konar, P. D. Laible, D. F. Bocian, D. Holten, C. Kirmaier, and J. P. Ogilvie.

Primary processes in the bacterial reaction center probed by two-dimensional electronic spectroscopy.
Proc. Natl. Acad. Sci. U. S. A. **115**, 3563–3568 (2018).

[205] Y. Song, C. Hellmann, N. Stingelin, and G. D. Scholes.
The separation of vibrational coherence from ground- and excited-electronic states in P3HT film.
J. Chem. Phys. **142**, 212410 (2015).

[206] D. B. Turner, K. W. Stone, K. Gundogdu, and K. A. Nelson.
Three-dimensional electronic spectroscopy of excitons in GaAs quantum wells.
J. Chem. Phys. **131**, 144510 (2009).

[207] J. O. Tollerud, C. R. Hall, and J. A. Davis.
Isolating quantum coherence using coherent multi-dimensional spectroscopy with spectrally shaped pulses.
Opt. Express **22**, 6719–6733 (2014).

[208] S. Irgen-Gioro, A. P. Spencer, W. O. Hutson, and E. Harel.
Coherences of bacteriochlorophyll a uncovered using 3D-electronic spectroscopy.
J. Phys. Chem. Lett. **9**, 6077–6081 (2018).

[209] D. Hayes and G. S. Engel.
Extracting the excitonic Hamiltonian of the Fenna-Matthews-Olson complex using three-dimensional third-order electronic spectroscopy.
Biophys. J. **100**, 2043–2052 (2011).

[210] Z. Zhang, P. H. Lambrev, K. L. Wells, G. Garab, and H.-S. Tan.
Direct observation of multistep energy transfer in LHCII with fifth-order 3D electronic spectroscopy.
Nat. Commun. **6**, 7914 (2015).

[211] L. P. DeFlores, R. A. Nicodemus, and A. Tokmakoff.
Two-dimensional Fourier transform spectroscopy in the pump–probe geometry.
Opt. Lett. **32**, 2966–2968 (2007).

[212] J. A. Myers, K. L. Lewis, P. F. Tekavec, and J. P. Ogilvie.
Two-color two-dimensional Fourier transform electronic spectroscopy with a pulse-shaper.
Opt. Express **16**, 17420–17428 (2008).

[213] S.-H. Shim and M. T. Zanni.
How to turn your pump–probe instrument into a multidimensional spectrometer: 2D IR and VIS spectroscopies via pulse shaping.
Phys. Chem. Chem. Phys. **11**, 748–761 (2009).

[214] Z. Zhang, K. L. Wells, and H.-S. Tan.
Purely absorptive fifth-order three-dimensional electronic spectroscopy.
Opt. Lett. **37**, 5058–5060 (2012).

[215] K. J. Karki, L. Kringle, A. H. Marcus, and T. Pullerits.
Phase-synchronous detection of coherent and incoherent nonlinear signals.
J. Opt. **18**, 015504 (2016).

[216] V. Tiwari, Y. A. Matutes, A. Konar, Z. Yu, M. Ptaszek, D. F. Bocian, D. Holten, C. Kirmaier, and J. P. Ogilvie.
Strongly coupled bacteriochlorin dyad studied using phase-modulated fluorescence-detected two-dimensional electronic spectroscopy.
Opt. Express **26**, 22327–22341 (2018).

[217] S. Goetz, D. Li, V. Kolb, J. Pflaum, and T. Brixner.
Coherent two-dimensional fluorescence micro-spectroscopy.
Opt. Express **26**, 3915–3925 (2018).

[218] P. Malý and T. Mančal.
Signatures of exciton delocalization and exciton–exciton annihilation in fluorescence-detected two-dimensional coherent spectroscopy.
J. Phys. Chem. Lett. **9**, 5654–5659 (2018).

[219] L. Ji, M. Haehnel, I. Krummenacher, P. Biegger, F. L. Geyer, O. Tverskoy, M. Schaffroth, J. Han, A. Dreuw, T. B. Marder, and U. H. F. Bunz.
The radical anion and dianion of tetraazapentacene.
Angew. Chem. Int. Ed. **55**, 10498–10501 (2016).

[220] L. Ji, A. Friedrich, I. Krummenacher, A. Eichhorn, H. Braunschweig, M. Moos, S. Hahn, F. L. Geyer, O. Tverskoy, J. Han, C. Lambert, A. Dreuw, T. B. Marder, and U. H. F. Bunz.
Preparation, properties, and structures of the radical anions and dianions of azapentacenes.
J. Am. Chem. Soc. **139**, 15968–15976 (2017).

[221] C. Li, W. Wagner, M. Ciocca, and W. S. Warren.
Multiphoton femtosecond phase-coherent two-dimensional electronic spectroscopy.
J. Chem. Phys. **126**, 164307 (2007).

[222] D. Green, F. V. A. Camargo, I. A. Heisler, A. G. Dijkstra, and G. A. Jones.
Spectral filtering as a tool for two-dimensional spectroscopy: A theoretical model.
J. Phys. Chem. A **122**, 6206–6213 (2018).

[223] J. Seibt and T. Pullerits.
Beating signals in 2D spectroscopy: Electronic or nuclear coherences? Application to a quantum dot model system.
J. Phys. Chem. C **117**, 18728–18737 (2013).

[224] V. Butkus, J. Alster, E. Bašinskaitė, R. Augulis, P. Neuhaus, L. Valkunas, H. L. Anderson, D. Abramavicius, and D. Zigmantas.
Discrimination of diverse coherences allows identification of electronic transitions of a molecular nanoring.
J. Phys. Chem. Lett. **8**, 2344–2349 (2017).

[225] F. A. Damtie, A. Wacker, T. Pullerits, and K. J. Karki.
Two-dimensional action spectroscopy of excitonic systems: Explicit simulation using a phase-modulation technique.
Phys. Rev. A **96**, 053830 (2017).

[226] T. Förster.
Zwischenmolekulare Energiewanderung und Fluoreszenz.
Ann. Phys. **437**, 55–75 (1948).

[227] S. E. Braslavsky, E. Fron, H. B. Rodríguez, E. S. Román, G. D. Scholes, G. Schweitzer, B. Valeur, and J. Wirz.
Pitfalls and limitations in the practical use of Förster's theory of resonance energy transfer.
Photochem. Photobiol. Sci. **7**, 1444–1448 (2008).

[228] M. Aeschlimann, T. Brixner, A. Fischer, C. Kramer, P. Melchior, W. Pfeiffer, C. Schneider, C. Strüber, P. Tuchscherer, and D. V. Voronine.
Coherent two-dimensional nanoscopy.
Science **333**, 1723–1726 (2011).

[229] S. Roeding and T. Brixner.
Coherent two-dimensional electronic mass spectrometry.
Nat. Commun. **9**, 2519 (2018).

[230] I. Amat-Roldán, I. Cormack, P. Loza-Alvarez, E. Gualda, and D. Artigas.
Ultrashort pulse characterisation with SHG collinear-FROG.
Opt. Express **12**, 1169–1178 (2004).

[231] G. Otting, H. Widmer, G. Wagner, and K. Wüthrich.
Origin of t_1 and t_2 ridges in 2D NMR spectra and procedures for suppression.
J. Magn. Reson. (1969) **66**, 187–193 (1986).

[232] B. J. Walker, A. J. Musser, D. Beljonne, and R. H. Friend.
Singlet exciton fission in solution.
Nat. Chem. **5**, 1019–1024 (2013).

[233] H. Van Amerongen, L. Valkunas, and R. Van Grondelle.
Photosynthetic excitons.
First edition. World Scientific Publishing Co. Pte. Ltd., Singapore (2000).

[234] M. J. Frisch, G. W. Trucks, H. B. Schlegel, G. E. Scuseria, M. A. Robb, J. R. Cheeseman, G. Scalmani, V. Barone, B. Mennucci, G. A. Petersson, H. Nakatsuji, M. Caricato, X. Li, H. P. Hratchian, A. F. Izmaylov, J. Bloino, G. Zheng, J. L. Sonnenberg, M. Hada, M. Ehara, K. Toyota, R. Fukuda, J. Hasegawa, M. Ishida, T. Nakajima, Y. Honda, O. Kitao, H. Nakai, T. Vreven, J. A. Montgomery, Jr., J. E. Peralta, F. Ogliaro, M. Bearpark, J. J. Heyd, E. Brothers, K. N. Kudin, V. N. Staroverov, R. Kobayashi, J. Normand, K. Raghavachari, A. Rendell, J. C. Burant, S. S. Iyengar, J. Tomasi, M. Cossi, N. Rega, J. M. Millam, M. Klene, J. E. Knox, J. B. Cross, V. Bakken, C. Adamo, J. Jaramillo, R. Gomperts, R. E. Stratmann, O. Yazyev, A. J. Austin,

R. Cammi, C. Pomelli, J. W. Ochterski, R. L. Martin, K. Morokuma, V. G. Zakrzewski, G. A. Voth, P. Salvador, J. J. Dannenberg, S. Dapprich, A. D. Daniels, Ö. Farkas, J. B. Foresman, J. V. Ortiz, J. Cioslowski, and D. J. Fox.
Gaussian 09, Revision D.01.
Gaussian, Inc., Wallingford CT (2009).

[235] V. May.
Kinetic theory of exciton–exciton annihilation.
J. Chem. Phys. **140**, 054103 (2014).

[236] B. Brüggemann and V. May.
Exciton exciton annihilation dynamics in chromophore complexes. I. Multiexciton density matrix formulation.
J. Chem. Phys. **118**, 746–759 (2003).

[237] J. Süß, J. Wehner, J. Dostál, T. Brixner, and V. Engel.
Mapping of exciton–exciton annihilation in a molecular dimer via fifth-order femtosecond two-dimensional spectroscopy.
J. Chem. Phys. **150**, 104304 (2019).

[238] A. V. Pisliakov, T. Mančal, and G. R. Fleming.
Two-dimensional optical three-pulse photon echo spectroscopy. II. Signatures of coherent electronic motion and exciton population transfer in dimer two-dimensional spectra.
J. Chem. Phys. **124**, 234505 (2006).

[239] L. Valkunas, G. Trinkunas, V. Liuolia, and R. Van Grondelle.
Nonlinear annihilation of excitations in photosynthetic systems.
Biophys. J. **69**, 1117–1129 (1995).

[240] L. Valkunas, I. H. M. van Stokkum, R. Berera, and R. van Grondelle.
Exciton migration and fluorescence quenching in LHCII aggregates: Target analysis using a simple nonlinear annihilation scheme.
Chem. Phys. **357**, 17–20 (2009).

[241] P. Malỳ, J. Lüttig, A. Turkin, J. Dostál, C. Lambert, and T. Brixner.
From wavelike to sub-diffusive motion: exciton dynamics and interaction in squaraine copolymers of varying length.
Chem. Sci. **11**, 456–466 (2020).

[242] T. Bittner, K.-D. Irrgang, G. Renger, and M. R. Wasielewski.
Ultrafast excitation energy transfer and exciton-exciton annihilation processes in isolated light harvesting complexes of photosystem II (LHC II) from spinach.
J. Phys. Chem. **98**, 11821–11826 (1994).

[243] V. Gulbinas, L. Valkunas, D. Kuciauskas, E. Katilius, V. Liuolia, W. Zhou, and R. E. Blankenship.
Singlet–Singlet Annihilation and Local Heating in FMO Complexes.

J. Phys. Chem. **100**, 17950–17956 (1996).

[244] G. Trinkunas, J. L. Herek, T. Polivka, V. Sundström, and T. Pullerits.
Exciton delocalization probed by excitation annihilation in the light-harvesting antenna LH2.
Phys. Rev. Lett. **86**, 4167 (2001).

[245] I.-W. Hwang, T. Kamada, T. K. Ahn, D. M. Ko, T. Nakamura, A. Tsuda, A. Osuka, and D. Kim.
Porphyrin boxes constructed by homochiral self-sorting assembly: optical separation, exciton coupling, and efficient excitation energy migration.
J. Am. Chem. Soc. **126**, 16187–16198 (2004).

[246] M. G. Müller, M. Hucke, M. Reus, and A. Holzwarth.
Annihilation processes in the isolated D1-D2-cyt-b559 reaction center complex of photosystem II. An intensity-dependence study of femtosecond transient absorption.
J. Phys. Chem. **100**, 9537–9544 (1996).

[247] H. Wu and M. A. Berg.
Multiple population-period transient spectroscopy (MUPPETS) in excitonic systems.
J. Chem. Phys. **138**, 034201 (2013).

[248] E. van Veldhoven, C. Khurmi, X. Zhang, and M. A. Berg.
Time-Resolved Optical Spectroscopy with Multiple Population Dimensions: A General Method for Resolving Dynamic Heterogeneity.
ChemPhysChem **8**, 1761–1765 (2007).

[249] C. Khurmi and M. A. Berg.
Parallels between multiple population-period transient spectroscopy and multidimensional coherence spectroscopies.
J. Chem. Phys. **129**, 064504 (2008).

[250] K. Sahu, H. Wu, and M. A. Berg.
Multiple population-period transient spectroscopy (MUPPETS) of CdSe/ZnS nanoparticles. I. exciton and biexciton dynamics.
J. Phys. Chem. B **117**, 15257–15271 (2013).

[251] C. Heshmatpour, P. Malevich, F. Plasser, M. Menger, C. Lambert, F. Šanda, and J. Hauer.
Annihilation dynamics of molecular excitons measured at a single perturbative excitation energy.
J. Phys. Chem. Lett. **11**, 7776–7781 (2020).

[252] B. Brüggemann and T. Pullerits.
Nonperturbative modeling of fifth-order coherent multidimensional spectroscopy in light harvesting antennas.
New J. Phys. **13**, 025024 (2011).

[253] M. I. S. Röhr, H. Marciniak, J. Hoche, M. H. Schreck, H. Ceymann, R. Mitric, and C. Lambert.
Exciton dynamics from strong to weak coupling limit illustrated on a series of squaraine dimers.
J. Phys. Chem. C **122**, 8082–8093 (2018).

[254] S. Draeger.
Rapid Two-Dimensional One-Quantum and Two-Quantum Fluorescence Spectroscopy.
Ph.D. thesis, Würzburg (2019).

[255] C. Zhong, D. Bialas, C. J. Collison, and F. C. Spano.
Davydov splitting in squaraine dimers.
J. Phys. Chem. C **123**, 18734–18745 (2019).

[256] M. Kasha, H. Rawls, and M. A. El-Bayoumi.
The exciton model in molecular spectroscopy.
Pure Appl. Chem. **11**, 371–392 (1965).

[257] M. H. Schreck.
Synthesis and Photophysics of Linear and Star-Shaped Oligomers of Squaraine Dyes.
Ph.D. thesis, Würzburg (2018).

[258] M. Lorenc, M. Ziolek, R. Naskrecki, J. Karolczak, J. Kubicki, and A. Maciejewski.
Artifacts in femtosecond transient absorption spectroscopy.
Appl. Phys. B **74**, 19–27 (2002).

[259] D. Paleček, P. Edlund, E. Gustavsson, S. Westenhoff, and D. Zigmantas.
Potential pitfalls of the early-time dynamics in two-dimensional electronic spectroscopy.
J. Chem. Phys. **151**, 024201 (2019).

[260] M. Rodríguez and T. Kramer.
Machine learning of two-dimensional spectroscopic data.
Chem. Phys. **520**, 52–60 (2019).

[261] T. Kenneweg.
Personal communication.
December 2020.

[262] G. Nardin, T. M. Autry, K. L. Silverman, and S. T. Cundiff.
Multidimensional coherent photocurrent spectroscopy of a semiconductor nanostructure.
Opt. Express **21**, 28617–28627 (2013).

[263] H. Li, A. Gauthier-Houle, P. Grégoire, E. Vella, C. Silva-Acuña, and E. R. Bittner.
Probing polaron excitation spectra in organic semiconductors by photoinduced-absorption-detected two-dimensional coherent spectroscopy.
Chem. Phys. **481**, 281–286 (2016).

[264] R. D. Schaller and V. I. Klimov.
High efficiency carrier multiplication in PbSe nanocrystals: implications for solar energy conversion.
Phys. Rev. Lett. **92**, 186601 (2004).

[265] R. D. Schaller, M. Sykora, J. M. Pietryga, and V. I. Klimov.
Seven excitons at a cost of one: Redefining the limits for conversion efficiency of photons into charge carriers.
Nano Lett. **6**, 424–429 (2006).

[266] O. E. Semonin, J. M. Luther, S. Choi, H.-Y. Chen, J. Gao, A. J. Nozik, and M. C. Beard.
Peak external photocurrent qantum efficiency exceeding 100% via MEG in a quantum dot solar cell.
Science **334**, 1530–1533 (2011).

[267] A. Shabaev, C. S. Hellberg, and A. L. Efros.
Efficiency of multiexciton generation in colloidal nanostructures.
Acc. Chem. Res. **46**, 1242–1251 (2013).

[268] D. Timmerman, I. Izeddin, P. Stallinga, I. Yassievich, and T. Gregorkiewicz.
Space-separated quantum cutting with silicon nanocrystals for photovoltaic applications.
Nat. Photonics **2**, 105–109 (2008).

[269] A. Franceschetti, J. An, and A. Zunger.
Impact ionization can explain carrier multiplication in PbSe quantum dots.
Nano Lett. **6**, 2191–2195 (2006).

[270] R. J. Ellingson, M. C. Beard, J. C. Johnson, P. Yu, O. I. Micic, A. J. Nozik, A. Shabaev, and A. L. Efros.
Highly efficient multiple exciton generation in colloidal PbSe and PbS quantum dots.
Nano Lett. **5**, 865–871 (2005).

[271] A. Shabaev, A. L. Efros, and A. J. Nozik.
Multiexciton generation by a single photon in nanocrystals.
Nano Lett. **6**, 2856–2863 (2006).

[272] H. M. Jaeger, K. Hyeon-Deuk, and O. V. Prezhdo.
Exciton multiplication from first principles.
Acc. Chem. Res. **46**, 1280–1289 (2013).

[273] C. Smith and D. Binks.
Multiple Exciton Generation in Colloidal Nanocrystals.
Nanomaterials **4**, 19–45 (2014).

[274] H. Goodwin, T. C. Jellicoe, N. J. Davis, and M. L. Böhm.
Multiple exciton generation in quantum dot-based solar cells.
Nanophotonics **7**, 111–126 (2018).

[275] H. Tahara, M. Sakamoto, T. Teranishi, and Y. Kanemitsu.
Harmonic quantum coherence of multiple excitons in PbS/CdS core-shell nanocrystals.
Phys. Rev. Lett. **119** (2017).

[276] H. Tahara and Y. Kanemitsu.
Coherent spectroscopy of multiple excitons in colloidal nanocrystal quantum dots.
Chem. Nano. Mat. **5**, 977–984 (2019).

[277] J. O. Tollerud and J. A. Davis.
Separating pathways in double-quantum optical spectroscopy reveals excitonic interactions.
Laser Photonics Rev. **11**, 1600249 (2017).

[278] A. B. Madrid, K. Hyeon-Deuk, B. F. Habenicht, and O. V. Prezhdo.
Phonon-induced dephasing of excitons in semiconductor quantum dots: Multiple exciton generation, fission, and luminescence.
ACS Nano **3**, 2487–2494 (2009).

[279] E. Harel.
Four-dimensional coherent electronic Raman spectroscopy.
J. Chem. Phys. **146**, 154201 (2017).

[280] N. Christensson, H. F. Kauffmann, T. Pullerits, and T. Mancal.
Origin of long-lived coherences in light-harvesting complexes.
J. Phys. Chem. B **116**, 7449–7454 (2012).

[281] M. Ferretti, V. I. Novoderezhkin, E. Romero, R. Augulis, A. Pandit, D. Zigmantas, and R. v. Grondelle.
The nature of coherences in the B820 bacteriochlorophyll dimer revealed by two-dimensional electronic spectroscopy.
Phys. Chem. Chem. Phys. **16**, 9930–9939 (2014).

[282] L. E. Kay, G. M. Clore, A. Bax, and A. M. Gronenborn.
Four-dimensional heteronuclear triple-resonance NMR spectroscopy of interleukin-1 beta in solution.
Science **249**, 411–414 (1990).

[283] V. Motáčková, J. Nováček, A. Zawadzka-Kazimierczuk, K. Kazimierczuk, L. Žídek, H. Šanderová, L. Krásnỳ, W. Koźmiński, and V. Sklenář.
Strategy for complete NMR assignment of disordered proteins with highly repetitive sequences based on resolution-enhanced 5D experiments.
J. Biomol. NMR **48**, 169–177 (2010).

[284] H. W. Orton, J. Stanek, T. Schubeis, D. Foucaudeau, C. Ollier, A. W. Draney, T. Le Marchand, D. Cala-De Paepe, I. C. Felli, R. Pierattelli, et al.
Protein NMR Resonance Assignment without Spectral Analysis: 5D SOlid-State Automated Projection SpectroscopY (SO-APSY).
Angew. Chem. Int. Ed. **59**, 2380–2384 (2020).

[285] A. P. Spencer, W. O. Hutson, and E. Harel.
Four-dimensional coherent spectroscopy of complex molecular systems in solution.
J. Phys. Chem. C **123**, 6303–6315 (2019).

[286] E. Harel, A. F. Fidler, and G. S. Engel.
Single-shot gradient-assisted photon echo electronic spectroscopy.
J. Phys. Chem. A **115**, 3787–3796 (2011).

[287] H. Nyquist.
Certain topics in telegraph transmission theory.
Proc. IEEE **90**, 280–305 (2002).

[288] N. M. Kearns, R. D. Mehlenbacher, A. C. Jones, and M. T. Zanni.
Broadband 2D electronic spectrometer using white light and pulse shaping: Noise and signal evaluation at 1 and 100 kHz.
Opt. Express **25**, 7869–7883 (2017).

[289] M. H. Levitt, P. Madhu, and C. E. Hughes.
Cogwheel Phase Cycling.
J. Magn. Reson. **155**, 300–306 (2002).

[290] E. Harel.
Zooming in on vibronic structure by lowest-value projection reconstructed 4D coherent spectroscopy.
J. Chem. Phys. **148**, 194201 (2018).

[291] V. Butkus, D. Zigmantas, L. Valkunas, and D. Abramavicius.
Vibrational vs. electronic coherences in 2D spectrum of molecular systems.
Chem. Phys. Lett. **545**, 40–43 (2012).

[292] R. Tempelaar, T. L. Jansen, and J. Knoester.
Vibrational beatings conceal evidence of electronic coherence in the FMO light-harvesting complex.
J. Phys. Chem. B **118**, 12865–12872 (2014).

[293] J. Cao, R. J. Cogdell, D. F. Coker, H.-G. Duan, J. Hauer, U. Kleinekathöfer, T. L. C. Jansen, T. Mančal, R. J. D. Miller, J. P. Ogilvie, V. I. Prokhorenko, T. Renger, H.-S. Tan, R. Tempelaar, M. Thorwart, E. Thyrhaug, S. Westenhoff, and D. Zigmantas.
Quantum biology revisited.
Sci. Adv. **6**, eaaz4888 (2020).

Individual Contributions

All co-authors of those publications, which were reprinted in Chapters 2–4 in this thesis, have been informed about the specified own contributions, as stated below, and they agree to them.

Molecular Coherent Three-Quantum Two-Dimensional Fluorescence Spectroscopy

S. Mueller and T. Brixner, *J. Phys. Chem. Lett.* **11**, 5139–5147 (2020).

Author	**S.M.**	**T.B.**
Idea and method development	100%	
Implementation of the method	100%	
Performing 2D experiments	100%	
Analysis and interpretation of the data	75%	25%
Theoretical simulations	100%	
Internal discussions, discussion of results	50%	50%
Writing first version of the manuscript	100%	
Correction of the manuscript		100%
Publication coordination		100%

Observing Multiexciton Correlations in Colloidal Semiconductor Quantum Dots via Multiple-Quantum Two-Dimensional Fluorescence Spectroscopy

S. Mueller, J. Lüttig, L. Brenneis, D. Oron, and T. Brixner, *ACS Nano* **15**, 4647–4657 (2021).

Author	**S.M.**	**J.L.**	**L.B.**	**D.O.**	**T.B.**
Idea and method development	100%				
Implementation of the method	100%				
Performing 2D experiments	55%	30%	15%		
Analysis and interpretation of experimental data	50%	15%	5%	20%	10%
Performing theoretical simulations and calculations	100%				
Discussion of results	20%	20%	20%	20%	20%
Writing first version of the manuscript	100%				
Correction of the manuscript		20%	5%	20%	55%
Publication coordination					100%

Rapid Multiple-Quantum Three-Dimensional Fluorescence Spectroscopy Disentangles Quantum Pathways

S. Mueller, J. Lüttig, P. Malý, L. Ji, J. Han, M. Moos, Todd B. Marder, Uwe H. F. Bunz, A. Dreuw, C. Lambert, and T. Brixner, *Nat. Commun.* **10**, 4735 (2019).

Author	**S.M.**	**J.L.**	**P.M.**	**L.J.**	**J.H.**	**M.M.**	**T.B.M.**	**U.H.F.B.**	**A.D.**	**C.L.**	**T.B.**
Idea and method development	100%										
Implementation of the method	100%										
Performing 3D spectroscopy	50%	50%									
Analysis and interpretation of 3D spectra	70%	10%					10%				10%
Synthesis of the TIPS-tetraazapentacene dianion		20%		80%							
Spectroelectrochemistry: performing experiment and analyzing data						50%				50%	
Development of a theoretical model for the simulation of 3D spectra	50%		50%								
Performing simulations of the 3D spectra	100%										
TD–DFT calculations: performing calculations and analyzing data					50%				50%		
Discussion of results	10%	9%	9%	9%	9%	9%	9%	9%	9%	9%	9%
Writing first version of the manuscript	90%	10%									
Correction of the manuscript		15%	15%	5%	5%	5%	15%	5%	5%	5%	25%
Publication coordination							50%				50%

Acknowledgements

Although in this thesis I mainly wrote about methods that measure phenomena happening on an ultrashort timescale, the actual timescale on which this thesis was created was much, much longer. Nonetheless, it feels like time has passed very quickly. I think this may be a result of science being just such an exciting matter to me. But more importantly, it is a result of working in a great team with many talented and motivated people. For me, it has been a pleasure to work in such an environment. In fact, this work has been build on a fundament of fruitful collaboration with many people, for which I am very grateful. In particular, I would like to express special thanks to the following people.

- My supervisor and mentor **Prof. Dr. Tobias Brixner** for constant support throughout the past years and for the appreciation of my ideas and contributions. I am grateful for every piece of advice and deeply appreciate the array of opportunities which he offered to develop new skills and to stimulate personal growth. Above all, I am very thankful for the freedom he has given me in designing research.

- **Julian Lüttig** for all the fruitful collaborations together, the great time with experiments in the lab as well as for all valuable scientific as well as humorous discussions inside or outside the lab.

- To round up the Lab 5 crew, great thanks goes to **Dr. Pavel Malý**. I really enjoyed the great collaboration in the TIPS–TAP and (F/C)EEI2D projects on the squaraine heterodimers. It was pretty goat! In particular, I am grateful for the help on the mathematical formulation of the FDEEI2D signals.

- **Prof. Dr. Dr. h.c. Todd B. Marder** for all the stimulating and pleasant discussions concerning the TIPS–TAP project. Thanks also for initiating the cooperation with many other nice people, which was undoubtedly helpful for the success of the project.

- **Prof. Dr. Christoph Lambert** for the nice collaboration within the TIPS–TAP project and the (F/C)EEI2D project on the squaraine heterodimers.
- **Prof. Dr. Dan Oron** for all the very helpful advice and the stimulating discussions concerning the quantum dot project.
- **Dr. Matthias Hensen** and **Sebastian Pres** for being valued colleagues in physical and rock music science and who had always an open ear for my questions and bass lines.
- **Dr. Simon Draeger** for the collaboration and the nice time at the beginning of my PhD.
- **Bernhard Huber** for his valuable contributions to the QD toolbox.
- **Prof. Dr. Uwe H. F. Bunz** for providing the TIPS–TAP molecules and **Dr. Lei Ji** for the synthesis of the dianion.
- **Michael Moos** for the measurement of electrochemistry and **Evripidis Michail** for the two-photon absorption measurement of the TIPS–TAP dianion.
- **Dr. Jie Han** and **Prof. Dr. Andreas Dreuw** for the TD-DFT calculations of the TIPS–TAP dianion.
- **Florian Hirsch** for help concerning the design of the tubing system for the TIPS–TAP measurements.
- **Heiko Hildenbrand** for the countless times he offered the world's best taxi service to me. I especially liked the music!
- **Hans-Peter Solowan** for organizing the wonderful accommodations during the DPG spring meetings in Erlangen and Rostock.
- **Lysanne Dietrich** for organizing the best ski seminar ever!
- **Sabine Fuchs**, **Belinda Böhm**, and **Ivonne Vollert** for taking care of technical matters concerning the Spitfire and the MaiTai laser systems and for kind help in organizing lab equipment.
- **Uwe Reuß** and **Reiner Eck** for help with technical issues and support in matters of electronics.

- **Andrea Gehring** and **Susanne Pfarr** for great and friendly support in all organizational matters.

- **Dr. Victor Lisinetskii** for LabVIEW programming. His contribution was highly important for the transition from 32 to 64 bit LabVIEW.

- **Dr. Christoph Brüning** und **Aleksander Paravac** from the Rechenzentrum of our university for support concerning the high-performance cluster.

- **Dr. Roland Colditz** and **Dr. Hans–Christian Schmitt** for the organization of the "Praktikum Physikalische Chemie." I am not sure which version of the Praktikum I liked most, the new one or the old one. In any case, I enjoyed teaching in both versions of the Praktikum.

- **Tristan Kenneweg** and **Prof. Dr. Walter Pfeiffer** for offering me to continue working on the QD toolbox. I think we had a great time during our Matlab programming sessions as well as during writing the QDT paper draft!

- My excellent Bachelor students **Luisa Brenneis, Niklas Klosterhalfen**, and **Julian Kütt**. I was very lucky to be your supervisor. You have all done a very good job, for which I would like to express my gratitude. I hope you will all continue to follow a path in science, be it inside or outside university. I wish you all the best for that!

- My Master's intern **Alexander Geis** for his contribution to the quantum dot project.

- **All other members of the Chair of Physical Chemistry I** for the nice and cooperative working atmosphere and the unforgettable time.

- My family, especially my parents **Günter** and **Evangelia** for their unwavering support and belief in me.

- My love **Lea** for her tireless support and dedication what has given me strength and brightens my life every day.

Affidavit

I hereby confirm that the present thesis entitled

"Coherent Multiple-Quantum Multidimensional Fluorescence Spectroscopy"

is the result of my own work and that I have created this dissertation independently, i.e., in particular without any help or support from commercial consultants.
I further declare that I have not used any sources or resources other than those indicated by me. The text passages of this thesis, which were taken from other work in terms of their wording or meaning, have been signified by me through indicating the source.

I also declare that this dissertation as a whole or a part of this dissertation has not been submitted in any other examination process neither in identical nor in similar form.

Würzburg, May 7, 2021

Stefan Müller

Eidesstattliche Erklärung

Hiermit erkläre ich an Eides statt, dass die vorliegende Dissertation mit dem Titel

"Kohärente Multidimensionale Multiquanten-Fluoreszenzspektroskopie"

das Resultat meiner eigenen Arbeit ist und ich diese Dissertation selbstständig, d.h. insbesondere ohne Hilfe eines kommerziellen Promotionsberaters, angefertigt habe. Ich erkläre weiterhin, dass ich keine anderen als die von mir angegebenen Quellen und Hilfsmittel verwendet habe. Die Stellen der Arbeit, die dem Wortlaut oder dem Sinn nach anderen Werken entnommen sind, wurden von mir unter Angabe der Quelle kenntlich gemacht.
Ich erkläre außerdem, dass diese Dissertation als Ganzes oder ein Teil der Dissertation weder in gleicher noch in ähnlicher Form bereits in einem anderen Prüfungsverfahren vorgelegen hat.

Würzburg, den 07. Mai 2021

Stefan Müller